CHEMISTRY OF METAL COMPLEXES IN THE GAS PHASE

AMENEH GHOLAMI

Chemistry of Metal Complexes in the Gas phase

by

Ameneh Gholami

B.Sc., Guilan University, Rasht-Iran, 2003

M.Sc., Tarbiat Modares University, Tehran-Iran, 2006

A thesis submitted to the School of Graduate Studies in partial fulfillment of the requirements for the degree of Doctor of Philosophy

Department of Chemistry

Memorial University

St. John's, Newfoundland, Canada

April 2013

Abstract

Gas phase chemistry of ions provides important insight into the reactivity, thermochemistry, reaction mechanisms, and structures of ions without the added complexity of solvent. Fourier Transform Ion Cyclotron Resonance (FT-ICR) mass spectrometry is the most commonly used and ideally suited technique to study chemistry of ions in the gas phase. The ICR cell is like a small laboratory with controllable conditions, where ions are trapped and undergo rcactions, therefore elementary steps of reactions can be easily tracked. Structural studies employing activation/fragmentation techniques such as infrared multiple photon dissociation (IRMPD) or sustained off resonance irradiation collisionally induced dissociation (SORI-CID) can be easily conducted using an FTICR instrument.

This thesis presents study of transition metal complexes reactions with neutral molecules in the gas phase. The first kinetic experiments were conducted for the association reactions of unsaturated ruthenium complexes $[Ru(bipy)X]^{2+}$ (X bipyridine, 2-(pyridin-4-yl)-1,3-benzothiazole, or 5-aminophenathroline) with CO and O_2 to explore mechanism of the ion-molecule reactions in the low pressure environment of the ICR cell. The association adduct complex $[Ru(bipy)_2CO]^{2+}$ was then used to activate C-H or C-C bonds of various alkanes. Computational chemistry was also employed to further investigate the mechanism of the dehydrogenation and demethanation reactions between chemically activated $[Ru(bipy)_2CO]^{2+}$ and alkane molecules.

Finally, structures and fragmentation pathways of Zn^{2+} complexes with proline were studied. IRMPD spectroscopy in conjunction with computational chemistry was used to explore the structures of the deprotonated zinc-proline complex, $[Zn(Pro-H)]^+$, and the singly hydrated complex $[Zn(Pro-H)(H_2O)]^+$. Furthermore, fragmentation reactions of deprotonated zinc-amino acid dimer complexes $[Zn(A-H)(A)]^+$ (A = proline, sarcosine, alanine, and glycine) were studied using IRMPD and SORI-CID. The different fragmentation channels observed for secondary amine complexes, proline and sarcosine, and primary amine complexes, alanine and glycine, were interpreted by computational chemistry results.

Acknowledgment

First and foremost I would like to express my deeply-felt thanks to my wonderful supervisor, Prof. Travis D. Fridgen, who supported me with his great knowledge experience, and patience throughout this study. I was so fortunate to have Prof. Fridgen as my supervisor.

I would like to thank Dr. Peter Pickup and Dr. Sunil Pansare for their input and assistance as part of supervisory committee.

I would also like to thank our research group members specially Dr. Elizabeth Gillis for her generous assistance.

My special thanks to kind staffs in general office of chemistry department, Viola, Rosalind, Mary, Gina, and Ebony.They provide a warm and lovely environment for students.

My endless love goes to my parents, Shahrbanou and Hassan, whose greatest support and never ending love have always been with me. I wish to express my deepest love to my husband, Reza, who has always been there for me.

Table of Content

List of Figures and Appendices

List of Tables

List of Schemes

List of Abbreviations and Terms

Ab initio	a Latin term for "from the beginning"
Ala	Alanine
B3LYP	Becke-(3 parameter)-Lee-Yang-Parr
bipy	2,2'-bipyridine
CW	continuous wave
CRM	charged residue model
CID	collision-induced dissociation
DNA	deoxyribonucleic acid
DFT	density functional theory
ESI	electrospray ionization
ECP	effective core potential
FEL	free electron laser
FT	Fourier transform
FTICR	Fourier transform ion cyclotron resonance
FTICR-MS	Fourier transform ion cyclotron resonance mass spectrometry
Gly	glycine
HF	Hartree-Fock
ICR	ion cyclotron resonance
IEM	ion evaporation model
IR	infrared

IRMPD	infrared phodissociation spectroscopy
IVR	intravibrational redistribution
KTP	potassium titanyl phosphate
laser	light amplification by stimulated emission of radiation
LANL2DZ	Los Alamos National Laboratory 2-double-z
LDA	local density approximation
MCTS	multicentered transition state
MP2	Møller-Plesset
MS	mass spectrometry
MS/MS or MS^n	tandem mass spectrometry
Nd:YAG	Nd:$Y_3A_{l5}O_{12}$ (neodymium-doped yttrium aluminium garnet)
OPA	optical parametric amplifier
OPO	optical parametric oscillator
phen	5-aminophenathroline
Pro	proline
QIT	quadrupole ion trap
RNA	ribonucleic Acid
RF	radio frequency
RRKM	Rice–Ramsperger–Kassel–Marcus
Sar	sarcosine
sn	2-(pyridin-4-yl)-1,3-benzothiazole
SORI-CID	sustained off-resonance collision-induced

TOF	time of flight

Chapter 1. Introduction

1.1. General Introduction: Ion Chemistry in the Gas Phase

Why study the chemistry of ions in the gas phase? The demand for knowledge about gas phase chemistry of ions has grown over the last decade. Definitely, this interest has been due to obtaining intrinsic properties of bare or ligated transition metal ions, without the added complexity of solvent as is the case for the condensed phase. Gas phase studies of ions not only provide valuable links to reaction mechanisms and structures of ions, but also allow one to assess the effect of solvent on reactivities or properties of ions.[1] Particular attention has been paid to gas phase ion-molecule reactions since better understanding the reactivity and reaction mechanisms helps to improve catalytic processes.[2-6] Gas phase experiments can provide a low pressure environment where reactant concentrations are sufficiently low to allow us to study an ion-molecule reaction on a step by step basis. For example, the Degussa process for hydrogen cyanide synthesis on the industrial scale was modeled for the first time by monitoring reactions between methane and ammonia on a single platinium cation Pt^+ in the gas phase.[7] Investigation of the elementary steps for the reaction showed that Pt^+ selectively reacts with methane rather than ammonia to produce $PtCH_2^+$ (Scheme 1.1). Following the initial step, $PtCH_2^+$ reacts with NH_3 followed by dehydrogenation processes to produce $PtHCN^+$ (Scheme 1.1). This has been then extended to an industrial scale, and is used as one of the processes for production of HCN in industry. In this area, various transition metals and metal cluster ions were also studied for increasing selectivity of production of HCN.[8,9]

$Pt^+ + CH_4 \rightarrow PtCH_2^+ + H_2$

$PtCH_2^+ + NH_3 \rightarrow PtCH_2NH_3^+ \rightarrow PtCH_2NH^+ + H_2 \rightarrow PtHCN^+ + H_2$

Scheme 1.1. The reaction mechanism for Degussa process modeled by the gas phase studies of reaction between Pt^+ and ammonia and methane.[7]

Since carbon and hydrogen are the major atoms in petroleum compounds, metal mediated activation of C-H and C-C bonds are very important for production of useful petroleum-based compounds. In recent years, development of gas phase ion-molecule reactions has led to considerable attempts to introduce new metal complexes for catalytic activation and functionalization of organic complexes. C-H bond activation leads either to dehydrogenation processes, producing olefins which are commonly used as industrial feedstocks in polymerization, or functionalization processes involving addition of various functional groups such as O-H, S-H, N-H, or aromatic groups across C-H bonds.[10-14] These processes are catalyzed by metal complexes. More knowledge about the mechanisms and elementary steps of these reactions using simple systems in the gas phase can help to design and develop more efficient catalysts.

Reactions of interstellar clouds can be studied in a gas phase laboratory. In the interstellar medium, molecules or atoms are ionized by absorbing energy from UV radiation. These ions then react with atmospheric molecules initiating synthesis of polyatomic compounds.[15] For example, reactions of H_3^+ and CH_3^+ with different neutral atmospheric molecules play a critical role in growth of interstellar clouds.[16] In this

respect, gas phase studies have allowed determination of the mechanisms and rate coefficient of reactions.[17-19]

The study of gas phase ion-molecule reactions began with small ligands such as CO[20], H_2O[21], NH_3[19], CO_2[20], and small hydrocarbons[5,22] and has continued with large biological molecules such as amino acids, peptides, and proteins.[23-31] Interactions of metal ions with proteins can induce new fragmentation processes that can be studied by means of tandem mass spectrometry, which is commonly used for determining amino acid sequences.[32-35] Furthermore, binding metal ions with biological molecules can stabilize a particular conformation which is genetically or chemically significant. For example, cobalt ion has been known to induce the conversion of the B-conformation of DNA to the Z-conformation.[36] Metal ions also have been shown to stabilize double helix or single helix forms of nucleic acids.[35] Thus, the gas phase study of metal-biological complexes is useful for exploring the influence of metal ions on conformational changes of biomolecules. Study of the interactions between metals and biological molecules is beneficial for exploring the catalytic effect of metal ions on the aggregation of amino acids leading to progression of Alzheimer's disease. [37,38]

In this thesis, various gas-phase experiments under ICR mass spectrometer conditions have been carried out for three different goals. The first was a kinetic and mechanistic study of reactions between ruthenium complexes and neutral molecules producing association ion-molecule complexes. In Chapter 3 kinetic modeling of radiative association reactions helped characterize the association reaction between coordinatively unsaturated ruthenium complexes and small neutral molecules. Secondly,

catalytic dehydrogenation and demethanation of alkanes by newly formed complexes from the association of neutral molecules with ruthenium complexes were studied and are reported in Chapter 4. Finally, the structures as well as fragmentation reactions of Zn^{2+}-bound amino acid complexes are explored in chapters 5 and 6. In particular, the fragmentation pathway and reaction mechanism for dehydrogenation of a deprotonated proline dimer complexes with Zn^{2+}, $[Zn(Pro\text{-}H)(Pro)]^+$, were investigated using activation/fragmentation mass spectrometry techniques in conjunction with computational chemistry, and is discussed in Chapter 6.

1.1.1. Ion-Molecule Radiative Association Reactions

Gas phase ion-molecule association reactions are a principal step in catalytic activation of neutral molecules in interstellar molecule synthesis reactions and industrial petroleum reactions.[17,39] Kinetics and thermodynamic studies of these reactions are required for modeling and detailed characterization of reactions.

Mass spectrometry is well-suited for such studies, where ions are generated by one of many ionization techniques, then allowed to react with neutral molecules. In this method, intensities of reactant ions and ion-molecule adduct ions are monitored as a function of reaction time. In the early years of working with mass spectrometers, the ion source was the reaction vessel for gas phase ion-molecule reactions.[40] However, study ion-molecule reactions under highly-controlled conditions, various ion trapping methods such as Fourier transform ion cyclotron resonance FTICR mass spectrometry and

quadrupole ion trap QIT mass spectrometry were employed.[5,41,42] In the last 10 years thousands of papers have been published about gas phase ion-molecule reactions in an ion trap. This shows the influence of mass spectrometry on the characterization and development of new chemical processes.

FTICR mass spectrometry is the most commonly used and ideally suited technique to study ion-molecule reactions, where ions are passively trapped inside the ICR cell and undergo reactions with neutral molecules. Under the low pressure conditions of the ICR cell, radiative association is the common mechanism for formation of ion-molecule complexes. Modeling of radiative association kinetics has been extensively employed to obtain useful information such as bond strengths for various ion-molecule complexes.[43-50] These studies indicated that the kinetic modeling can give the bond strength of ion-neutral complexes with a sufficient precision.

A radiative association reaction can be described as

$$A^+ + B \xrightarrow{k_{ra}} AB^+ + h\nu \qquad 1.1$$

where k_{ra} is a phenomenological second-order rate constant, and $h\nu$ is the photon emitted in the infrared region. A more detailed mechanism for an ion-molecule association reaction is

$$A^+ + B \underset{k_b}{\overset{k_f}{\leftrightarrow}} AB^{+*} \xrightarrow{k_r} AB^+ + h\nu \qquad 1.2$$

$$AB^{+*} \xrightarrow{k_{c\beta[M]}} AB^+ \qquad 1.3$$

where k_f is a collision rate constant for formation of a metastable ion-molecule complex AB^{+*}, and k_b is an unimolecular dissociation rate constant of the newly formed AB^{+*}. This metastable complex, AB^{+*}, is stabilized by emission of infrared photons with rate constant k_r to generate AB^+. The AB^{+*} ion can also be stabilized by collision with a neutral molecule; k_cß is the rate constant for collisional stabilization, ß is the fraction of neutral molecules that stabilizes the complex through collisions, which is assumed ß=1 for the strong collisional stabilization, and [M] is the concentration of neutral molecules.[51] In this mechanism, redissociation of AB^{+*} to its reactants is in competition with the stabilization of AB^{+*} through infrared photon emission. For pressures above 10^{-7} mbar, collisional stabilization can be important. At pressures lower than 10^{-7} mbar, radiative emission becomes the dominant channel for stabilization.[52] By steady state analysis for the concentration of AB^{+*}, an observed bimolecular rate constant for formation of the ion-molecule complex is given by

$$k_{obs} = \frac{k_f(k_r+k_c[M])}{k_b+k_r+k_c[M]} \qquad 1.4$$

By performing a Taylor series expansion about [M]=0, k_{obs} is presented as

$$k_{obs} = \frac{k_f k_r}{k_b+k_r} + \frac{k_f k_b k_c[M]}{(k_b+k_r)^2} \qquad 1.5$$

As seen in Eq 1.5 the bimolecular rate constant equation is first order in the concentration of neutral molecules. Therefore, a pressure dependent experiment can provide k_b and k_r, respectively, from slope and intercept of the observed rate constant, k_{obs}, as a function of pressure as long as one assumes k_f and k_c are simply collision rate constants that can be

computed.[53] Theoretical k_b values can also be calculated by the Rice–Ramsperger–Kassel–Marcus (RRKM) kinetic modeling of the radiative association reaction. In this model, the strong dependence of k_b on the energy distribution E and angular momentum j of the complex, AB^+, are employed to obtain the theoretically estimated k_b values.[50] k_b also is dependent on the binding energy of the ion-molecule complexes. The agreement between measured value of k_b with the estimated k_b value from RRKM modeling has been used to determine the dissociation energy of ion-molecule complexes. [43-49]

1.1.1.1 Determination of Binding Energy by FTICR Radiative Association Kinetics Measurements

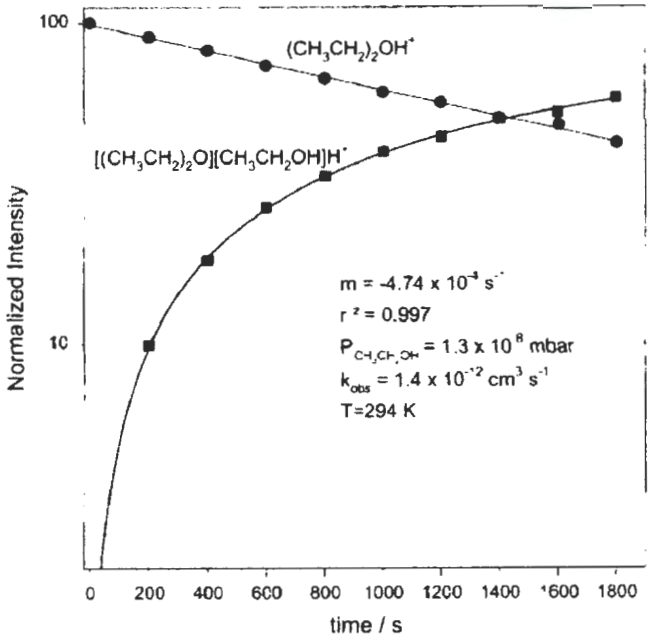

Figure 1.1. A plot of intensity as a function of time for the association reaction of protonated diethyl ether with ethanol. Figure adapted from J. Phys. Chem. A 2002, 106, 1576-1583 with permission from American Chemical Society.[48]

There are many studies focused on low pressure radiative association to obtain binding energy of various ion-molecule complexes.[43,46,48,49] Fridgen and McMahon, determined the binding energies of the unsymmetric diethyl ether/ethanol proton-bound dimer, using radiative association kinetics measurements.[48] At the very low pressures of the ICR cell, the collision between protonated diethyl ether and ethanol results in the association of ethanol to protonated ethyl ether, Eq. 1.6.

$$[(CH_3CH_2)_2OH]^+ + CH_3CH_2OH \xrightarrow{k_{ra}} [(CH_3CH_2)_2O][CH_3CH_2OH]H^+ \quad 1.6$$

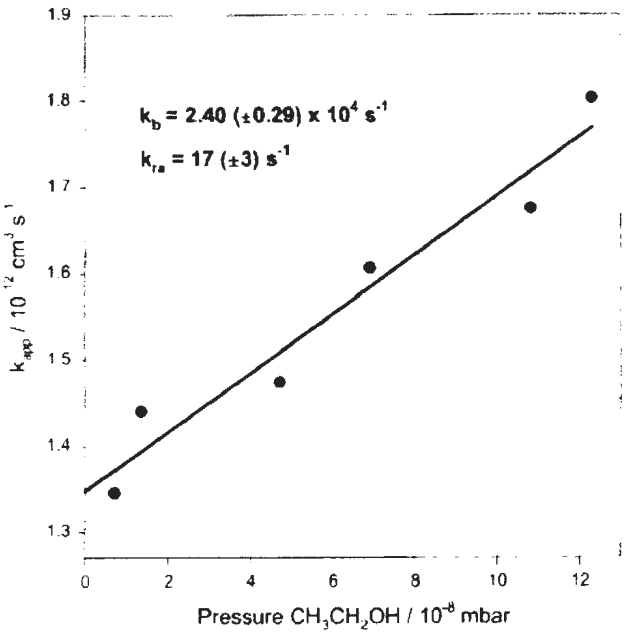

Figure 1.2. A plot of observed rate constant, k_{app}, as a function of pressure of neutral ethanol for the association reaction of protonated diethyl ether with ethanol. k_b and k_{ra} were obtained from the slope and intercept. Figure reprinted from J. Phys. Chem. A 2002, 106, 1576-1583 with permission from American Chemical Society.[48]

A plot of normalized intensities as a function of time for the association of neutral ethanol to protonated ethyl ether, $(CH_3CH_2)_2OH^+$, at an ethanol pressure of 1.3×10^{-8} is shown in Figure 1-1. There was a pressure dependency for the rate constant for the association reaction at a range of pressures between $(0.5-12) \times 10^{-8}$ mbar as shown in Figure 1.2; the higher the pressure, the greater the rate constant for the formation of proton bound dimer due to the increase in the number of third-body collisions and consequent increase in the rate of stabilization (k_c) of the nascent ion-molecule complex.

Further, there was a non-zero intercept in the plot of rate constant as a function of pressure (see Figure 1.2), indicating that the nascent complex can also be stabilized in a collision free condition by emission of infrared photons. Using Eq (1.5), unimolecular dissociation rate constant, k_b, was determined to be $2.4(\pm 6.29) \times 10^{-4}$ s^{-1} from the slope of the rate constant as a function of pressure plot with ion–polar molecule rate constants, k_f and k_c, having been computed using an algorithm of Su and Chesnavich.[53]

The theoretical values of the unimolecular rate constant, k_b, were also estimated at various binding energies of the nascent ion-molecule complex (Figure 1.3) using RRKM kinetic modeling.[54] As shown in Figure 1.3 the experimental and theoretical k_b nicely match at the binding energy of 109±1 kJ mol^{-1}. This binding energy was also in good agreement with that obtained from calculations using B3LYP/6-311G** level of theory (114.6 kJ mol^{-1}).

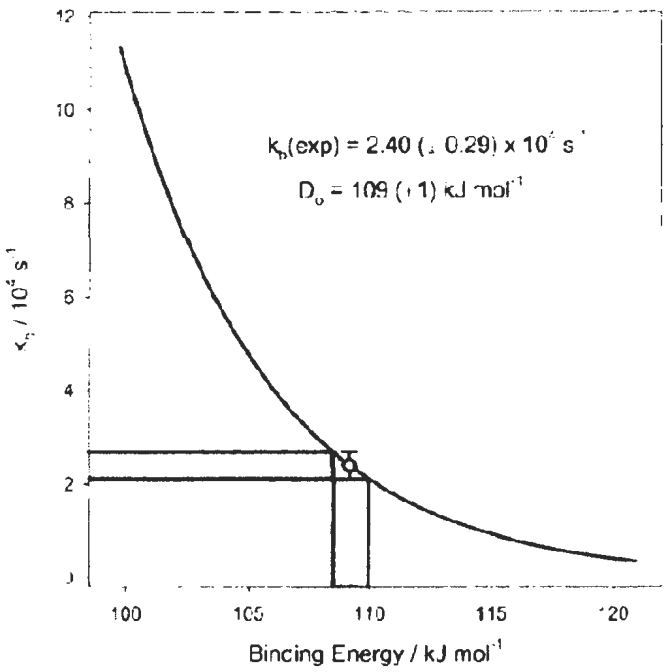

Figure 1.3. Plot of the RRKM unimolecular dissociation rate constant at various binding energies for an ion-molecule adduct complex between diethyl ether and ethanol. Figure reprinted from J. Phys. Chem. A, 2002, 106, 1576-1583 with permission from American Chemical Society.[48]

1.1.1.2. Structural Characterization of Metal Ion Clusters in the Reaction with Polar and Nonpolar Molecules by FTICR Radiative Association Kinetics Study

Radiative association reactions were also used to better understand the reactivity and to structurally characterize clusters composed of transition metal ions.[55-58] As an example, the gas phase reactivity of metallocarbohedrene $Ti_8C_{12}^+$ with small molecules such as NH_3, H_2O, CH_3CN, C_6H_6, and C_2H_4 was examined using an FTICR mass spectrometer.[58] In this study, the radiative association reaction efficiency was monitored

as the coordination number increases. For the reactions between neutral molecules and $Ti_8C_{12}^+$, a simple sequential addition was observed to produce $Ti_8C_{12}(L)_n^+$. The pseudo-first order kinetic plots showed decaying slopes of reactant ion intensity versus time with addition of each ligand indicating a reduction of the reaction rates as a function of the number of ligands. A significant decrease in addition of a fifth polar molecule such as NH_3, H_2O, and CH_3CN was observed indicating a dramatic change in binding of the ligand with the $Ti_8C_{12}^+$ cluster at this point. These results were explained by two proposed structures of $Ti_8C_{12}^+$, a pentagonal dodecahedral structure with T_h symmetry and a tetracapped tetrahedral withT_d symmetry (Figure 1.4).

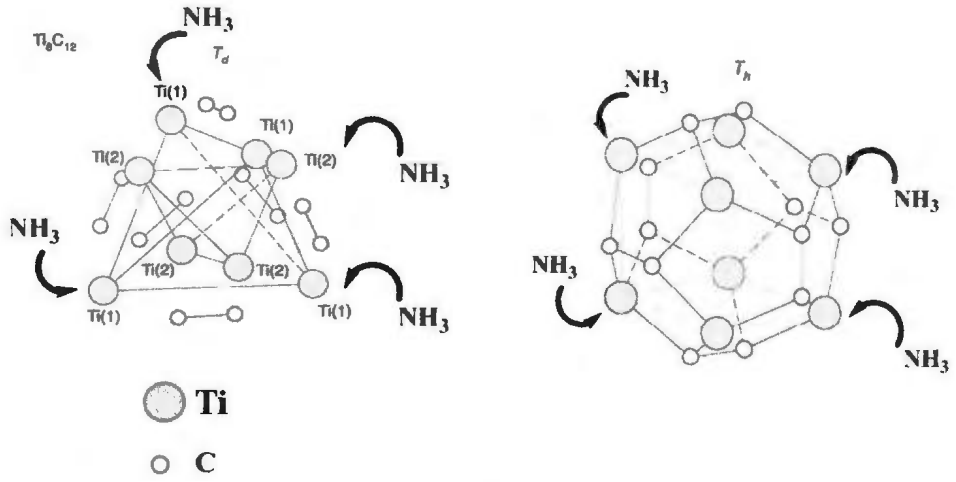

Figure 1.4. The proposed structures of Td and Th for $Ti_8C_{12}^+$ based on the experimental results obtained from monitoring rate efficiencies for the sequential addition of neutral molecules. Figure modified and reprinted from http://what-when-how.com/nanoscience-and-nanotechnology/nanocrystalline-materials-synthesis-and-properties-part-1-nanotechnology.

In the T_d symmetry of the structure of $Ti_8C_{12}^+$, four metal atoms are in each outer and inner shell. Four outer shell metals form a skeleton for the tetrahedral structure, whereas four inner shell metals are located in the faces of the tetrahedral skeleton. Based on this structure, the four metal atoms in the outer shell are more accessible than the inner shell atoms, explaining why a significant decrease of the rate efficiency was observed from the addition of fourth ligand to fifth ligand.[58]

T_h was the other proposed structure used to explain the experimental results obtained from the reactivity of $Ti_8C_{12}^+$ for the sequential addition of neutral molecules.[58] In the T_h structure of $Ti_8C_{12}^+$, four atoms are nonadjacent, and a fifth metal atom is in coordination with three metal atoms. The greater accessibility of four nonadjacent metal atoms can be the reason for the significant drop-off of the rate constant for the association of the fifth ligand. Indeed, coordination of the fifth metal atom with three metal atoms sterically hinders the attachment of the fifth ligand. In the reaction of H_2O with $Ti_8C_{12}^+$, there was less reduction in the efficiency of addition of the fifth ligand compared to NH_3 addition which is probably due to hydrogen bonding of adjacent water molecules. In the reaction of CH_3CN with $Ti_8C_{12}^+$, the association reaction was sharply cut off after the fourth ligand, and no higher number of CH_3CN was added even at longer reaction times.[58] It was suggested that CH_3CN is coordinated with two bridged metal atoms through a p - system; hence coordination of four ligands confines all eight metal atoms in $Ti_8C_{12}^+$. Non polar molecules, C_6H_6 and C_2H_4, also reacted with $Ti_8C_{12}^+$ to yield $Ti_8C_{12}(L)_n^+$ complexes. Rate constants for association of C_6H_6 were monotonically reduced from n=1 to n=4, and stopped at the fourth ligand suggesting the coordination of

a single metal atom with η^6-C_6H_6 through a p -bound. The η^6-coordination of four C_6H_6 sterically blocks the other four metal atoms in both the T_d or T_h structures. In addition, the association of C_2H_4 was observed to be slower than the other molecules, which can be explained by a relatively weaker binding energy between C_2H_4 and $Ti_8C_{12}^+$.[58] Under low pressure conditions within the ICR cell, third-body collisions are too rare; therefore, radiative stabilization is the likely pathway available for removing the excess energy of nascent ion-molecule complexes. The radiative stabilization is strongly dependent on the binding energy of the ion-molecule adduct explaining the slow association reactions of weakly-bound ligands with $Ti_8C_{12}^+$.[58,59] As seen, by this example a simple FTICR kinetic study of ion-molecule association reactions gives some useful information about the structures of metal clusters and their interactions with neutral molecules.

1.1.2. Gas phase Metal and Metal Complex Ions in Catalytic Reactions

1.1.2.1. Petroleum Reforming Processes

Conversion of hydrocarbons, the most common form of compounds in crude oil, to more useful petroleum products is essential to the petroleum industry. In the reforming process, the octane rating of hydrocarbons is upgraded by removing hydrogens to produce compounds such as alkenes, parafins, dienes, alkynes, or aromatics. Thermal cracking of hydrocarbons is another type of reforming process that involves breaking apart the long heavy hydrocarbons into lighter or short chained ones. Moreover, functionalization of hydrocarbons involving insertion of atoms or functional groups into

C-H or C-C bonds is the other important reforming process for use of fossil resources in industry.[10] For instance, a simple functionalizing process in industry is insertion of oxygen into a C-H bond of methane, converting it to methanol.[60]

1.1.2.2. Catalytic Reforming

Activation of a C-H or C-C bond is a crucial step in all the processing reactions mentioned above. Because the C-H and C-C bonds are the least reactive bonds in the chemistry of organic compounds, the activation or breakage of these bonds requires high temperature processes. Higher temperature makes these reactions faster, but it can also change molecular structures of the products. In the case of hydrocarbon functionalization processes, products might also be more reactive than reactants, activating further conversion of products to undesired compounds. Oil and gas industries annually spend a great deal of energy for high temperature processing of petroleum compounds. To overcome this important problem, one may consider catalytic conversion. Catalytic processing is a powerful method to selectively activate a particular C-H or C-C bond so that the rest of the molecule remains unchanged. A large amount of research has been focused on the design and development of catalytic systems for activation of hydrocarbons. The most common catalysts being used in petroleum reforming contain transition metals such as Cr, Mo, Co, Ni, and Pt.[61-64]

1.1.2.3. Gas Phase Activation of Hydrocarbons via Transition Metal Ions

As a result of high activity and selectivity of transition metals in activation of hydrocarbons, much attention is devoted to development of these catalytic reactions. In this respect, gas phase experiments can help us to understand the elementary steps of catalytic activation of alkanes under well-controlled conditions. Research on the gas phase activation of alkanes by transition metal ions began three decades ago.[65] Irikura and Beauchamp studied reactions between the smallest alkane, methane, and many singly charge transition metals (M^+) in the gas phase.[66,67] They found that transition metal cations can react with methane to yield H_2 and MCH_2^+. The H_2 elimination from methane is an endothermic reaction by 465 kJ mol^{-1}.[68] Hence, only metals with M-CH_2 binding energies larger than 465 kJ mol^{-1} were observed to react with methane through the H_2 elimination channel (see table 1.1).[69-71]

Bohme and coworkers studied the reactivity of 59 mono cations including those from the fourth, fifth, and sixth period transition metals with methane.[68] Atomic metals were ionized in an inductively-coupled plasma (ICP) source and allowed to be thermalized through multiple collisions with helium and argon gas. In the reaction of thermalized ions with methane two different reaction channels, elimination of H_2 and addition of CH_4 were observed. Fourth and fifth period transition metals reacted with CH_4 to form only the adduct products $M(CH_4)^+$. H_2 elimination efficiently occurred only for the sixth period transition metal ions, Ta^+, W^+, Os^+, Ir^+, and Pt^+. In order for the dissociation reaction of CH_4 into CH_2 and H_2 to take place, the binding energy $(M\text{-}CH_2)^+$

must be equal to or larger than 465 kJ mol^{-1}, which is the case for only sixth period transition metal ions Ta^+, W^+, Os^+, Ir^+, and Pt^+ as shown in Table 1.1.

Table 1.1. Methylene binding energies (kJ mol^{-1}) of fourth, fifth, and sixth period metal cations. Table reproduced from J. Phys. Chem. A, 2009, 113, 5602-5611 with permission from American Chemical Society.[68]

Fourth period		Fifth period		Sixth period	
M^+	$D_{0\ M\text{-}CH2+}$ [a]	M^+	$D_{M\text{-}CH2+}$ [a]	M^+	$D_{M\text{-}CH2+}$ [a]
Sc^+	402 ± 23	Y^+	388 ± 13	La^+	401 ± 7
Ti^+	380 ± 9	Zr^+	477 ± 4	Hf^+	435 ± 21 [b]
V^+	325 ± 6	Nb^+	427 ± 9	Ta^+	481 ± 21 [b]
Cr^+	217 ± 4	Mo^+	329 ± 12	W^+	459 ± 6
Mn^+	286 ± 9	Tc^+	347 ± 21 [c]	Re^+	400 ± 6 [d]
Fe^+	341 ± 4	Ru^+	344 ± 5	Os^+	471 [e]
Co^+	317 ± 5	Rh^+	356 ± 8	Ir^+	475 ± 3 [f]
Ni^+	306 ± 4	Pd^+	285 ± 5	Pt^+	463 ± 3
Cu^+	256 ± 5	Ag^+	>107 ± 5	Au^+	372 ± 3 [g]

a from ref [70], b from ref[72], c from ref[73], d from ref[74], e [75], f from ref[69], g from ref[76]

1.1.2.4. Mechanism for the Dehydrogenation and Demethanation of Alkanes by Metal Ions

Oxidative addition-reductive elimination is a well-known mechanism for alkane dehydrogenation or demethanation via metal ions. Oxidative addition is an important type of reaction in both synthesis and catalysis chemistry. In the oxidative addition of AB to L_nM, the A-B bond is cleaved and ligands A and B donate one electron each into the metal coordination sphere to form M-A and M-B bonds (Eq 1-7). A pair of electrons is transferred from the A-B bond into the σ orbital of the metal and in return a pair of electrons from the metal is transferred into the σ* orbital of the A-B bond resulting in the A-B bond's cleavage.[77]

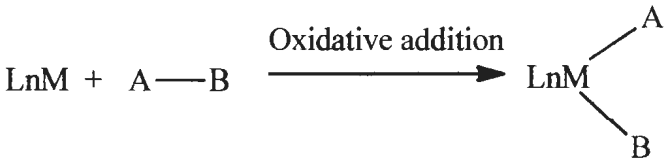

1.7

In this process, since the oxidation state and coordination number of the metal each increases by two units, it is called oxidative addition. It is a specific characteristic of transition metals that change their formal oxidation state by taking an additional covalent bond via an oxidation step and releasing a covalent bond in a reduction step of a reaction. Therefore, the metal must have the capacity to reach an oxidation state two units higher than the more stable oxidation state to undergo an oxidative addition process.[77]

Reductive elimination is the product-releasing step of a catalytic reaction which follows an oxidative addition process. Reductive elimination is the reverse of oxidative

addition and leads to the expulsion of A-B from $L_nM(A)(B)$ (Eq 1.8). It obviously means that the oxidation state of the metal is reduced by 2 units when a 2 e^- coordination site is opened up by loss of A and B. Reductive elimination reactions are favoured when the A-B bond is stronger than the M-A and M-B bonds. For example, alkyl metal hydride and dihydride complexes release neutral alkane and H_2, respectively, via the reductive elimination process.[77]

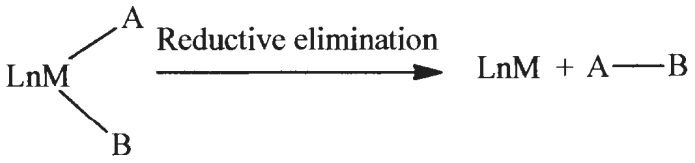

1.8

On this basis, the mechanism of dehydrogenation of methane involves activation of a C-H bond and consequently insertion of the metal into the C-H bond to form $H\text{-}M\text{-}CH_3^+$. The next step in this mechanism is α-migration of a second H to the metal center and formation of a dihydrido intermediate $(H)_2MCH_2^+$ (3 in Scheme 1.2), which then leads to a dihydrogen complex $(H_2)MCH_2^+$ (4) via a reductive elimination.[78] In the following step, the dihydrogen complex eliminates H_2 to form the product ion MCH_2^+. The α-transfer of a second H can also directly lead to a dihydrogen complex $(H_2)MCH_2^+$ followed by expulsion of H_2.[68,78]

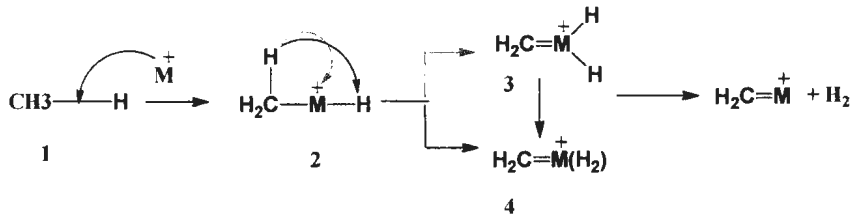

Scheme 1.2. The mechanism of dehydrogenation of methane via oxidative addition/reductive elimination. Scheme reproduced and reprinted from Chem. Rev. 2009, 110, 1170-1211 with permission from American Chemical Society. [80]

For alkanes larger than methane, dehydrogenation was found to be the major reaction channel in the reaction with transition metal ions.[79-81] For this reaction to take place, the energy of the metal carbene bond must exceed the energy of hydrogenation of olefins estimated, at 90-130 kJ mol^{-1}, which is possible for most of the transition metals.[78] For the mechanism, it is now postulated that the metal ion inserts into the C-H bond followed by ß-transfer of hydrogen leading to reductive 1,2-elimination of H_2 as illustrated in Scheme 1.3. It was reported that 1,1-dehydrogenation is an insignificant process for alkanes with at least two carbon atoms.[82] Roithova and Schroeder postulated two possible channels for dehydrogenation of alkanes longer than ethane as shown in Scheme 1.3.[78]

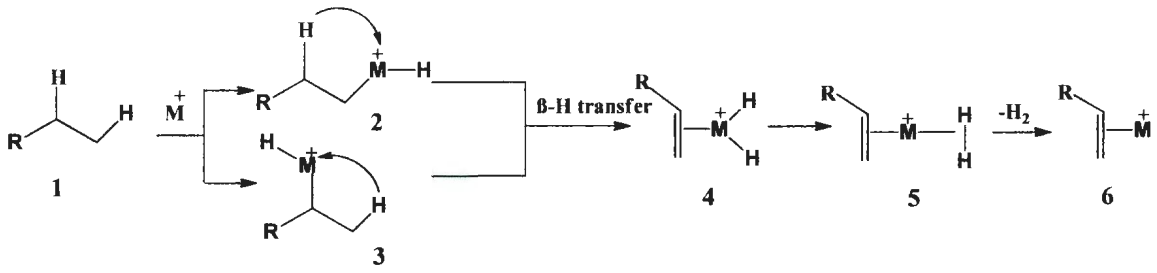

Scheme 1.3. Two possible channels for dehydrogenation of alkanes longer than ethane. Scheme reproduced and reprinted from Chem. Rev. 2009, 110, 1170-1211 with permission from American Chemical Society. [78]

One possible channel is insertion of the metal cation into the C-H bond of the terminal methyl group via an oxidative addition mechanism to give intermediate product 2 in Scheme 1.3. The second possibility is the secondary C-H bond cleavage by metal to yield the intermediate product 3. The intermediate structures from oxidative addition can continue the process by ß-H transfer to lead a dihydrido complex 4. The dihydido complex then eliminates neutral H_2 to produce the dehydrogenation product via reductive elimination. However, although the 1,2-elimination reaction was mostly observed in the reaction of alkanes with transition metals, a specific 1,4-elimination of alkane was reported in the case of Ni^+.[83] Labeling experiments revealed that the nickel cation inserts into the central C-C bond followed by ß-H transfer (Scheme 1.4). After this step, the second ß-H transfer occurs leading to dihydrido intermediate complex which then yields neutral H_2 and $Ni(C_4H_8)^+$ via reductive elimination. It should be noted that the preference of Ni^+ for insertion into a C-C bond rather than a C-H bond is energetically reasonable

considering the nickel ion-methyl binding energy $D_{0(Ni^+-CH3)}$ = 201 kJ mol^{-1} in comparison with nickel ion-hydride binding energy $D_{0(Ni^+-H)}$ = 180 kJ mol^{-1}.[83]

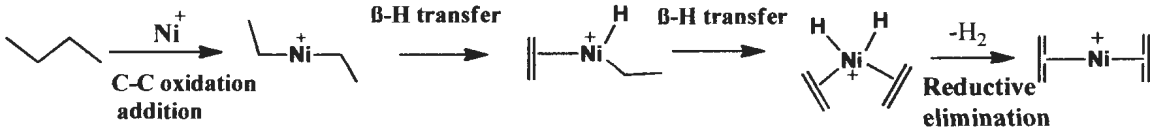

Scheme 1.4. The mechanism for dehydrogenation of n-butane by Ni^+ revealed by H/D labeling experiment. Scheme reproduced and reprinted from Chem. Rev. 2009, 110, 1170-1211 with permission from American Chemical Society.[78]

Furthermore, theoretical studies suggested the concerted pathway for dehydrogenation of hydrocarbons involving a multicentered transition state (MCTS) instead of the intermediate produced from the ß-H transfer. The MCTS structure could explain the experimental results for which the elimination of H_2 or CH_4 was not observed from the reaction of Fe^+ with C_2H_6.[78] As shown in Figure 1.5, the iron cation inserts into a C-H bond with an energy barrier of 33.5 kJ mol^{-1} lower than the energy of reactants.[84] In the next step, H-Fe-C_2H_5 follows a concerted pathway to lead a MCTS lying 29.3 kJ mol^{-1} above the energy of reactants. The MCTS is directly transferred to the dihydrogen complex $H_2M(C_2H_4)^+$ followed by elimination of H_2. This mechanism could account for why the dehydrogenation product was not observed in the Fe^+/C_2H_6 reaction in the gas phase.

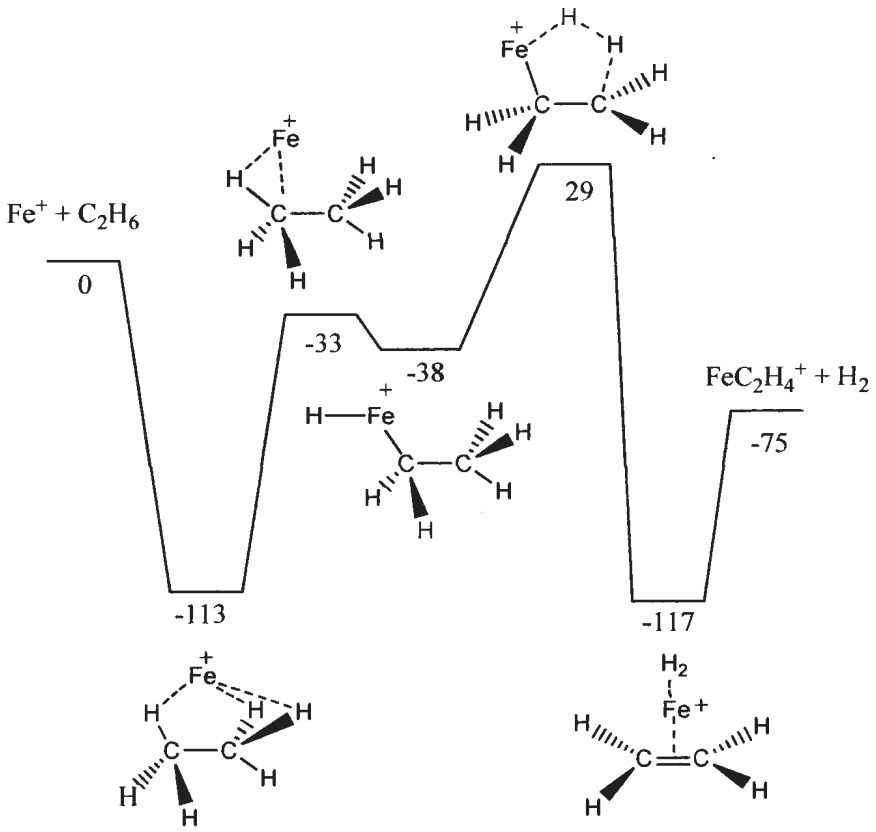

Figure 1.5. Energy diagram for dehydrogenation of ethylene by Fe^+. Energies are given in kJ mol^{-1}. Scheme reproduced and reprinted from J. Phys. Chem. 1996, 100, 6236-6242 with permission from American Chemical Society.[84]

The absence of C-C bond activation and consequently the absence of CH_4 elimination in the reaction of ethane with Fe^+ could be also explained with a similar mechanism involving the MCTS. Based on this mechanism, the oxidative addition process leading to the insertion of metal into the C-C bond produces a CH_3-M-CH_3 intermediate. It is followed by a MCTS lying 92 kJ mol^{-1} higher than the energy of the reactants (Figure 1.6).[84] This energy diagram clearly explains why loss of methane was

not a product of the Fe^+/C_2H_6 reaction. Accordingly, all the experimental results for distribution of H_2 and CH_4 products in the reactions of Fe^+, Ni^+, and Co^+ with propane are in agreement with the concerted pathway in which bond insertion CH_3-M-CH_3 leads to an exit channel complex via a MCTS. DFT calculations based on this mechanism revealed that the elimination of CH_4 is energetically favored for the reactions of Ni^+ and Fe^+ with propane, whereas loss of H_2 is energetically preferred in the reaction of Co^+ with propane.[85]

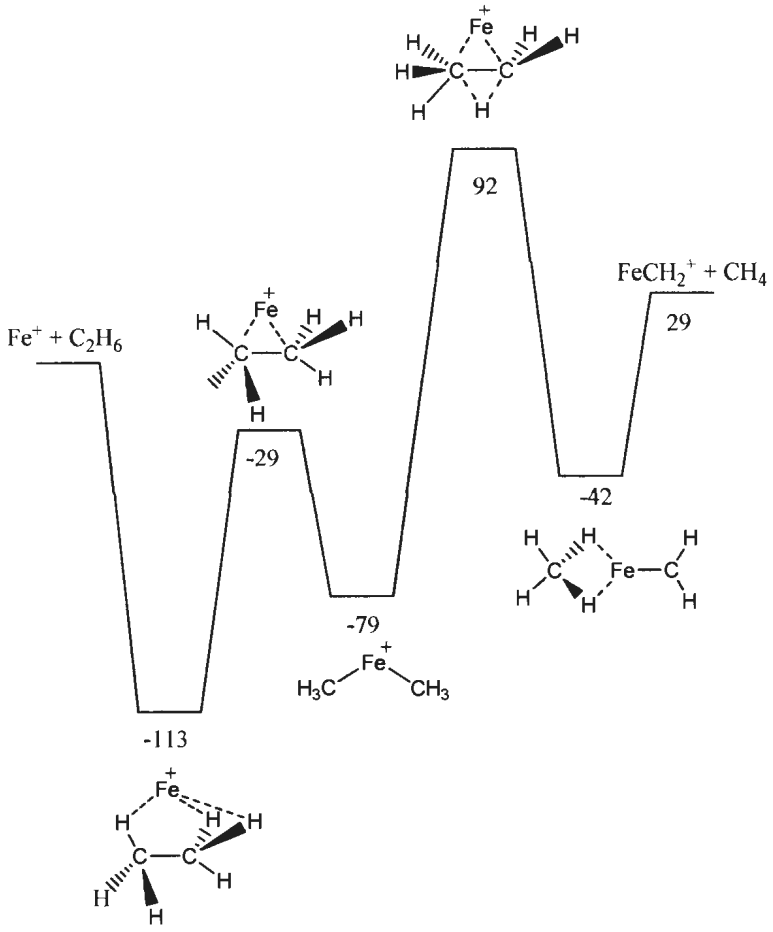

Figure 1.6. Energy diagram for demethanation of ethylene by Fe^+. Energies are given in kJ mol^{-1}. Scheme reproduced and reprinted from J. Phys. Chem. 1996, 100, 6236-6242 with permission from American Chemical Society.[84]

1.1.2.5. C-H Bond Activation by Ligated Metals or Metal Complexes

Despite a large amount of work in the gas phase activation of alkanes, studies of ligated transition metals are limited. Bare metals have been extensively focused on and found to be active catalysts for the C-H and C-C activation of alkanes in the gas phase.

The study of reactions of ligated metals with alkanes is essential to provide insight into more realistic catalysts for activation of alkanes in the condensed phase, where a metal is surrounded with different ligands or solvents. Dehydrogenation and demethanation of alkanes have been studied for transition metal ions ligated with CO, H_2O, F, Cl, OH, or O.[86,87] The reactivity and selectivity of transition metal ions can be affected by ligation, which is discussed further in Chapter 4. Moreover, C-H bond activation was investigated for transition metal ions coordinated with larger ligands. Butschke *et al.*[88] investigated activation of methane (where methane was fully deuterated CD_4) in the reaction with $[Pt(CH_3)(L)]^+$ inside a hexapole collision cell where L was a pyridine containing ligand such as pyridine (py), 2-2' bipyridine (bipy), or 1-10' phenanthroline (phen). The collision-induced dissociation experiments showed that these complexes reacted with CD_4 to undergo one, two, or three H/D exchanges which is accordingly indicative of the platinum complexes capability to activate three C-D bonds of methane. CID experiments revealed the elementary steps of H/D exchange reactions between methyl group and deuterated methane which involves an addition of CD_4 to $[(CH_3)Pt(L)]^+$ to form an adduct complex $[(CH_3)Pt(L)(CD_4)]^+$ followed by a C-D bond activation of CD_4 leading to the cleavage of a C-D bond. In the following step, the deuterium migrates to the methyl group to form $[(CH_3D)Pt(L)(CD_3)]^+$ (Scheme 1.5). The reaction continues by C-H bond activation of the CH_3D ligand and leads to transfer of the hydrogen to the CD_3 ligand to form $[(CH_2D)Pt(L)(CHD_3)]^+$. This product can undergo further H/D exchange reactions to form a fully deuterated methyl group $[(CD_3)Pt(L)(CH_4)]^+$.[88]

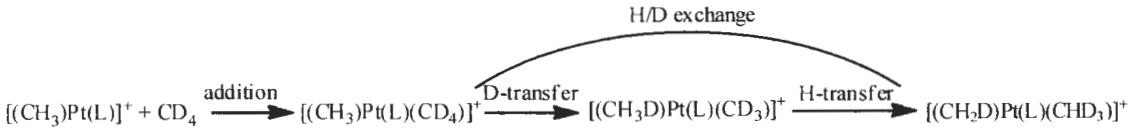

Scheme 1.5. C-D bond activation of fully deuterated methane by $[Pt(CH_3)(L)]^+$ where L was pyridine (py), 2-2' bipyridine (bipy), or 1-10' phenanthroline (phen).

Two different mechanisms were proposed for the H/D exchanges within the complex. The cleavage of a C-D bond can occur by insertion of Pt(II) into the C-D bond to produce a Pt(IV) via an oxidative addition mechanism followed by D transfer from Pt to the CH_3 group (Scheme 1.6). The other possible scenario is termed σ-bond metathesis, which involves an addition of a C-D bond as a ligand to a platinum center without a change of the metal oxidation state. In the following step, the cleavage of the C-D bond and transfer of D directly to the methyl group would occur simultaneously (Scheme 1.6).[88]

σ-bond metathesis oxidative addition

Scheme 1.6. Representation of σ-bond metathesis and oxidative addition of CD_4 to $[Pt(CH_3)(L)]^+$ complex.[88]

Furthermore, Butschke and coworkers studied the C-H bond activation of benzene in a reaction with $[Pt(CH_3)(L)]^+$ complex where L=2,2'-bipyridine (bipy).[89] It was shown that the gas phase reaction between $[Pt(CH_3)(bipy)]^+$ and benzene resulted in methane elimination. Indeed, the product ion $[Pt(bipy)(C_6H_5)]^+$ was indicative of C-H bond activation and consequently C-H bond cleavage of benzene followed by a proton-transfer process and liberation of methane. DFT calculations have provided the potential energy surfaces for the liberation of methane via both the oxidative addition/reductive elimination and metathesis mechanistic pathways. However, no distinctive preference to either of these pathways was shown except a slight stabilization of the rate determining transition state via the metathesis mechanism.[89]

1.1.2.6. C-H Bond Activation via σ-bond Complex Intermediate

In the activation of a C-H bond via σ-bond complex, the C-H bond as a ligand binds to a coordinatively unsaturated metal with a ≤16-electron configuration without any bond cleavage or change in metal oxidation state. A sigma complexation occurs rather than oxidation addition when the metal is a good σ acid to accept two electrons from the C-H bond but is not a good p base for back donating of electrons to the C-H σ* orbital to break the C-H bond. In this case a 3-center–2-electron (3c-2e) interaction is formed, where metal is bonded to both hydrogen and carbon. σ-bond complexation is an important process in C-H bond activation by unsaturated metal complexes. For example, in ligand exchange reactions between ML^+ and R-H, a σ-complex is formed followed by proton-transfer to the ligand to form L-H and MR^+ (Scheme 1.7).[78] Similarly, in the

reaction between C_6H_6 and $[Pt(CH_3)(bipy)]^+$, as discussed above, activation of the C-H bond can occur through a σ-bond complexation between $[Pt(CH_3)(bipy)]^+$ and the C-H bond of benzene. This complex then undergoes the proton-transfer to methyl group and liberation of methane.[89]

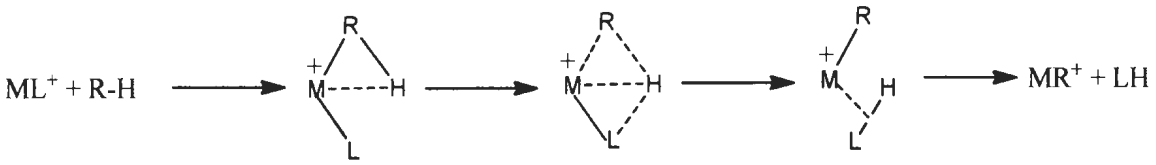

Scheme 1.7. Representation of σ-bond metathesis mechanism for C-H bond activation by unsaturated metal complexes.

1.1.3. Structural Studies of Biological Cations in the Gas phase

Gas phase studies provide the opportunity to picture detailed structures of biological ions in the absence of solvent. However, gas phase studies allow the effect of adding various numbers of solvent molecules to be examined on the structural configurations of biomolecular ions. In recent years, infrared multiphoton dissociation (IRMPD) spectroscopy has emerged as a powerful technique for structural analysis to provide evidence for gas phase structures of biological molecules such as cationized amino acids, peptides, and proteins. IRMPD spectroscopy is a technique used in a quadrupole ion trap or Fourier transform ion cyclotron resonance mass spectrometer coupled with an intense and tunable infrared light source. IRMPD spectroscopy relies on the absorption of infrared photons by trapped ions resulting in the fragmentation of ions. Fragmentation of ions in a range of infrared wavelength produces characteristic

absorption bands that can identify specific functional groups in a biomolecular structure. A more detailed description of the IRMPD technique is provided in chapter 2.

Recently, studies on the structures of metal ion complexed with biological molecules have been of great scientific interest. Over the past few years IRMPD has been used to investigate the effects of large numbers of metals on the conformational changes of a variety of biomolecules. Atkins and co-workers studied the structure of the simplest aliphatic amino acid, glycine, complexed with lead (II) by IRMPD spectroscopy.[90] The IRMPD spectrum of lead(II)-deprotonated glycine, $[Pb(gly-H)]^+$, along with the computed IR spectra for four structures is shown in Figure 1.7.[90] The band observed at 3552 cm^{-1} was assigned to the carboxylic acid O-H stretch, which can spectroscopically rule out the structures ii, iii, and iv. The IRMPD spectrum is consistent with the computed spectrum of the lowest energy structure of $[Pb(Gly-H)]^+$, structure i, where Pb^{2+} is bound to the deprotonated amine nitrogen and carbonyl oxygen. Therefore, IRMPD spectroscopy provided evidence indicating that glycine prefers to be deprotonated at N in interaction with lead $[Pb(Gly-H)]^+$.

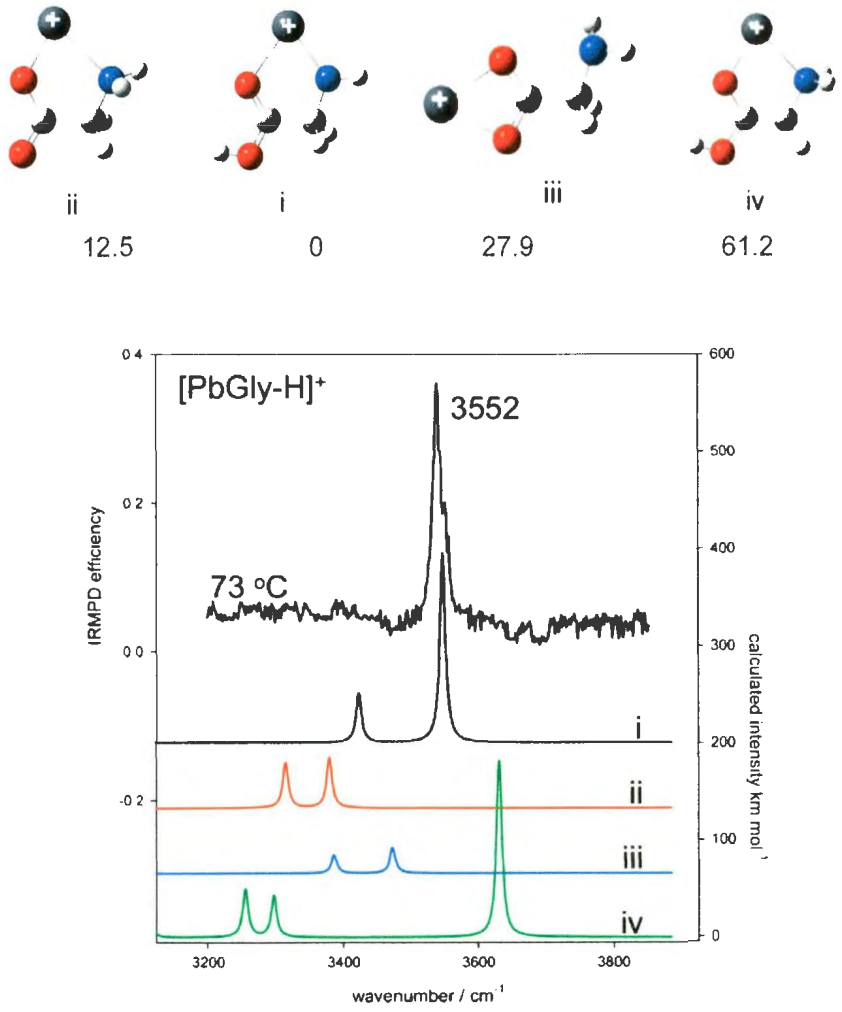

Figure 1.7. IRMPD spectrum of $[Pb(Gly-H)]^+$ compared with computed spectra for four structures. The computed spectra were taken from the B3LYP/6-31+G(d,p) optimized structures of i, ii, iii, and iv. The 298 K relative enthalpies (kJ mol^{-1}) were calculated by the B3LYP/6-31+G(d,p)//MP2(full)/6-311++G(2d,2p) method. In all calculations, the LANL2DZ basis set and effective core potential were used for Pb^{2+}. Figure reprinted from J. Phys. Chem. B. 2009, 113, 14457– 14464 with permission from American Chemical Society.[90]

Similar to the IRMPD spectrum of $[Pb(Gly-H)]^+$, the O-H stretch band at 3552 cm^{-1} was also observed in the IRMPD spectrum of the monohydrated complex $[Pb(Gly-H)(H_2O)]^+$ (Figure 1.8). Two additional bands, one strong band in the O-H stretching region at 3661 cm^{-1} and one weaker band in the N-H stretching region at 3365 cm^{-1}, were also observed. The spectrum interestingly rules out the structures in which intact water is attached to Pb^{2+} (structures c, e, f, and g) due to lack of an asymmetric O-H stretch predicted to be located around 3730 cm^{-1}.[91] By comparing the IRMPD spectrum and IR-computed spectra, it is clear that the most stable structure, a, is the best match with IRMPD spectrum. Indeed, in the gas phase reaction of water with $[Pb(Gly-H)]^+$ complex, the IRMPD spectrum suggested that the proton and hydroxyl group belonging to the water have transferred to the amine group (which was deprotonated at the bare complex) and Pb^{2+}, respectively.

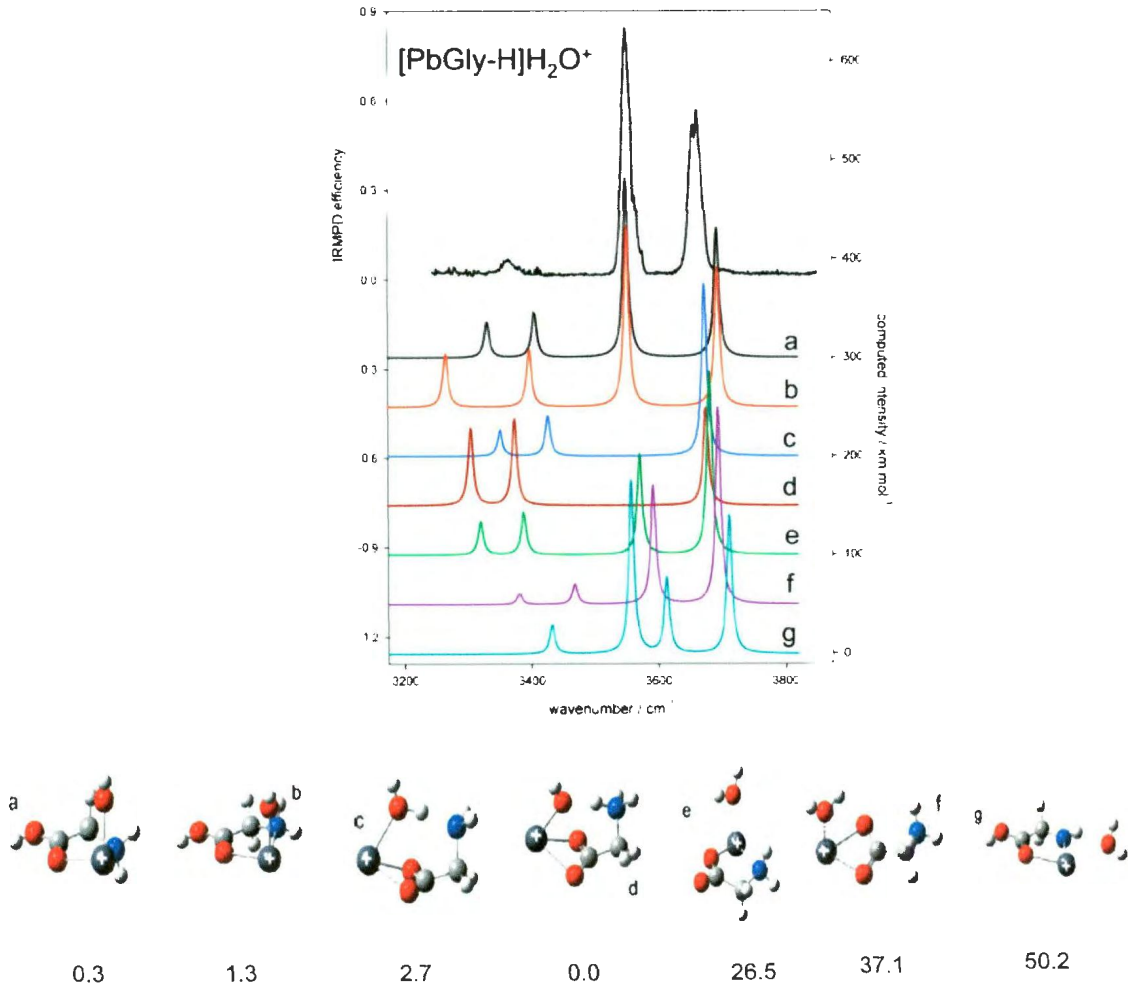

Figure 1.8. IRMPD spectrum of $[Pb(Gly\text{-}H)(H_2O)]^+$ compared with seven computed structures. The computed spectra were determined from the B3LYP/6-31+G(d,p) optimized structures of i, ii, iii, and iv. The 298 K relative enthalpies (kJ mol^{-1}) were calculated by the B3LYP/6-31+G(d,p)//MP2(full)/6-311++G(2d,2p) method. In all calculations, LANL2DZ basis set and effective core potential were used for Pb^{2+}. Figure reprinted from J. Phys. Chem. B. 2009, 113, 14457– 14464 with permission from American Chemical Society.[90]

Compared to amino acids or small peptides containing two or three amino acids, there are a limited number of IRMPD studies for determining the conformational structures of larger biomolecules such as proteins or enzymes. The reason is that the huge numbers of vibrational modes of large molecules make a complicated IR spectrum that is difficult to interpret. Cytochrome c of bovine heart is one of the largest molecules studied by IRMPD spectroscopy in the gas phase.[92] Infrared photodissociation spectra of potassiated-cytochrome c in different charge states are shown in Figure 1.9. In this case the metal cation, potassium ion, helps for observing IR-induced fragmentation of the protein since no dissociation product could be detected from the protonated protein. Thus, detachment of K^+ from the potassiated-cytochrome c was the only favorable fragmentation pathway induced by IRMPD. As seen in Figure 1.9, the spectra contain three main features at 1483, 1535 and 1660 cm^{-1} with different intensities in different charge states of the protein. The 1660 and 1535 cm^{-1} bands were assigned to C=O stretch and N-H bending vibrational modes, respectively. The C=O stretching mode is known as the most useful feature in solution phase for determining the secondary structures of proteins, which was found to be in the 1630-1640 cm^{-1} range for antiparallel ß-sheets and 1648-1658 cm^{-1} for α-helix.[93] From solution phase to gas phase, a blue shift for C=O stretching suggests an α-helix secondary structure for the backbone of cytochrome c in the gas phase which is consistent with its structure in solution.[93] The vibrational mode at 1483 cm^{-1} is not well understood because no similar band was observed in solution. One possibility for this band is the COH in plane bending mode of COOH groups, which

grows with increasing the protein charge states due to the higher degree of COO^- protonation.

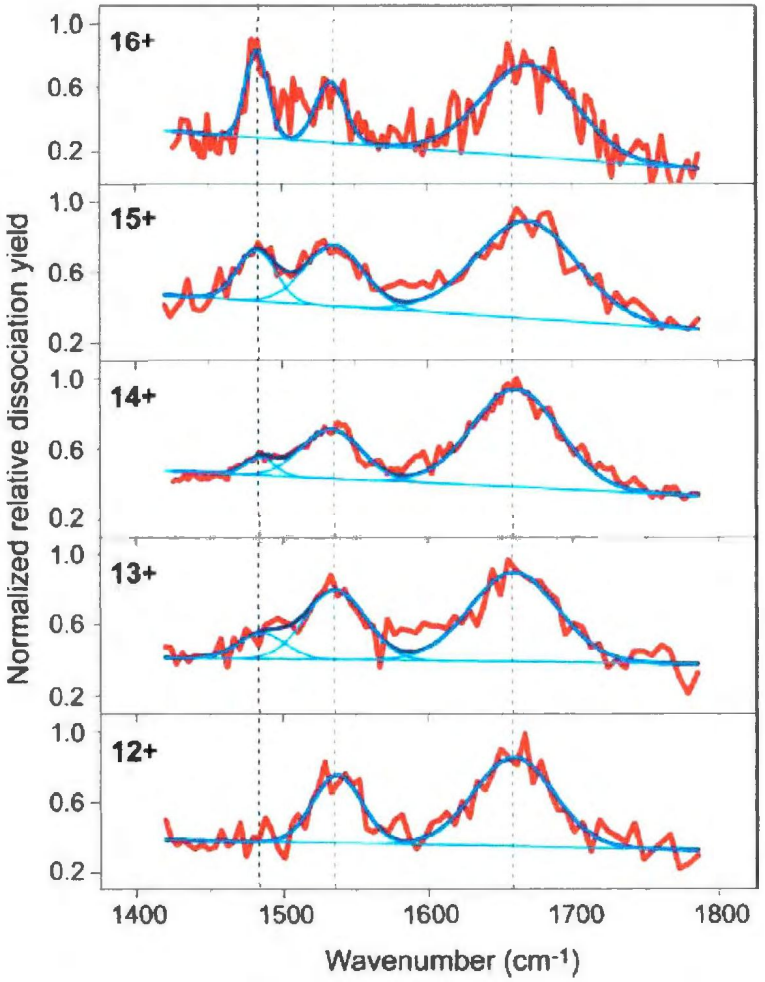

Figure 1.9. IRMPD spectra (red) of bovin cytochrome c in its several charge states. The blue curves depict the averages of several multiple scans. Figure reprinted from Mass Spectrom. Rev. 2009, 28, 468 – 494 with permission from John Wiley and Sons Inc.[92,94]

1.1.4. Fragmentation Reactions of Biological Cations in the Gas phase

In addition to IRMPD spectroscopy, biological metal cations have also been increasingly investigated by coillision-induced dissociation (CID) technique. In this technique, the ions trapped inside an ICR mass spectrometer are accelerated via an electrical potential, and then activated by collision with neutral gas such as argon, helium, or nitrogen. Upon collision with the neutral gas, some of the kinetic energy of the ions is transferred into internal energy resulting in the fragmentation of the ions. In a similar manner, infrared multiple photodissociation (IRMPD) has also been used to dissociate ions of interest by absorbing enough infrared photons irradiated by an intense IR laser. By identifying fragment ions in the mass spectrum, sequences of peptides or proteins can be determined. [95-100] Furthermore, binding sites between metal cation and biological species as well as their structures can be explored using CID-MS or IRMPD-MS techniques. [101,102] Metal cations are able to catalyze dissociation reactions probably due to stabilizing transition states for the rate determining step.[103] A large amount of research has been focused on fragmentation studies of metal cationized amino acids providing valuable information about biological systems.[103-107] Dissociation techniques combined with computational methods have helped in the understanding of mechanistic details of fragmentation processes providing the opportunity to explore the role of either metals or amino acids on the most favorable dissociation channels. For example, dissociation pathways resulting in loss of small neutral molecules such as CO, H_2O, and NH_3 are the most commonly observed by CID-MS of alkaliated amino acids. Abirami *et al.* investigated the competition of various dissociation channels for alkaliated alanine

([Alanine+M]$^+$ M=Li, K, Na) using CID-MS in conjunction with computational methods.[103] The fragment ions produced from loss of CO, H_2O, NH_3, and CO+NH_3 were the dominant dissociation products for [Ala+Li]$^+$, where two additional fragment ions, a minor peak of [Na+H_2O]$^+$ and major peak of Na^+ were also observed for sodiated alanine [Ala+Na]$^+$. In the case of [Ala+K]$^+$, a very high-abundance peak of K^+, and minor peaks attributed to [K+H_2O]$^+$ and [Ala+K-H_2O]$^+$ were observed. Using density functional theory (DFT) calculations, the energy of rate determining steps for loss of CO, H_2O, and NH_3 from lithiated alanine [Ala+Li]$^+$ were determined to be 177, 182, and 206 kJ mol^{-1} which were in good agreement with the order of CID-threshold voltages for observing the fragment ions, –CO < –H_2O < –NH_3. In the dissociation patterns of [Ala+M]$^+$ complexes (where M = Li, Na, or K), the metal ion signal for [Ala+Li]$^+$ was not observed in contrast to the Na and K counterparts; this effect was attributed to the significantly smaller metal ionic size for Li (i.e. Li^+ < Na^+ < K^+).[108-110] The smallest ion Li^+ has the highest affinity to alanine making the strongest binding, consequently a dissociation channel leading to loss of the small neutral molecules such as CO, H_2O, or NH_3 is preferred. It is also reasonable that the largest ion K^+ favors a dissociation pathway producing K^+ since its binding energy with Ala (123 kJ mol^{-1}) is significantly lower than the barrier energies calculated for loss of small neutral molecules. [103]

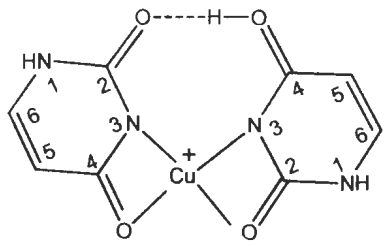

Figure 1.10. A schematic for the lowest energy structure of $[Cu(Ura)(Ura\text{-}H)]^+$ optimized by B3LYP/6-31+G(d,p) level of theory.[111]

Other biological metaliated complexes such as nucleobases have also been investigated using CID and IRMPD activation/fragmentation. Ali and Fridgen studied the fragmentation pathway of a complex between Cu^{2+} and two uracils, where one of the uracils is deprotonated $[Cu(Ura)(Ura\text{-}H)]^+$, using sustained off-resonance collision-induced (SORI-CID), IRMPD activation, and isotope labeling in conjunction with computational methods.[111] The SORI-CID technique is described in detail in Chapter 2. Unexpectedly, loss of intact uracil was not observed as a fragmentation product of $[Cu(Ura)(Ura\text{-}H)]^+$, but loss of HNCO followed by HCN was the main fragmentation pathway. Isotope labeling experiments indicated that the decomposition of HNCO involves the N3 and O2 atoms. The potential energy surface revealed the mechanisms and energies required the competitive losses of HNCO and intact uracil beginning with the lowest energy structure. The lowest energy structure was calculated to be a four-coordinate Cu^{2+} bound between $N3_{Ura\text{-}H}$, $O4_{Ura\text{-}H}$, $N3_{Ura}$, and $O2_{Ura}$ with an intramolecular hydrogen bond between $O4_{Ura}$ and $O2_{Ura\text{-}H}$ (Figure 1.10). For a neutral HNCO to be lost, the lowest energy structure undergoes an isomerization to the structure with Cu^{2+} bound

to $N1_{Ura-H}$ and $O2_{Ura}$ and an intramolecular hydrogen bond between $N1_{Ura}$ and $O2_{Ura-H}$. A significantly large barrier was calculated for this isomerization process. However, as seen in Figure 1.11, dissociation of HNCO including the isomerization step is energetically more favorable than the simple dissociation of intact uracil. Further, fragmentation reactions of $[M(Ura\_H)(Ura)]^+$ for a number of metals (M=Zn, Cu, Ni, Co, Fe, Mn, Cd, Pd, Mg, Ca, Sr, Ba, or Pb) were studied by the same group.[112] The fragment ion arising from the loss of HNCO was predominant for Zn, Cu, Ni, Co, Fe, Mn, Cd, Pd, Mg, while Ca, Sr, Ba, or Pb complexes preferred to lose a neutral uracil. A correlation between the size of the metal cation and the binding energy of intact uracil reasonably explained the presence or absence of uracil loss in the fragmentation results. Larger ions are loosely bound to intact uracil resulting in a binding energy lower than the energy required for loss of HNCO. This strong dependency of the binding energy on the size of metal ions can be evidence for an ion-dipole interaction between $[M(Ura-H)]^+$ and intact uracil.

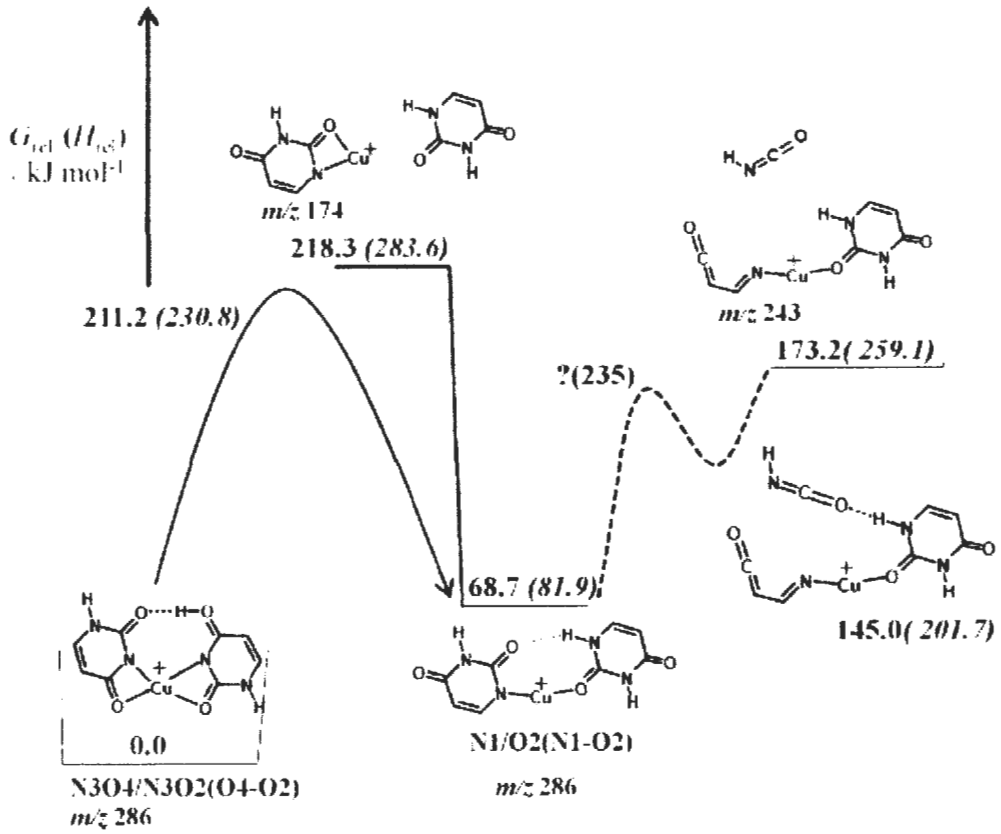

Figure 1.11. An energy diagram for loss of HNCO and loss of uracil from [Cu(Ura)(Ura-H)]$^+$. Figure modified from ChemPhysChem 2012, 13, 1507 – 1513 with permission from John Wiley and Sons Inc.[111]

1.2. Scope and Outline of Thesis

This thesis focus is on the study of the chemistry of metal-complexes in the gas phase. ICR mass spectrometry is used to investigate the ion-molecule reactions between unsaturated ruthenium complexes and small neutral molecules. The mechanistic study of ion-molecule reactions between $[Ru(bipy)_2]^{2+}$ complex and CO is conducted to show that

every ion-molecule collision would lead to a chemically activated association complex. In addition, this chemically activated ion-molecule complex, $[Ru(bipy)_2(CO)]^{2+*}$, is used to perform chemical reactions such as dehydrogenation and demethanation of alkanes. These experiments are complemented by computational chemistry which helps reveal detailed mechanism for the reactions by calculating and examining the energetic of structures involved. Further, the fragmentation pathways for $[Zn(A\text{-}H)(A)]^+$ complexes (where A=glycine, alanine, sarcosine, and proline) are examined using activation/fragmentation mass spectrometry techniques in conjunction with computational chemistry. In particular, the mechanism of dehydrogenation, as the most abundant fragmentation channel for $[Zn(proline\text{-}H)(proline)]^+$ complex, is investigated by tandem mass spectrometry, which involves deuterium labeling experiments. Finally, IRMPD spectroscopy examines the gas-phase structures of deprotonated proline/Zn^{2+} complex, $[Zn(Pro\text{-}H)]^+$, and the singly hydrated complex, $[Zn(Pro\text{-}H)(H_2O)]^+$. The research objectives for this thesis are summarized as follows:

1. Kinetic and mechanistic studies of low-pressure ion–molecule association reactions of unsaturated Ru(II) complexes with CO;
2. Gas-phase dehydrogenation and demethanation of 2-methylpropane and propane by the 16-electron complex $[Ru(bipy)_2CO]^{2+*}$ chemically activated by the association of $[Ru(bipy_2CO]^{2+}$ and CO;
3. Structures and fragmentations of $[Zn(Proline\text{-}H)]^+$, $[Zn(Proline\text{-}H)(H_2O)]^+$;
4. Structures and fragmentations of $[Zn(Proline\text{-}H)(Proline)]^+$ in the gas phase: H_2 elimination of $[Zn(A\text{-}H)(A)]^+$ complexes when A is a secondary amine;

References:

(1) Capron, L.; Mestdagh, H.; Rolando, C. *Coord. Chem. Rev.* **1998**, *178–180, Part 1*, 269.

(2) Operti, L.; Rabezzana, R. *Mass Spectrom. Rev.* **2003**, *22*, 407.

(3) Crabtree, R. H.; Holt, E. M.; Lavin, M.; Morehouse, S. M. *Inorg. Chem.* **1985**, *24*, 1986.

(4) Deem, M. L. *Coord. Chem. Rev.* **1986**, *74*, 101.

(5) Eller, K.; Schwarz, H. *Chem. Rev.* **1991**, *91*, 1121.

(6) Ryabov, A. D. *Chem. Rev.* **1990**, *90*, 403.

(7) Diefenbach, M.; Brönstrup, M.; Aschi, M.; Schröder, D.; Schwarz, H. *J. Am. Chem. Soc.* **1999**, *121*, 10614.

(8) Koszinowski, K.; Schröder, D.; Schwarz, H. *Organometallics* **2004**, *23*, 1132.

(9) Koszinowski, K.; Schröder, D.; Schwarz, H. *Organometallics* **2003**, *22*, 3809.

(10) Delp, S. A.; Munro-Leighton, C.; Goj, L. A.; Ramírez, M. A.; Gunnoe, T. B.; Petersen, J. L.; Boyle, P. D. *Inorg. Chem.* **2007**, *46*, 2365.

(11) Kanemasa, S.; Oderaotoshi, Y.; Wada, E. *J. Am. Chem. Soc.* **1999**, *121*, 8675.

(12) Munro-Leighton, C.; Blue, E. D.; Gunnoe, T. B. *J. Am. Chem. Soc.* **2006**, *128*, 1446.

(13) Rucker, R. P.; Whittaker, A. M.; Dang, H.; Lalic, G. *J. Am. Chem. Soc.* **2012**, *134*, 6571.

(14) Webb, J. R.; Bolaño, T.; Gunnoe, T. B. *ChemSusChem* **2011**, *4*, 37.

(15) Wakelam, V.; Smith, I. W. M.; Herbst, E.; Troe, J.; Geppert, W.; Linnartz, H.; Öberg, K.; Roueff, E.; Agúndez, M.; Pernot, P.; Cuppen, H. M.; Loison, J. C.; Talbi, D. *Space Science Reviews* **2010**, *156*, 13.

(16) Herbst, E.; Roueff, E.; Talbi, D. *Mol. Phys.* **2010**, *108*, 2171.

(17) Gerlich, D.; Horning, S. *Chem. Rev.* **1992**, *92*, 1509.

(18) Herbst, D. R. B. a. E. *in Rate Coefficients in Astrochemistry, edited by T.J. Millar and D.A. Williams, Kluwer Academic, Dordrecht,* **1988**.

(19) Petrie, S.; Dunbar, R. C. *J. Phys. Chem. A* **2000**, *104*, 4480.

(20) Herman, J.; Foutch, J. D.; Davico, G. E. *J. Phys. Chem. A* **2007**, *111*, 2461.

(21) Koyanagi, G. K.; Bohme, D. K.; Kretzschmar, I.; Schröder, D.; Schwarz, H. *J. Phys. Chem. A* **2001**, *105*, 4259.

(22) Grills, D. C.; van Eldik, R.; Muckerman, J. T.; Fujita, E. *J. Am. Chem. Soc.* **2006**, *128*, 15728.

(23) Allen, R. N.; Shukla, M. K.; Burda, J. V.; Leszczynski, J. *J. Phys. Chem. A* **2006**, *110*, 6139.

(24) Fridgen, T. D. *Mass Spectrom. Rev.* **2009**, *28*, 586.

(25) Chakrabarti, P. *Protein Eng.* **1990**, *4*, 49.

(26) Dunbar, R. C.; Oomens, J.; Orlova, G.; Bohme, D. K. *Int. J. Mass spectrom.* **2011**, *308*, 330.

(27) Dunbar, R. C.; Steill, J. D.; Oomens, J. *J. Am. Chem. Soc.* **2010**, *133*, 1212.

(28) Polfer, N. C.; Oomens, J.; Suhai, S.; Paizs, B. *J. Am. Chem. Soc.* **2007**, *129*, 5887.

(29) Polfer, N. C.; Paizs, B.; Snoek, L. C.; Compagnon, I.; Suhai, S.; Meijer, G.; von Helden, G.; Oomens, J. *J. Am. Chem. Soc.* **2005**, *127*, 8571.

(30) Cooper, H. J.; Case, M. A.; McLendon, G. L.; Marshall, A. G. *J. Am. Chem. Soc.* **2003**, *125*, 5331.

(31) Oh, H.; Breuker, K.; Sze, S. K.; Ge, Y.; Carpenter, B. K.; McLafferty, F. W. *PNAS* **2002**, *99*, 15863.

(32) Cody, R. B.; Amster, I. J.; McLafferty, F. W. *PNAS* **1985**, *82*, 6367.

(33) Chu, I. K.; Cox, D. M.; Guo, X.; Kireeva, I.; Lau, T.-C.; McDermott, J. C.; Siu, K. W. M. *Anal. Chem.* **2002**, *74*, 2072.

(34) Lin, T.; Payne, A. H.; Glish, G. L. *J. Am. Soc. Mass. Spectrom.* **2001**, *12*, 497.

(35) Shin, Y. A.; Heim, J. M.; Eichhorn, G. L. *Bioinorg. Chem.* **1972**, *1*, 149.

(36) Behe, M.; Felsenfeld, G. *PNAS* **1981**, *78*, 1619.

(37) Cuajungco, M. P.; Lees, G. J. *Brain Res. Rev.* **1997**, *23*, 219.

(38) Hajieva, P. B., C. *Curr. Pharm. Design* **2006**, *12*, 699

(39) Dunbar, R. C. *Ion-Molecule Radiative Association*; Wiley: New York,, 1994; Vol. Vol. II.

(40) Herman, Z.; Smith, D. *Chem. Rev.* **1992**, *92*, 1471.

(41) Mestdagh, H.; Morin, N.; Rolando, C. *Tetrahedron Lett.* **1986**, *27*, 33.

(42) Armentrout, P. B.; Hodges, R. V.; Beauchamp, J. L. *J. Chem. Phys.* **1977**, *66*, 4683.

(43) Dunbar, R. C.; Klippenstein, S. J.; Hrušák, J.; Stöckigt, D.; Schwarz, H. *J. Am. Chem. Soc.* **1996**, *118*, 5277.

(44) Dunbar, R. C.; Uechi, G. T.; Asamoto, B. *J. Am. Chem. Soc.* **1994**, *116*, 2466.

(45) Dunbar, R. C.; Uechi, G. T.; Solooki, D.; Tessier, C. A.; Youngs, W.; Asamoto, B. *J. Am. Chem. Soc.* **1993**, *115*, 12477.

(46) Ryzhov, V.; Klippenstein, S. J.; Dunbar, R. C. *J. Am. Chem. Soc.* **1996**, *118*, 5462.

(47) Ryzhov, V.; Yang, C.-N.; Klippenstein, S. J.; Dunbar, R. C. *Int. J. Mass spectrom.* **1999**, *185–187*, 913.

(48) Fridgen, T. D.; McMahon, T. B. *J. Phys. Chem. A* **2002**, *106*, 1576.

(49) Ho, Y.-P.; Yang, Y.-C.; Klippenstein, S. J.; Dunbar, R. C. *J. Phys. Chem. A* **1997**, *101*, 3338.

(50) Klippenstein, S. J.; Yang, Y.-C.; Ryzhov, V.; Dunbar, R. C. *J. Chem. Phys.* **1996**, *104*, 4502.

(51) Dunbar, R. C. *Int. J. Mass Spectrom. Ion Processes* **1997**, *160*, 1.

(52) Dunbar, R. C. *Current Topics in Ion Chemistry and Physics, Wiley, New York* **1994**, *Vol. II.*

(53) Su, T.; Chesnavich, W. J. *J. Chem. Phys.* **1982**, *76*, 5183.

(54) VARIFLEX, v. K., S. J.; Wagner, A. F.; Dunbar, R. C.; Wardlaw, D. M.; Robertson S. H. **1999**.

(55) Byun, Y. G.; Kan, S. Z.; Lee, S. A.; Kim, Y. H.; Miletic, M.; Bleil, R. E.; Kais, S.; Freiser, B. S. *J. Phys. Chem.* **1996**, *100*, 6336.

(56) Yeh, C. S.; Afzaal, S.; Lee, S. A.; Byun, Y. G.; Freiser, B. S. *J. Am. Chem. Soc.* **1994**, *116*, 8806.

(57) Byun, Y. G.; Yeh, C. S.; Xu, Y. C.; Freiser, B. S. *J. Am. Chem. Soc.* **1995**, *117*, 8299.

(58) Auberry, K. J.; Byun, Y. G.; Jacobson, D. B.; Freiser, B. S. *J. Phys. Chem. A* **1999**, *103*, 9029.

(59) Woodin, R. L.; Beauchamp, J. L. *Chem. Phys.* **1979**, *41*, 1.

(60) Golisz, S.; Brent Gunnoe, T.; Goddard, W.; Groves, J.; Periana, R. *Catal. Lett.* **2011**, *141*, 213.

(61) Hill, J. M.; Cortright, R. D.; Dumesic, J. A. *Appl. Catal., A.* **1998**, *168*, 9.

(62) Weckhuysen, B. M.; Schoonheydt, R. A. *Catal. Today* **1999**, *51*, 223.

(63) Guo, Y.; Zhou, L.; Kameyama, H. *Int. J. Hydrogen Energy* **2011**, *36*, 5321.

(64) Speight, G. J.; Ozum, B. *Petroleom Refining Processes*; Taylor & Francies e-Library, 2009.

(65) Allison, J.; Ridge, D. P. *J. Am. Chem. Soc.* **1977**, *99*, 35.

(66) Irikura, K. K.; Beauchamp, J. L. *J. Am. Chem. Soc.* **1991**, *113*, 2769.

(67) Irikura, K. K.; Beauchamp, J. L. *J. Phys. Chem.* **1991**, *95*, 8344.

(68) Shayesteh, A.; Lavrov, V. V.; Koyanagi, G. K.; Bohme, D. K. *J. Phys. Chem. A* **2009**, *113*, 5602.

(69) Li, F.-X.; Zhang, X.-G.; Armentrout, P. B. *Int. J. Mass spectrom.* **2006**, *255–256*, 279.

(70) Armentrout, P. B. *Int. J. Mass spectrom.* **2003**, *227*, 289.

(71) Armentrout, P. B.; Shin, S.; Liyanage, R. *J. Phys. Chem. A* **2005**, *110*, 1242.

(72) Irikura, K. K.; Goddard, W. A. *J. Am. Chem. Soc.* **1994**, *116*, 8733.

(73) Bauschlicher, C. W.; Partridge, H.; Sheehy, J. A.; Langhoff, S. R.; Rosi, M. *J. Phys. Chem.* **1992**, *96*, 6969.

(74) Armentrout, M. M.; Li, F.-X.; Armentrout, P. B. *J. Phys. Chem. A* **2004**, *108*, 9660.

(75) Zhang, G.; Li, S.; Jiang, Y. *Organometallics* **2003**, *22*, 3820.

(76) Aguirre, F.; Husband, J.; Thompson, C. J.; Metz, R. B. *Chem. Phys. Lett.* **2000**, *318*, 466.

(77) Crabtree, R. H. In *The Organometallic Chemistry of the Transition Metals*; John Wiley & Sons, Inc.: 2005, p 159.

(78) Roithová, J.; Schröder, D. *Chem. Rev.* **2009**, *110*, 1170.

(79) Mandich, M. L.; Halle, L. F.; Beauchamp, J. L. *J. Am. Chem. Soc.* **1984**, *106*, 4403.

(80) Tolbert, M. A.; Mandich, M. L.; Halle, L. F.; Beauchamp, J. L. *J. Am. Chem. Soc.* **1986**, *108*, 5675.

(81) Tolbert, M. A.; Beauchamp, J. L. *J. Phys. Chem.* **1986**, *90*, 5015.

(82) Pruesse, T.; Fiedler, A.; Schwarz, H. *J. Am. Chem. Soc.* **1991**, *113*, 8335.

(83) Halle, L. F.; Houriet, R.; Kappes, M. M.; Staley, R. H.; Beauchamp, J. L. *J. Am. Chem. Soc.* **1982**, *104*, 6293.

(84) Holthausen, M. C.; Fiedler, A.; Schwarz, H.; Koch, W. *J. Phys. Chem.* **1996**, *100*, 6236.

(85) Yi, S. S.; Reichert, E. L.; Holthausen, M. C.; Koch, W.; Weisshaar, J. C. *Chem. Eur. J.* **2000**, *6*, 2232.

(86) Schröder, D.; Schwarz, H. *PNAS* **2008**.

(87) Armentrout, P. B.; Tjelta, B. L. *Organometallics* **1997**, *16*, 5372.

(88) Butschke, B. S., M.;Schwarz,H.;Schreoder,D. *Z. Naturforsch* **2007**, *62b*, 309.

(89) Butschke, B.; Schröder, D.; Schwarz, H. *Organometallics* **2009**, *28*, 4340.

(90) Atkins, C. G.; Banu, L.; Rowsell, M.; Blagojevic, V.; Bohme, D. K.; Fridgen, T. D. *J. Phys. Chem. B* **2009**, *113*, 14457.

(91) Gillis, E. A. L.; Fridgen, T. D. *Int. J. Mass spectrom.* **2010**, *297*, 2.

(92) Oomens, J.; Polfer, N.; Moore, D. T.; van der Meer, L.; Marshall, A. G.; Eyler, J. R.; Meijer, G.; von Helden, G. *PCCP* **2005**, *7*, 1345.

(93) Barth, A.; Zscherp, C. *Q REV BIOPHYS* **2002**, *35*, 369.

(94) Polfer, N. C.; Oomens, J. *Mass Spectrom. Rev.* **2009**, *28*, 468.

(95) Chu, I. K.; Guo, X.; Lau, T.-C.; Siu, K. W. M. *Anal. Chem.* **1999**, *71*, 2364.

(96) Adams, J.; Gross, M. L. *J. Am. Chem. Soc.* **1986**, *108*, 6915.

(97) Adams, J.; Gross, M. L. *Anal. Chem.* **1987**, *59*, 1576.

(98) Leary, J. A.; Williams, T. D.; Bott, G. *Rapid Commun. Mass Spectrom.* **1989**, *3*, 192.

(99) Leary, J. A.; Zhou, Z.; Ogden, S. A.; Williams, T. D. *J. Am. Soc. Mass. Spectrom.* **1990**, *1*, 473.

(100) Lin, T.; Glish, G. L. *Anal. Chem.* **1998**, *70*, 5162.

(101) Reiter, A.; Adams, J.; Zhao, H. *J. Am. Chem. Soc.* **1994**, *116*, 7827.

(102) Teesch, L. M.; Adams, J. *J. Am. Chem. Soc.* **1990**, *112*, 4110.

(103) Abirami, S.; Wong, C. C. L.; Tsang, C. W.; Ma, N. L. *Chem. Eur. J.* **2005**, *11*, 5289.

(104) Buchmann, W.; Spezia, R.; Tournois, G.; Cartailler, T.; Tortajada, J. *J. Mass Spectrom.* **2007**, *42*, 517.

(105) Hoppilliard, Y.; Rogalewicz, F.; Ohanessian, G. *Int. J. Mass spectrom.* **2001**, *204*, 267.

(106) Rogalewicz, F.; Hoppilliard, Y.; Ohanessian, G. *Int. J. Mass spectrom.* **2000**, *195–196*, 565.

(107) Shoeib, T.; Hopkinson, A. C.; Siu, K. W. M. *J. Phys. Chem. B* **2001**, *105*, 12399.

(108) Marino, T.; Russo, N.; Toscano, M. *Inorg. Chem.* **2001**, *40*, 6439.

(109) Marino, T.; Russo, N.; Toscano, M. *J. Inorg. Biochem.* **2000**, *79*, 179.

(110) Hoyau, S.; Ohanessian, G. *Chem. Eur. J.* **1998**, *4*, 1561.

(111) Ali, O. Y.; Fridgen, T. D. *ChemPhysChem* **2012**, *13*, 588.

(112) Ali, O. Y.; Randell, N. M.; Fridgen, T. D. *ChemPhysChem* **2012**, *13*, 1507.

Chapter 2. Experimental and Theory

The purpose of this chapter is to describe the instrumentation used in the experimental works of this thesis. The FT-ICR MS used for our experiments is described in detail. The activation techniques employed in this work to explore structures and reaction mechanisms of the metal complexes including collision induced dissociation (CID), sustained off resonance irradiation collisionally induced dissociation (SORI-CID) and infrared multiple photon dissociation (IRMPD) as well as computational methods are explained throughout this chapter.

2.1. Instrumentation

In all of the experiments performed for this thesis, a Bruker Apex Qe70 Fourier transform ion cyclotron mass spectrometer (FTICR-MS) at Memorial University was used. Figure 2.1 depicts the FTICR-MS used in this work. Four main regions of the FTICR-MS are the ion source, quadrupole region, ion transfer optics, and ICR cell. The gas phase ions are generated from a solution containing an aqueous or organic solvent using the electrospray ionization (ESI) source. In the ESI technique, ions are produced under atmospheric pressure, whereas the ICR cell requires a very low pressure ($\sim 10^{-10}$ mbar) for optimal operation. Therefore, differential pumping stages are required to achieve the very high vacuum of the ICR cell. Electrosprayed ions are accelerated through a series of ion funnels that act to focus and increase the amount of electrosprayed ions transmitted to the low pressure (10^{-6} mbar) through the first hexapole ion guide after which ions can be mass selected in a quadrupole mass filter. The ions can then be

accumulated in the hexapole collision/accumulation/reaction cell which is kept typically at approximately 10^{-2} mbar. After a period of time (ranging from milliseconds to seconds) to accumulate ions are accelerated and focused into the ICR cell using a series of ion optics. Ions are trapped inside the ICR cell and allowed to either react with neutral molecules or be irradiated by IR photons.

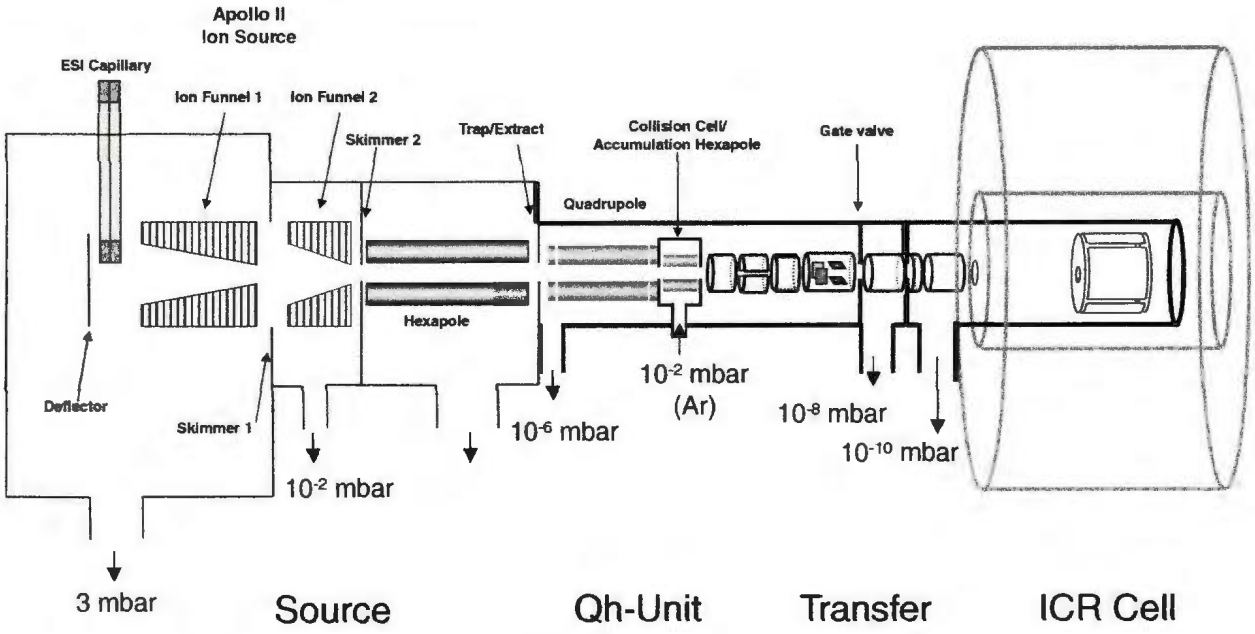

Figure 2.1. A schematic of the Bruker Apex Qe 7.0 FT-ICR mass spectrometer at Memorial University. Figure adapted from J. Am. Soc. Mass Spectrom. 2009, 20, 411 – 418 with permission from Elsevier.[1]

2.1.1. Electrospray Ionization

The ion source used in our experiments is an Apollo II electrospray source. To study gas phase ions of organic, inorganic or biological reactions, the most important step is transferring ions from solution phase to gas phase. John Fenn was awarded the 2002

Noble Prize in chemistry for the development of electrospray ionization (ESI) to study large biological compounds.[2] ESI is called a soft ionization technique since analyte ions are very gently extracted from solution, a process generating gas phase ions without any fragmentation.[3] In this gentle ionization process, even weakly bound non-covalent complexes can be conserved making ESI the best ionization method for retaining structures and interactions of biomolecular complexes as they are transferred from solution phase to the gas phase. In recent years, a variety of weakly bound complexes such as antibody-antigen, protein-DNA or RNA, and interamolecular non-covalent interactions responsible for secondary structures of proteins were characterized using electrospray ionization mass spectrometry (ESI-MS).[4-8]

Figure 2.2[9] represents a schematic of the electrospray ionization process. The analyte of interest is dissolved in a solution with conventional solvents such as water, methanol, acetonitrile, etc. This solution passes through a capillary tube, where a strong electric field is applied between the tip of the capillary and a counter electrode. At the tip of the capillary, accumulation of charges causes distortion of the solution meniscus to a cone shape which finally breaks the surface tension of the solution to produce a highly charged droplet. Applying a high temperature as well as a flow of nebulizer gas helps to evaporate solvent from the droplet. Evaporation of solvent decreases the size of the droplet to a critical radius where columbic repulsion overcome surface tension, leading to Columbic fission of the droplet into smaller droplets. The limiting charge for a droplet, Q, can be determined by the Rayleigh stability limit, which is given by Eq 2.1.[10]

$$Q = 64\pi^2\varepsilon_0\lambda r^3 \qquad 2.1$$

where λ is surface tension for a spherical droplet with radius of r, and ε_0 is the electrical permittivity of vacuum.

There are two mechanisms, the ion evaporation model (IEM) and the charged residue model (CRM), proposed for the final step of ESI in which ions are transferred from the droplets into the gas phase. In the IEM, when the sizes of the droplet radii reduces to the Rayleigh limit (e.g. radius <10 nm), analyte ions are desorbed from the surface of the droplet to reduce Columbic repulsion (see Figure 2.3a).[11] The CRM predicts that fission events repeat until a droplet with only one analyte ion but multiple charges is produced. In the following step, evaporation of the last solvent molecules in the droplet brings a free multiply charged ion into the gas phase (see Figure 2.3 b).[12,13] It was also suggested that small analytes (for example inorganic ions and small metal complexes) follow a different mechanism than large molecules (for example large proteins and polymers). The IEM is the most dominant mechanism for producing small gas phase ions, whereas species with masses over 100 kDa are most likely ionized with CRM.[14] Multiply charged ions, often observed in the electrospray ionization of large biological molecules like proteins, provide a strong support for the charged residue mechanism.[15]

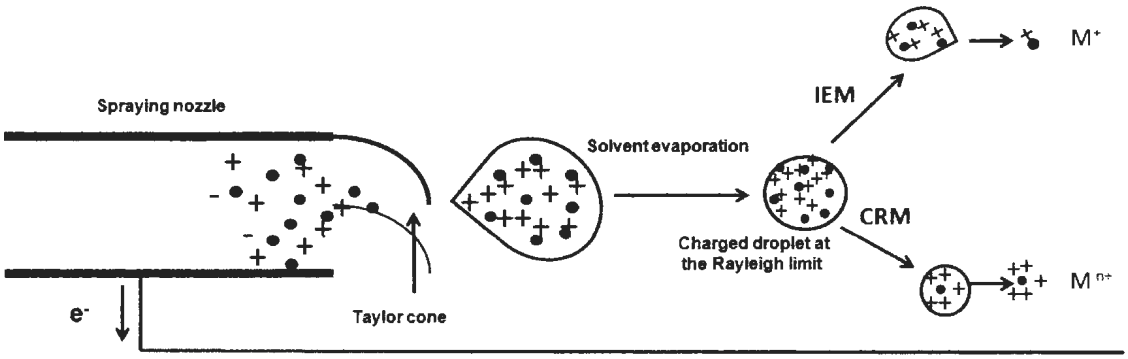

Figure 2.2. A schematic of the electrospray ionization process. Figure modified and reprinted from Anal. Chem. 1993, 65, 972A – 986A with permission from the American Chemical Society.[10]

2.1.2. Fourier Transform Ion Cyclotron Resonance Mass Spectrometry

This technique measures ionic mass to charge ratios based on ion cyclotron frequencies. Fourier transform ion cyclotron resonance (FTICR) mass spectrometry is a powerful technique not only because of its high mass resolving power, but also due to its capability for trapping ions for extended periods of time to perform tandem mass spectrometry (MS/MS) for structural and thermochemical studies. Furthermore, the ICR mass spectrometer can be used to study ion-molecule reactions and these studies can be used to reveal the elementary steps and mechanisms of reactions. The main part of a FTICR mass spectrometer is the cylindrical cell where ions are isolated, analyzed, and detected. This cell is located inside a high magnetic field in the present case a 7.0 Tesla super-conducting magnet.

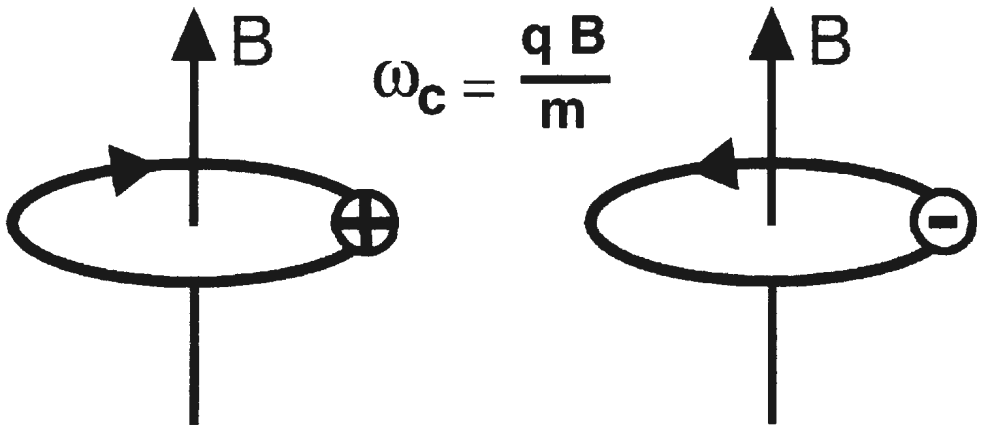

Figure 2.3. Cyclotron motion of ions within a magnetic field (B). Upon the Lorentz force positive and negative ions move in opposite directions which is perpendicular to the magnetic field. Figure reprinted from Int. J. Mass spectrom. 2002, 215, 59-75 with permission from Elsevier .[16]

In the presence of a magnetic field, trapped ions experience a centripetal force called the Lorentz force, F, (Eq 2.2) which is perpendicular to the magnetic field, B, and the ions' direction velocity, v. As illustrated in Figure 2.3, the Lorentz force keeps ions in a circular trajectory with radius r which is perpendicular to the magnetic field.[16,17]

$$F = qv \times B \qquad 2.2$$

For an ion in a stable circular trajectory the Lorentz force is balanced with centrifugal force (Eq 2.3 and Eq 2.4)

$$F' = \frac{mv^2}{r} \qquad 2.3$$

$$qv \times B = \frac{mv^2}{r} \qquad 2.4$$

by substitution of $\omega = \frac{v}{r}$ (w = angular frequency) and q= ez, Eq 2.4 can be written as

$$\frac{m}{z} = \frac{eB}{\omega} \qquad 2.5$$

According to Eq. 5, the mass-to-charge ratio (m/z) of an ion is directly proportional to the magnetic field strength B and inversely proportional to its cyclotron frequency ω. In another words, all ions with the same m/z have identical cyclotron frequencies.

A diagram for a cylindrical ICR cell can be seen in Figure 2.4. The cell is composed of three pairs of plates: end-cap trapping plates, excitation plates, and detection plates. Ions of interest are trapped inside the cell since the magnetic field keeps the ions in a plane perpendicular to the paper. In addition, applying an electric field across the end-cap trapping plates prevents ions escaping the cell along the magnetic field.[18,19] Before detection, ions must be excited to a larger cyclotron radius because the radius of cyclotron motion is not sufficiently large to be detected by the detection plates. Excitation of ions is achieved by sweeping a RF voltage across the excitation plates. An RF frequency on-resonance with an ion's cyclotron frequency causes absorption of the resonant energy and increases the ion's kinetic energy. Since the cyclotron frequency of the excited ion remains the same, more kinetic energy causes the ion to acheive a larger orbit where it is closer to the detection plates, and consequently it will produce an image current in the detection plates.[16,17] Excitation of the ions also produces coherent ion packets of the same mass to charge ratio. As a result, ions with a cyclotron frequency different from the RF frequency cannot be excited, so remain unaffected in the center of

cell. By sweeping a range of RF frequencies, a wide range of m/z can be excited to a detectable radius. [16,17] In order to isolate an ion of a particular m/z, all m/z other than the desired m/z are excited to a radius larger than the ICR cell dimension, where they collide with the detection plates, and consequently are neutralized. Thus, only ions of interest remain within the ICR cell with detectable cyclotron motion.

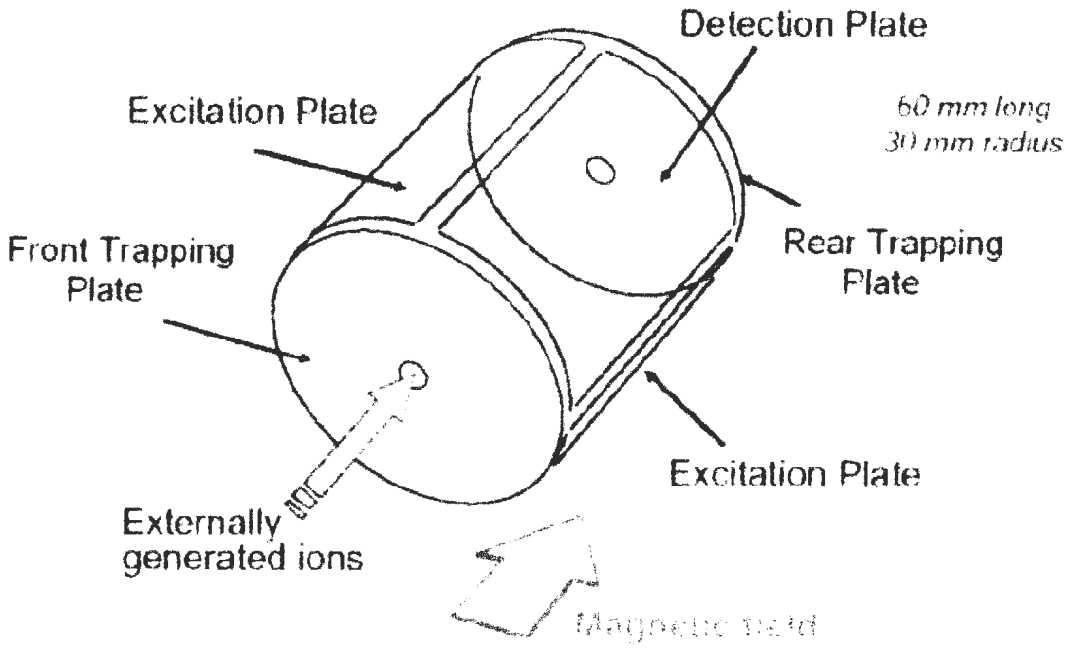

Figure 2.4. A schematic of a cylindrical ICR cell with trapping, excitation, and detection plates. The figure reprinted from the Bruker Daltonics Apex-Qe Series Generation II User Manual.

The excited ions induce charge in the detection plates. As a consequence of the periodic cyclotron motion of the ions, a sinusoidal image signal (image current) would be generated. The magnitude of the image current is indicative of the number of ions of the

same m/z. This sinusoidal image current is recorded for a period of time, and amplified. For a simple sinusoidal waveform signal, which can be obtained by a single m/z, ion frequency can be calculated by the distance between the subsequent sinusoidal peaks. However, there is often more than a single m/z for an electrosprayed sample. That is, various isotopes of an ion can be simultaneously detected to produce a complicated sinusoidal signal. In this respect, a Fourier transform is required to convert the time dependent wave-form signal into a frequency domain signal (Figure 2.5).[18,20] This frequency domain signal can further be converted to mass spectrum (m/z versus intensity) using eq. 2.4.

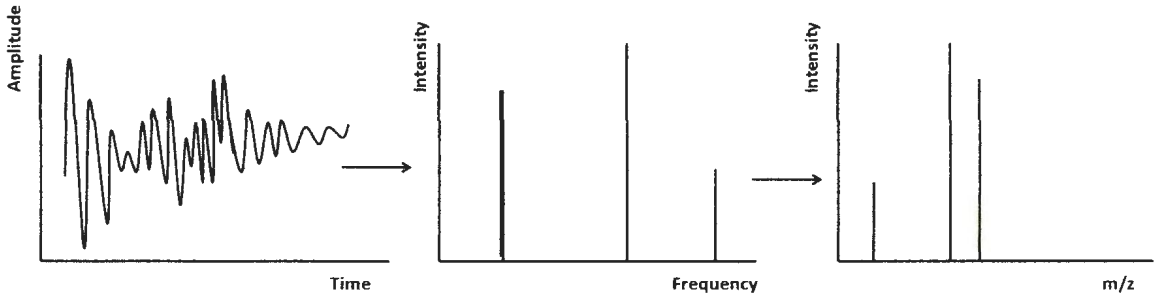

Figure 2.5. Transforming time domain signals to a mass spectrum using Fourier transform.

2.2. Tandem Mass Spectrometry

One of the important advantages of ICR mass spectrometry is that ions of interest can be confined within the cell for a desired length of time to perform tandem mass spectrometry techniques. In this work, three different activation/fragmentation techniques: collision induced dissociation (CID), sustained off-resonance irradiation

collision induced dissociation (SORI-CID), and infrared photon multiple dissociation (IRMPD) have been used.

2.2.1. Collision-induced Dissociation

CID is the most common activation/fragmentation technique in which dissociation of a precursor ion is activated by increasing its internal energy through collisions with neutral atoms or molecules. In the CID process, precursor ions are accelerated to high kinetic energies by applying a voltage in collision cell. The ions with high kinetic energy are then allowed to collide with the target gas which is chemically inert such as Ar, He, N_2, or CO_2, therefore, kinetic energy of precursor ions is converted into internal energy through collision with the target gas.[21-23] This internal energy then provides the energy required for dissociation of the ions. In such a process, the maximum internal energy (E_{com}) accessible for a precursor ion per collision is equal to the center of mass collision energy, which depends on the collisional voltage applied in the cell, called laboratory frame kinetic or collisional energy (E_{lab}), molar mass of the target gas (N), and molar mass of the precursor ion (m_P) (Eq.2.6).[24]

$$E_{com} = E_{lab}\left(\frac{N}{m_p+N}\right) \qquad 2.6$$

In an inelastic collision, a decrease in kinetic energy occurs that simultaneously increases the ion's internal energy. Based on the conservation of energy, any certain change in translational energy is converted into the ion's internal energy since there is a zero final kinetic energy in an inelastic collision between a target gas and precursor ion. As seen in

Eq. 2.6, the amount of translational energy converted into internal energy increases with the mass of the target gas; mass of the target gas, the more kinetic energy to be converted into internal energy.[24] Considering collision energy, there are two distinct energy regimes for CID experiments resulting in different CID spectra: high energy CID (fast activation) and low-energy CID (slow activation).

In high-energy CID, where collisional activation energy is in the order of keV, an ion is mostly excited to higher electronic levels. This high energy is then redistributed into vibrational modes through a single (or a few) collisions, and the internal energy of the ion easily surpasses the threshold for dissociation. As a result, bonds cleavage and rearrangement reactions that require high energy can occur in high-energy CID experiments. High-energy CID is commonly conducted in time-of-flight (TOF) or sector mass spectrometers, and helium is usually employed as a target gas. In order to increase the yield of transferring kinetic energy into internal energy, heavier gases such as argon or xenon are preferred.

Low-energy CID is often performed in quadrupole ion traps or FTICR mass spectrometers. An inert gas, often Ar or N_2, is introduced into the collision cell via a leak valve or pulse valve to a pressure about 10^{-8} mbar. In low-energy CID, the collisional energy typically ranges between 1-100 eV in the center of mass frame of reference. The low energy of each collision results in slow activation of the ions so that tens to hundreds of collisions are required to reach the threshold for dissociation, which may be followed by rearrangement or isomerisation, and can be observed in the resulting CID spectrum.

The wide range of collision energies available in CID allow determination of threshold energies required for dissociation of precursor ions. In our CID experiments, which are discussed in chapter 3, a stepwise increase of laboratory frame collisional energies is conducted until the threshold energy is surpassed, and the fragmentation occurs. In our experiments, the low energy CID is conducted in a hexapole collision cell which is placed between the ionization source and the ICR cell. For the target gas, we used Ar to induce fragmentation through collisions. By studying threshold fragmentation energies, useful information about bond strength of metal complexes was obtained.

2.2.2. Sustained off Resonance Irradiation Collisionally Induced Dissociation (SORI-CID)

SORI-CID is CID technique usually used in FT-ICR mass spectrometer. In this technique, trapped ions are excited by applying a RF frequency slightly higher than the ion natural cyclotron frequency. As a result, the ion will undergo a periodical acceleration and deceleration.[25] During this cyclic motion, the ion collides with neutral collision gas at a pressure of *ca.* 10^{-8} mbar, which is introduced into the ICR cell through a pulse valve, to convert the kinetic energy into internal energy. Ar or N_2 is often used as the collision gas for SORI-CID experiments. The maximum kinetic energy in SORI excitation process, called laboratory frame collision energy, can be calculated using Eq 2.7.[24,25] Each collision occurs with a maximum kinetic energy converted into internal energy which is equal to E_{com} and is calculated using Eq 2.6.

$$E_{lab} = \frac{\beta^2 q^2 V_{p-p}}{32\pi^2 m d^2 \Delta v^2} \qquad 2.7$$

Where ß and d are a geometrical factor and the diameter of the ICR cell, respectively, q and m are the ion charge and mass, respectively, V_{p-p} is the peak-to-peak excitation voltage and Δv is difference between the ion natural cyclotron frequency and RF excitation frequency. Since the ion kinetic energy is relatively low in SORI-CID, the activation process would be so long (activation times of hundreds of millisecond) that the ion can experience hundreds of collisions until the threshold dissociation energy is achieved and dissociation takes place. Therefore, rearrangement reactions and low energy fragmentation may appear in SORI-CID mass spectra, which make this technique a powerful means for structural elucidation.

2.2.3. Infrared Multiple Photon Dissociation

Photodissociation is a powerful technique for structural identification based on the absorption of a photon irradiated by a tunable laser, which results in dissociation of the ion of interest. The multiple photon dissociation technique employs a low to medium power laser to gradually increase the internal energy of the ion to its lowest energy dissociation threshold. Sequential absorption of photons allows studying all possible dissociation pathways, whereas for example a lowest energy dissociation pathway is

rarely achieved by a high power laser due to its relatively greater excitation rates. Infrared multiple photon dissociation (IRMPD) spectroscopy is a photodissociation technique that requires a tunable infrared laser. In this method, infrared photons resonant with a vibrational mode are sequentially absorbed resulting in vibrational excitation, resulting in ion dissociation as its internal energy exceeds the threshold. Beauchamp and coworkers[26-29] were pioneers for employing a low-power infrared laser for multiple photon dissociation of trapped ions inside an ICR cell. In early years of their research, they used a CW (continuous wave) CO_2 laser with intensities of 1-100 W cm^{-1} for photon dissociation of the proton bound dimer of diethyl ether $[(C_2H_5)_2O]_2H^+$.[27] Irradiation with the tuned CO_2-laser beam allowed the trapped ions to be activated by infrared photon absorption resulted in photodissociation of the dimer. Monitoring the experiment as a function of time showed that $(C_2H_5)_2OH^+$ was the sole fragment ion resulting from infrared photon dissociation since the decay in intensity of $[(C_2H_5)_2O]_2H^+$ exactly matched with the growth in intensity of $(C_2H_5)_2OH^+$ [27]

$$[C_2H_5)_2O]_2H^+ + nh\nu \rightarrow (C_2H_5)_2OH^+ + (C_2H_5)_2O \qquad 2.8$$

Continued advancement in IR-lasers has empowered researchers in the field to perform the structural characterization of a large number of small molecules [30-36] as well as large biological molecules such as peptides[37], proteins[38], and oligonucleotides [39,40] by identifying fragments produced from IRMPD and putting them together. CO_2

laser/IRMPD has also been used as a complementary method to CID to probe mechanistic details of fragmentation reactions. [41-43]

2.3. IRMPD Spectroscopy

The applications of IRMPD became more popular by measuring fragmentation intensity as a function of infrared laser wavelength called IRMPD spectroscopy. In early studies, a CW CO_2 laser was the only irradiation source using a few output lines from a grating laser. Most of these early studies utilized CO_2-IRMPD spectroscopy to differentiate isomeric structures. For example, Bensimon *et al.* found that four isomers formed from cationized heptene ($C_7H_{14}^{+\cdot}$) have different infrared absorption features over the 9.2-10.6μm region (see Figure 2.6).[41] However, the very limited tunable lines of the CO_2 laser was the reason for construction and development of lasers with wider tunable ranges. In the next sections, the most commonly used IR laser sources for IRMPD spectroscopy such as CO_2 laser, free electron laser (FEL), and optical parametric oscillation (OPO) are discussed.

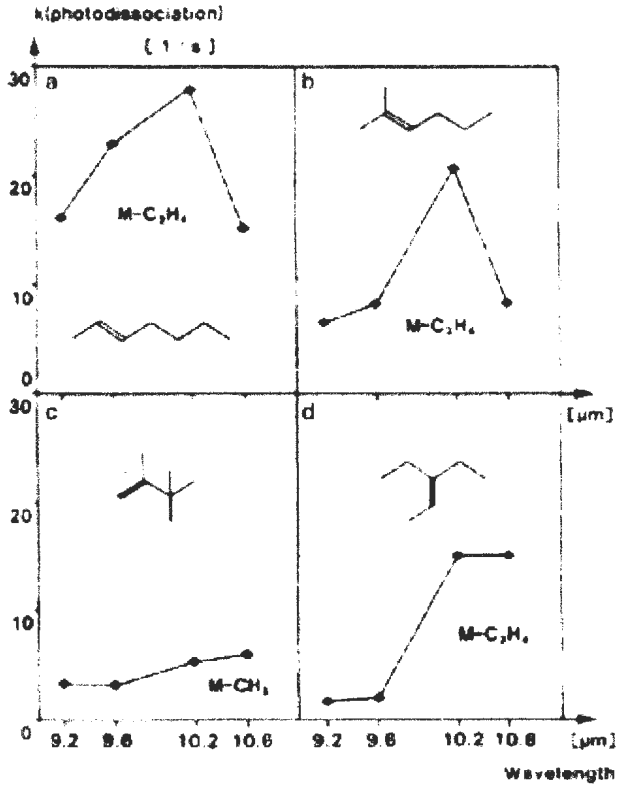

Figure 2.6. IRMPD spectra of four cationized heptene isomers using a CW CO_2 laser. Figure reprinted from Int. J. Mass Spectrom. Ion Process. 1986, 72, 125-135 with permission from Elsevier.[41]

2.3.1. CO_2 Laser

The CO_2 laser is a gas laser, invented by Petal[44,45] in 1964 and became one of the most powerful lasers up to 100 kW over the mid-IR range, 1087- 926 cm^{-1}. The laser medium consists of CO_2, N_2, and He gases. N_2 molecules are vibrationally excited to the v=1 vibrational level by electron impact, and then this energy is transferred to CO_2 molecules through collisions resulting in vibrational excitation of CO_2 molecules. CO_2

has three vibrational modes: the symmetric stretch, v_1, the bending vibration, v_2, and the antisymmetric stretch, v_3. The highest vibrational level of CO_2, v_1, is near to the v=1 vibrational level of N_2. As a result, de-excitation of N_2 molecules efficiently occurs by collision with CO_2 molecules transferring the energy to the CO_2 vibrational levels. Radiative decay of excited CO_2 molecules from all the v_1, v_2, and v_3 vibrational levels produces infrared laser beams. Collision of the helium with CO_2 molecules helps in removing the excitation energy from the CO_2 to increase laser efficiency. Because of the high powers of CO_2 lasers, gold or silver mirrors and zinc selenides windows are often used.

2.3.2. Free-Electron Laser (FEL)

A free-electron laser (FEL) produces the widest tunable frequency range. FEL's are different from conventional lasers. They consist of a relativistic electron beam moving through a magnetic field instead. These free electrons pass through a spatially periodic magnet called undulator in which the electrons are exposed to the Lorentz force obtaining a wiggle-like motion (Figure 2.7) resulting in emission of synchrotron radiation.[46,47] Since the emitted photons are in phase with the free electron beam passing through the magnetic field, they are added together to enhance the power of the laser. The laser beam is further amplified by oscillating between two mirrors at both ends of laser cavity. The emitted FEL beam can be tuned by adjusting magnetic field amplitude and period.

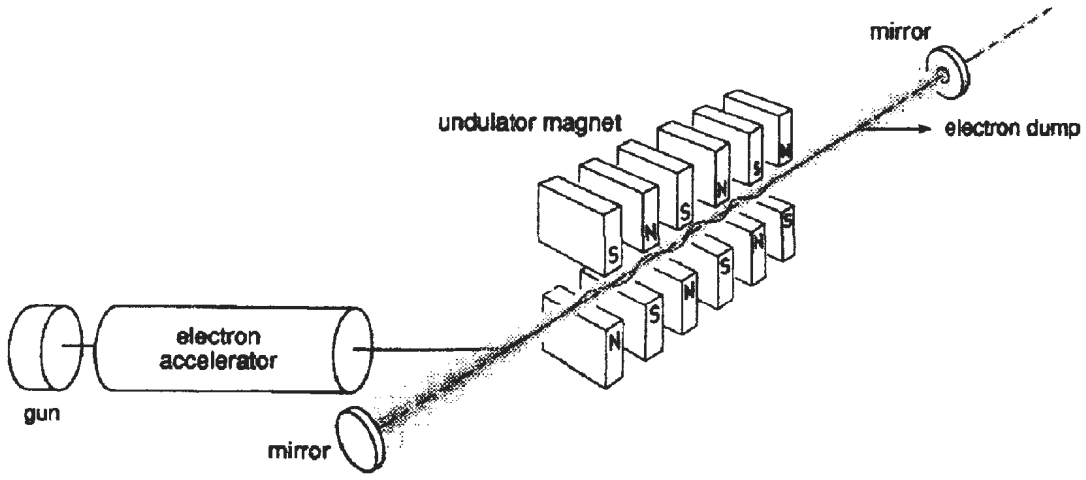

Figure 2.7. A diagram of a free-electron laser (FEL). Figure reprinted from Infrared Phys. Tech, 1995, 36, 297-308 with permission from Elsevier.[46]

2.3.3. Optical Parametric Oscillators (OPO)

Optical Parametric Oscillators (OPO) are parametric oscillators which convert a high energy laser beam, called pump wave, to two lower frequency beams.[48,49] An input beam ω_p from a high energy laser, such as a Nd:YAG laser, is focused into a non-linear crystal, such as lithium niobate ($LiNbO_3$) or potassium titanyl phosphate (KTP) and is split into signal and idler beams of frequency ω_s and ω_i, where

$$\omega_s + \omega_i = \omega_p \qquad 2.9$$

Interaction of the waves in a laser cavity results in amplification of output frequencies if their phases match.[50] By adjusting angles of the crystal and pump wavelength a wide mid-infrared beam can be readily tuned. More amplification of the output laser beam can be obtained by placing several mirrors in the optical cavity which allows photons to be

sent back and forward through the cavity to stimulate laser emissions. The laser beam then is reflected and amplified by passing through a turning mirror into the ICR cell.

2.3.4. Laser System at Memorial University (MUN)

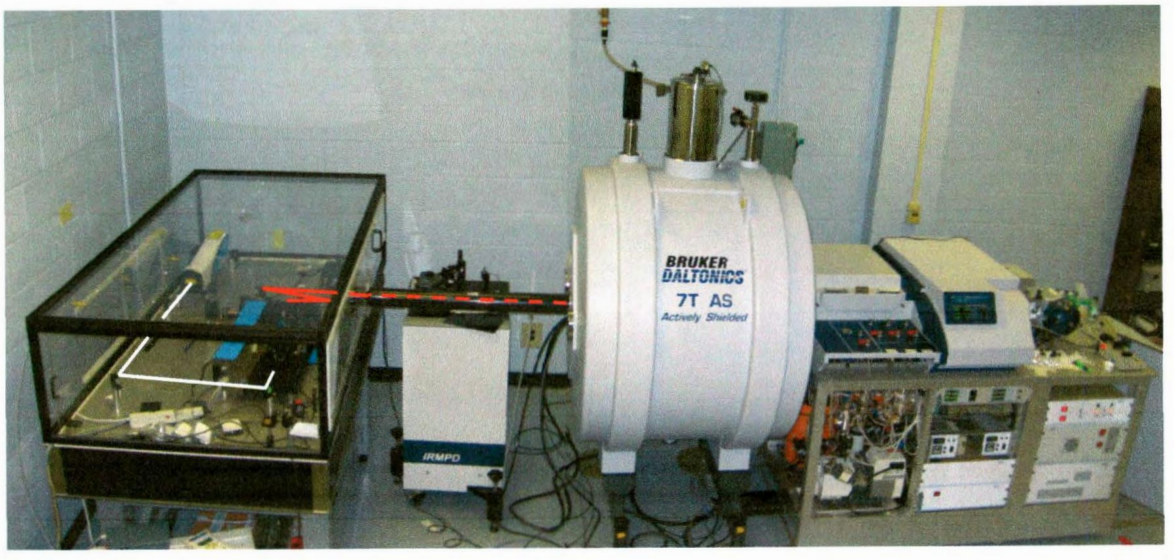

Figure 2.8. A picture of a bench-top laser system coupled with an FT-ICR mass spectrometer at Memorial University showing the beam paths for both a CO_2 laser beam (white line) and an OPO laser beam (red line).

In MUN's OPO laser, the 1064 nm Nd:YAG (Brilliant B Quantel) pumps light into a KTP crystal to produce signal and idler beams of 1.5 – 2.1 and 2.1 – 3.5 μm, respectively. The signal frequency is discarded by passing through a filter and the idler frequency is amplified in an optical cavity composed of two dichroic reflecting mirrors. The output beam is focused through a CaF_2 lens and then directed towards the ICR cell by passing through a BaF_2 window (Figure 2.8). The energy of the output beam exited from the output mirrors changes as a function of frequency. The maximum laser

conversion efficiency lies at 2.6 μm and significantly drops off at 3.5 μm (Figure 2.9). This explains why the usable range of our OPO laser for spectroscopy experiments is limited to 3200-4000 cm^{-1}. All MUN laser systems have bench-top configuration which is advantageous for easy install in laboratory.

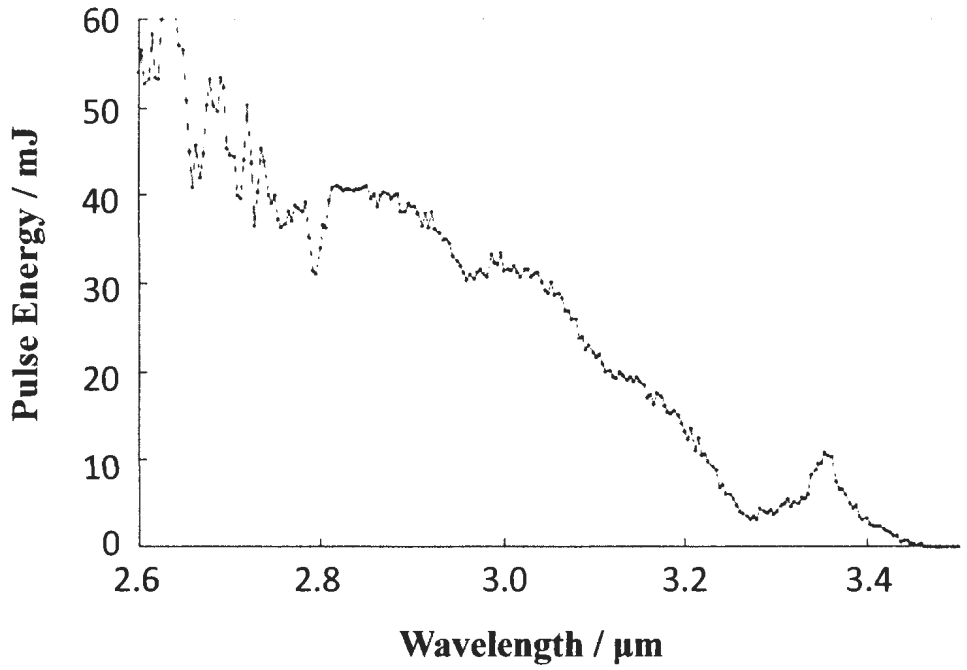

Figure 2.9. OPO Laser intensity as a function of waelength. Figure given by Dr. André Peremans.

2.3.5. IRMPD Mechanism

When infrared radiation is irradiated into the ICR cell, it is absorbed by trapped ions if the wavelength of radiation is resonant with one of the ion vibrational modes. Considering the accessible energy 5-48 kJ mol^{-1} by a mid-infrared frequency range 400-

4000 cm^{-1}, an individual photon is not sufficient for dissociation of a covalent bond which typically requires greater than 100 kJ mol^{-1}. Therefore, many infrared photons are required to induce dissociation of an ion through its lowest energy channel. In a harmonic system for vibrational modes where spaces between modes are the same, incoming multiple photons resonant with $v=1$ can cause subsequent transitions ($v=0 \rightarrow 1 \rightarrow 2 \rightarrow 3 \rightarrow \ldots \rightarrow n$) until the dissociation level is reached. In a real system spacing between energy levels are different, called anharmonic vibrational modes, and decrease at higher levels; therefore multiple photon with the same frequency are not simply able to make subsequent transitions to reach the dissociation level. In this case, a photon resonant with $v=0 \rightarrow 1$ is absorbed to excite the ion to first vibrational level, and then this energy is distributed throughout the rest of the molecule, a process called intramolecular vibrational energy redistribution (IVR).[51,52] In this process, the vibrational excited state returns back to the ground state $v=0$ allowing it to absorb another incoming photon. This process repeats itself to reach the threshold energy required for the ion's lowest dissociation pathway. A schematic of the IRMPD mechanism through an IVR process is shown in Figure 2.10.

An IRMPD spectrum is obtained by plotting the IRMPD yield (Eq. 2.10) as a function of radiation wavenmber as the KTP/OPO is scanned between 3200-3800 cm^{-1}. Each functional group absorbs irradiated energy at a particular frequency and distributes this energy throughout the ion's structure inducing the IRMPD-activated ion to be dissociated through the lowest energy dissociation pathway. In order to determine the

IRMPD yield using Eq. 2.10, a FT-ICR mass spectrometer is used to monitor the intensity of the parent, $I_{parent,}$ and fragment ion $I_{fragment,}$ over the frequency range.

$$IRMPD\ Yield = -\log_{10}\left(\frac{I_{parent}}{I_{parent}+\sum_i I_{fragment}}\right) \quad 2.10$$

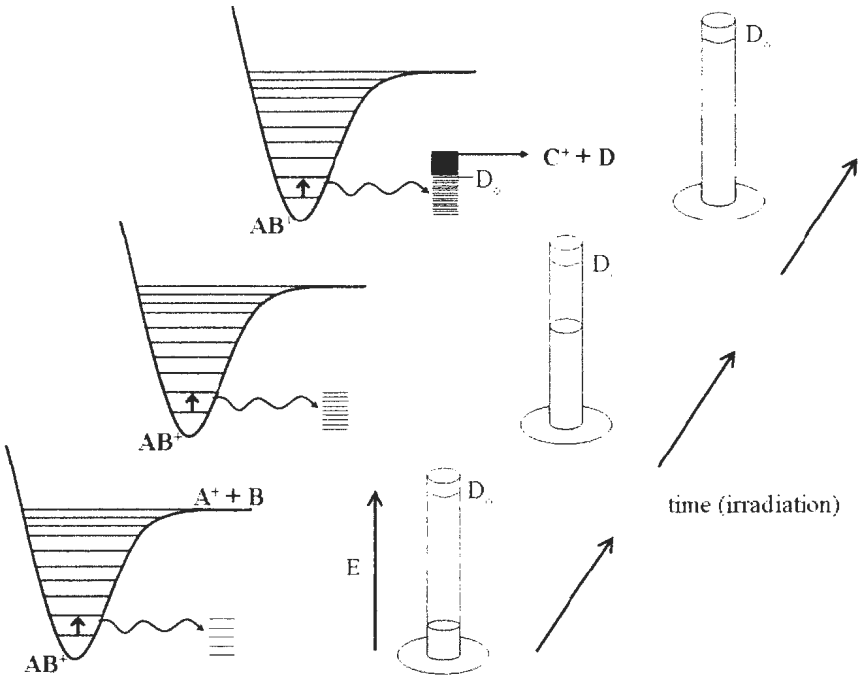

Figure 2.10. A diagram for intramolecular vibrational energy redistribution (IVR) in an IRMPD process. Figure reprinted with permission from Dr. Travis D. Fridgen (Memorial University).

2.4. Electronic Structure Calculations

The development of electronic structure calculations initiated a new chapter in the study of the gas phase chemistry of ions by providing information about structures,

relative stabilities, mechanisms for reactions, and product distributions of reactions. The two quantum mechanical methods used in this thesis for electronic structure calculations are density functional theory (DFT) and ab initio. These methods are employed to calculate geometries, energies, frequencies, and infrared spectra for the ions under study. Mechanisms of reactions were verified by examining relative energies of structures involved in reaction pathways including transition states, which are consistent with the product distributions observed by our experiments.

2.4.1. Ab initio Method

Ab initio is a Latin term for "from the beginning". Ab initio methods are mathematical approximations to solve the Schrodinger equation for systems containing more than one electron.[53] The most common types of ab initio methods are Hartree-Fock (HF) and Post-Hartree-Fock methods, MP2. HF is the simplest approximation technique for calculations of wave-functions of many body systems. The HF method solves a time-independent Schrodinger equation for a multi-electron system using the central field approximation. In the central field approximation, it is assumed that the coordinates of an electron are independent of other electrons, so they move independent of each other.[53] As a result, an average electric field is considered instead of columbic electron-electron repulsion.[53] The HF approximation results in a series of differential equations called Hartree-Fock equations which can be solved using an additional approximation leading to a set of algebraic equations. It assumes that an N-electron molecule is made up from

many hydrogen atoms; therefore a molecular orbital consists of linear combinations of atomic orbitals or a basis set of wave functions. Energy calculated from the HF approximation (limiting Hartree-Fock energy) is larger than the exact energy resulting from the Schrodinger equation. The difference between the limiting Hartree-Fock energy and the exact energy is called correlation energy.[53] This is because in the HF approximation an overall electric field is considered with the assumption that each electron feels a charge cloud of all other electrons, but in a real system the electrons' motions correlate with motion of other electrons leading to a reduction in electron repulsion energy as the correlation energy.[53] The correlation energy may be significantly large for the calculation of relative energies of molecules in a reaction. However, the Hartree-Fock model is useful for geometry optimizations because they are less sensitive to correlation effects. A higher level model like Møller- Plesset (MP2) takes correlation effects into account to obtain more accurate calculated energies.[54,55] MP2 calculates an energy close to the exact value by adding the perturbation parameter, $\hat{V}$, to the Hartree-Fock Hamiltonian as shown in Eq. 2.11.

$$H_{exact} = H_{HF} + \lambda\hat{V} \qquad 2.11$$

where λ is a dimensionless parameter.

MP2 is one of the most accurate models for geometry optimization and reaction energy calculations, but this high level model significantly increases the time and cost required. For this reason, other models are used to calculate an initial approximate geometry that can be improved by MP2 calculations.

2.4.2. Density Functional Theory (DFT)

Density functional theory has been developed based on the Hohenberg-Kohn theorem stating that the energy of many-electron molecules in their ground state are determined by an electron probability density, ρ. DFT models therefore solve the Schrodinger equation using a functional relation of electronic energy with electron probability density, written as E[ρ], instead of a complicated set of molecular wave functions, E[Ψ.].[56-58] A functional is function of another function since electronic energy is a function of electron density, and electron density is a function of position, ρ(r). A density-functional calculation is usually done in a self-consistent method. The first step in the DFT technique is an initial guess for calculation of the system's electron density. The simplest choice is to assume a molecule is formed of many individual homogeneous electrons in order to simply calculate the molecule's electron density using local density approximation (LDA).[53.56-58] In the next step, an initial guess for the electron density is used to obtain an initial estimate of atomic orbitals; these initial orbitals are then used to obtain an improved value for electron probability density. The energy of the molecule is then computed by the electron density functional. This process is repeated until the calculated electron density and energy do not significantly change. One advantage of a DFT method is that some portion of electron correlation are considered in calculations to obtain accurate enough geometry optimization in lower computational cost and time compared to HF methods. Hybrid DFT methods such as B3LYP [59.60] are the most common and reliable method for ions geometry optimization especially ionized metal-ligand complexes. It is called a hybrid method because it uses some functionals from HF

calculations to obtain more accurate results. However, there is not sufficient accuracy with DFT calculations for thermochememical data which are strongly sensitive to the correlation effects. This is the reason why we employed B3LYP functional level to compute an accurate geometry optimization, and then performed single-point Møller-Plesset second-order (MP2) perturbation theory on the optimized structures to obtain more accurate theremochemical values in an appropriate calculation time. Frequency calculations in order to obtain predicted IR spectra are performed using the B3LYP method as MP2 requires significantly longer time.

2.4.3. Basis sets

B3LYP and MP2 methods require a finite number of functions called basis sets to perform calculations. These are a linear combination of well-defined basis functions which are atomic orbitals to create ion's molecular orbital.[53] The basis sets used in this thesis are 6-31+G(d,p) and 6-311++G(2d,2p). These are split-valence basis sets representing each valence orbital by more than one basis function (e.g. valence double, triple-zeta) where a fixed single basis function is used for linear combination of primitive Guasian functions.[61] First number, 6, in the basis sets 6-31+G(d,p) and 6-311++G(2d,2p) refers to core atomic orbitals describing a single basis function formed by linear combination of six primitive Gaussian functions. The second set of numbers (31 and 311) is referred to valence atomic orbitals. For 6-31+G(d,p), there is a single Guassian function for outer valence orbitals combined with three primitive Guassian functions for

inner valence orbitals.[53] In the case of 6-311++G(2d,2p), components of valence atomic orbitals are expanded to three sets of basis functions. Additional functions (d,p) called polarization functions that allow distortion of electron distribution away from nucleus positions to produce more accurate molecular orbitals.[53] For example, 6-31+G(d,p) provides a set of five d-type functions on main group elements, and a set of three p-type functions on hydrogen and helium. In the case of 6-311++G(2d,2p), two sets of d and p-type functions are added. Diffuse functions which are represented by notations + and ++ in the basis sets indicate some additional functions for considering long distance interactions such as van der Waals interactions.[53] Diffuse interactions are very important in calculations of anions, ions with lone pairs, and structures involving hydrogen bonds. 6-31+G(d,p) adds diffuse s- and p-type functions on non-hydrogen elements, while an extra diffuse s-type function is added on each hydrogen atom in 6-311++G(2d,2p).[53] Finally, an effective core potential (ECP) basis set is used for larger atoms for which typical all-electron basis sets are not available. In this work, LANL2DZ with an ECP is used for ruthenium (studied in chapter 3-4), which is a common basis set employed for computations of systems containing atoms with a large number of electrons.[62,63] LANL2DZ provides a collective potential on the valence orbitals. This collective potential is a result of the effect of core electrons on valence electrons. As a result, LANL2DZ uses a relativistic core potential rather than a series of complicated functions resulted from inner shell orbitals.

2.4.4. Calculation Procedure

The electronic energy calculations throughout this work were done by the following procedure.

H_{corr} and G_{corr} are obtained from B3LYP calculations as described by Eq.2.12 and 2.13.

$$H_{corr} = E_{tot} + RT \quad (2.12)$$

$$G_{corr} = E_{tot} + RT - TS_{tot} \quad (2.13)$$

where E_{tot} is the summation of translational, rotational, vibrational, and electronic which is calculated by B3LYP density functional (Eq. 2.14).

$$E_{tot} = E_{tran} + E_{vib} + E_{elc} \quad (2.14)$$

-Higher level single point MP2 calculations were performed to calculate more accurate thermochemical values (ΔE_{MP2}).

-Enthalpy and free energy corrections were taken from B3LYP frequency calculations to be added to the MP2 calculated energy values to determine single point enthalpies and free energies values, respectively as defined by Eq.2.15 and 2.16.

$$\Delta H_{mp2} = \Delta E_{mp2} + H_{corr}(B3LYP) \quad (2.15)$$

$$\Delta G_{mp2} = \Delta E_{mp2} + G_{corr}(B3LYP) \quad (2.16)$$

References

(1) Rajabi, K.; Easterling, M. L.; Fridgen, T. D. *J. Am. Soc. Mass. Spectrom.* **2009**, *20*, 411.

(2) Yamashita, M.; Fenn, J. B. *J. Phys. Chem.* **1984**, *88*, 4451.

(3) Heck, A. J. R.; van den Heuvel, R. H. H. *Mass Spectrom. Rev.* **2004**, *23*, 368.

(4) Sannes-Lowery, K. A.; Hu, P.; Mack, D. P.; Mei, H.-Y.; Loo, J. A. *Anal. Chem.* **1997**, *69*, 5130.

(5) Konermann, L.; Pan, J.; Liu, Y.-H. *Chem. Soc. Rev.* **2011**, *40*, 1224.

(6) Guo, X.; Liu, Z.; Liu, S.; Bentzley, C. M.; Bruist, M. F. *Anal. Chem.* **2006**, *78*, 7259.

(7) Tito, M. A.; Miller, J.; Walker, N.; Griffin, K. F.; Williamson, E. D.; Despeyroux-Hill, D.; Titball, R. W.; Robinson, C. V. *Biophys. J.* **2001**, *81*, 3503.

(8) Blake, R. C.; Blake, D. A. *Anal. Chem.* **2012**, *84*, 6899.

(9) Banerjee, S.; Mazumdar, S. *Int. J. Anal. Chem.* **2012**, *2012*.

(10) Kebarle, P.; Tang, L. *Anal. Chem.* **1993**, *65*, 972A.

(11) Iribarne, J. V.; Thomson, B. A. *J. Chem. Phys.* **1976**, *64*, 2287.

(12) Dole, M.; Mack, L. L.; Hines, R. L.; Mobley, R. C.; Ferguson, L. D.; Alice, M. B. *J. Chem. Phys.* **1968**, *49*, 2240.

(13) Mack, L. L.; Kralik, P.; Rheude, A.; Dole, M. *J. Chem. Phys.* **1970**, *52*, 4977.

(14) Kebarle, P.; Verkerk, U. H. *Mass Spectrom. Rev.* **2009**, *28*, 898.

(15) Cole, R. B. *J. Mass Spectrom.* **2000**, *35*, 763.

(16) Marshall, A. G.; Hendrickson, C. L. *Int. J. Mass spectrom.* **2002**, *215*, 59.

(17) Marshall, A. G.; Hendrickson, C. L.; Jackson, G. S. *Mass Spectrom. Rev.* **1998**, *17*, 1.

(18) Marshall, A. G. *Acc. Chem. Res.* **1985**, *18*, 316.

(19) Marshal, A. G.; Grosshans, P. B. *Anal. Chem.* **1991**, *63*, 215A.

(20) Buchanan, M. V.; Comisarow, M. B. In *Fourier Transform Mass Spectrometry*; American Chemical Society: 1987; Vol. 359, p 1.

(21) McLuckey, S. A. *J. Am. Soc. Mass. Spectrom.* **1992**, *3*, 599.

(22) Shukla, A. K.; Futrell, J. H. *J. Mass Spectrom.* **2000**, *35*, 1069.

(23) de Hoffmann, E.; Stroobant, V. *Mass spectrometry, Principles and applications,*; 3rd edition, ed.; John Wily and Sons, Ltd,, 2007; Vol. Chapter 4.

(24) Sleno, L.; Volmer, D. A. *J. Mass Spectrom.* **2004**, *39*, 1091.

(25) Herrmann, K. A.; Somogyi, Á.; Wysocki, V. H.; Drahos, L.; Vékey, K. *Anal. Chem.* **2005**, *77*, 7626.

(26) Woodin, R. L.; Bomse, D. S.; Beauchamp, J. L. *J. Am. Chem. Soc.* **1978**, *100*, 3248.

(27) Bomse, D. S.; Woodin, R. L.; Beauchamp, J. L. *J. Am. Chem. Soc.* **1979**, *101*, 5503.

(28) Woodin, R. L.; Bomse, D. S.; Beauchamp, J. L. *Chem. Phys. Lett.* **1979**, *63*, 630.

(29) Bomse, D. S.; Beauchamp, J. L. *Chem. Phys. Lett.* **1981**, *77*, 25.

(30) Bomse, D. S.; Beauchamp, J. L. *J. Am. Chem. Soc.* **1980**, *102*, 3967.

(31) Osterheld, T. H.; Brauman, J. I. *J. Am. Chem. Soc.* **1990**, *112*, 2014.

(32) Osterheld, T. H.; Baer, T.; Brauman, J. I. *J. Am. Chem. Soc.* **1993**, *115*, 6284.

(33) Osterheld, T. H.; Brauman, J. I. *J. Am. Chem. Soc.* **1993**, *115*, 10311.

(34) Baykut, G.; Watson, C. H.; Weller, R. R.; Eyler, J. R. *J. Am. Chem. Soc.* **1985**, *107*, 8036.

(35) Watson, C. H.; Baykut, G.; Battiste, M. A.; Eyler, J. R. *Anal. Chim. Acta* **1985**, *178*, 125.

(36) Watson, C. H.; Baykut, G.; Eyler, J. R. In *Fourier Transform Mass Spectrometry*; American Chemical Society: 1987; Vol. 359, p 140.

(37) van der Rest, G.; He, F.; Emmett, M. R.; Marshall, A. G.; Gaskell, S. J. *J. Am. Soc. Mass. Spectrom.* **2001**, *12*, 288.

(38) Kruppa, G.; Schnier, P. D.; Tabei, K.; Van Orden, S.; Siegel, M. M. *Anal. Chem.* **2002**, *74*, 3877.

(39) Little, D. P.; Speir, J. P.; Senko, M. W.; O'Connor, P. B.; McLafferty, F. W. *Anal. Chem.* **1994**, *66*, 2809.

(40) Null, A. P.; Muddiman, D. C. *J. Mass Spectrom.* **2001**, *36*, 589.

(41) Bensimon, M.; Rapin, J.; Gäumann, T. *Int. J. Mass Spectrom. Ion Processes* **1986**, *72*, 125.

(42) Watson, C. H.; Baykut, G.; Mowafy, Z.; Katritzky, A. R.; Eyler, J. R. *Instrumentation Science & Technology* **1988**, *17*, 155.

(43) Ali, O. Y.; Fridgen, T. D. *ChemPhysChem* **2012**, *13*, 588.

(44) Patel, C. K. N.; Tien, P. K.; McFee, J. H. *Appl. Phys. Lett.* **1965**, *7*, 290.

(45) Patel, C. K. N. *Physical Review* **1964**, *136*, A1187.

(46) Oepts, D.; van der Meer, A. F. G.; van Amersfoort, P. W. *Infrared Physics & Technology* **1995**, *36*, 297.

(47) Colson, W. B.; Johnson, E. D.; Kelley, M. J.; Schwettman, H. A. *Physics Today* **2002**, *55*, 35.

(48) Tittel, F.; Richter, D.; Fried, A. In *Solid-State Mid-Infrared Laser Sources*; Sorokina, I., Vodopyanov, K., Eds.; Springer Berlin / Heidelberg: 2003; Vol. 89, p 458.

(49) Armstrong, J. A.; Bloembergen, N.; Ducuing, J.; Pershan, P. S. *Physical Review* **1962**, *127*, 1918.

(50) Yang, S. T.; Eckardt, R. C.; Byer, R. L. *Opt. Lett.* **1993**, *18*, 971.

(51) Eyler, J. R. *Mass Spectrom. Rev.* **2009**, *28*, 448.

(52) Fridgen, T. D. *Mass Spectrom. Rev.* **2009**, *28*, 586.

(53) Lewars, E. G. *Computational chemistry : Introduction to the theory and applications of molecular and quantum mechanics*; 2nd ed.; Springer: Dordrecht ; London,, 2010.

(54) Head-Gordon, M.; Pople, J. A.; Frisch, M. J. *Chem. Phys. Lett.* **1988**, *153*, 503.

(55) Møller, C.; Plesset, M. S. *Physical Review* **1934**, *46*, 618.

(56) Vignale, G.; Rasolt, M. *Phys. Rev. Lett.* **1987**, *59*, 2360.

(57) Hohenberg, P.; Kohn, W. *Physical Review* **1964**, *136*, B864.

(58) Sousa, S. F.; Fernandes, P. A.; Ramos, M. J. *J. Phys. Chem. A* **2007**, *111*, 10439.

(59) Becke, A. D. *J. Chem. Phys.* **1993**, *98*, 5648.

(60) Lee, C.; Yang, W.; Parr, R. G. *Phys. Rev. B.* **1988**, *37*, 785.

(61) Davidson, E. R.; Feller, D. *Chem. Rev.* **1986**, *86*, 681.

(62) Wadt, W. R.; Hay, P. J. *J. Chem. Phys.* **1985**, *82*, 284.

(63) Russo, T. V.; Martin, R. L.; Hay, P. J. *J. Phys. Chem.* **1995**, *99*, 17085.

Chapter 3. Kinetic and Mechanistic Studies of Low-pressure Ion–Molecule Association Reactions of Unsaturated Ru(II) Complexes with CO

This work has been published in part as A. *Gholami and T.D. Fridgen.*, Kinetic and mechanistic studies of low-pressure ion–molecule association reactions of unsaturated Ru(II) complexes with CO, International Journal of Mass Spectrometry., 2012, 313-316, 192-198. This work has been done and written by me and under supervision of Dr. Travis D. Fridgen.

3.1. Introduction

Radiative association reactions between ions and neutral molecules at very low pressures have been of extensive scientific importance. They are rarely studied in the laboratory despite their role in, for example, the chemistry and evolution of interstellar clouds.[1-6] The focus of many radiative association studies has been to obtain binding energies of gaseous ion–molecule complexes by measuring pressure dependent association rate constants (k_{ass}) which can subsequently be used to obtain radiative association rate constants (k_{ra}), and more importantly, back dissociation rate constants (k_b) of the chemically activated ion–molecule complexes. Comparison of experimental k_{ra} and k_b values with the theoretically determined rate constants can result in good estimates of the binding energy of the ion–molecule complexes.[7-11]

In a large number of organic and biological systems, transition metal complex-based enzymes can be activated by attachment to CO.[12] In some proteins, carbon monoxide is a promotive ligand, activating transition metal-based enzymes, leading to many important biological reactions. On the other hand, CO can be harmful as it acts as a poisoning ligand since it strongly binds to hemoglobin.[12,13] In this regard, the reaction of CO with transition metals is very important and of considerable interest.

Herman et al. have investigated gas phase reactions between Ti^+, V^+, Fe^+, Ni^+, Cu^+, Zn^+ and CO where the adduct complex $M(CO)^+$ was the only reaction product.[13] The rate of addition of CO to these metals was found to be very slow, and the trend in the reactivity followed the trend in M–CO binding energy. The transition from bare ions into ligated ions increases reactivity, so finding proper ligated metal ions in catalytic

transformation processes, and understanding the influence of ligand on the reactivity is essential.

The gas phase ion–molecule reaction of unsaturated 2,2'- bipyridine dication with molecular oxygen has been studied recently.[14,15] A series of divalent metal ion complexes $[M(bipy)_2]^{2+}$ (M = Cr, Mn, Fe, Co, Ni, Cu, Ru, Os) were exposed to dioxygen under multiple collision conditions in the collision cell of a triple quadrupole mass spectrometer; the dioxygen product was observed only when M = Cr, Ru and Os.[15] Under low-pressure conditions, in a Fourier transform ion cyclotron resonance (FTICR) mass spectrometer, it was shown that the efficiency of the reaction between $[M(bipy)_2]^{2+}$ (M = Cr, Ru and Os) and O_2 was low, just a few percent of the gas-collision rate and independent of pressure which indicates the importance of radiative emission in the formation of the adduct complexes.[15]

In this chapter, we report on a mechanistic study of the reaction of $[Ru(bipy)_2]^{2+}$ with carbon monoxide and oxygen in the gas phase. Also examined in this work is the comparison of the reactivity for three unsaturated ruthenium complexes $[Ru(bipy)(X)]^{2+}$ with carbon monoxide, where X = bipyridine, 2- (pyridin-4-yl)-1,3-benzothiazole, and 5-aminophenathroline. This was done experimentally using the low pressure conditions of the FTICR mass spectrometer. The effect of different ligands on the kinetics of CO association to the ruthenium center is explored. Initially, the goal of this work was to determine binding energies of $[Ru(bipy)(X)]^{2+}$/CO complexes using the experimental back dissociation rate constant and RRKM modeling of the unimolecular back dissociation as a function of binding energies. The radiative emission and unimolecular

dissociation rate constants, and dissociation energies of $[Ru(bipy)(X)]^{2+}$/CO complexes are calculated to aid in the understanding of the mechanism of these association reactions at low pressures.

3.2. Methods

3.2.1. Experimental

All experiments were performed using Bruker ApexQe 70 Fourier transform ion cyclotron resonance (FTICR) mass spectrometer with an Apollo II electrospray source. $[Ru(bipy)_3Cl_2]$ (bipy = bis(2,2'-bipyridine)) salt was purchased from Sigma– Aldrich. Two other complexes, $[Ru(bipy)_2(phen)Cl_2]$ (phen = 5-aminophenathroline) and $[Ru(bipy)_2(sn)Cl_3]$ (sn = 2-(pyridin-2- yl)-1,3-benzothiazole) were synthesized and characterized by the Pickup group at Memorial University.[16]

$[Ru(bipy)_2X]^{2+}$ ions were electrosprayed from 0.1 mM solutions of the respective ruthenium complexes in pure methanol. The coordinatively unsaturated ruthenium complexes were generated by loss of bipyridine (Scheme 3.1) in energetic collisions, 12–40 eV lab frame (E_{cm}: 0.8–2.6 eV), with Argon at 10^{-2} mbar in the hexapole collision cell of the mass spectrometer. Prior to being transferred to the ICR cell, ions were stored in the hexapole storage/collision cell for ~2 s where they are cooled through numerous collisions (~10^5) with the Ar bath gas. The ions produced in the collision cell were then transferred to the ICR cell where they were trapped radially by a 7 T magnetic field and axially by a ~1 V DC trapping potential. Following ~1–2 s after the trapping event, the

$[Ru(bipy)X]^{2+}$ ions were isolated in the ICR cell and their reaction with CO or O_2 over varying periods of time was monitored. CO and O_2 gases were introduced into the ICR cell through a heated precision leak valve. The pressure inside the ICR cell was measured via a calibrated ionization gauge and kept constant during the timeframe of the experiment.

For temperature dependent experiments, the internal temperature of the ICR cell was increased using a heating jacket wrapped around the ICR cell and flight tube vacuum chamber. The temperature at the center of the ICR cell was calibrated to the outside temperature of the vacuum chamber.

3.2.2. Theoretical work

The Gaussian 09[17] suite of programs was used in this work. Geometry optimizations as well as vibrational frequency and intensity calculations were done using the B3LYP hybrid density functional and 6-31+G(d,p) basis set for all atoms except Ru, for which LANL2DZ basis set and effective core potential was used. Single point calculations were done on these B3LYP optimized geometries at the MP2(full) level of theory and the 6-31+G(d,p) basis set on all atoms except Ru, for which the LANL2DZ basis set and effective core potential was used. MP2(full)/6-31+G(d,p) electronic energies and the thermal contribution to free energies from B3LYP/6-31+(d,p) calculations were then used to compute relative enthalpies and Gibbs energies. This method has been

abbreviated MP2(full)/6-31+G(d,p)//B3LYP/6-31+G(d,p) but it should be noted that the LANL2DZ basis set and effective core potential was used on Ru.

All ion–molecule collision rate constants in this work were computed using the algorithm of ion–polar molecule collision rates determined by Su and Chesnavich.[18] Rate constants for radiative emission (k_{ra}) were modeled using Eq. 3.1 as described previously.[19,20]

$$k_r(s^{-1}) = \sum_{i=1}^{N_m}\sum_{n=0}^{\infty} 1.25\times10^{-7}.nP(n)I_i(km\,mol^{-1}).\tilde{\nu}_i^2(cm^{-1}) \qquad 3.1$$

Briefly, the first and second summations are over the all the normal vibrational modes (i) and the number of vibrational levels (n) included for each mode which, for practical purposes, only 5–6 levels contributed significantly. Vibrational wavenumbers ($\tilde{\nu}$) and intensities (I) were obtained from the B3LYP/6-31+G(d,p) calculations and used without scaling. The canonical distribution of states, $P_i(n,T)$, was calculated using Eq. 3.2.

$$P_i(n,T) = \exp\left(-\frac{h\nu_i n}{k_B T}\right)\left[1-\exp\left(-\frac{h\nu_i}{k_B T}\right)\right] \qquad 3.2$$

where h and k_B are Planck and Boltzmann constants, respectively, and the ν_i is the vibrational frequency in s^{-1}. T represents the internal temperature of the ion and is determined as the solution to Eq. 3.3

$$E_t = \sum_i\left[\frac{h\nu_i N_A}{e^{h\nu_i/k_B T}-1}\right] \qquad 3.3$$

where E_t is the threshold dissociation energy which was estimated using the (full)/6-31+G(d,p)//B3LYP/6-31+G(d,p) calculations. RRKM energy dependent unimolecular dissociation rate constants (k_{uni}) were calculated using Eq. 3.4.[21]

$$k_{uni}(E) = \sigma \frac{N^*(E - E_0)}{h\rho(E)} \qquad 3.4$$

where σ is the symmetry number and the sum (N^*) and density (ρ) of states were calculated using the Beyer–Swinehart direct count algorithm using the B3LYP/6-31+G(d,p) computed vibrational frequencies and rotational constants. The unimolecular rate constants reported in this work were averaged over a Boltzmann distribution of internal energies. Unimolecular dissociation rate constants were calculated at the dissociation energies as well as at ±15 kJ mol^{-1} values. These values were computed for both neutral and loose transition states. For the neutral transition states, the frequency for the reaction coordinate was eliminated from the transition state to compute the sums of states for the transition state producing an Arrhenius preexponential factor of about 10^{14} s^{-1}. For a loose transition state, the frequency for the reaction coordinate was eliminated and the five lowest vibrational frequencies were reduced to produce an Arrhenius preexponential factor of 10^{19} ($\Delta S^{\neq}$ = 115 J KΓ^1 molΓ^1).

3.3. Results and Discussion

3.3.1. Structures

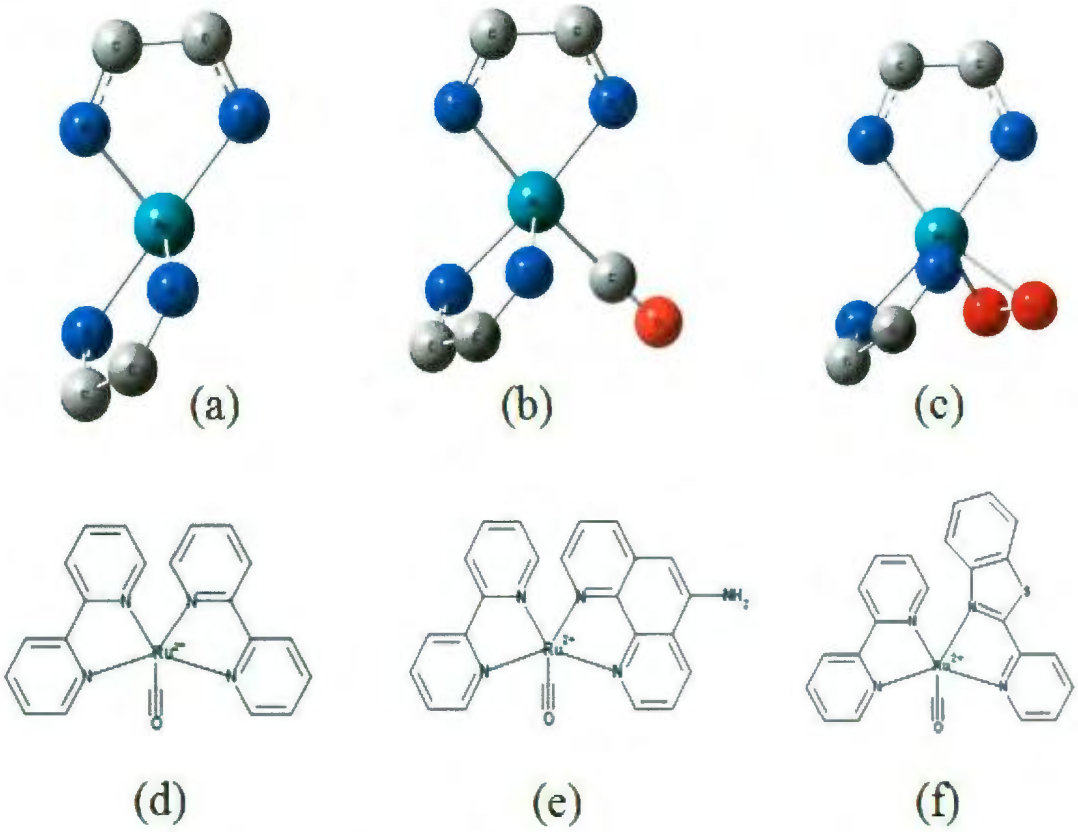

Figure 3.1. Optimized structures for the lowest energy of (a) $[Ru(bipy)_2]^{2+}$, (b) $[Ru(bipy)_2(CO)]^{2+}$, (c) $[Ru(bipy)_2(O_2)]^{2+}$(note that the bulk of the bipy ligand has been removed for clarity), and schematic of (d) $[Ru(bipy)_2(CO)]^{2+}$, (e) $[Ru(bipy)(phen)(CO)]^{2+}$, and (f) $[Ru(bipy)(sn)(CO)]^{2+}$.

In Fig. 3.1, the lowest energy structures for $[Ru(bipy)_2]^{2+}$, $[Ru(bipy)_2(CO)]^{2+}$ and $[Ru(bipy)_2(O_2)]^{2+}$complexes are shown as well as a schematic of structures for $[Ru(bipy)(X)(CO)]^{2+}$ (where X = bipy, sn, and phen). In all complexes, the ground state

structure was found to be a singlet which has roughly octahedral geometry with one or two missing perpendicular sites as illustrated in Fig. 3.1a for $[Ru(bipy)_2]^{2+}$. It was found that $[Ru(bipy)(X)(CO)]^{2+}$ lies in a lower energy state with CO bound to the ruthenium through the carbon rather than oxygen, as expected (Fig. 3.1b). The structure where O_2 coordinates in an η^2 fashion (Fig. 3.1c) with an O-O bond distance of 134 pm, characteristic of a superoxide, was found to be the most stable structure for $[Ru(bipy)_2(O_2)]^{2+}$. Based on density functional calculations, Howe et al. found similar structures for $[Cr(bipy)_2]^{2+}$ and $[Fe(bipy)_2]^{2+}$ binding to O_2: O_2 having an η^2-bond superoxide structure .[22] Nielsen *et al.* proposed superoxide or peroxo structures as the probable structures of $[Cr(bipy)_2(O_2)]^{2+}$ and $[Ru(bipy)_2(O_2)]^{2+}$ based on the mass spectrometric results. The low collision energy required for loosing O_2 from $[Cr(bipy)_2(O_2)]^{2+}$ or $[Ru(bipy)_2(O_2)]^{2+}$ as well as the low efficiency resulted in the formation of these adduct complexes were the interpretation of the proposed structures.[15]

3.3.2. CID of $[Ru(bipy)_2(X)]^{2+}$

Electrospray mass spectra were virtually free of contaminants and showed only the $[Ru(bipy)_2(X)]^{2+}$ ions. The CID spectra of each precursor ion are shown in Fig. 3.2 for a collision voltage of 14.5 eV (1.6–1.8 eV center of mass frame of reference). $[Ru(bipy)_3]^{2+}$ solely loses a bipy ligand upon CID (Fig. 2a). $[Ru(bipy)_2(phen)]^{2+}$ also loses only a bipy ligand (Fig. 3.2c) which is experimental evidence of stronger binding of the phen ligand vs bipy. $[Ru(bipy)_2(sn)]^{2+}$ loses either the sn or the bipy ligand upon CID

(Fig. 3.2b) since both $[Ru(bipy)_2]^{2+}$ and $[Ru(bipy)(sn)]^{2+}$ are observed. Since both ligands are lost in virtually equal amounts and that there are two bipy ligands and only one sn, it can be concluded from the experiments that bipy is probably slightly more strongly bound than sn. Calculations of the ligand dissociation energies for the $[Ru(bipy)_2(X)]^{2+}$ are listed in Table 3.1 and the values are consistent with the conclusions from experiment in that phen is more strongly bound than bipy, by 21 kJ mol^{-1}. However, calculations also show that bipy is more strongly bound than sn, by about 19 kJ mol^{-1}. It is reasonable that since there are two bipy ligands and at the high internal energy of the species undergoing CID, that the rate constant for bipy loss might be similar to the loss of sn which is why losses observed are both bipy and sn.

Table 3.1. Calculated gas phase MP2/6-31+G(d,p) 0 K dissocition energies of $[Ru(bipy)_2X]^{2+}$ complex ions.

Reaction	**Do / kJ molΓ^1**
$[Ru(bipy)_3]^{2+} \rightarrow [Ru(bipy)_2]^{2+} + bipy$	453
$[Ru(bipy)_2(phen)]^{2+} \rightarrow [Ru(bipy)(phen)]^{2+} + bipy$	450
$\rightarrow [Ru(bipy)_2]^{2+} + phen$	471
$[Ru(bipy)_2(sn)]^{2+} \rightarrow [Ru(bipy)(sn)]^{2+} + bipy$	461
$\rightarrow [Ru(bipy)_2]^{2+} + sn$	442

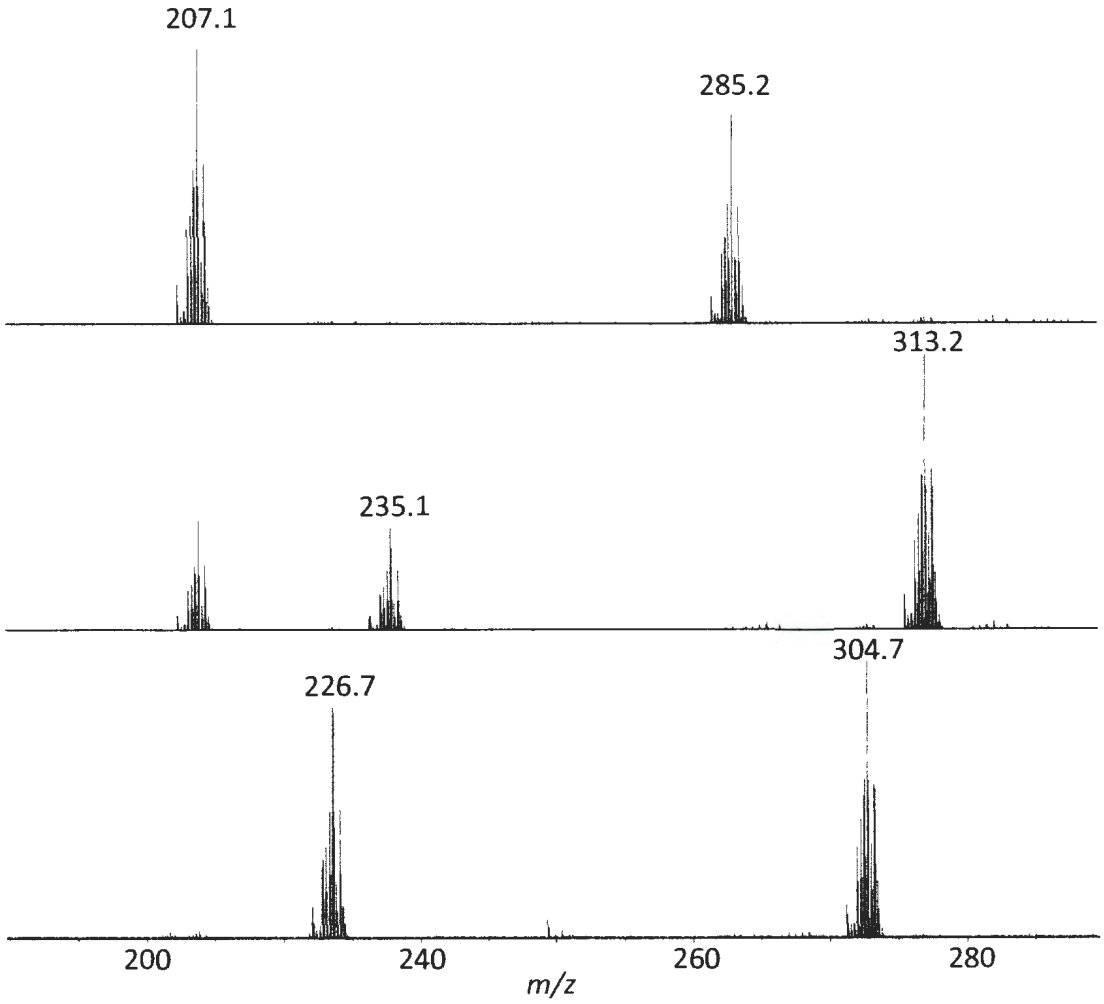

Figure 3.2. CID mass spectra of (a) $[Ru(bipy)_3]^{2+}$, (b) $[Ru(bipy)_2(sn)]^{2+}$, and (c) $[Ru(bipy)_2(phen)]^{2+}$ excited to 14.5 eV lab frame collision energy (1.6–1.8 eV center of mass frame) with argon as the target gas.

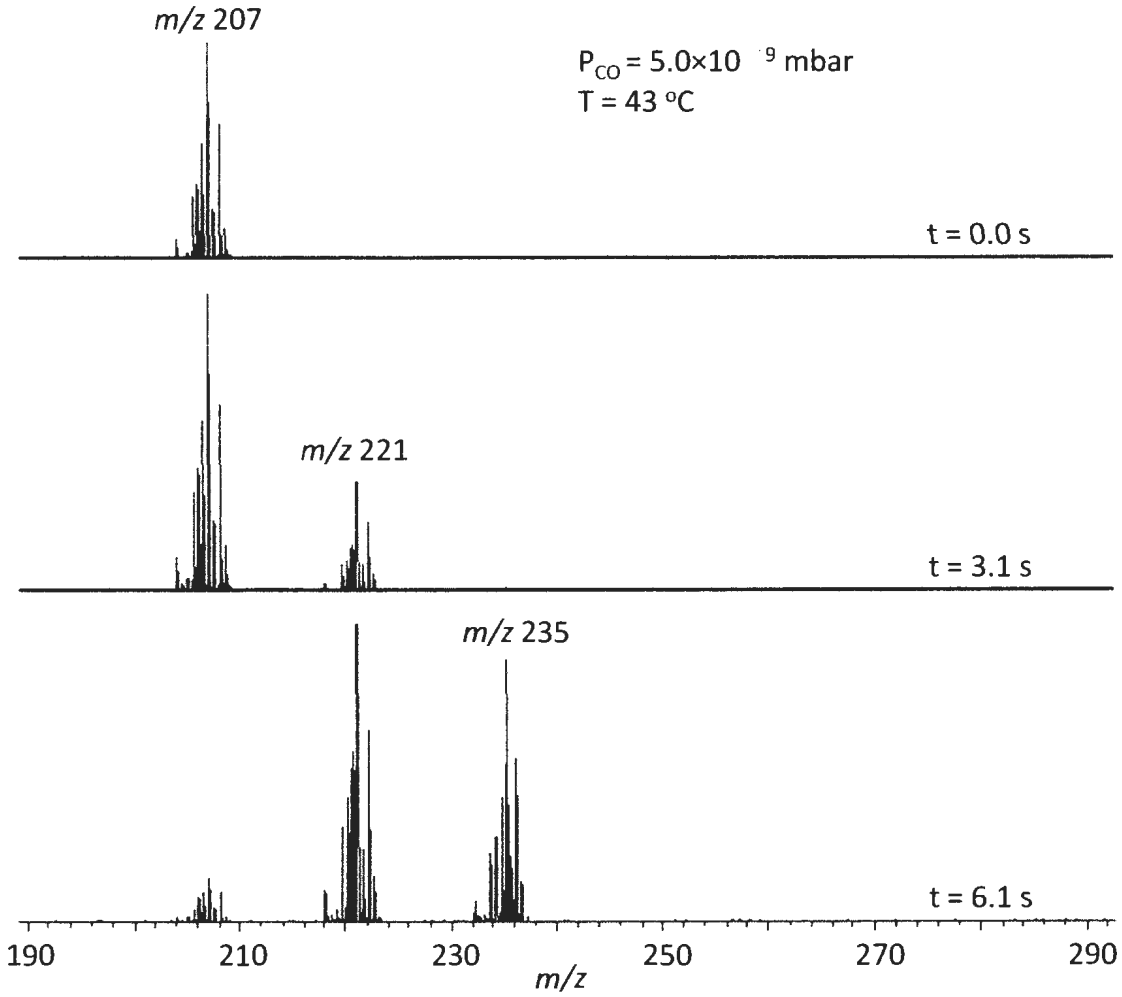

Figure 3.3. Mass spectra recorded at various reaction times, with CO, following isolation of $[Ru(bipy)_2]^{2+}$.

3.3.3. Association of O_2 or CO with $[Ru(bipy)_2(X)]^{2+}$

The reactions of both O_2 and CO with $[Ru(bipy)(X)]^{2+}$ occurs solely by addition. Addition of only one O_2 molecule was observed and this is consistent with previous studies.[15] However, up to two CO molecules were found to bind to $[Ru(bipy)(X)]^{2+}$ as is

shown in Fig. 3.3 for the reaction of $[Ru(bipy)_2]^{2+}$ at 3.1 and 6.1 s following isolation of $[Ru(bipy)_2]^{2+}$.

The reaction of $[Ru(bipy)(X)]^{2+}$ with CO occurs by two sequential CO additions as shown in Eq. 3.5

$$[Ru(bipy)(X)]^{2+} \xrightarrow{[CO]k_{app,1}} [Ru(bipy)(X)(CO)]^{2+} \xrightarrow{[CO]k_{app,2}} [Ru(bipy)(X)(CO)_2]^{2+} \quad 3.5$$

where $k_{app,1}$ and $k_{app,2}$ are the apparent (experimental) second order rate constants for addition of the first and second CO molecules. An example of the time dependence of the ion intensities for $[Ru(bipy)_2]^{2+}$ in a background of CO gas is shown in Fig. 3.4. It is also seen from Fig. 3.4 that there is an onset of about 2–3 s before normal first-order decay of the reactant ion signal is observed. This onset is pressure dependent; the higher the pressure, the shorter the onset time. The onset is most likely due to translational excitation of the reactant ion due to the axial trapping potential (~1 V).

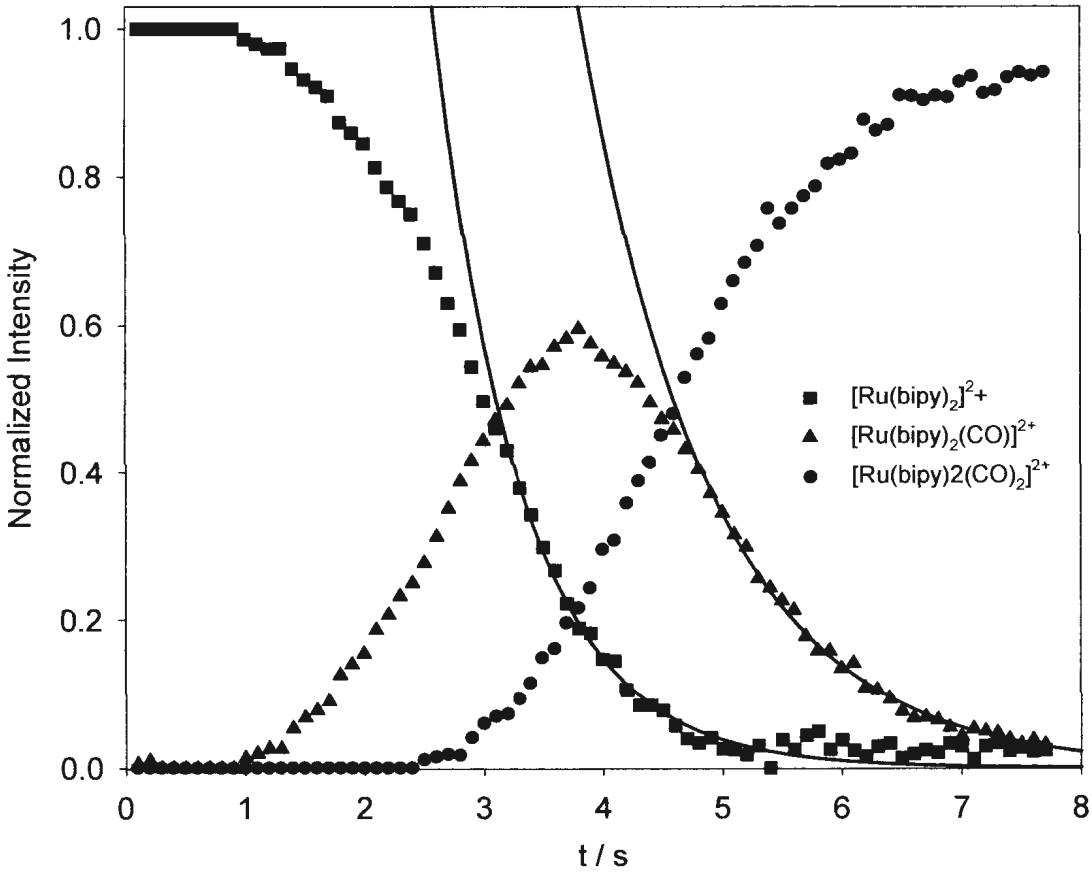

Figure 3.4. Normalized intensity as a function of time for the association of CO to $[Ru(bipy)_2]^{2+}$ at P = 8.0 × 10^{-9} mbar and 293 K. The solid lines are an exponential fit used to determine the pseudo first-order rate constants.

The pseudo-first order rate constants were obtained by fitting the later intensity vs time data to an exponential fit as shown in Fig. 3.4. The second order rate constants were obtained by dividing the pseudo-first order rate constants by the number density of neutral reactant in the ICR cell. It can be seen in Fig. 3.5a that the second order rate constants are independent of pressure which is consistent with a radiative mechanism for stabilization of the ion–molecule addition complexes. We will have more to say about the mechanism for formation of the addition complexes below. The same pressure independence for O_2 addition was also observed and consistent with previous results.[15] The rate constants were also determined for a range of temperatures from 293 to 340 K and are shown in Fig. 3.5b. There is a slight negative temperature dependence that is also characteristic of radiative association reactions as the rate constant for dissociation of the nascent complex increases slightly. The small negative temperature dependence is due to the small increase in internal energy with increasing temperature with respect to the large amount of internal energy of the nascent complex obtained by forming a strongly bound association complex with CO (vida infra).

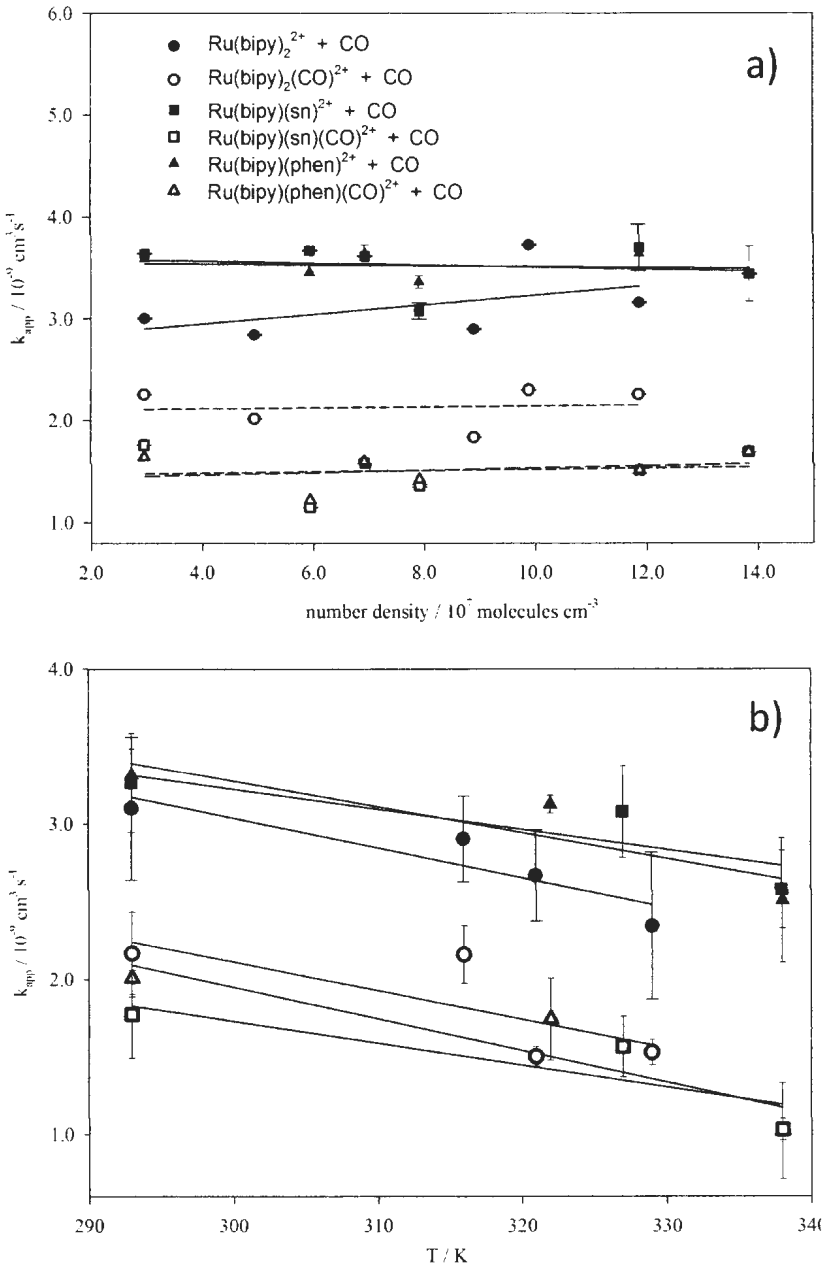

Figure 3.5. Plots of the (a) pressure and (b) temperature dependence of the reactions of $[Ru(bipy)X]^{2+}$ and $[Ru(bipy)XCO]^{2+}$ with CO.

The established mechanism for ion–molecule association reactions in a low pressure ICR cell, for the reaction between CO and $[Ru(bipy)_2]^{2+}$ is shown in Scheme 3.1.

$$[Ru(bipy)_2]^{2+} + CO \underset{k_b}{\overset{k_f}{\leftrightarrow}} [Ru(bipy)_2CO]^{2+*} + M \xrightarrow{k_c} [Ru(bipy)_2CO]^{2+} + M$$

$$\xrightarrow{k_{ra}} [Ru(bipy)_2CO]^{2+} + h\nu$$

Scheme 3.1. The mechanism for ion-molecule association reaction in a low pressure ICR cell.

The nascent ion–molecule complex ($[Ru(bipy)(X)(CO)^{2+}]^*$) is assumed to be formed at the ion molecule collision rate (k_f). During the lifetime of $[Ru(bipy)(X)(CO)^{2+}]^*$ it can be stabilized either by one collision (k_c) with a third body (M, most likely the background gas, CO) or by emission of an infrared photon (k_{ra}) (IR-chemiluminescence). Failing collisioinal or radiative stabilization, $[Ru(bipy)(X)(CO)^{2+}]^*$ can eventually redissociate (k_b), in the present case to lose CO. In this mechanism we have assumed that one collision with, or emission of one photon from $[Ru(bipy)(X)(CO)^{2+}]^*$ will decrease the internal energy of the complex and increase the lifetime of the complex so that redissociation does not occur.

By applying the steady state approximation to the intermediate, $[Ru(bipy)(X)(CO)]^{2+*}$, a bimolecular apparent rate constant for the addition of CO to $[Ru(bipy)(X)]^{2+}$ is given by Eq. 3.6

$$k_{app} = \frac{k_f(k_{ra} + k_c[\mathrm{M}])}{k_b + k_{ra} + k_c[\mathrm{M}]} \qquad 3.6$$

By performing a Taylor series expansion about [M] = 0 to first order in [M], the association rate constant in Eq. 3.6 can be expressed as

$$k_{app} = \frac{k_f k_{ra}}{k_b + k_{ra}} + \frac{k_f k_b k_c[\mathrm{M}])}{(k_b + k_{ra})^2} \qquad 3.7$$

Over the pressure regime studied in these experiments the association rate constant for CO or O_2 addition was shown to be independent of pressure. Eq. 3.7, therefore, can be simplified to eliminate the pressure dependent term,

$$k_{app} = \frac{k_f k_{ra}}{k_b + k_{ra}} \qquad 3.8$$

The independence of pressure is understandable at the low pressures that these experiments are conducted, third-body collisions are simply too rare.

In Table 3.2, the experimental second order rate constants (averaged over pressure) for association of O_2 and CO to the unsaturated $[Ru(bipy)(X)]^{2+}$ complexes at 293 K are summarized along with the calculated collision rate constants, k_f. It is interesting to compare the rate constant for O_2 addition to $[Ru(bipy)_2]^{2+}$ determined here (2.5×10^{-10} cm^3 s^{-1}) and that determined by Nielsen *et al.*[15] more than an order of magnitude smaller at 1.5×10^{-11} cm^3 s^{-1}. The difference in these rate constants can be explained based on how $[Ru(bipy)_2]^{2+}$ is formed in the two experiments. In the present experiments, $[Ru(bipy)]^{2+}$ were formed by CID in and stored in a region of high pressure ($\sim 10^{-2}$ mbar) where there will be many collisions that will dissipate the excess internal energy of the product ions. In the previous experiments[15] , $[Ru(bipy)]^{2+}$ were formed in

the ICR cell by SORI-CID under low pressure conditions and in the absence of collisions to remove the excess energy imparted to the product ions in the CID process. Besides the larger rate constants determined in the present experiments, evidence for cooler ions in the present work may also be that the onset times are much shorter in our experiments ~3 s at $\sim 10^{-8}$ mbar vs ~20 s in the previous experiments at $\sim 10^{-7}$ mbar.

The rate constant for O_2 association to $[Ru(bipy)_2]^{2+}$ is only about 20–25% of the collision rate constant. From the expression for the apparent rate constant (Eq. 3.8), this means that the ratio $k_{ra}/k_b + k_{ra}$ is between 0.2 and 0.25, which in turn means that k_b and k_{ra} are similar in magnitude.

The binding energy of the $[Ru(bipy)_2]^{2+}/O_2$ association product is determined to be 97.5 kJ mol^{-1} using B3LYP/6-31G(d)//MP2/6- 31G(d). The computed k_{ra} values for the nascent $[Ru(bipy)_2O_2]^{2+}$ complex is 3.5 s^{-1} while k_b is calculated to be 2.3×10^{-5} s^{-1} for the neutral transition state and 0.41 s^{-1} for the loose transition state (see Fig. 3.6a). The computed values of k_{ra} and k_b quite similar in magnitude as expected based on the efficiency of collisions resulting in association product formation. The values for k_{ra} and k_b computed at the dissociation threshold, however, do not provide the exact efficiency, nor would we expect such crude estimates of the rate constants to be quantitative. The computed rate constants are determined using computed vibrational frequencies and intensities which obviously have some error associated with them and there is also probably some error associated with the dissociation energy used, which is also a computed value. Plots of k_b vs dissociation energy are provided in Fig. 3.6a. It is also

interesting to compare the results of the k_b calculations for O_2 association to that for the CO association reactions.

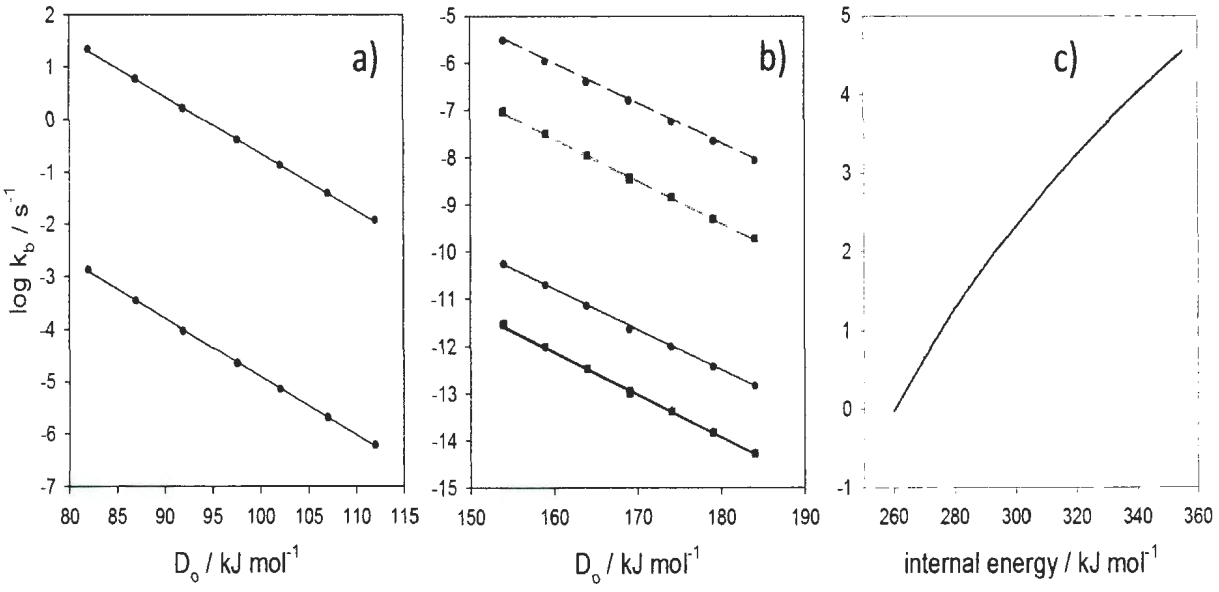

Figure 3.6. Plots of the base 10 logarithm of the computed back dissociation rate constants as a function of dissociation energy for (a) the nascent $[Ru(bipy)_2O_2]^{2+}$ complex and (b) the nascent $[Ru(bipy)_2CO]^{2+}$ as well as (c) the logarithm of the back dissociation rate constant vs internal energy $[Ru(bipy)_2(CO)_2]^{2+}$.

Table 3.2. Experimental and collision rate constants (k_{app} and k_f, respectively) for association of the first and second CO to $[Ru(bipy)_2]^{2+}$, $[Ru(bipy)(sn)]^{2+}$, and $[Ru(bipy)(phen)]^{2+}$, and association of O_2 to $[Ru(bipy)_2]^{2+}$ at 293 K.

	Complex		
	$[Ru(bipy)_2]^{2+}$	$[Ru(bipy)(sn)]^{2+}$	$[Ru(bipy)(phen)]^{2+}$
$k_{app,1}(CO)$ / $cm^3\ s^{-1}$	$3.1\pm 0.8\times10^{-9}$	$3.4\pm 0.8\times10^{-9}$	$3.4\pm 1.0\times10^{-9}$
$k_{app,2}(CO)$ / $cm^3\ s^{-1}$	$2.1\pm0.6\times0^{-9}$	$1.6\pm 0.7\times10^{-9}$	$1.7\pm 0.5\times10^{-9}$
$k_f(CO)$ / $cm^3\ s^{-1}$	1.9×10^{-9}	1.9×10^{-9}	1.9×10^{-9}
$k_{ass}O_2$ / $cm^3\ s^{-1}$	$2.5\pm 0.8\times0^{-10}$		
$k_f O_2$ / $cm^3\ s^{-1}$	1.1×10^{-9}		

The $[Ru(bipy)(X)]^{2+}$/CO association reactions all occur at the collision rate (Table 3.2). This means that each collision results in an association complex observed in the mass spectrometer. In order for this to be true, according to the radiative association mechanism the back dissociation rate constant, k_b, must be significantly smaller than the radiative association rate constant, k_{ra} so that Eq. 3.8 simplifies to $k_{app} = k_f$. The binding energy of the $[Ru(bipy)(X)]^{2+}$/CO complexes are all calculated to be about 169 kJ mol^{-1}. That the binding energies are virtually identical to each other might also explain why the association rate constants for all three $[Ru(bipy)(X)]^{2+}$/CO reactions are the same. Due to the strong binding energy the back dissociation rate constants are calculated to be significantly lower than for the nascent $[Ru(bipy)(X)]^{2+}/O_2$ complexes: $2.3 \times 10^{-12}\ s^{-1}$ for

$[Ru(bipy)_2]^{2+}$ and 1×10^{-13} s^{-1} when x = sn or phen for the neutral transition state. For the more realistic loose transition state, the k_b values increase to between 10^{-7} and 10^{-9} s^{-1} (Fig. 3.6b). The k_{ra} values for the CO association complexes are between 8 and 13 s^{-1} and are significantly larger than the computed k_b values resulting in $k_{app} = k_f$, as observed experimentally.

3.3.4. Association of a Second CO to $[Ru(bipy)(X)CO]^{2+}$

Based on the estimated rate constants, radiative emission life-times are on the order of seconds and decrease as the internal energy decreases. Experimentally, collisional stabilization is also an inefficient means of removing energy. It would be expected then that the observed $[Ru(bipy)(X)CO]^{2+}$ are internally quite hot, or chemically activated species. That the rate constant for the second addition of CO to $[Ru(bipy)(X)CO]^{2+}$ is smaller, by two thirds to one half that for association of the first CO may be evidence of this. So, the back dissociation rate constant for the nascent $[Ru(bipy)(X)CO]^{2+}$/CO association complex must be similar to the radiative rate constant (Table 3.3).

Table 3.3. Computed binding energies, calculated radiative rate constants and unimolecular dissociation rate constants of $[Ru(bipy)_2(O_2)]^{2+}$, $[Ru(bipy)_2(CO)]^{2+}$, $[Ru(bipy)(phen)(CO)]^{2+}$, and $[Ru(bipy)(sn)(CO)]^{2+}$.

Rate constant		$Ru(bipy)_2CO^{2+}$	$Ru(bipy)(sn)CO^{2+}$	$Ru(bipy)(phen)CO^{2+}$	$Ru(bipy)_2O_2^{2+}$
k_b / s^{-1}	$A=10^{14}$ s^{-1}	2.3×10^{-12}	1.1×10^{-13}	9.5×10^{-14}	2.3×10^{-5}
	$A=10^{19}$ s^{-1}	1.6×10^{-7}	3.2×10^{-9}	3.9×10^{-9}	0.41
k_{ra} / s^{-1}		8.3	7.6	13	3.5
D_0 / kJ mol^{-1}		168.7	169.8	169.2	97.5

The dissociation energy of the second CO to $[Ru(bipy)_2CO]^{2+}$ is calculated to be higher than the first CO, 184 kJ mol^{-1}. Assuming an internal energy of $[Ru(bipy)_2(CO)_2]^{2+}$ is the sum of the energy of association of both CO additions, 353 kJ mol^{-1}, the radiative emission rate constant is estimated to be 32 s^{-1}. At this internal energy the back dissociation rate constant is 3×10^4 s^{-1} (Fig. 3.6c), much larger than k_{ra}, so that the observed rate constant should be orders of magnitude lower than the collision rate. It is reasonable to assume, that some of this internal energy may be dissipated radiatively, with the higher k_{ra}. At an internal energy of approximately 285 kJ mol^{-1} the back dissociation rate constant is computed to be similar in value to k_{ra}, and will reduce the efficiency of the association reaction to slightly below unity. The energy difference

between 353 kJ mol^{-1} and 285 kJ mol^{-1} corresponds to about three infrared photons at the frequency of the CO stretch (2150 cm^{-1}).

3.4. Conclusions

The mechanism for the association reactions between $[Ru(bipy)(X)]^{2+}$ (X = bipy, sn, phen) and either O_2 or CO were investigated at low pressure in a FTICR cell. This study showed that both CO and O_2 addition occurs close to the collision rate meaning almost every ion–molecule collision leads to the observed association product. Using MP2(full)/6-31+G(d,p) calculations on B3LYP/6-31+(d,p) computed structures (LANL2DZ on Ru), the binding energies were determined to be 169 kJ mol^{-1} for $[Ru(bipy)(X)(CO)]^{2+}$ and 97.5 kJ mol^{-1} for $[Ru(bipy)_2O_2]^{2+}$ which is equal to the internal energy of nascent ion–molecule complex. Assuming loose transition states, unimolecular back dissociation rate constants for $[Ru(bipy)(X)(CO)]^{2+}$ were determined to be 10^{-7} to 10^{-9} s^{-1}. The very small values of k_b for $[Ru(bipy)(X)(CO)]^{2+}$ are attributed to the large size of ion–molecule complexes and the very large binding energies. The small back dissociation rate constants are responsible for the reaction occurring at the collision rate. For the $[Ru(bipy)_2O_2]^{2+}$ complex k_b is 0.4 s^{-1}, similar in magnitude to k_{ra} resulting in less than unit efficiency for $[Ru(bipy)_2^{2+}/O_2]$ collisions. The addition of a CO to $[Ru(bipy)_2CO]^{2+}$ is experimentally determined to be slightly less efficient than addition of the first CO. The rate constants, k_{ra} and k_b, are determined to be similar in magnitude after emission of about three photons from the CO stretching vibration. In the next, we

used these chemically activated ion–molecule complexes to perform chemical reactions (i.e. dehydrogenation) which might not be possible with the ground state species.

References

(1) Operti, L.; Rabezzana, R. *Mass Spectrom. Rev.* **2003**, *22*, 407.

(2) Herbst, E.; Roueff, E.; Talbi, D. *Mol. Phys.* **2010**, *108*, 2171.

(3) Talbi, D.; Bacchus-Montabonel, M.-C. *Chem. Phys. Lett.* **2007**, *443*, 40.

(4) Ayouz, M.; Lopes, R.; Raoult, M.; Dulieu, O.; Kokoouline, V. *Physical Review A* **2011**, *83*, 1.

(5) Franz, J.; Gustafsson, M.; Nyman, G. *Monthly Notices of the Royal Astronomical Society* **2011**, *414*, 3547.

(6) Höckendorf, R. F.; van der Linde, C.; Balaj, O. P.; Herber, I.; Beyer, M. K. *Int. J. Mass spectrom.* **2011**, *300*, 44.

(7) Dunbar, R. C.; Klippenstein, S. J.; Hrušák, J.; Stöckigt, D.; Schwarz, H. *J. Am. Chem. Soc.* **1996**, *118*, 5277.

(8) Fridgen, T. D.; McMahon, T. B. *J. Phys. Chem. A* **2002**, *106*, 1576.

(9) Ho, Y.-P.; Yang, Y.-C.; Klippenstein, S. J.; Dunbar, R. C. *J. Phys. Chem. A* **1997**, *101*, 3338.

(10) Ryzhov, V.; Klippenstein, S. J.; Dunbar, R. C. *J. Am. Chem. Soc.* **1996**, *118*, 5462.

(11) Ryzhov, V.; Yang, C.-N.; Klippenstein, S. J.; Dunbar, R. C. *Int. J. Mass spectrom.* **1999**, *185–187*, 913.

(12) Pickett, C. J.; Vincent, K. A.; Ibrahim, S. K.; Gormal, C. A.; Smith, B. E.; Fairhurst, S. A.; Best, S. P. *Chemistry (Weinheim an der Bergstrasse, Germany)* **2004**, *10*, 4770.

(13) Herman, J.; Foutch, J. D.; Davico, G. E. *J. Phys. Chem. A* **2007**, *111*, 2461.

(14) Molina-Svendsen, H.; Bojesen, G.; McKenzie, C. J. *Inorg. Chem.* **1998**, *37*, 1981.

(15) Nielsen, S. B.; Øiestad, Å. M. L.; Bojesen, G.; Uggerud, E. *Int. J. Mass spectrom.* **2005**, *243*, 231.

(16) Begum, A.; Pickup, P. G. *Electrochem. Commun.* **2007**, *9*, 2525.

(17) Frisch et al, M. J. *Gaussian 09, Revision A.01; Gaussian, Inc.: Wallingford, CT,* **2009**.

(18) Su, T.; Chesnavich, W. J. *J. Chem. Phys.* **1982**, *76*, 5183.

(19) Klippenstein, S. J.; Yang, Y.-C.; Ryzhov, V.; Dunbar, R. C. *J. Chem. Phys.* **1996**, *104*, 4502.

(20) Shi, J.; Bernfeld, D.; Barker, J. R. *J. Chem. Phys.* **1988**, *88*, 6211.

(21) Baer, T.; Mayer, P. M. *J. Am. Soc. Mass. Spectrom.* **1997**, *8*, 103.

(22) Howe, P. R.; McGrady, J. E.; McKenzie, C. J. *Inorg. Chem.* **2002**, *41*, 2026.

Chapter 4. Gas-Phase Dehydrogenation and Demethanation of 2-Methylpropane and Propane by the 16-Electron Complex $[Ru(bipy)_2CO]^{2+*}$ Chemically Activated by the Association of $[Ru(bipy)_2]^{2+}$ and CO

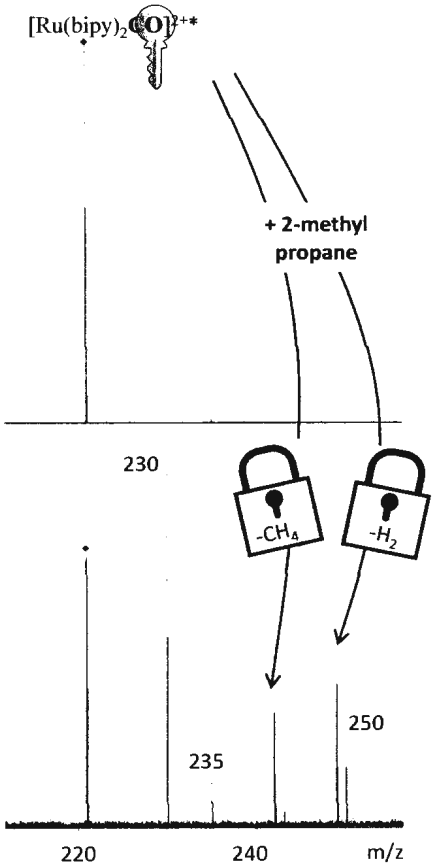

This work has been published in part as A. *Gholami and T.D. Fridgen.*, Dehydrogenation and demethanation of 2-methylpropane and propane in the gas-phase by the 16-electron complex $[Ru(bipy)_2(CO)]^{2+}$* chemically activated by the association of $[Ru(bipy)_2]^{2+}$ and CO_2. Dalton Transactions, 2013, 42(11), 3979-3985. This work has been done and written by me under supervision of Dr. Travis D. Fridgen.

4.1. Introduction

Catalytic reforming of hydrocarbons is an important aspect of research for the petroleum industry. Activations of C-H and C-C bonds are two reactions that occur in the hydrocarbon reforming processes which consequently lead to dehydrogenation and cracking of hydrocarbons. For example, the conversion of normal alkanes into olefins or aromatic hydrocarbons, and cracking paraffin into smaller molecules are the common catalytic reforming processes which produce essential materials for synthesis of plastics, rubbers, fibers, and detergents.[1,2] The C-H bond is one of the least reactive bonds of organic compounds and its cleavage is an endothermic reaction which typically requires very high temperatures.[3] On the other hand, high temperature processes also lead to cracking of C-C bonds and production of undesired products.[4] Transition metals have gained a great deal of attention in the development of catalysts for dehydrogenation of alkanes.[5-11] Hence, our goal is to provide insights which could aid in the design of a catalytic reaction for C-H or C-C cleavage of alkanes.

Due to solvation effects, ion pairing, or aggregation it is often difficult to understand the elementary steps of C-H or C-C activation by transition metal complexes in large scale solution-phase processes. In this respect, gas phase experiments can help us to understand the elementary steps of catalytic activation of alkanes under well-controlled conditions.[12,13] In an ion cyclotron resonance (ICR) mass spectrometer, ions are isolated inside the cell, and are allowed to react with a neutral gas of interest at very low pressures, 10^{-10} – 10^{-7} mbar. Numerous studies have been devoted to determining the products and mechanism of activation of hydrocarbons by bare metals in the gas phase.[13-22] Freiser *et al.* studied gas phase reactions between a wide range of singly and doubly charged transition metals and alkanes using the ICR MS.[13,17,21] In their work, metal ions were formed using highly energetic sources such as laser ablation, thermal vaporization, fast atom bombardment, and secondary ion techniques. These sources produced metal ions that were mostly in electronically excited states when they reacted with alkanes. The major elimination products were H_2, $2H_2$, CH_4, and C_2H_6 in these reactions.[21]

Despite the large amount of work in this area, studies of the reactions between hydrocarbons and ligated transition metal complex ions have been limited. The Uggerud group investigated the mechanism for C-H bond activation of ethylene by $18e^-$ Rh(III) and $16e^-$ Rh(III) complexes inside the ICR cell in which H_2 elimination was observed in the reaction of ethylene and Cp-Rh(C_2H_4-μH)$^+$ complexes.[23] DFT calculations showed that vinylic C-H bond activation is an energetically unfavorable process. Rather, it was shown that vinylic C-H activation is possible if a collision between C_2H_4 and [Cp-Rh(C_2H_4-μH)]$^+$ forms an energy rich-adduct product, Cp-Rh(C_2H_4-μH)(C_2H_4)$^{+*}$, which

undergoes the vinylic C-H cleavage. The same group also studied the gas phase ion-molecule reactions between $[Ru(bipy)_2]^{2+}$ and alkenes (propene and butene).[24] The $[Ru(bipy)_2(C_2H_3)(alkene)]^{2+}$ and $[Ru(bipy)_2(C_3H_5)(alkene)]^{2+}$ products were indicative of C-C bond activation of alkenes catalyzed by the $Ru(bipy)_2^{2+}$ complex.

Recently the kinetics for the association reaction between $[Ru(bipy)_2]^{2+}$ and CO at low pressures in a FTICR cell was studied.[25] The association reaction was found to occur at the collision rate. An RRKM estimation of the rate constant for back dissociation of the nascent ion molecule complex, $[Ru(bipy)_2CO]^{2+}*$, revealed that due to the high binding energy and the size of the complex, it has a very long lifetime to dissociation. Due to the low pressures in the ICR cell the only method to alleviate energy is the rather inefficient radiative mechanism. Therefore, much of the energy of association (some 180 kJ mol^{-1}) could be available to help perform chemical reactions.

In this work, the reactions of $[Ru(bipy)_2]^{2+}$ and $[Ru(bipy)_2CO]^{2+}*$ with 2-methylpropane, propane, and propene are investigated and compared. Computational methods are also used to help deduce the mechanism for the observed dehydrogenation and demethanation reactions.

4.2. Methods

4.2.1. Experimental.

All experiments were performed using a Bruker ApexQe 70 FTICR MS with an Apollo II electrospray source. Tris(2,2'-bipyridine) ruthenium perchlorate salt was

purchased from Sigma-Aldrich. $[Ru(bipy)_2]^{2+}$ ions were electrosprayed from 0.1 mM solutions of ruthenium complexes in pure methanol. The coordinatively unsaturated ruthenium complexes were generated by loss of bipyridine in energetic collisions, 12-40 eV lab frame (E_{cm}:0.8-2.6 eV), with Argon at 10^{-2} mbar in the hexapole collision cell of the mass spectrometer. Prior to being transferred to the ICR cell, ions were stored in the hexapole storage/collision cell for ~2 s where they undergo cooling through numerous collisions with the Ar bath gas. The ions produced in the collision cell were then transferred to the ICR cell where they were trapped radially by a 7 T magnetic field and axially by a ~1 V DC trapping potential. The $[Ru(bipy)_2]^{2+}$ ions were isolated in the ICR cell and allowed to react with ms pulses of 2-methylpropane, propane, or propene. Alternatively, a pulse of CO was allowed in the ICR cell followed by isolation of $[Ru(bipy)_2CO]^{2+}$ after which 2-methylpropane was pulsed into the ICR cell. The pulse sequences for these experiments are shown in Fig. 4.1.

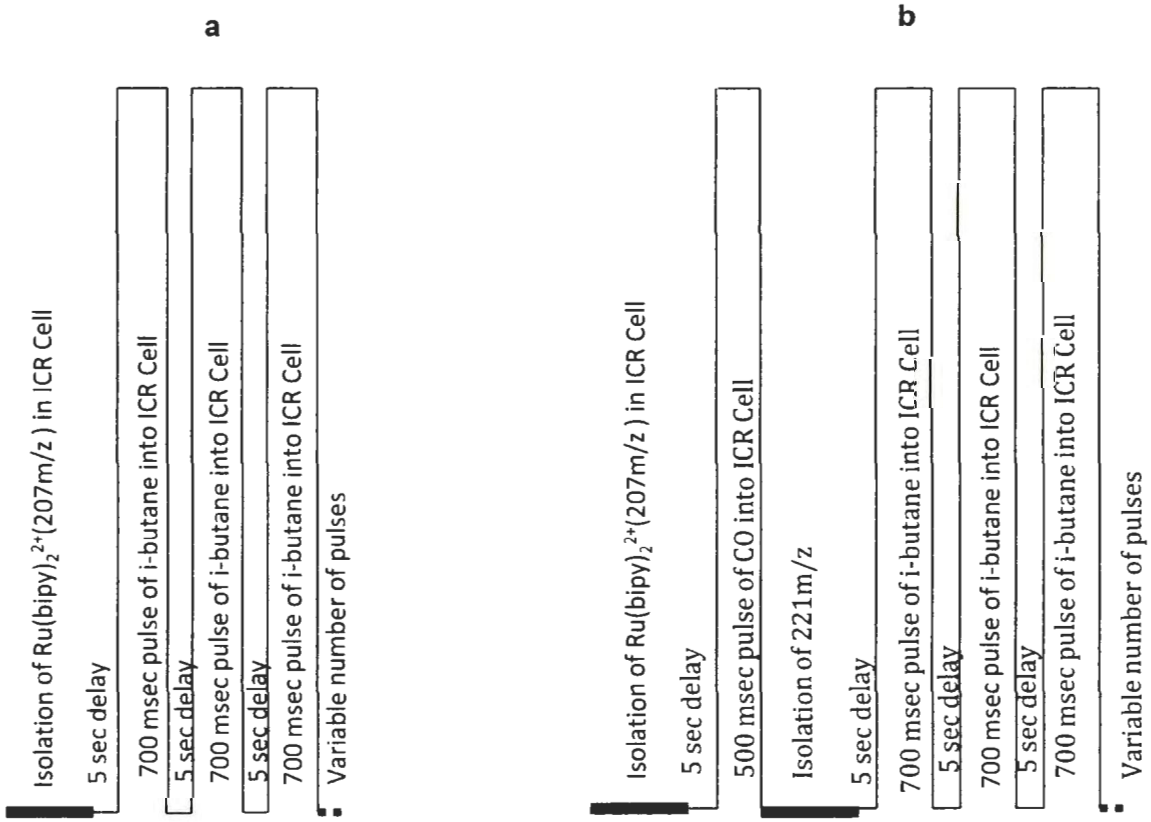

Figure 4.1. Pulse sequences for experiments conducted on the reaction of a) $[Ru(bipy)_2]^{2+}$ and b) $[Ru(bipy)_2CO]^{2+}$.

Infrared multiple photodissociation (IRMPD) was used as an activation technique to help characterize the products of the various ion-molecule reactions. The source of infrared radiation was a standard pulsed CO_2 laser of 25 W at full power.

4.2.2. Computational.

The Gaussian 09[26] suite of programs was used for the computational part of this work. Geometry optimizations as well as vibrational frequency and intensity calculations

were done using the B3LYP hybrid density functional and the 6-311+G(d,p) basis set for all atoms except Ru, for which LANL2DZ basis set and effective core potential was used. Single point calculations were done on these B3LYP optimized geometries at the MP2(full) level of theory and the 6-311+G(d,p) basis set on all atoms except Ru, for which the LANL2DZ basis set and effective core potential was used. MP2(full)/6-311+G(d,p) electronic energies and the thermal contribution to enthalpies from the B3LYP/6-311+(d,p) calculations were then used to compute relative enthalpies and Gibbs energies. This method has been abbreviated MP2(full)/6-311+G(d,p)//B3LYP/6-311+G(d,p) but it should be noted that the LANL2DZ basis set and effective core potential was used on Ru.

4.3. Results and Discussion

4.3.1. 2-Methylpropane

Interestingly, there is a significant difference in the products of the $[Ru(bipy)_2]^{2+}$/2-methylpropane and the $[Ru(bipy)_2CO]^{2+}$/2-methylpropane reactions, where $[Ru(bipy)_2CO]^{2+}$ was produced by association of carbon monoxide to $[Ru(bipy)_2]^{2+}$ in the ICR cell. Spectra for 10 pulses of 2-methylpropane with $[Ru(bipy)_2]^{2+}$ (*m/z* 207) are shown in Figure 4.2. The reaction of 2-methylpropane with $[Ru(bipy)_2]^{2+}$ ions leads only to the adduct ion-molecule product $[Ru(bipy)_2(C_4H_{10})]^{2+}$ (*m/z* 236) according to Scheme 4.1.

$$[Ru(bipy)_2]^{2+} + C_4H_{10} \longrightarrow [Ru(bipy)_2(C_4H_{10})]^{2+}* \xrightarrow{-h\nu \text{ or } [M]} [Ru(bipy)_2(C_4H_{10})]^{2+}$$

Scheme 4.1. The reaction between 2-methylpropane and $[Ru(bipy)_2]^{2+}$ in the ICR cell.

Stabilization of the nascent ion/molecule complex could occur either radiatively and/or by third-body collision. However, even at the pressures of a gas pulse $\sim 10^{-7}$ mbar which last on the order of microseconds, third-body collisions are rare so radiative stabilization is most likely the main mechanism for stabilization of the nascent intermediate.

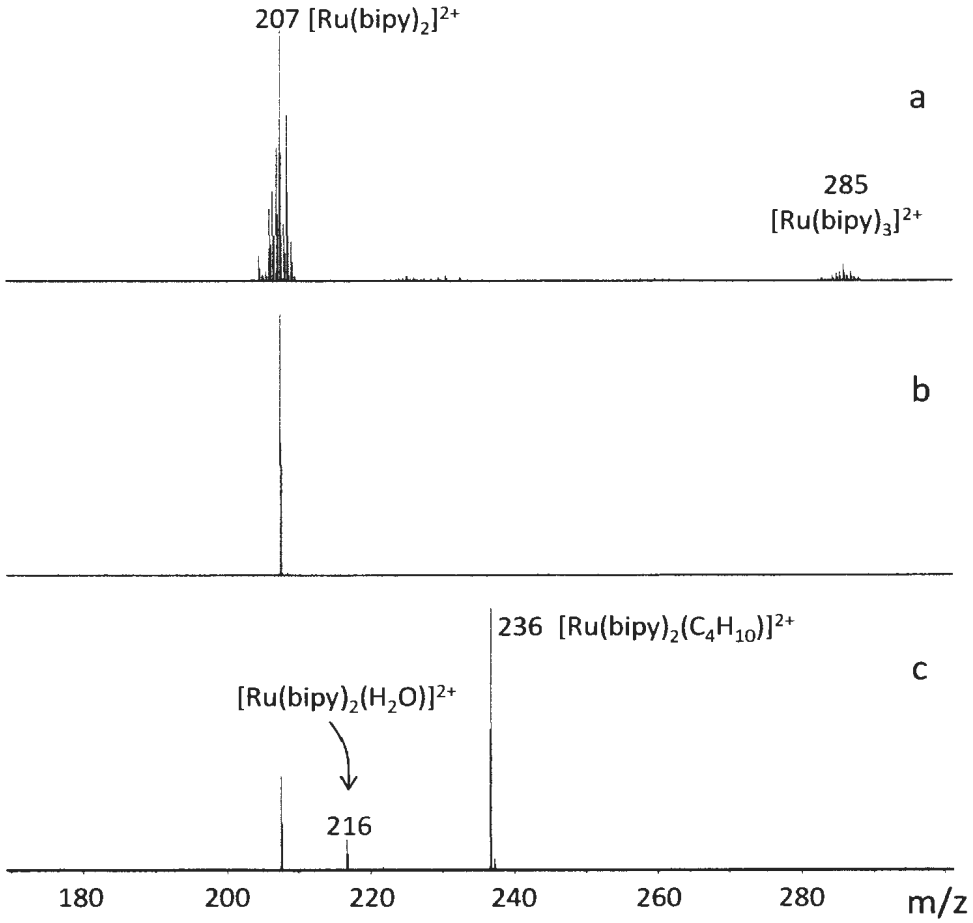

Figure 4.2. Mass spectra following a) CID of $[Ru(bipy)_3]^{2+}$ b) isolation of $[^{102}Ru(bipy)_2]^{2+}$, c) reaction between $[Ru(bipy)_2]^{2+}$ and 2-methylpropane

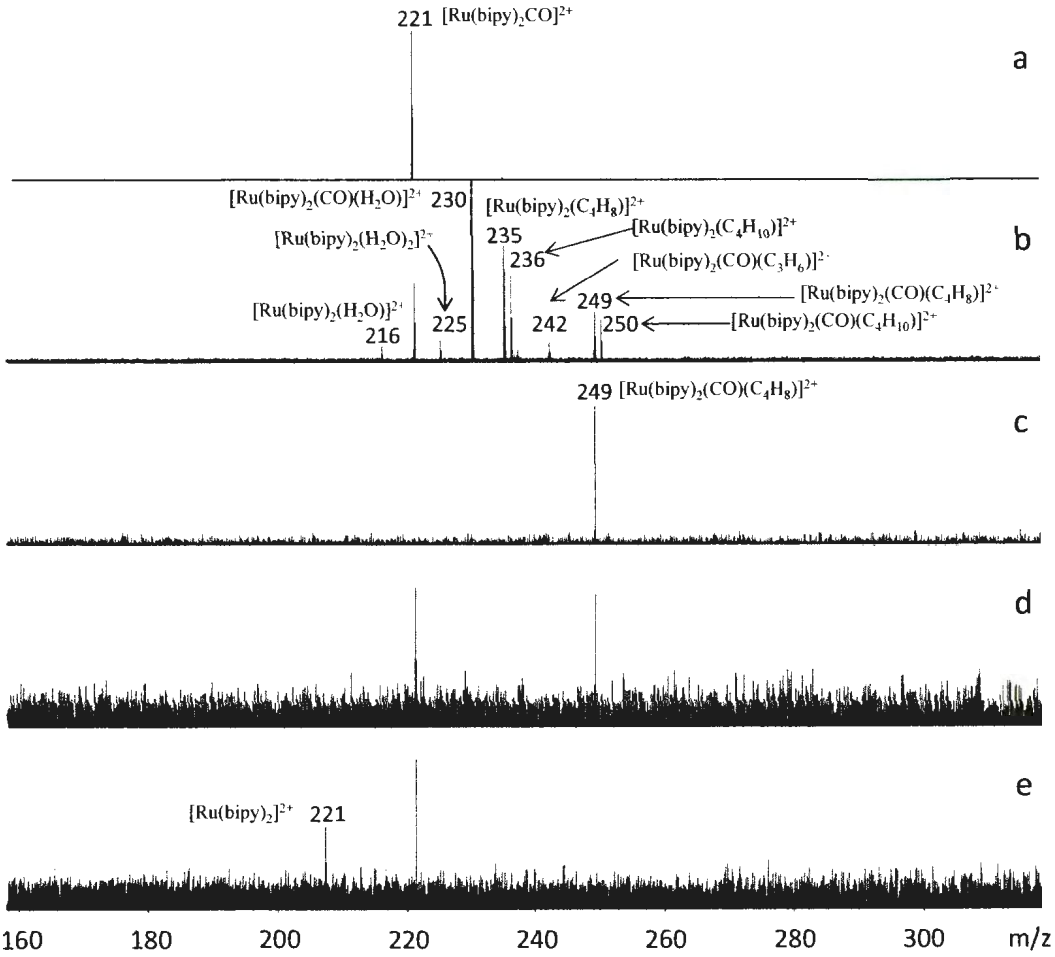

Figure 4.3. Mass spectra following a) isolation of $[^{102}Ru(bipy)_2CO]^{2+}$, b) reaction of $[Ru(bipy)_2CO]^{2+}$ with 2-methylpropane (10 pulses) c) isolation of dehydrogenation product, *m/z* 249, d) CO_2 laser IRMPD of *m/z* 249 m/z for 2 sec at 20 % laser power and e) at 50 % laser power.

When a pulse of carbon monoxide gas is introduced to the ICR cell, the product $[Ru(bipy)_2CO]^{2+}$ at *m/z* 221 was produced. The mass spectrum following isolation of m/z 221 can be seen in Fig. 4.3a. Following its isolation, $[Ru(bipy)_2CO]^{2+}$ was allowed to react with 2-methylpropane, and the result after 10 pulses can be seen in Fig. 4.3b.

Among the products are the association complex, $[Ru(bipy)_2(CO)(C_4H_{10})]^{2+}$ at *m/z* 250, is observed as is the substitution complex, $[Ru(bipy)_2(C_4H_{10})]^{2+}$ at *m/z* 236. These products are formed according to the mechanism suggested in Scheme 4.2.

$$[Ru(bipy)_2CO]^{2+}* \xrightarrow{C_4H_{10}} [Ru(bipy)_2CO(C_4H_{10})]^{2+}* \xrightarrow{-h\nu \text{ or } [M]} [Ru(bipy)_2CO(C_4H_{10})]^{2+}$$
$$m/z\ 250$$
$$\longrightarrow [Ru(bipy)_2(C_4H_{10})]^{2+} + CO$$
$$m/z\ 236$$

Scheme 4.2. The mechanism suggested for the reaction between i-butane and $[Ru(bipy)_2CO]^{2+*}$ inside the ICR cell.

Since CO is far more strongly bound than 2-methylpropane (*vide infra*), the substitution product is further support that $[Ru(bipy)_2CO]^{2+}$ (*m/z* 221) is still internally excited, as suggested previously,[25] due to the inefficient mechanisms to alleviate the energy of CO association. If *m/z* 221 was internally cool, loss of CO would not be observed. It was previously shown that *m/z* 221 is not translationally excited due to the ~1 V axial trapping potential; the translational energy was shown to be released prior to association of CO.[25]

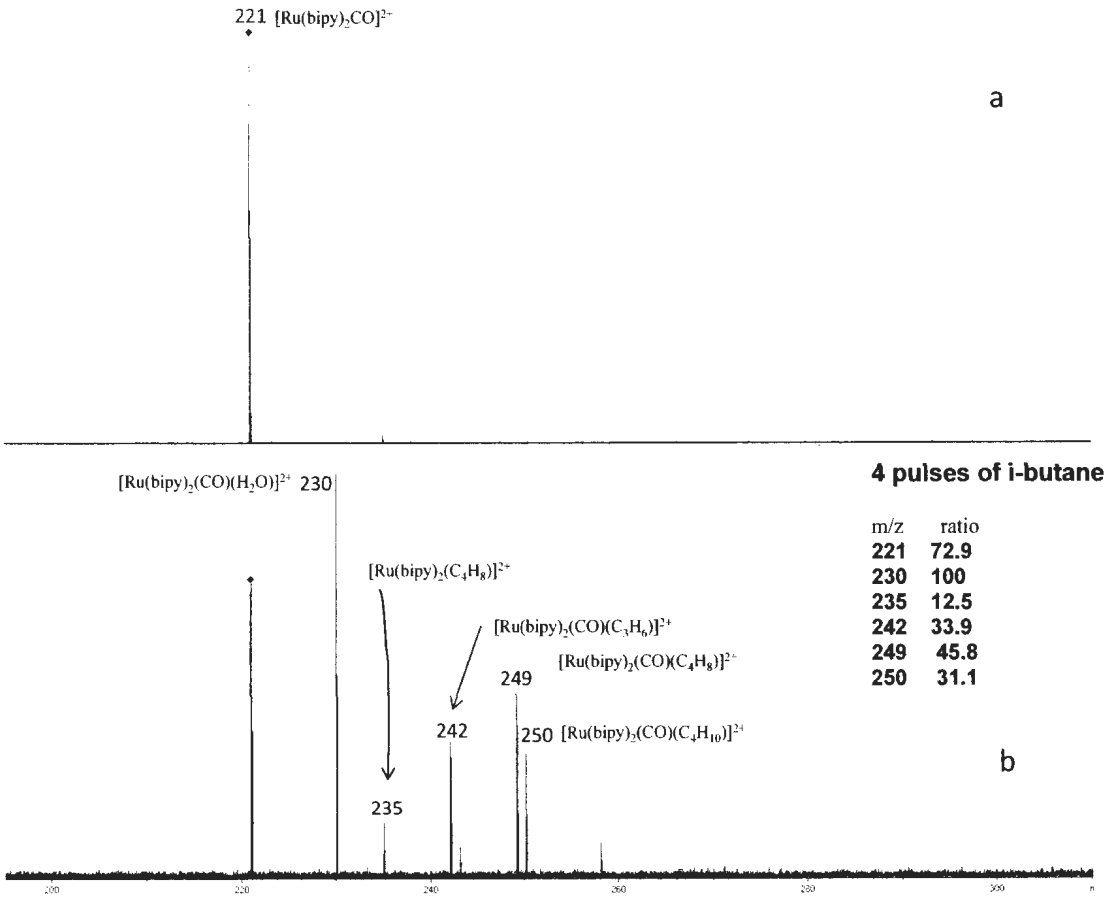

Figure 4.4. Mass spectra following the isolation of a) $[^{102}Ru(bipy)_2CO]^{2+}$ and b) its reaction with 2-methylpropane on a day where water impurities were low.

Products of the elimination of H_2 forming $[Ru(bipy)_2(CO)(C_4H_8)]^{2+}$ at *m/z* 249 and $[Ru(bipy)_2(C_4H_8)]^{2+}$ at *m/z* 235 were also observed as well as the product of CH_4 elimination, $[Ru(bipy)_2(CO)(C_3H_6)]^{2+}$, at *m/z* 242. CO_2 laser-IRMPD fragmentation of m/z 249 resulted in the loss of C_4H_8 (20 % laser power) and loss of the original CO (50 % laser power) as seen in Figs. 4.3d and e. The recovery of reactants from laser irradiation of *m/z* 249 as well as the appearance of *m/z* 235 loss of CO following dehydrogenation suggests that *m/z* 249 and *m/z* 242 are not a result of direct reaction between Ru-bound

CO and 2-methylpropane. These results indicate that $[Ru(bipy)_2(CO)(C_4H_8)]^{2+}$ and $[Ru(bipy)_2(CO)(C_3H_6)]^{2+}$ are the products of dehydrogenation and demethanation, respectively, in the $[Ru(bipy)_2(CO)]^{2+}$/2-methylpropane reaction. The absence of H_2 or CH_4 eliminations in the $[Ru(bipy)_2]^{2+}$/2-methylpropane reaction means that ligation of the ruthenium complex with CO is necessary for activation of the hydrocarbon to the two elimination reactions of 2-methylpropane. The mechanisms for H_2 and CH_4 eliminations, summarized in scheme 4.3, will be discussed in more detail below.

$$[Ru(bipy)_2CO]^{2+}* \xrightarrow{C_4H_{10}} \underset{m/z\ 250}{[Ru(bipy)_2CO(C_4H_{10})]^{2+}*} \longrightarrow \underset{m/z\ 249}{[Ru(bipy)_2CO(C_4H_8)]^{2+}} + H_2$$

$$\longrightarrow \underset{m/z\ 242}{[Ru(bipy)_2CO(C_3H_6)]^{2+}} + CH_4$$

Scheme 4.3. Dehydrogenation and demethanation of i-butane by $[Ru(bipy)_2CO]^{2+*}$.

Also observed were products such as those at *m/z* 216, 230, and 236 corresponding to $[Ru(bipy)_2(H_2O)]^{2+}$, $[Ru(bipy)_2(CO)(H_2O)]^{2+}$, and $[Ru(bipy)_2(H_2O)_2]^{2+}$, respectively, which are due to presence of water inside the ICR cell. An example of a reaction between $[Ru(bipy)_2(CO)]^{2+}$ and 2-methylpropane (4 pulses) on a day when H_2O impurities were significantly less can be seen in Figure 4.4.

The question then becomes, why does ligation of CO result in significant changes in reaction pathways? To explain this, the potential energy surfaces for possible mechanisms of dehydrogenation of 2-methylpropane by $[Ru(bipy)_2]^{2+}$ and $[Ru(bipy)_2(CO)]^{2+}$ have been explored. In the pathway of alkane dehydrogenation via bare or M^{+n} metal centers, it is believed that the metal inserts into the C-H bond to form a

H-M-alkyl.[5,16,17] This oxidative addition is followed by a reductive elimination of H_2 leaving the M-alkene complex. This mechanism of H_2 loss via bare metal is summarized in Scheme 4.4.[5,16,17]

$$M(C_4H_{10}) \xrightarrow{\text{oxidative addition}} H-M-C_4H_9 \xrightarrow[-H_2]{\text{reductive elimination}} M(CH_2=C(CH_3)_2)$$

Scheme 4.4. Dehydrogenation of i-butane by bare metal via oxidative addition/reductive elimination.

In the case of the $16e^-$ $[Ru(bipy)_2CO]^{2+}$, ruthenium has only one vacant coordination position so it is impossible for oxidative addition to occur unless another site is made vacant by losing one Ru-N bond. In Figure 4.5, a potential energy diagram determined for the mechanism is proposed where one of the η^2-bipy ligands becomes η^1 prior to the oxidative addition step. All stationary states of this potential energy diagram were computed except the oxidative addition transition state and product, as well as the reductive elimination transition state. The two transition state energies were estimated from the oxidative addition and reductive elimination transition states for Co^{2+}/isobutane reactions.[27] The oxidative addition product relative energy was taken to be the same as that for the non-CO bound potential energy surface (Figure 4.6). The large positive barrier (36 kJ mol^{-1}) estimated for this mechanism makes it unlikely to be responsible for the dehydrogenation that is observed in the reaction between $[Ru(bipy)_2CO]^{2+}$ and 2-methylpropane. Without CO association, the energy barrier is in excess of 90 kJ mol^{-1} (Fig. 4.6).

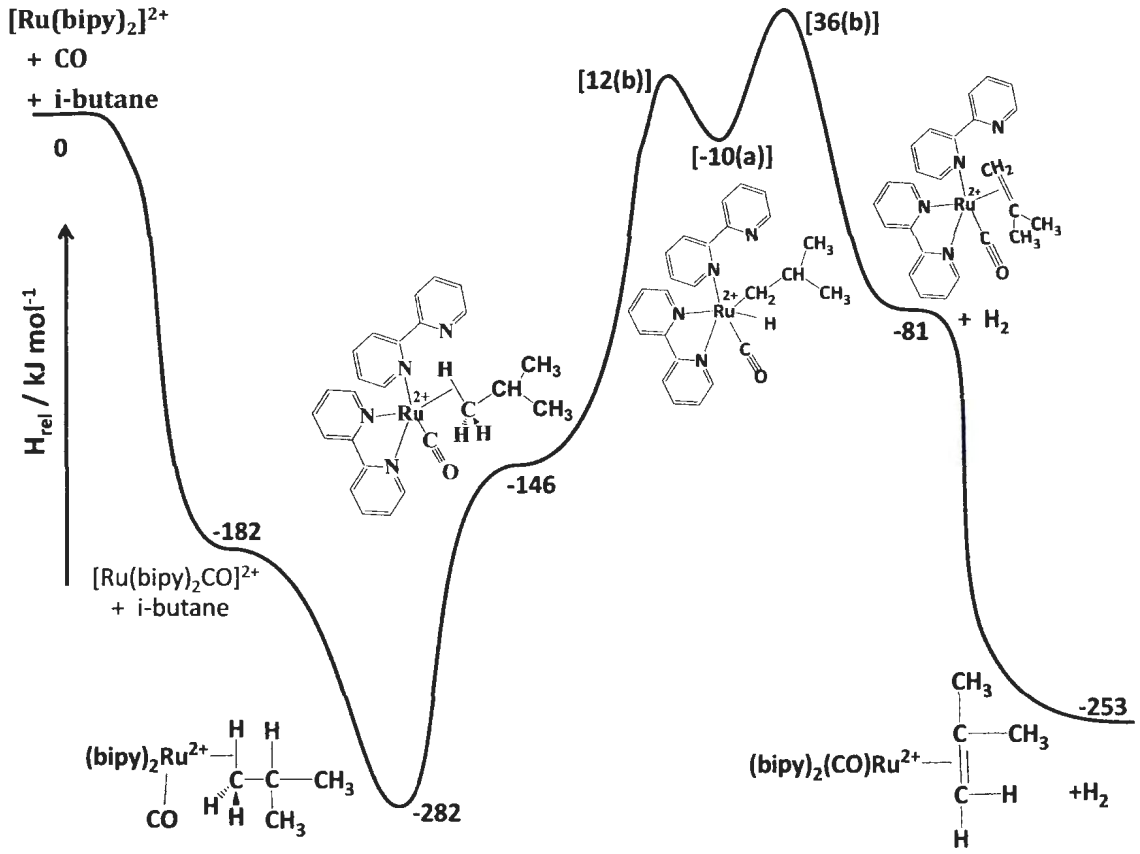

Figure 4.5. Computed potential energy diagram for the dehydrogenation of 2-methylpropane by $[Ru(bipy)_2CO]^{2+}$ via an oxidative addition/reductive elimination mechanism following the partial dissociation of an Ru-N bond. The energy of the oxidative addition product (a) is estimated from the non-CO-associated complex (a) (Figure 4.6) and the two main transition state energies (b) are estimated from the oxidative addition and reductive elimination transition states for Co^{2+}/isobutane reaction.[27]

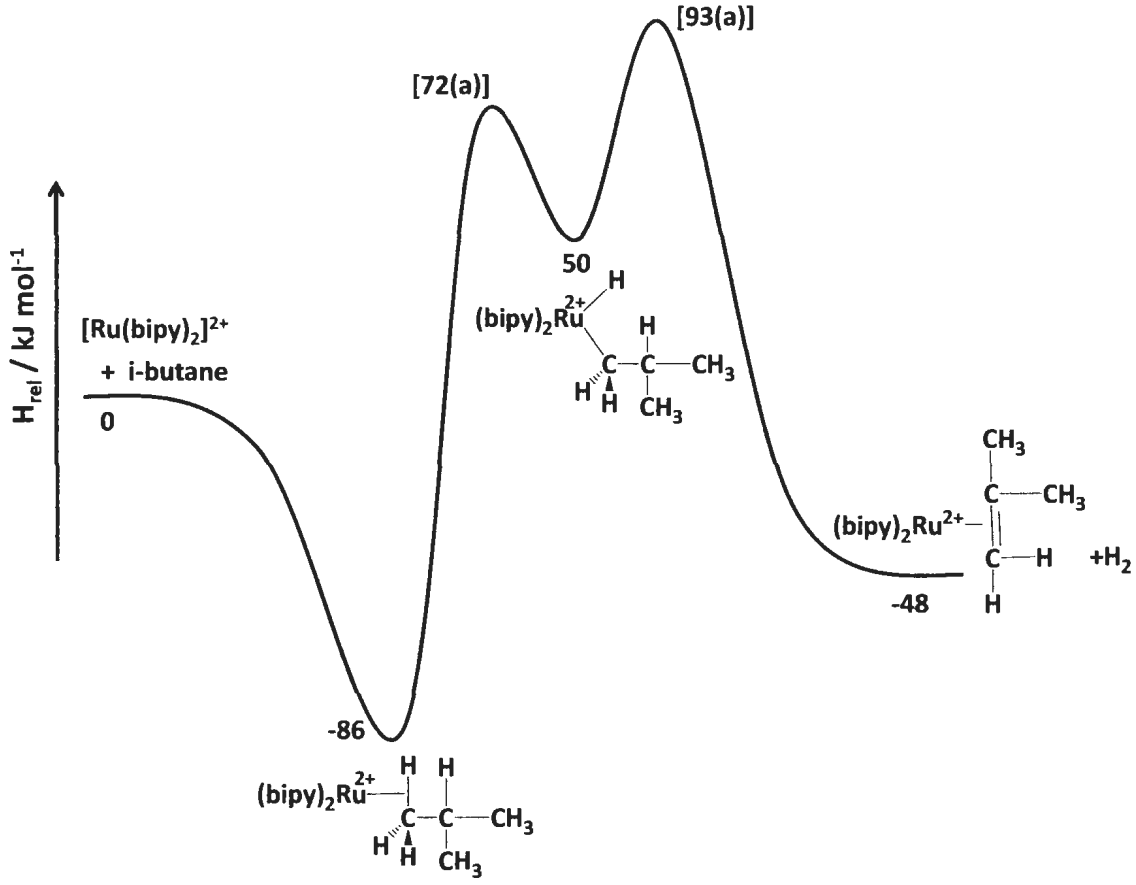

Figure 4.6. Calculated potential energy diagram for the dehydrogenation reaction of 2-methyl propane with $[Ru(bipy)_2]^{2+}$ via an oxidative addition/reductive elimination mechanism. The two main transition state energies were estimated from the $Co^{2+/}$isobutane reaction.[27]

A mechanism that does not include oxidative addition is shown in Scheme 4.5. In this mechanism, activation of the C-H bond is through a σ-bound complex in which ruthenium is coordinated with both carbon and hydrogen of C-H.[28,29] This σ-bound complex then undergoes a concerted H_2 elimination where the second H comes from the β C-H bond.

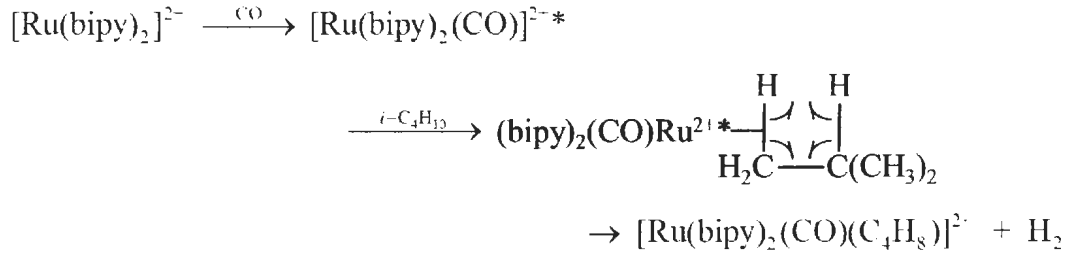

Scheme 4.5. Dehydrogenation of i-butane by $[Ru(bipy)_2CO]^{2+}$* via a concerted mechanism.

The B3LYP/6-311+G(d,p) optimized structure of the complex featuring an agostically-complexed 2-methyl propane with $[Ru(bipy)_2CO]^{2+}$ is shown in Figure 4.7a). The Ru-H bond length and Ru-H-C angle were found to be 2.00Å and 135.5°, respectively, which are consistent with an agostic interaction.[30,31] The distance between hydrogen and carbon in Ru-H-C was found to be 1.13 Å which is slightly longer than the usual C-H bond length. The strength of this agostic interaction is computed to be 100 kJ mol^{-1} (see Fig. 4.8) which is 14 kJ mol^{-1} stronger than when there is no CO ligand (Fig. 4.9).

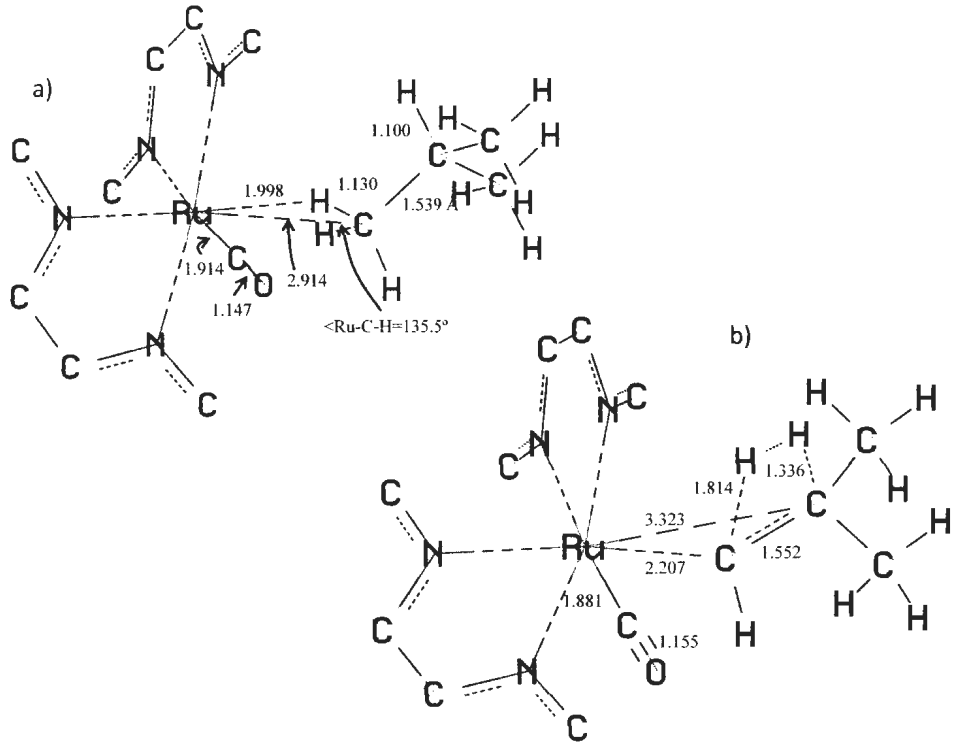

Figure 4.7. Computed structures for a) the σ-bound complex $[Ru(bipy)_2CO(C_4H_{10})]^{2+}$ complex and b) the transition state for concerted elimination of H_2.

In Figure 4.8, the calculated potential energy surface for the mechanism of Scheme 4.5 is shown (solid line). The energy barrier for H_2 loss for this mechanism is estimated to be about 68 kJ mol^{-1} less than for the oxidative addition/reductive elimination mechanism of Figure 4.5. More importantly, the transition state energy is below that of the unassociated reactants. Inherent in this mechanism is that no significant loss of the energy of association of both CO and 2-methylpropane can occur prior to H_2 loss.

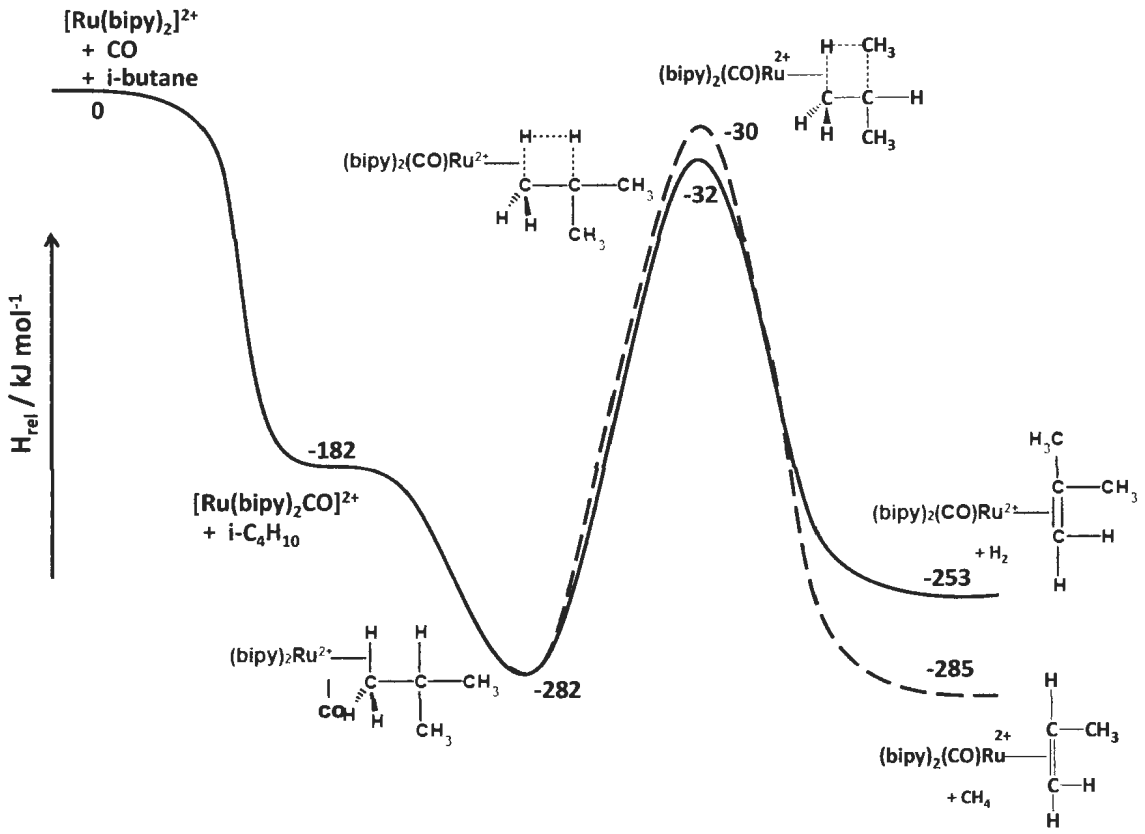

Figure 4.8. Computed potential energy diagram for the concerted dehydrogenation (solid line) and demethanation (dashed line) reactions of 2-methylpropane by $[Ru(bipy)_2CO]^{2+}$*.

Primarily, it is the strong binding energy of CO that drives the reaction, dumping 180 kJ mol^{-1} of internal energy into the complex. This is the reason that dehydrogenation is not observed for the bare $[Ru(bipy)_2]^{2+}$ complex (see Figures 4.2 and 4.9). Indeed association of ethylene, N_2, or O_2 (bound by only 72, 98, and 107 kJ mol^{-1}, respectively) prior to reaction with 2-methylpropane resulted only in the substitution and addition of 2-methyl propane. Association of these to $[Ru(bipy)_2]^{2+}$, and assuming the same

mechanism as in Scheme 4.5, the energy barrier to H_2 loss would be positive by over 40 kJ mol^{-1}. It is also interesting to note that the energy barrier for H_2 loss is calculated to be 250 kJ mol^{-1} (Figure 4.8) for the CO-associated concerted transition state but almost 40 kJ mol^{-1} more (289 kJ mol^{-1}, Figure 4.9) without CO.

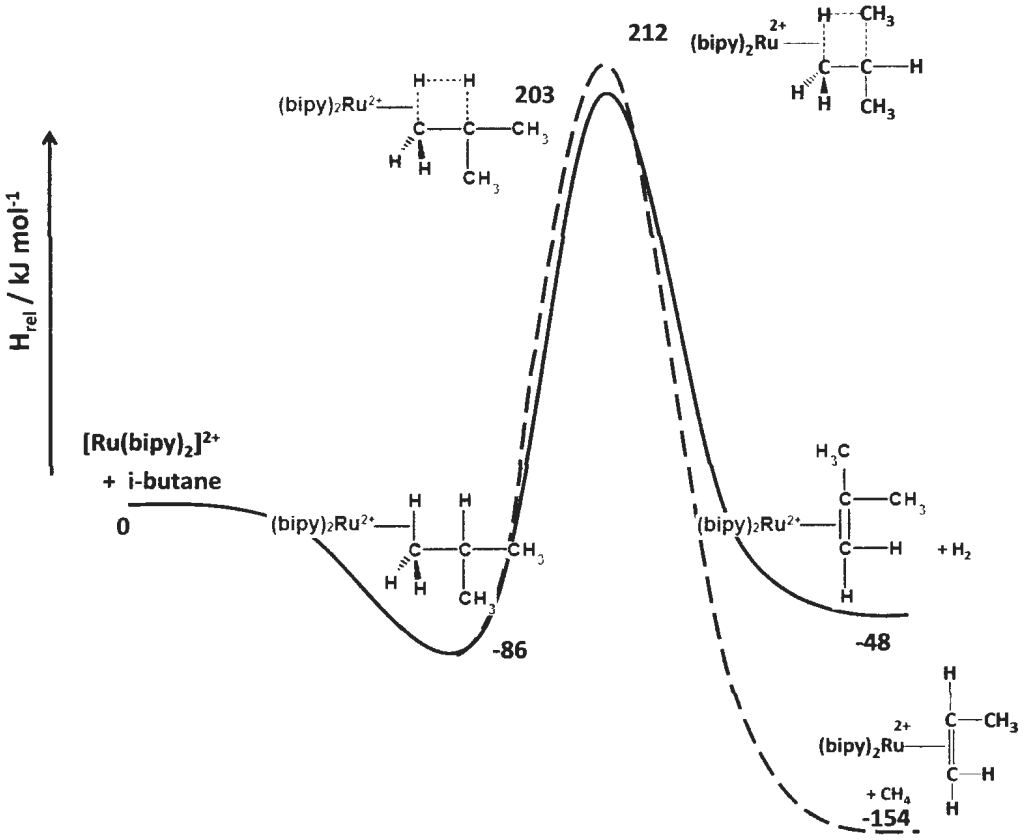

Figure 4.9. Computed potential energy diagram for the dehydrogenation (solid line) and demethanation (dashed line) reactions of 2-methylpropane by $[Ru(bipy)_2]^{2+}$ via a concerted mechanism.

Without this real lowering of the energy barrier—catalysis—the transition state energy would be above the energy of the reactants and dehydrogenation would not likely be observed. Furthermore, the barrier to concerted dehydrogenation of 2-methylpropane

was calculated to be 483 kJ mol^{-1} (Figure 4.10), showing the very strong effect of the σ-bound complexation of metal with C-H bond in activating the dehydrogenation process.

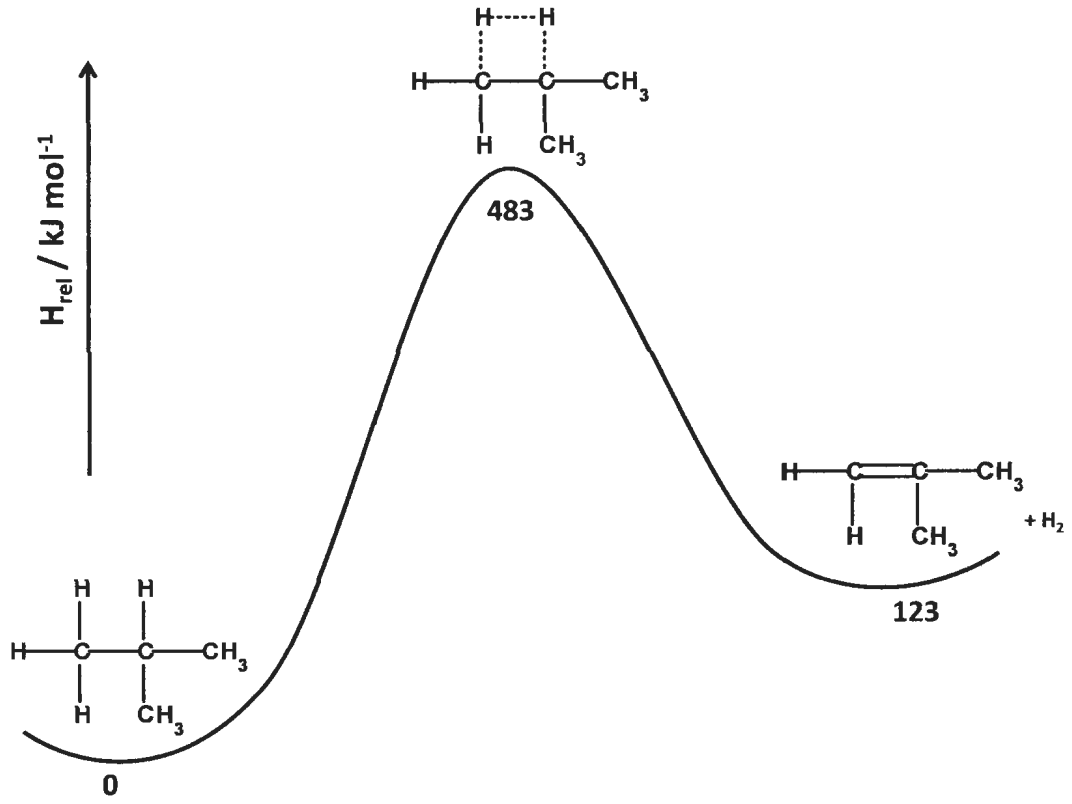

Figure 4.10. Computed potential energy diagram for the concerted dehydrogenation of 2-methylpropane.

A similar explanation for the observation of methane loss is proposed given the very similar potential energy surface calculated for the concerted loss of methane, shown in the dashed lines in Figures 4.8 and 4.9. The calculations show that the energy barrier for methane loss is slightly higher than that for dehydrogenation, in agreement with the observed, relatively smaller amount of methane loss product observed.

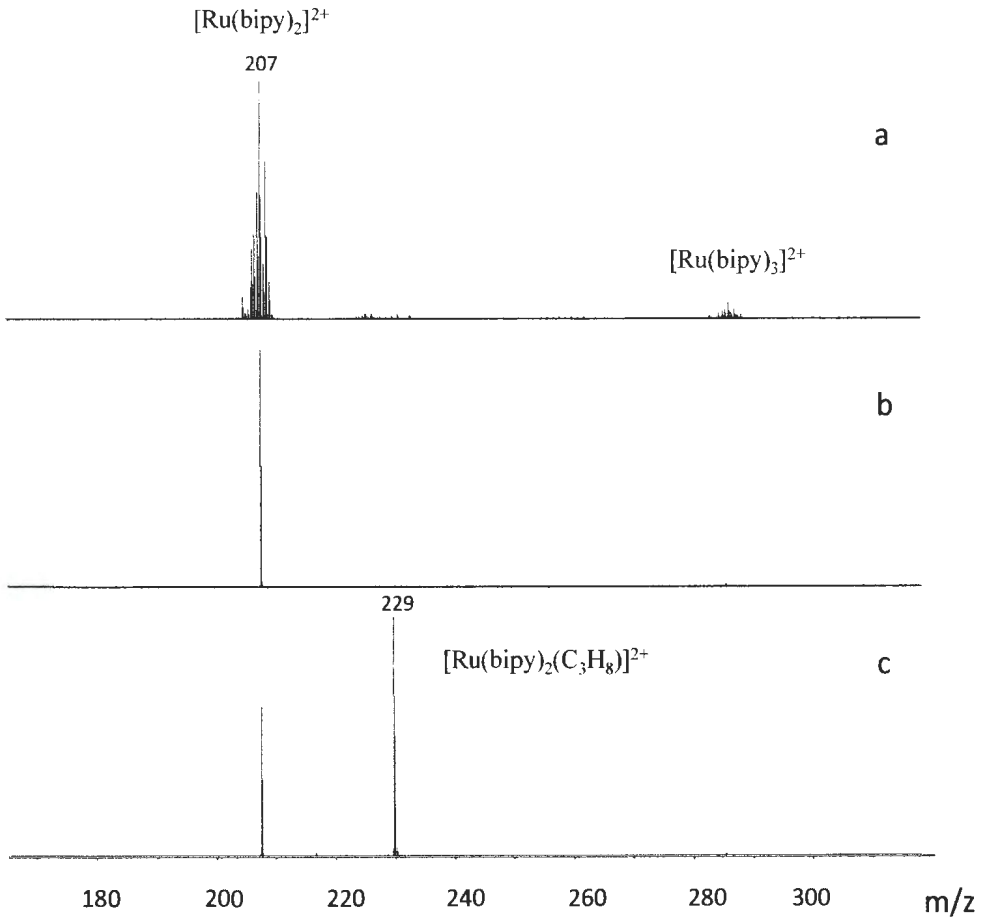

Figure 4.11. Mass spectra following a) CID of $[Ru(bipy)_3]^{2+}$ b) isolation of $[^{102}Ru(bipy)_2]^{2+}$, and c) reaction between $[^{102}Ru(bipy)_2]^{2+}$ and propane.

4.3.2. Propane and Propene.

Similar to 2-methylpropane, the reaction of $[Ru(bipy)_2]^{2+}$ (*m/z* 207) with propane led only to the association of one molecule of propane to form $[Ru(bipy)_2(propane)]^{2+}$ (*m/z* 229, Figure 4.11). The reaction of $[Ru(bipy)_2(CO)]^{2+}$ with propane was found to result in dehydrogenation, $[Ru(bipy)_2(CO)(C_3H_6)]^{2+}$; demethanation, $[Ru(bipy)_2(CO)(C_2H_4)]^{2+}$; as well as association and substitution (Figure 4.12). In

addition, a small amount of product resulting from both demethylation and dehydrogenation, $[Ru(bipy)_2(CO)(C_2H_2)]^{2+}$ was observed at m/z 234. This product could be the result of sequential loss of H_2 and CH_4, or vice-versa, since product formation can leave the resultant ions, $[Ru(bipy)_2(CO)(C_3H_6)]^{2+}$ or $[Ru(bipy)_2(CO)(C_2H_4)]^{2+}$ with an excess of internal energy. It is not understood why these sequential reactions were not observed in the 2-methylpropane reactions.

In contrast to propane and 2-methylpropane, dehydrogenation and demethylation were not observed in the reaction of propene with $[Ru(bipy)_2(CO)]^{2+}$ (Figure 4.13). Rather, in this reaction, only addition and substitution of CO was observed.

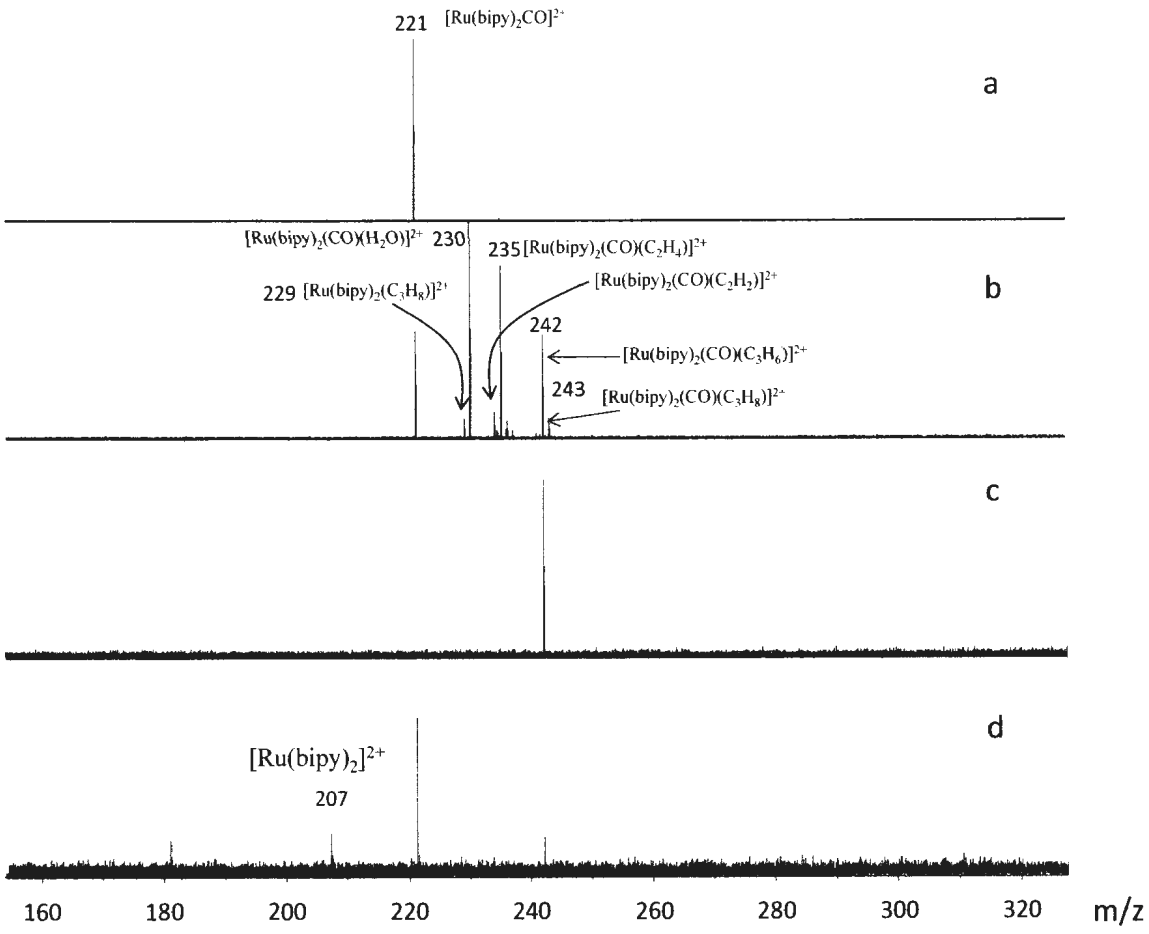

Figure 4.12. Mass spectra following a) reaction of $[^{102}Ru(bipy)_2]^{2+}$ with CO then isolation of $[^{102}Ru(bipy)_2CO]^{2+}$, b) the reaction of $[^{102}Ru(bipy)_2CO]^{2+}$ with propane (10 pulses of propane) c) isolation of dehydrogenation product, m/z 242, and d) CO_2 laser-IRMPD of m/z 242 for 10 sec at 20 % power.

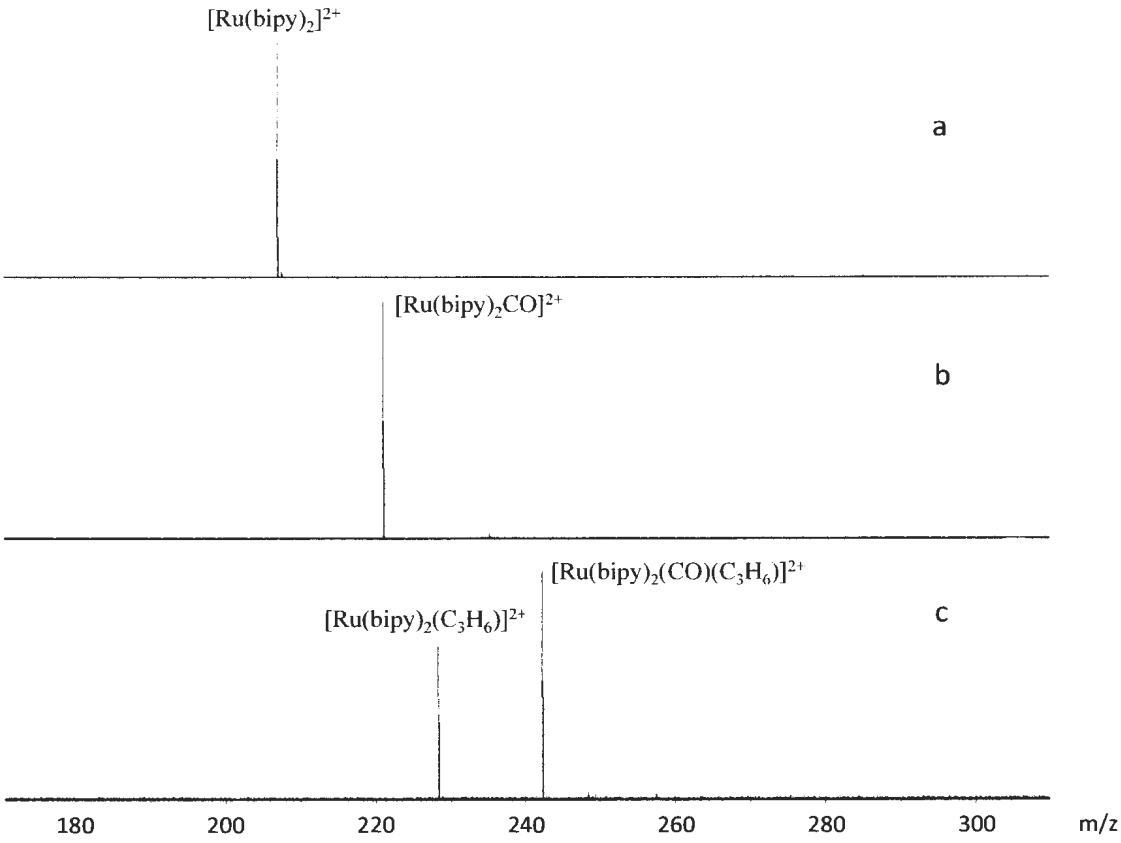

Figure 4.13. Mass spectra following a) the isolation of $[^{102}Ru(bipy)_2]^{2+}$, b) its reaction with a pulse of CO and isolation, and c) the reaction of $[^{102}Ru(bipy)_2(CO)]^{2+}$ with propene.

4.4. Conclusion

The reactions of $[Ru(bipy)_2]^{2+}$ and $[Ru(bipy)_2CO]^{2+}$ with 2-methylpropane, propane, and propene have been investigated. $[Ru(bipy)_2]^{2+}$ reactions resulted solely in addition of the hydrocarbon. Interestingly, for the reactions of 2-methylpropane and propane with $[Ru(bipy)_2CO]^{2+}$, dehydrogenation as well as demethanation were

observed. These reactions were further investigated by computational means and it was concluded that both dehydrogenation and demethanation occur by a concerted mechanism, resulting in an energy barrier that is lower than the unassociated reactants $[Ru(bipy)_2]^{2+}$, CO, and 2-methylpropane (or propane). Furthermore, that the elimination reactions do not occur without CO shows that the intermediate $[Ru(bipy)_2CO]^{2+}*$ must be chemically activated, maintaining much of the ~180 kJ mol^{-1} of internal energy acquired upon association of CO with $[Ru(bipy)_2]^{2+}$.

In contrast with the reactions of propane and 2-methylpropane, propene simply associates with or replaces CO in its reaction with $[Ru(bipy)_2CO]^{2+}$. The energy barrier for concerted dehydrogenation or demethanation is undoubtedly too high as a result of the sp^2 hybridization and of the preferred binding of propene through its B electrons rather than C-H σ-bound complexation.

References

(1) Gary, J. H.; Handwerk, G. E. *Petroleum Refining Technology and Economics* 2nd ed., 1984.

(2) Matar, S.; Hatch, L. F.; Gulf Professional Pub-Boston 2001.

(3) Crabtree, R. H.; Holt, E. M.; Lavin, M.; Morehouse, S. M. *Inorg. Chem.* **1985**, *24*, 1986.

(4) Shee, D.; Sayari, A. *Appl. Catal., A* **2010**, *389*, 155.

(5) Gascón, J.; Téllez, C.; Herguido, J.; Menéndez, M. *Appl. Catal., A* **2003**, *248*, 105.

(6) Haenel, M. W.; Oevers, S.; Angermund, K.; Kaska, W. C.; Fan, H.-J.; Hall, M. B. *Angew. Chem. Int. Ed.* **2001**, *40*, 3596.

(7) Labinger, J. A.; Bercaw, J. E. *Nature* **2002**, *417*, 507.

(8) Li, W.; Geng, Z.; Wang, Y.; Yan, P.; Zhang, X.; Wang, Z.; Liu, F. *J. Phys. Chem. A* **2009**, *113*, 1807.

(9) Lillehaug, S.; Jensen, V. R.; Børve, K. J. *J. Phys. Org. Chem.* **2006**, *19*, 25.

(10) Palacio, L. A.; Echavarría, A.; Sierra, L.; Lombardo, E. A. *Catal. Today* **2005**, *107–108*, 338.

(11) Zaera, F. *Catal. Lett.* **2003**, *91*, 1.

(12) Eller, K.; Zummack, W.; Schwarz, H. *J. Am. Chem. Soc.* **1990**, *112*, 621.

(13) Jacobson, D. B.; Freiser, B. S. *J. Am. Chem. Soc.* **1983**, *105*, 5197.

(14) Armentrout, P. B. *Int. J. Mass spectrom.* **2003**, *227*, 289.

(15) Armentrout, P. B.; Chen, Y.-M. *J. Am. Soc. Mass. Spectrom.* **1999**, *10*, 821.

(16) Byrd, G. D.; Burnier, R. C.; Freiser, B. S. *J. Am. Chem. Soc.* **1982**, *104*, 3565.

(17) Byrd, G. D.; Freiser, B. S. *J. Am. Chem. Soc.* **1982**, *104*, 5944.

(18) Eller, K.; Schwarz, H. *Chem. Rev.* **1991**, *91*, 1121.

(19) Freiser, B. S. *Acc. Chem. Res.* **1994**, *27*, 353.

(20) Holthausen, M. C.; Fiedler, A.; Schwarz, H.; Koch, W. *J. Phys. Chem.* **1996**, *100*, 6236.

(21) Huang, Y.; Wise, M. B.; Jacobson, D. B.; Freiser, B. S. *Organometallics* **1987**, *6*, 346.

(22) Tolbert, M. A.; Mandich, M. L.; Halle, L. F.; Beauchamp, J. L. *J. Am. Chem. Soc.* **1986**, *108*, 5675.

(23) Fooladi, E.; Krapp, A.; Sekiguchi, O.; Tilset, M.; Uggerud, E. *Dalton Trans.* **2010**, *39*, 6317.

(24) Nielsen, S. B.; Øiestad, Å. M. L.; Bojesen, G.; Uggerud, E. *Int. J. Mass spectrom.* **2005**, *243*, 231.

(25) Gholami, A.; Fridgen, T. D. *Int. J. Mass spectrom.* **2012**, *316–318*, 192.

(26) Frisch et al, M. J. *Gaussian 09, Revision A.01; Gaussian, Inc.: Wallingford, CT,* **2009**.

(27) Reichert, E. L.; Thurau, G.; Weisshaar, J. C. *J. Chem. Phys.* **2002**, *117*, 653.

(28) Schneider, J. J. *Angew. Chem. Int. Ed.* **1996**, *35*, 1068.

(29) Armélin, M.; Schlangen, M.; Schwarz, H. *Chem. Eur. J.* **2008**, *14*, 5229.

(30) Brookhart, M.; Green, M. L. H. *J. Organomet. Chem.* **1983**, *250*, 395.

(31) Brookhart, M.; Green, M. L. H.; Parkin, G. *PNAS* **2007**, *104*, 6908.

Chapter 5. Structures and Unimolecular Reactivity of Gas Phase[Zn(Proline-H)]$^+$ and [Zn(Proline-H)(H_2O)]$^+$

This work has been published in part as A. *Gholami and T.D. Fridgen.*, Structures and Unimolecular Reactivity of Gas Phase [Zn(Proline-H)]$^+$ and [Zn(Proline-H)(H_2O)]$^+$,. Journal of Physical Chemistry B, 2013, DOI: 10.1021/jp404697g. This work has been done and written by me under supervisioin of Dr. Travis D. Fridgen.

5.1. Introduction

Studying complexes of metal ions and amino acids is very important since these studies can provide information on the nature of binding of metal ions to larger biological systems. Zn^{2+} is known to affect protein activities by inducing conformational changes through coordinate bonding.[1-6] For example, the tumor suppressor p53 is a proline enriched protein which shows anticancer activity when bound to DNA. It is understood that tumor suppressor p53 binds to DNA via a wild-type folded conformation stabilized by chelating with zinc.[1,7,8] Furthermore, binding of zinc to peptides or proteins could be one of the factors contributing to the development of Alzheimer's disease.[9] Zinc was reported to induce abnormal aggregation of proteins in vitro through its interactions with several proteins resulting in Alzheimer or Parkinson's diseases.[9] Obtaining knowledge about binding sites of Zn^{2+} and amino acids, protein building blocks, could provide useful insight into the mechanism of biological processes, and lead to new methods for treatment of these diseases.

Recently, a large amount of research has been focused on the characterization of structure and binding sites of gas phase metal-amino acid or peptide complexes.[10-24] Atkins *et al.* determined the structure of the deprotonated Pb^{2+}/glycine complex using IRMPD spectroscopy and density functional calculation.[25] The presence of a carboxylic acid O-H stretching band around 3540 cm^{-1} revealed that the complex is deprotonated at the amine group, leaving the carboxylic acid group intact, and that Pb^{2+} was coordinated to the deprotonated-amine nitrogen and carbonyl oxygen.[25] The structures of [Pb(Pro-

H)]$^+$ and [Pb(Pro-H)(H_2O)] (proline = Pro) were also characterized by comparing gas phase IRMPD spectra and computed IR spectra. The amine-deprotonated structure which involves Pb^{2+} in coordination with the amine nitrogen and carbonyl oxygen (A type structure in Figure 5.1) was concluded to be the structure responsible for the IRMPD spectrum. For the monohydrated complex, IRMPD suggested a structure with intact water bound to the carboxylate oxygens and is also strongly hydrogen bound to the amine nitrogen resulting in one O-H stretch at about 3700 cm^{-1}. It was suggested that during the hydration process [Pb(Pro-H)(H_2O)]$^+$ complexes isomerize from the structure with Pb^{2+} bound to the amine N and carbonyl O (A-type) to the one with Pb^{2+} placed between the two carboxylate oxygens (C-type).[22]

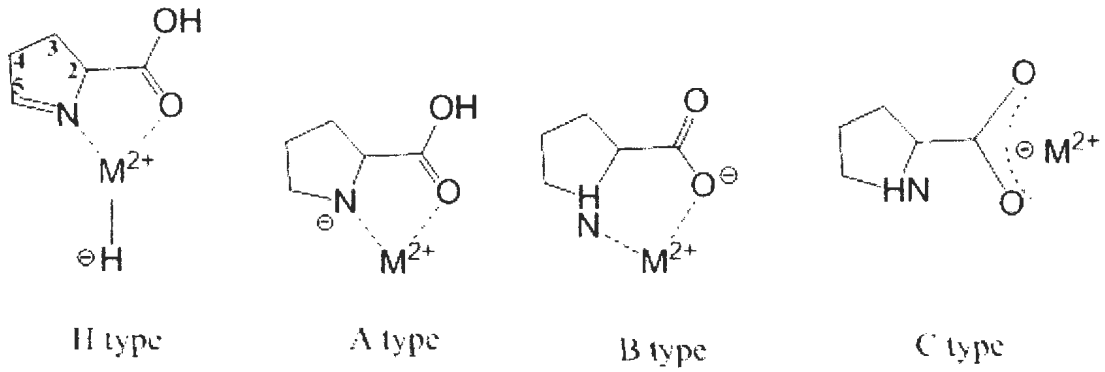

H type A type B type C type

Figure 5.1. 4 types of [M(Pro-H)]$^+$ conformers (M=Zn^{2+} and Pb^{2+}). Conventional nomenclature of the three isomers (i.e. A, B, and C) used by Burt *et al.*[22]

IRMPD spectroscopy was also employed in conjunction with electronic structure calculations to study the gas-phase structure of [Zn(His-H)]$^+$ (histidine= His).[26] The proton lost in [Zn(His-H)]$^+$ was found to be from the carboxylic acid group. The structure most consistent with the IRMPD spectrum was that in which histidine coordinated in a

tridentate fashion with Zn^{2+} bound to the carbonyl, N1 of imidazole, and the α-amino group (CO, N1,N_α).[26]

The Zn^{2+} complex with the conjugate base of amino acids has also been studied using gas phase fragmentation techniques. Ohanssien and co-workers have done a series of studies to determine the structures and fragmentations of deprotonated glycine-Zn(II) complex in the gas phase.[27-30] Accurate ab initio calculations were used to obtain three types of structures including complexes deprotonated at the amine group, carboxyl acid or deprotonated at the α-carbon among the lowest energy structures of $[Zn(Gly-H)]^+$ (glycine= Gly).[27] The energetically most favourable structure in the gas phase was found to be one where nitrogen is deprotonated and where H is transferred from the α-carbon to Zn^{2+} effectively forming a complex between dehydrogenated Gly and ZnH^+.[27]

The focus of this work was to characterize the structures of deprotonated zinc-proline complexes. Proline is the only naturally occurring amino acid with a secondary α-amine group. Here, the structures of the bare and monohydrated complexes, $[Zn(Pro-H)]^+$ and $[Zn(Pro-H)(H_2O)]^+$ have been elucidated using collision induced dissociation, CID, and IRMPD spectroscopy in combination with electronic structure calculations.

5.2. Methods

5.2.1. Experimental

The $[Zn(Pro-H)]^+$complex was electrosprayed from a solution containing 0.1 mM $ZnCl_2$ and 0.1 mM amino acid in a 90/10 mixture of methanol/water using an Apollo II ion source of a Bruker Apex Qe 7 T FTICR MS. The $[Zn(Pro-H)]^+$ ions were allowed to accumulate in a hexapole collision cell for 2s before being transferred to the ICR cell. To prepare the hydrated complex of $[Zn(Pro-H)]^+$, water is introduced to the collision cell via a vapour inlet line.[31] For IRMPD experiments, $[Zn(Pro-H)]^+$or $[Zn(Pro-H)(H_2O)]^+$ were isolated in the ICR cell and irradiated with a KTP OPO laser coupled to the FT-ICR for 7 sec over the range of 3200-3800 cm^{-1} at intervals of 1.5 cm^{-1}.[22] The IRMPD spectrum was obtained by plotting the negative of the natural logarithm of the normalized precursor ion intensity, IRMPD efficiency, as a function of OPO radiation frequency.

SORI/CID was also used to perform tandem mass spectrometry inside the ICR cell. The isolated ions were fragmented by energetic collisions, 1.1-7.8 eV lab frame or 0.19-1.4 eV in the center of mass (c.o.m.) frame, with a pulse of argon to a pressure of 10^{-8} mbar in the ICR cell of the mass spectrometer.

5.2.2. Computational

Calculations were performed using the Gaussian 09 software package.[32] Many possible structures with different deprotonation sites and zinc coordination were

optimized, and frequency calculations for each optimized structure were done using B3LYP density functional theory with the 6-31+G(d,p) basis function. The vibrational frequencies were scaled by factor of 0.955 to compare with the experimental IRMPD spectra. Single point energy calculations were also performed at the MP2 level of theory using 6-311++G(2d,2p) basis set. The relative enthalpies and Gibbs energies reported are a combination of the MP2 electronic energies and the 298 K thermochemistry from the B3LYP calculations called MP2(full)/6-311++G(2d,2p)//B3LYP/6-31+G(d,p).

5.3. Results and Discussion

5.3.1. IRMPD spectra of $[Zn(Pro\text{-}H)]^+$ and $[Zn(Pro\text{-}H)(H2O)]^+$.

Upon resonant absorption of the OPO laser $[Zn(Pro\text{-}H)]^+$ the only fragmentation observed was loss of neutral zinc to produce an ion at *m/z* 114. A small amount of *m/z* 68 was also observed and is formed by subsequent $[2H,C,2O]$ from $[Pro\text{-}H]^+$. No other dissociation products were observed. The slow activation by the OPO laser results in dissociation pathway with the lowest energy requirement to be accessed; in the present case loss of neutral Zn.

In the case of the hydrated complex, $[Zn(Pro\text{-}H)(H_2O)]^+$ (*m/z* 196), the fragment ions were observed *m/z* 178 and *m/z* 114 which are losses of H_2O and H_2O+Zn, respectively.

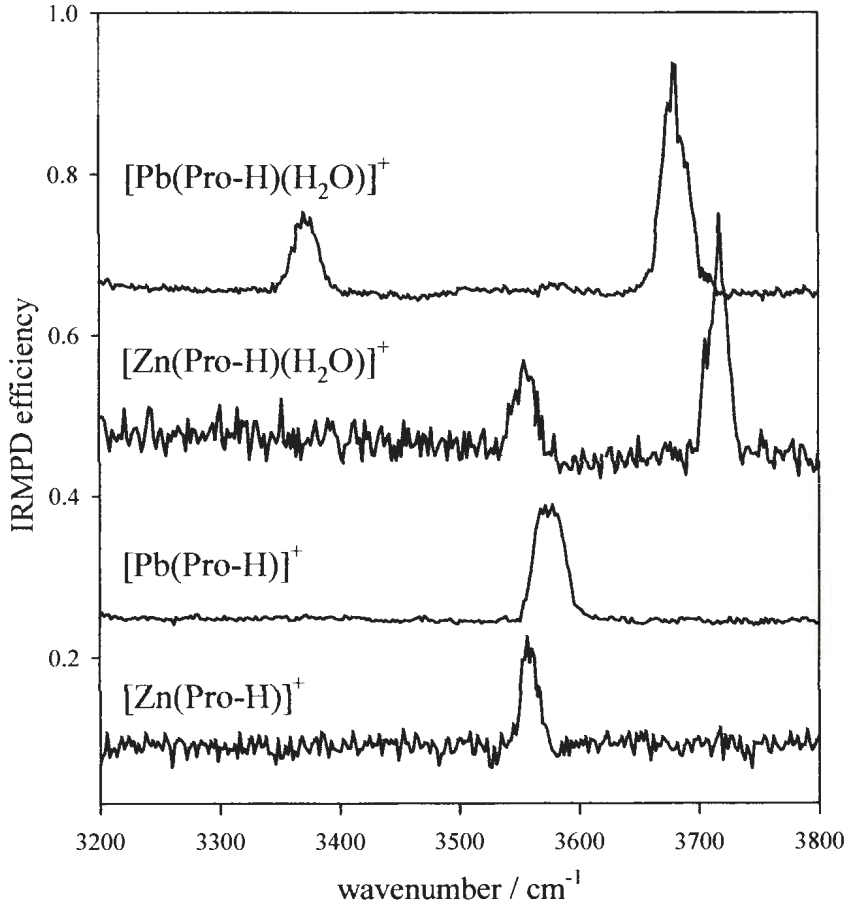

Figure 5.2. Comparison of IRMPD spectra of $[Zn(Pro\text{-}H)]^+$, $[Zn(Pro\text{-}H)(H_2O)]^+$, $[Pb(Pro\text{-}H)]^+$, and $[Pb(Pro\text{-}H)(H_2O)]^+$ in the 3200-3800 cm^{-1} range. IRMPD spectra of $[Pb(Pro\text{-}H)]^+$, and $[Pb(Pro\text{-}H)(H_2O)]^+$ adapted with permission from *J. Phys. Chem. B,* **2011**, 115, 11506-11518.[22]

The IRMPD spectra of $[Zn(Pro\text{-}H)]^+$ and $[Zn(Pro\text{-}H)(H_2O)]^+$ in the 3200-3800 cm^{-1} range are compared with the previously reported IRMPD spectra of $[Pb(Pro\text{-}H)]^+$ and $[Pb(Pro\text{-}H)(H_2O)]^+$ in Figure 5.2. The IRMPD spectrum of $[Zn(Pro\text{-}H)]^+$ exhibits a single absorption at 3557 cm^{-1} in the O-H stretching region, and there is no absorption observed in the N-H stretch region. A similar IRMPD spectrum was observed for

$[Pb(Pro\text{-}H)]^+$, a single band assigned to the carboxylic acid O-H stretch.[22] This implies that the $[Zn(Pro\text{-}H)]^+$ complex is amine deprotonated similar to the $[Pb(Pro\text{-}H)]^+$ complex, having an intact carboxyl group.[22]

The IRMPD spectrum of the singly hydrated complex, $[Zn(Pro\text{-}H)(H_2O)]^+$, contains an absorption in a similar position to the one observed in the bare complex at 3562 cm^{-1} and can be assigned to the carboxylic acid O-H stretch. There is also a stronger absorption at 3718 cm^{-1} which can be attributed to the stretching of a free O-H group attached to zinc. The absence of two water bands, the symmetric and antisymmetric water stretching absorptions, rules out a water molecule being bound to zinc and free from other interactions. The absence of the symmetric stretch could be explained by one of the water hydrogens involved in an intramolecular hydrogen bond. The band assigned to the MO-H stretch was similarly observed for IRMPD spectrum of $[Pb(Pro\text{-}H)(H_2O)]^+$. However, the carboxyl O-H stretch band observed in the bare complex $[Pb(Pro\text{-}H)]^+$ was absent in the IRMPD spectrum of $[Pb(Pro\text{-}H)(H_2O)]^+$. Instead, a band assigned to an N-H stretch was present, suggesting that $[Pb(Pro\text{-}H)(H_2O)]^+$ is deprotonated at the carboxylic acid, due to an isomerization that occurred during solvation.

5.3.2. Computed structures and spectra of $[Zn(Pro\text{-}H)]^+$ and $[Zn(Pro\text{-}H)(H_2O)]^+$.

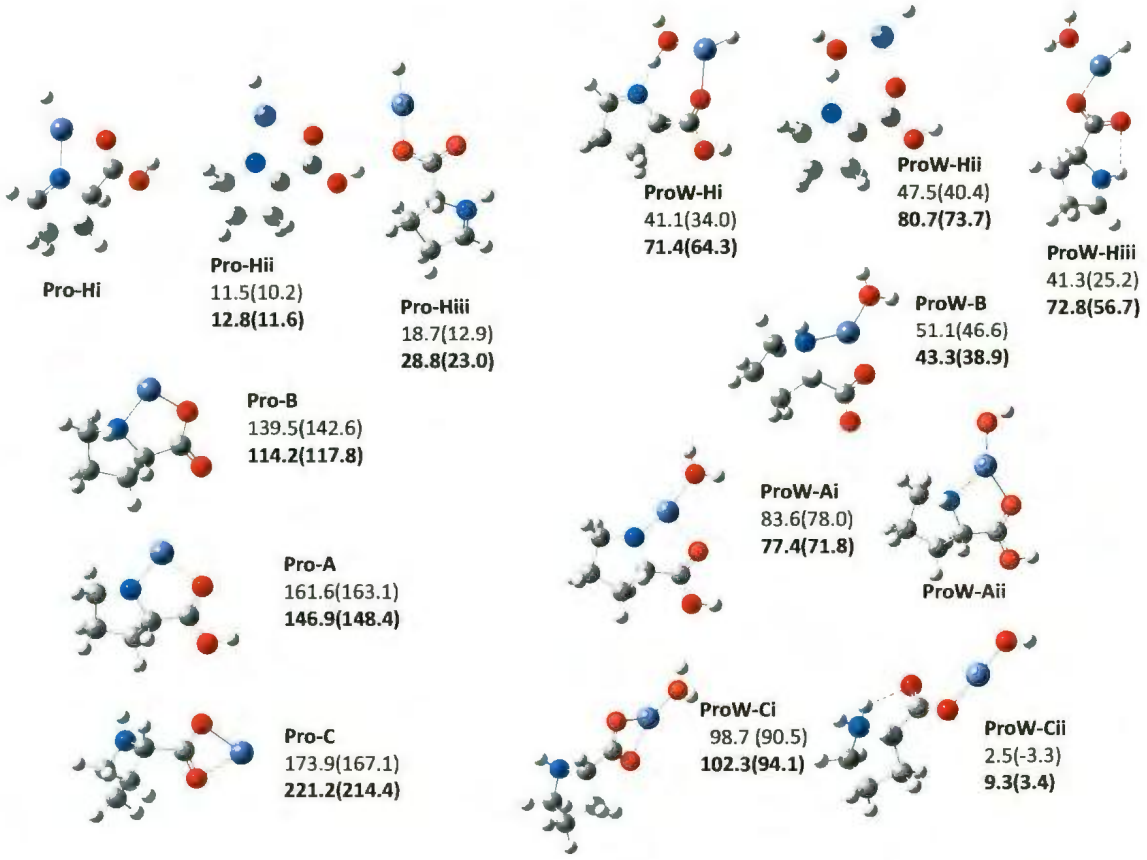

Figure 5.3. Computed structures for $[Zn(Pro\text{-}H)]^+$ and $[Zn(Pro\text{-}H)(H_2O)]^+$ complexes. The 298 K enthalpies and Gibbs energies (in parentheses) are reported at the B3LYP/6-31+G(d,p) and MP2(full)/6-311++G(2d,2p)//B3LYP/6-31+G(d,p) (in bold) and are in kJ mol^{-1}.

Many $[Zn(Pro\text{-}H)]^+$ and $[Zn(Pro\text{-}H)(H_2O)]^+$ structures as well as their relative enthalpies and 298K Gibbs energies are shown in Figure 5.3. The lowest energy

structure of [Zn(Pro-H)]+, Pro-Hi, was found to be one in which a hydrogen is transferred from the C5 group to zinc, and Zn2+ is bound to the deprotonated amine nitrogen and the carbonyl oxygen of the carboxyl group. Pro-Hii is a similar H-type structure, where hydrogen is transferred from C2 to the zinc atom. Effectively, these structures are dehydrogenated proline bound to ZnH+. The MP2 and B3LYP calculations predict the Hii structure to be higher in Gibbs energy than the Hi structure by 12.8 and 11.5 kJ mol-1, respectively. A third H-type structure, Pro-HC still higher in energy, is carboxylate deprotonated with ZnH+ bound to the carboxylate group.

Pro-B involves metal chelation between the amine nitrogen and one carbonyl oxygen of carboxylic acid deprotonated proline, and is higher in energy by more than 100 kJ mol^{-1} than Pro-Hi. The relative energies are similar to those seen for the H and B type isomers of $[Zn(Gly-H)]^{+}$.[27] They suggested that the B-type structure of $[Zn(Gly-H)]^{+}$ is the solution phase complex and during desolvation it isomerizes to the H type structure.[27] In Pro-A the zinc atom is bound between the deprotonated amine group and the carbonyl oxygen of the intact carboxylic acid group. The Pro-A structure is higher in Gibbs energy than Pro-B by 30.6 kJ mol^{-1}, and higher by 148.4 kJ mol^{-1} in Gibbs energy than the lowest energy H type structure. Pro-C is carboxylic acid-deprotonated with Zn^{2+} between the two carboxylate oxygens and is in excess of 150 kJ mol^{-1} higher in energy than the global minimum energy structure. In contrast, the H type structure is significantly higher in energy, 32 kJ mol^{-1}, than the lowest energy structure computed for $[Pb(Pro-H)]^{+}$. The amine- and carboxylic acid-deprotonated structures for $[Pb(Pro-H)]^{+}$ were computed to be the lowest in energy and virtually isoenergetic, with Pb^{2+} coordinated between the

carbonyl O and amine N.[22] The significant difference between Pb^{2+} and Zn^{2+} can be largely rationalized by the higher affinity of Zn^{2+} for hydrogen.[37] The reported values of the metal-hydrogen bond energy, $D_{298}(M^{+}\text{-H})$, for Zn^{2+} and Pb^{2+} are 241 kJ mol^{-1} and 175 kJ mol^{-1}, respectively.[37]

Computed structures for $[Zn(Pro\text{-}H)(H_2O)]^{+}$ resulting from attaching water to the $[Zn(Pro\text{-}H)]^{+}$ structures are depicted on the right side of Figure 5.3. Simply adding water to Zn of Pro-A produces ProW-Ai, but a hydrogen transfer from water to N produces the lowest energy structure, ProW-Aii, which can be described as proline bound to $ZnOH^{+}$. ProW-Ai is 72 kJ mol^{-1} higher in Gibbs energy than ProW-Aii. In ProW-Hi and ProW-Hii water is bound to Zn and inserts into the Zn—N bond bridged to N by an OH hydrogen bond. ProW-Hi and ProW-Hii are 64 and 74 kJ mol^{-1}, respectively, *higher* in Gibbs energy than the lowest energy structure. ProW-B and ProW-Ci result from the attachment of intact water to Pro-B and Pro-C, which are 40 and 94 kJ mol^{-1} higher in Gibbs energy than ProW-Aii, respectively. Another interesting C-type structure, effectively results from a proton transfer from water to N. In ProW-Cii proline is a zwitterion, stabilized by a $ZnOH^{+}$ moiety bound to the deprotonated oxygen. There is also a hydrogen bond between the carbonyl oxygen and one of the hydrogens of the protonated amine group. Finally, two solvated HC structures, one with two free O-H bonds and one which has one of the O-H bonds of water is hydrogen bonded to a carboxylate oxygen are also presented in Figure 5.3.

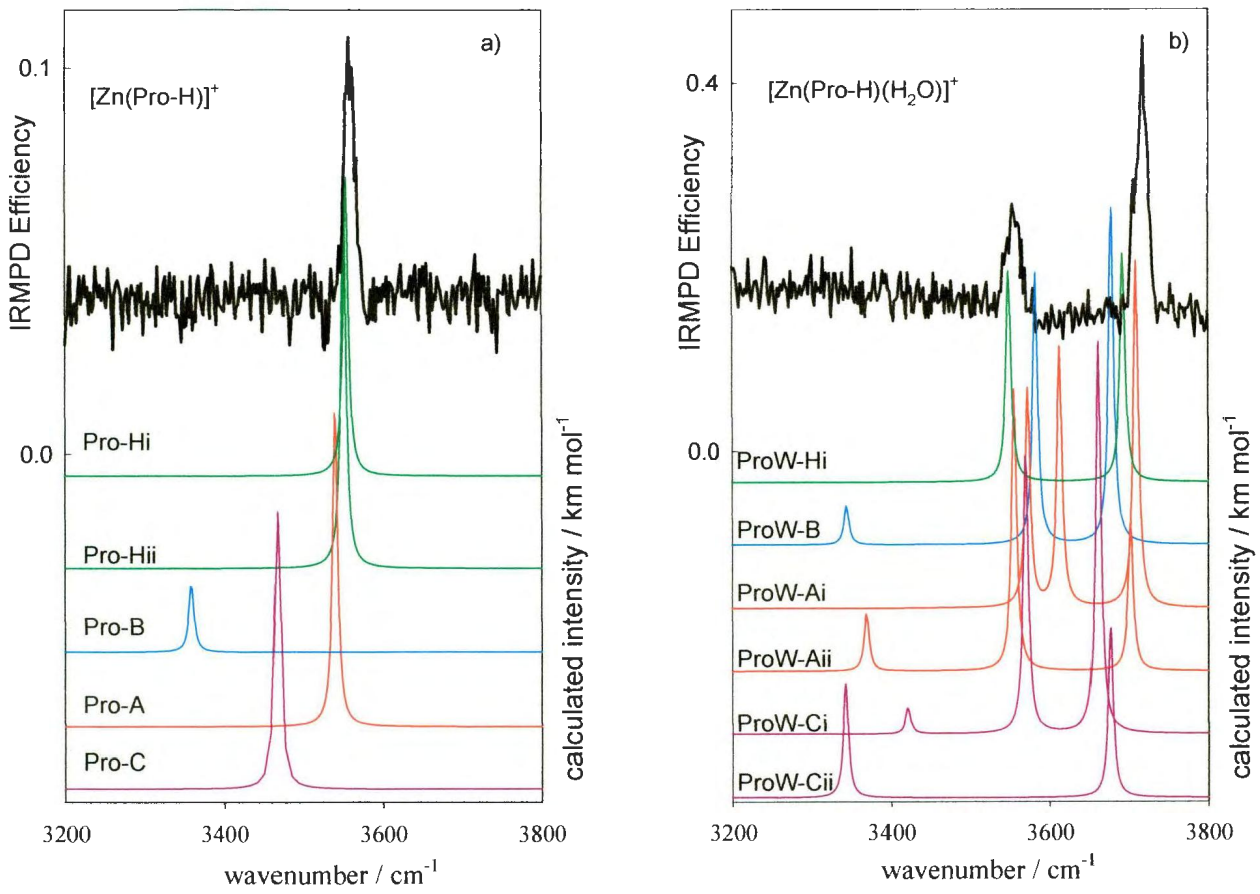

Figure 5.4. Comparison of the IRMPD spectrum with the B3LYP/6-31+G(d,p) computed spectra for some of the structures depicted in Figure 3 for a) $[Zn(Pro\text{-}H)]^+$ and b)$[Zn(Pro\text{-}H)(H_2O)]^+$.

In Figures 5.4 a) and b) and Figure 5.5 the computed IR spectra for some of the structures in Figure 2 are compared with the experimental IRMPD spectra for $[Zn(Pro-H)]^+$ and $[Zn(Pro-H)(H_2O)]^+$ complexes, respectively. The IRMPD spectrum of $[Zn(Pro-H)]^+$ can rule out the high energy structures Pro-B, Pro-C, and Pro_HC as the main contributors to the IRMPD spectrum due to the absence of the carboxylic acid OH stretch in their computed IR spectra which was the only feature observed in the experimental spectrum. The N-H stretch of Pro-C is predicted to occur at a higher wavenumber position and with more intensity than predicted for other proline complexes and observed in solvated [Pb(Pro-H)] complexes.[22] The Pro-H and Pro-A complexes both reproduce the COO-H stretch in the observed spectrum, both do not have an N-H bond, and cannot be distinguished by the IRMPD spectrum in the 3200 –3800 cm^{-1} region. However, using both B3LYP and MP2 methods, Pro-A is calculated to be about 148 kJ mol^{-1} higher in Gibbs energy than the Pro-Hi structure. The Pro-H type structures, N-deprotonated with H transferred from C2 or C5 to Zn, are both consistent with the IRMPD spectrum, and are also the lowest energy structures.

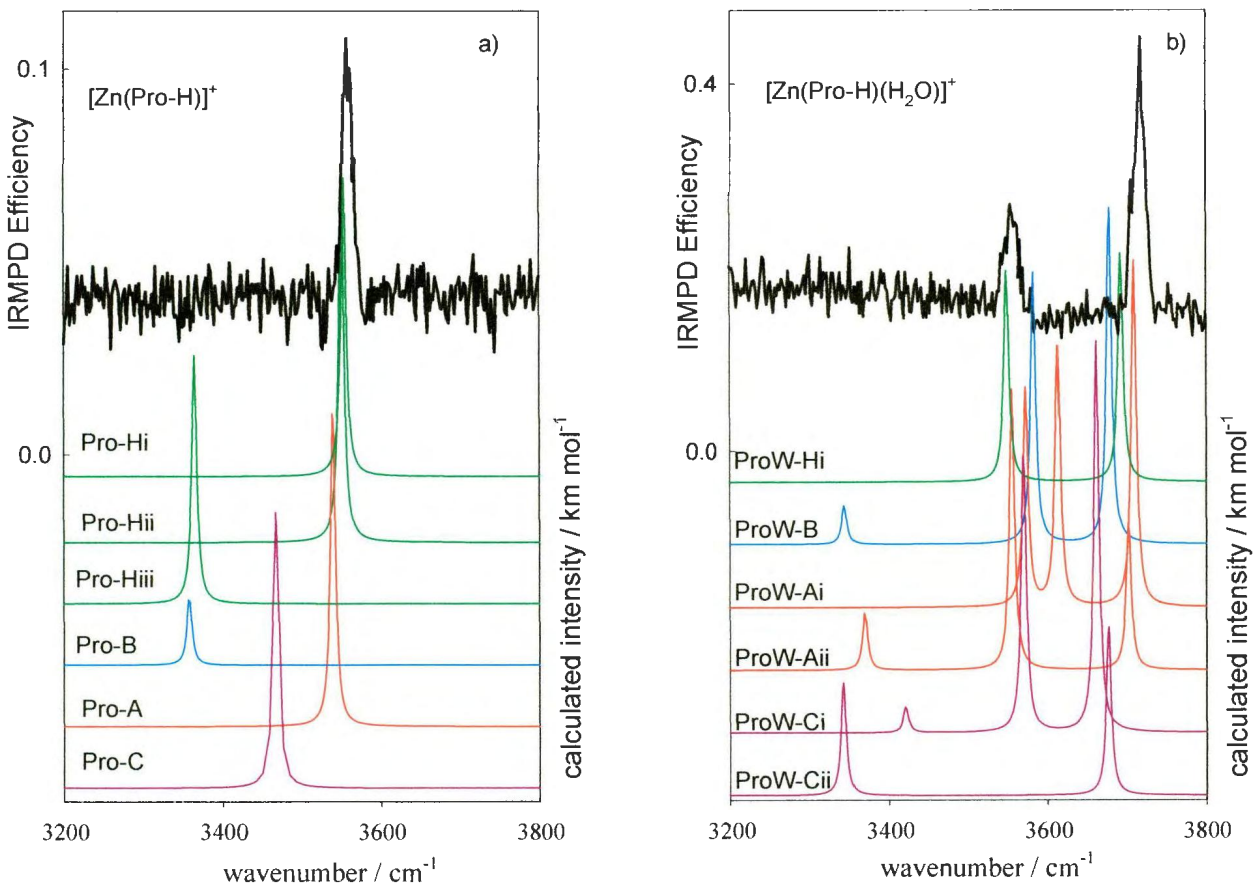

Figure 5.5. Comparison of the IRMPD spectrum with the B3LYP/6-31+G(d,p) computed spectra for some of the structures depicted in Figure 3 for a) $[Zn(Pro\text{-}H)]^+$ and b)$[Zn(Pro\text{-}H)(H_2O)]^+$.

The IRMPD spectrum of the hydrated complex has two bands in the OH stretch region, were assigned to the ZnO-H and carboxylic acid OH stretch based on their positions. Comparing the IRMPD spectrum and computed spectra of the hydrated complexes, Fig. 3 b), rules out the structure ProW-Aii, where intact water is added to Pro-A because its computed IR spectrum contains three OH stretch bands, water symmetric and antisymmetric stretch as well as the carboxylic acid OH stretch.

It is true that N-H stretching vibrations are weak in intensity for metal-amino acid complexes, however, in systems where there is an N-H stretch there is always at least a small amount of dissociation observed. In the solvated complexes, the N-H stretching vibrations are always observed with significant intensity (see for example the spectrum of $[Zn(Pro\text{-}H)(H_2O)]^+$ in Figure 5.2). There is no action whatsoever in the N-H stretch of the experimental IRMPD spectrum of $[Zn(Pro\text{-}H)(H_2O)]^+$, therefore ProW-Ai, which is the lowest energy structure, cannot explain the experimental spectrum. In addition, the IRMPD spectrum can rule out structures ProW-B, and the ProW-C structures (see also Fig. 5.5), which are also predicted to have a band in the N-H stretch region. The ProW-HC structures also will have an N-H stretch and can be ruled out (see also Fig. 5.4). The high energy ProW-Hi and ProW-Hii structures, where water is added to the H-type structures of $[Zn(Pro\text{-}H)]^+$ and are intramolecularly hydrogen bonded to the amine site, are the best matches for the IRMPD spectrum of $[Zn(Pro\text{-}H)(H_2O)]^+$. Furthermore, loss of neutral Zn following water loss when $[Zn(Pro\text{-}H)(H_2O)]^+$ absorbs the OPO laser suggesting a structure similar to the $[Zn(Pro\text{-}H)]^+$ complex.

5.3.3. Unimolecular Reactivity of Activated $[Zn(Pro-H)]^+$.

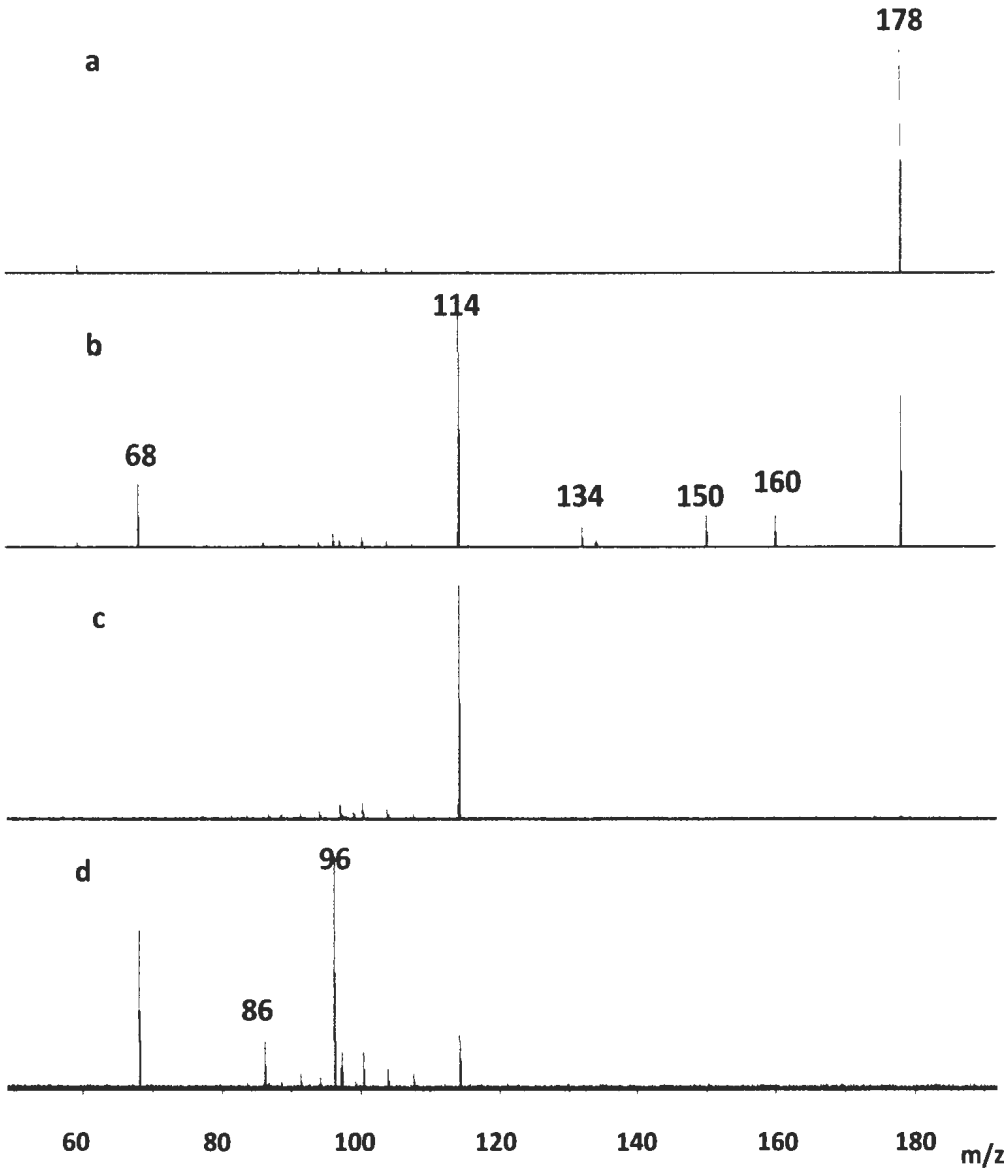

Figure 5.6. Electrospray mass spectra of $[Zn(Pro-H)]^+$ following a) isolation of *m/z* 178, b) SORI-CID of *m/z* 178 at 0.53 eV (c.o.m.), c) isolation of *m/z* 114 formed from SORI_CID of *m/z* 178, and d) SORI-CID of *m/z* 114 at 1.17 eV (c.o.m.).

In Figure 5.6 is the MS/MS spectrum of $[^{64}Zn(Pro\text{-}H)]^+$ using SORI-CID (Fig. 5.6 b), followed by isolation of *m/z* 178 inside the ICR cell (Fig. 5.6a). The main primary fragmentation product is *m/z* 114 assigned to $[Pro\text{-}H]^+$ and corresponds to loss of Zn (64 Da). In order to verify that the fragment ion *m/z* 114 comes from the loss of neutral zinc, the $[^{66}Zn(Pro\text{-}H)]^+$ precursor ion (*m/z* 180) was isolated and submitted to SORI-CID. The product ion remained at *m/z* 114, a loss of 66 Da this time which clearly confirms the loss of neutral Zn. Minor fragmentation products are also observed in the CID spectrum at *m/z* 160, *m/z* 150, and *m/z* 134, which are easily identified as losses of H_2O, CO, and CO_2, respectively. A peak at *m/z* 132 was also observed which corresponds to either a secondary loss of CO following loss of H_2O (or vice versa), or loss of formic acid (HCOOH), *vide infra.*

Other ions in the SORI-CID spectrum of *m/z* 178 were observed at *m/z* 68, 86 and 96. SORI-CID experiments conducted on the isolated *m/z* 114 fragment ion produced by SORI-CID of *m/z* 178, and the result is shown in Figure 4d. The fragment ions observed were, again, *m/z* 96 (loss of H_2O), *m/z* 86 (loss of CO), and *m/z* 68 (loss of H_2O and CO) showing that these ion in the SORI-CID of *m/z* 178 are most likely secondary fragmentations following the loss of neutral zinc. Shoeib *et al.* previously observed similar fragment ions at *m/z* 114 and *m/z* 68 following CID of the $[Ag\text{-}Proline]^+$ complex.[33]These ions were identified as $[Pro\text{-}H]^+$ formed by loss of neutral AgH and $C_4H_6N^+$ formed by secondary concurrent loss of H_2O and CO fragmentations of $[Pro\text{-}H]^+$. Effectively $[Pro\text{-}H]^+$ is protonated dehydrogenated proline and was identified as the immonium ion similar to that which ZnH^+ is bound to in structure Pro-Hi.

Dissociation of collisionally activated $[Zn(Gly-H)]^+$ showed three parallel primary dissociation pathways, loss of CO_2, loss of CO, and loss of H_2O (followed by loss of CO).[30] However, unlike $[Zn(Pro-H)]^+$, $[Zn(Gly-H)]^+$ does not lose neutral Zn. SORI-CID performed on $[Pb(Pro-H)]^+$ (*m/z* 322), resulted primarily in the loss of water (*m/z* 304) and no loss of neutral metal.

Kretschmer *et al.* discovered this novel leaving group, neutral atomic metal, for the S_N2 reaction between $M(CH_3)^+$ (M=Zn, Cd, Hg) and ammonia in the gas phase.[34] This type of reaction did not take place for the first-row transition metals other than Zn.[34] The different behaviour of the zinc triad elements, Cd, Zn, and Hg, is correlated with their relatively high ionization energy (IEs) in turn due to their closed-shell electron configurations.[35] With the help of calculations a pathway was proposed for C-N coupling, leading to the liberation of neutral metal involving coordination of NH_3 to the carbon of the methyl group. A pathway with ammonia coordinated to the metal center was ruled out for energetic reasons. Furthermore, the rate coefficients and the efficiencies for the elimination of neutral metal were observed to increase over the series Cd>Zn>Hg, which is consistent with the trend of the sum of the first and second ionization energies.[34,35] On this basis, the presence of liberation of neutral metal in activation/fragmentation of $[Zn(Pro-H)]^+$ in the present experiment and its absence in the case of $[Pb(Pro-H)]^+$ can also be correlated with the higher ionization energy of Zn compared to Pb.[36]

In order to determine the origin of hydrogen atoms lost in the SORI-CID experiments, activation was conducted on complexes composed of two deuterium

isotopomers of proline. The results of the SORI-CID esperiments on $[Zn(Pro-H)]^+$ where Pro was 2-d1-proline or 2,5,5-d3-proline are shown in Figure 5.7 a) and b), respectively. As expected, the peaks in the CID spectrum of normal $[Zn(Pro-H)]^+$ (Fig. 5.4) at *m/z* 114, 134, and 150 due to loss of Zn, CO_2, and CO, respectively, shift to *m/z* 115, 135, and 151, respectively for single deuterium substitution and to *m/z* 117, 137, and 153 for the triply deuterated complex.

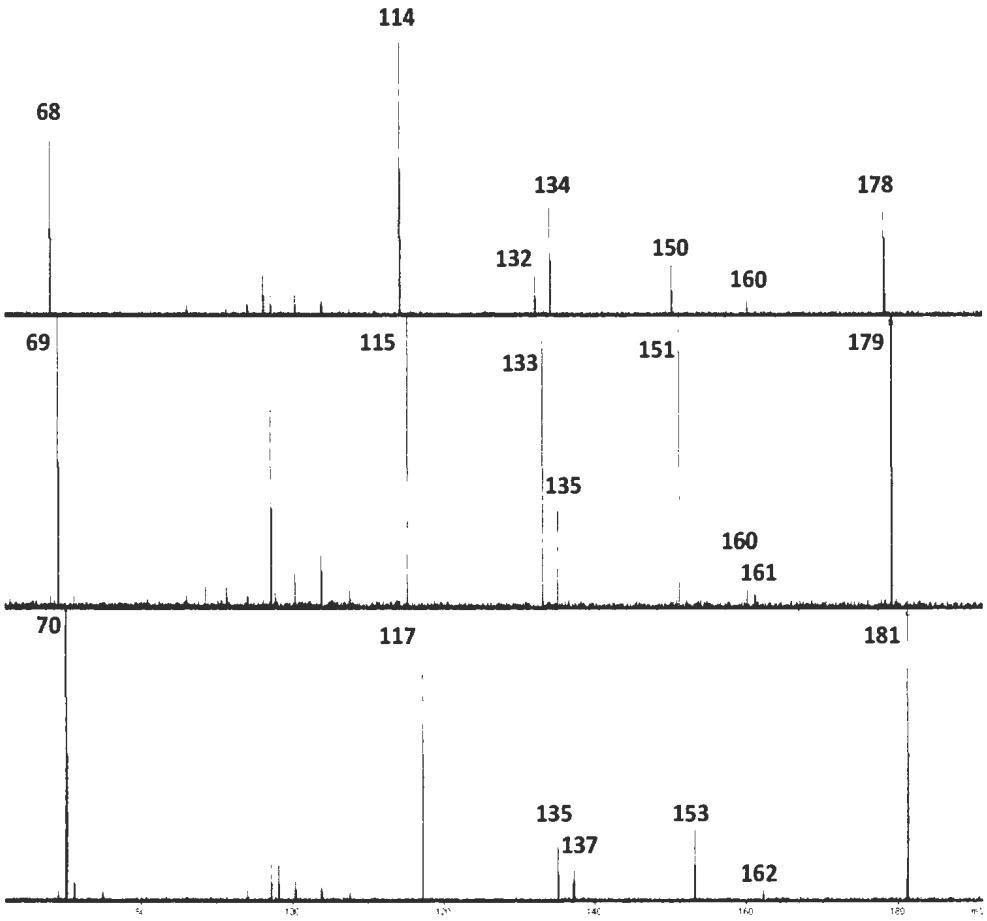

Figure 5.7. SORI-CID mass spectra of $[Zn(2\text{-}d_1\text{-Pro-H})]^+$ (*m/z* 179) following its isolation and $[Zn(2,5,5\text{-}d_3\text{-Pro-H})]^+$ (*m/z* 181) following its isolation.

For $[Zn(2\text{-}d_1\text{-Pro-H})]^+$ the *m/z* 160 peak associated with loss of water becomes two peaks, loss of 18 and 19 Da at *m/z* 161 and 160, respectively, suggesting two different routes to loss of H_2O, one involving the C2 hydrogen. For $[Zn(2,5,5\text{-}d_3\text{-Pro-H})]^+$, the water loss peak is observed solely at *m/z* 162, a loss of 19 Da. This result shows that there are two routes to the loss of water, one involving a hydrogen on C2 and one involving a hydrogen

on C5. From the results of the IRMPD spectroscopy experiments, showing an intact carboxyl group, it is safe to assume that H_2O loss also involves the carboxyl OH group.

The loss of 46 Da from $[Zn(Pro-H)]^+$ does not change with deuterium substitution at C2 or C5. Therefore, this fragmentation does not involve loss of water followed by loss of CO otherwise there would be a shift in this peak similar to that observed for the water-loss peak. These results show that the *m/z* 132 peak likely results from a fifth primary fragmentation channel, loss of 46 Da, which is most likely the carboxylate group and a hydrogen from C3 or C4.

5.3.4. Fragmentation pathways.

The main fragmention channel observed by IRMPD or CID for $[Zn(Pro-H)]^+$ was the loss of neutral Zn, whereas the only fragment ion produced by absorption of OPO laser by $[Pb(Pro-H)]^+$ was loss of H_2O.[22] Moreover, the fragmentation channels observed by CID of $[Zn(Gly-H)]^+$ were loss of CO_2, loss of CO, and successive loss of CO and H_2O.[30] Shoeib *et al.* investigated the mechanism of fragmentation of $[Ag(Pro)]^+$ complex leading to the loss of AgH.[33] They showed that H transfer occurs from C5 to Ag^+ to form a structure containing AgH bound to deprotonated proline. AgH was then eliminated to form deprotonated proline observed at *m/z* 114. It was determined above that the lowest energy structure, and one consistent with the IRMPD spectrum for $[Zn(Pro-H)]^+$ is an H type structure resembling ZnH^+ bound to dehydrogenated proline where proline is dehydrogenated at N and C5.

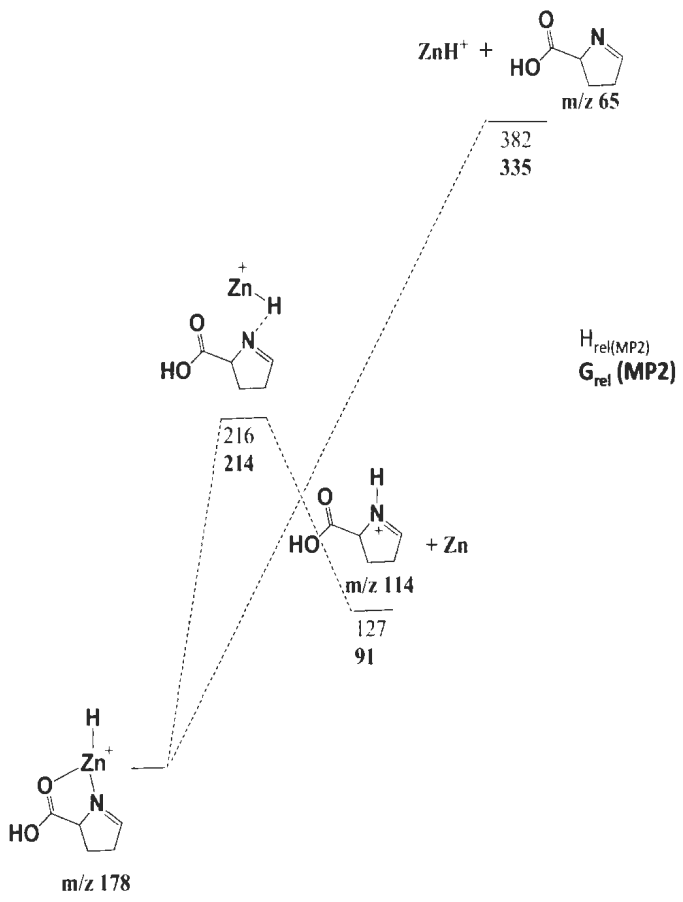

Figure 5.6. Energy profile in kJ mol^{-1} (unbolded values are enthalpies and bolded values are Gibbs energies) for the loss of neutral zinc and Pro-H_2 from $[Zn(Pro\text{-}H)]^+$ complex. Thermochemistries were computed using MP2(full)/6-311++G(2d,2p)//B3LYP/6-31+G(d,p).

Armed with the experimental data provided above, electronic structure calculations can provide some more insight into the primary fragmentation channels observed for $[Zn(Pro\text{-}H)]^+$. For example, calculations will be used to explain why the

fragmentation channel leading to the loss of neutral zinc was observed rather than the loss of dehydrogenated proline producing ZnH^+. The energy profiles for loss of Zn and loss of dehydrogenated proline from Pro-Hi are provided in Figure 5.8. The hydrogen of ZnH is transferred to nitrogen and neutral Zn is lost to give deprotonated proline at *m/z* 114 through a transition state with a Gibbs energy barrier of 213 kJ mol^{-1}, and the products are 91 kJ mol^{-1} higher in Gibbs energy than Pro-Hi. On the other hand, the energy required for dissociation of dehydrogenated proline to produce ZnH^+ was calculated to be 335 kJ mol^{-1}. This large dissociation energy explains why an ion ZnH^+ at *m/z* 65 was not observed.

In Figure 5.9 is the energy profile for the loss of water from Pro-Hi. The first step is rotation around the carboxyl C-C2 bond such that the OH oxygen is complexed to Zn. The next step is a transfer of hydrogen from Zn-H to the carboxyl carbon and transfer of the OH to Zn. This step is followed by a transfer of the H from the now carbonyl C to the OH group. In this mechanism, the H that was on Zn in Pro-Hi originally stemmed from C5 which is consistent with the deuterium isotope experiments which show that one of the hydrogens on water was deuterated. A similar mechanism and potential energy profile for the Pro-Hii complex, where the H on Zn originates from C2, is shown in Figure 5.10. The deuterium substitution experiments are consistent with both isomers, Pro-Hi and Pro-Hii, being present since when only 2-d1-proline is used, both H_2O and HDO loss is observed but when 2,5,5-d_3-proline is used only HDO loss is observed. Note that a thorough search for a mechanism where H was transferred from Zn was conducted. No attempts resulted in a transition state where H was transferred directly from Zn to the

OH group. The threshold for water loss is also computed to be significantly higher than that for loss of Zn, >296 compared to 213 kJ mol^{-1} in agreement with the Zn loss being the most abundant product of SORI-CID and IRMPD.

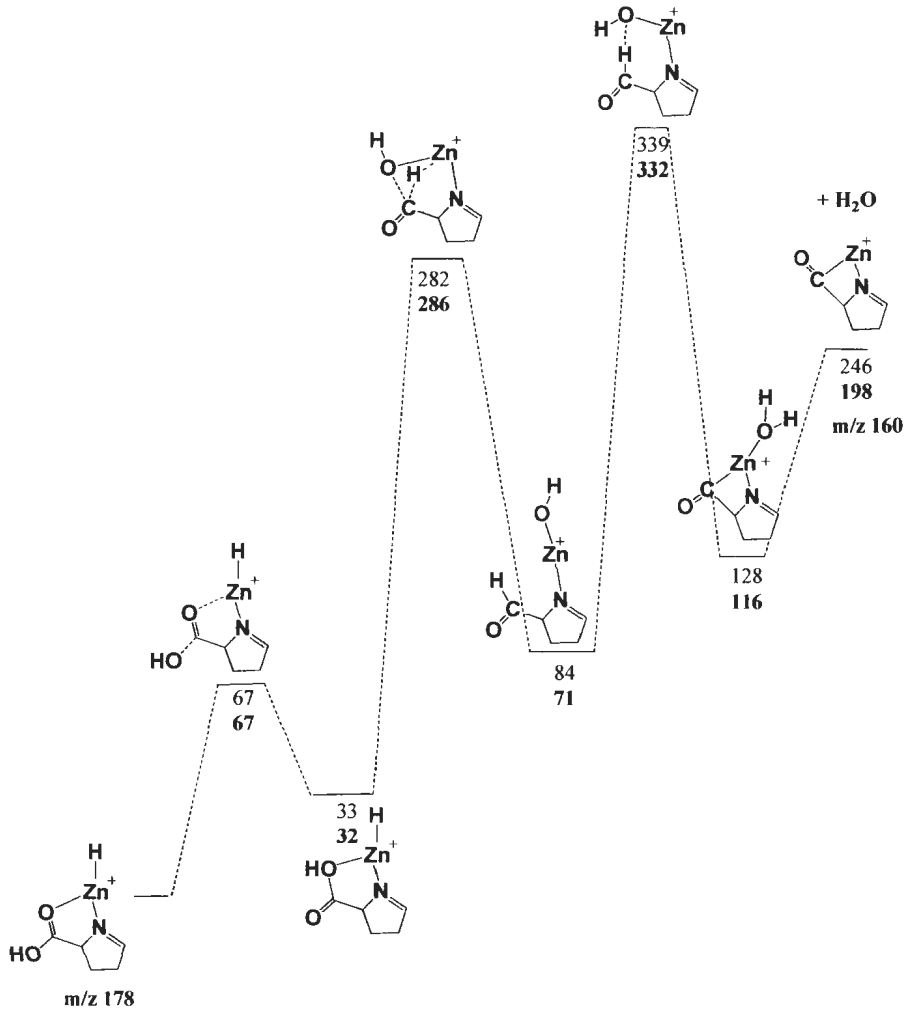

Figure 5.9.Energy profile in kJ mol^{-1} (unbolded values are enthalpies and bolded values are Gibbs energies) for the loss of water from $[Zn(Pro-H)]^+$ complex, Pro-Hi. Thermochemistries were computed using MP2(full)/6-311++G(2d,2p)//B3LYP/6-31+G(d,p).

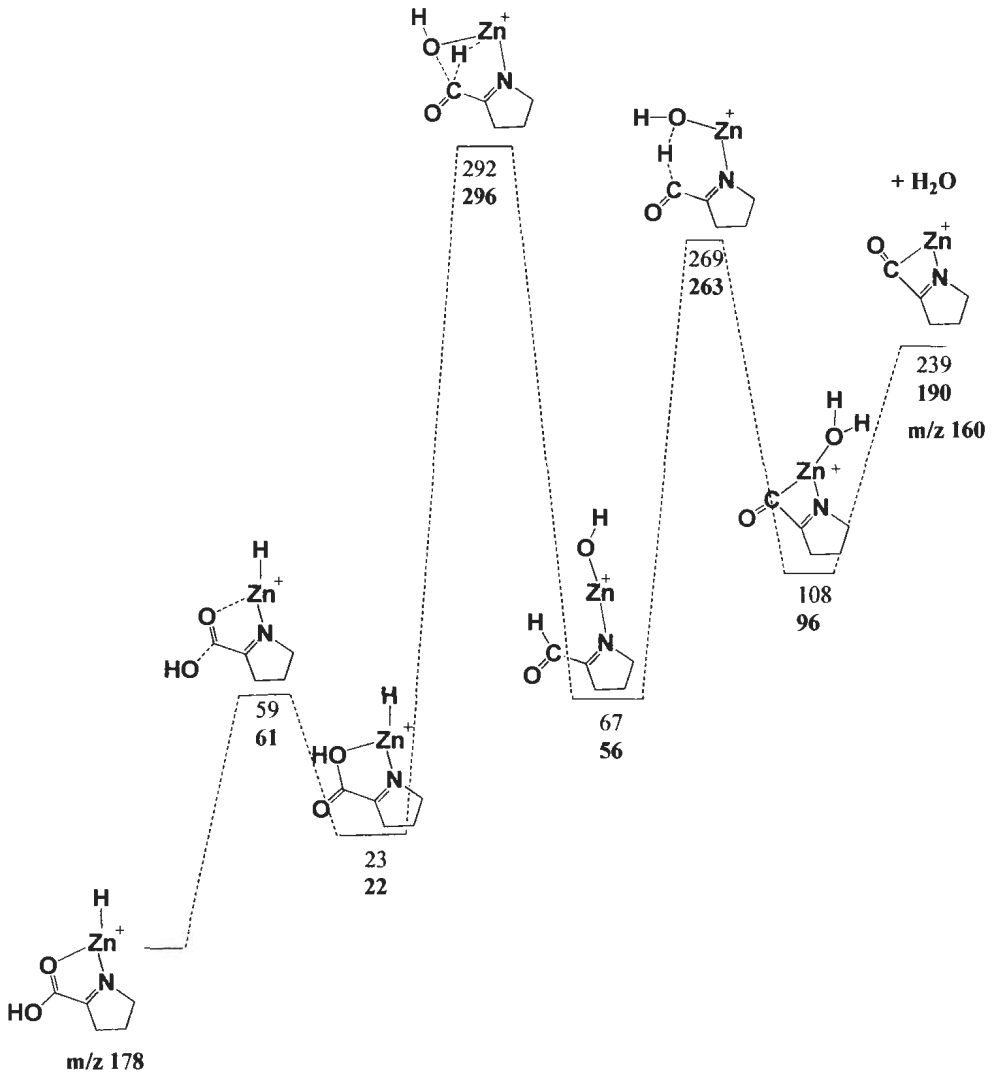

Figure 5.10.Energy profile in kJ mol^{-1} (unbolded values are enthalpies and bolded values are Gibbs energies) for the loss of water from $[Zn(Pro-H)]^+$ complex, Pro-Hii. Thermochemistries were computed using MP2(full)/6-311++G(2d,2p)//B3LYP/6-31+G(d,p).

In Figure 5.11 is the energy profile for loss of formic acid. The threshold for this pathway, a transfer of H from C3 to the carboxyl-C, is 390 kJ mol^{-1}, again significantly higher than for loss of neutral Zn. Furthermore, this mechanism is consistent with the results that no deuterium was observed to be lost when C2 or C5 were labeled with deuterium.

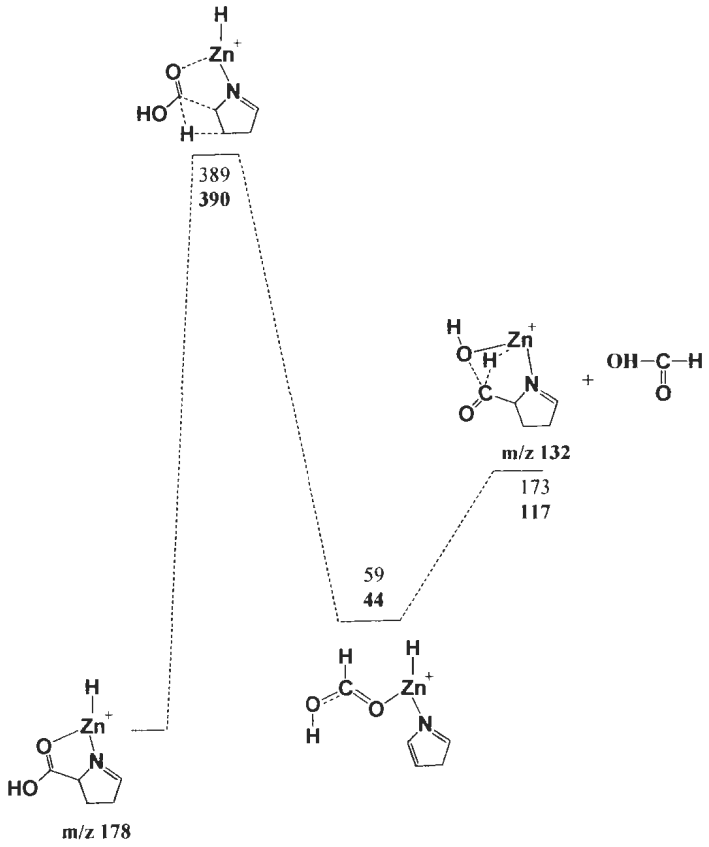

Figure 5.11. Energy profile in kJ mol^{-1} (unbolded values are enthalpies and bolded values are Gibbs energies) for the loss of formic acid from $[Zn(Pro-H)]^+$ complex, Pro-Hi. Thermochemistries were computed using MP2(full)/6-311++G(2d,2p)//B3LYP/6-31+G(d,p).

The energy profile for loss of CO from Pro-Hi is shown in Figure 5.12. The first step is a tautomerization from Zn to C5 forming Pro-A with an energy requirement of 250 kJ mol^{-1}. From Pro-A, there are two pathways displayed to loss of CO. The lowest energy route is a rotation about the carboxyl C-C(2) bond followed by OH transfer to Zn and then a facile CO loss. This lowest energy path for CO loss, like those for loss of H_2O and loss of HCOOH, has a considerably higher energy requirement than for loss of Zn.

Finally, the energy profile for loss of CO_2 from Pro-Hi is displayed in Figure 5.13. The first step is rotation about the carboxyl C-C(2) bond with a minimal energy requirement. This is followed by what is effectively a rotation about the C-O bond and a replacement of ZnH with H at the nitrogen. The largest energy requirement for loss of CO_2 is a replacement of CO_2 with Zn-H at C2. This 219 kJ mol^{-1} of Gibbs energy required for CO_2 loss is only about 6 kJ mol^{-1} higher than that required for loss of Zn, however, it is still consistent with the latter being the most abundant product.

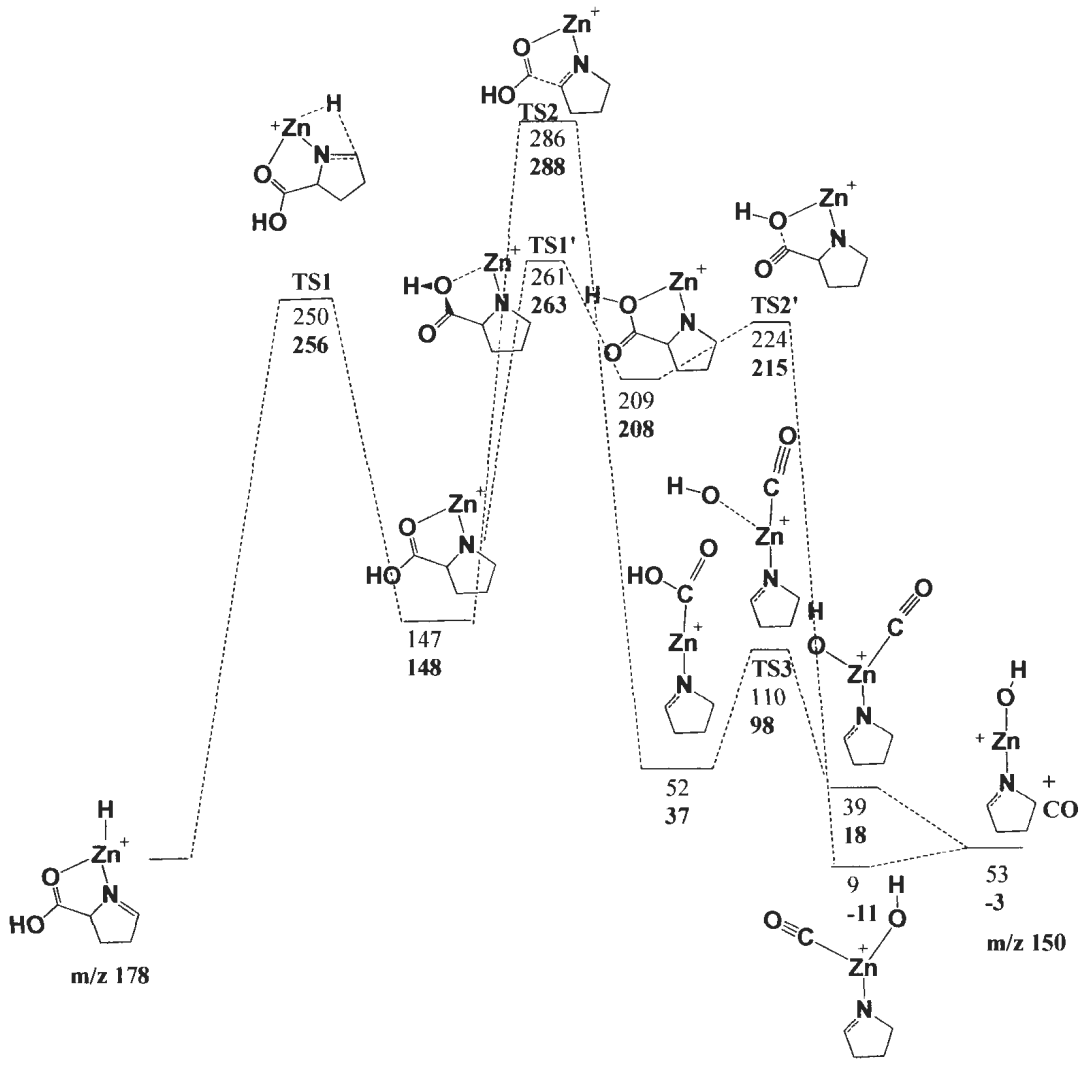

Figure 5.12. Energy profile in kJ mol^{-1} (unbolded values are enthalpies and bolded values are Gibbs energies) for the loss of carbon monoxide from Pro-Hi through the Pro-A. Thermochemistries were computed using MP2(full)/6-311++G(2d,2p)//B3LYP/6-31+G(d,p).

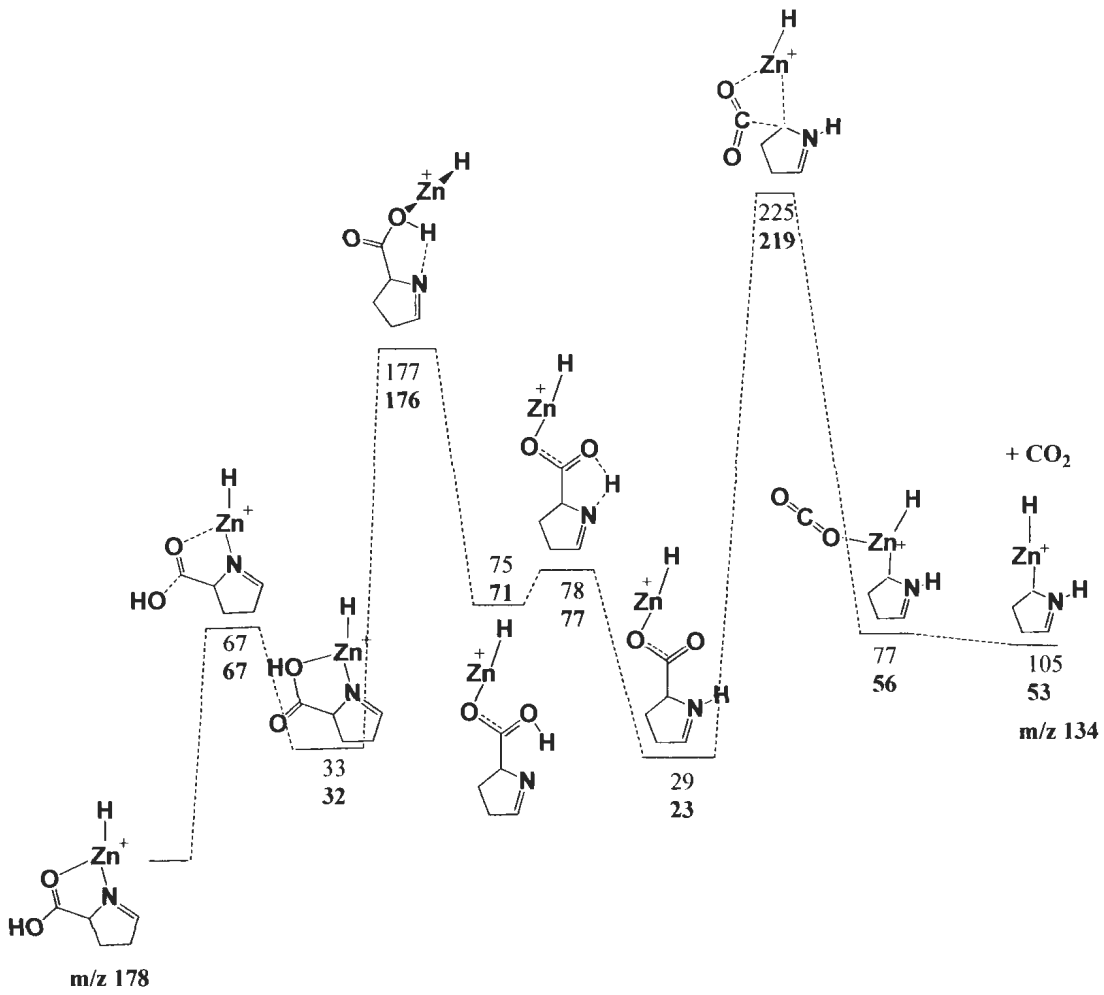

Figure 5.13.Energy profile in kJ mol^{-1} (unbolded values are enthalpies and bolded values are Gibbs energies) for the loss of carbon dioxide from Pro-Hi. Thermochemistries were computed using MP2(full)/6-311++G(2d,2p)//B3LYP/6-31+G(d,p).

5.4. Conclusion

CID and IRMPD spectroscopy in the 3200-3800 cm^{-1} range in combination with computational chemistry helped to elucidate the structures of $[Zn(Pro-H)]^+$ and $[Zn(Pro-H)(H_2O)]^+$ complexes in the gas phase. By comparing the IRMPD spectrum with the predicted IR-spectra of the lowest energy structures, it was confirmed that $[Zn(Pro-H)]^+$ complex is deprotonated at the amine moiety, and a hydrogen from either C2 or C5

migrated to Zn^{2+}. In this H-type complex, Zn^{2+} was chelated between the amine nitrogen and the carbonyl oxygen. For the singly-hydrated complex, $[Zn(Pro\text{-}H)(H_2O)]^+$, IRMPD spectroscopy confirms the structure with water added to the H type structure and intramolecularly hydrogen bonded to the deprotonated amine site.

The main fragmentation product by CID and OPO laser-IRMPD was loss of neutral zinc for $[Zn(Pro\text{-}H)]^+$ and successive loss of H_2O and neutral Zn for $[Zn(Pro\text{-}H)(H_2O)]^+$. The potential energy surface revealed that the loss of neutral zinc is energetically more favourable than the loss of dehydrogenated proline leading to ZnH^+ product. Computed energy profiles for all five primary decomposition routes, all beginning with the lowest energy structure, revealed that loss of Zn has the lowest energy requirement, consistent with it being the most abundant product of unimolecular dissociation following collisional or IR multiphoton activation.

It is interesting to contemplate on how the observed H-type structure (Pro-Hi) is formed since it has been pointed out that these types of species are unlikely to exist in solution.[27,28] The computed energies of the hydrated species also suggests that even if the deprotonated species exist, it is the A-type structure that may be most likely in solution since single solvation, greatly lowers the energy of the A-, B-, and C-type structures with respect to the H-type (Figure 2). Ragalewicz *et al.*[28] showed that isomerization to the lowest-energy gas-phase structure (H-type) from the B-type structure has a lower energy requirement than the final desolvation step, so these H-type complexes can be formed during electrospray. It was also speculated that they could be formed from the

deprotonated Zn^{2+} bound dimer of glycine.[30] We will address this possibility in a forthcoming article on the $[Zn(Pro\text{-}H)(Pro)]^+$ complex.

References

(1) Joerger, A. C.; Fersht, A. R. *Oncogene* 2007, *26*, 2226.

(2) Travaglia, A.; Pietropaolo, A.; La Mendola, D.; Nicoletti, V. G.; Rizzarelli, E. *J. Inorg. Biochem.* 2012, *111*, 130.

(3) Faller, P. *ChemBioChem* 2009, *10*, 2837.

(4) Berg, J. M.; Shi, Y. *Sci* 1996, *271*, 1081.

(5) Frankel, A. D.; Berg, J. M.; Pabo, C. O. *PNAS* 1987, *84*, 4841.

(6) Imanishi, M.; Matsumura, K.; Tsuji, S.; Nakaya, T.; Negi, S.; Futaki, S.; Sugiura, Y. *Biochem.* 2012, *51*, 3342.

(7) Cho, Y.; Gorina, S.; Jeffrey, P. D.; Pavletich, N. P. *Sci* 1994, *265*, 346.

(8) Stanga, S.; Lanni, C.; Govoni, S.; Uberti, D.; D'Orazi, G.; Racchi, M. 2010, *2*, 545.

(9) Cuajungco, M. P.; Lees, G. J. *Brain Res. Rev.* 1997, *23*, 219.

(10) Polfer, N. C.; Oomens, J.; Moore, D. T.; von Helden, G.; Meijer, G.; Dunbar, R. C. *J. Am. Chem. Soc* 2006, *128*, 517.

(11) Kamariotis, A.; Boyarkin, O. V.; Mercier, S. R.; Beck, R. D.; Bush, M. F.; Williams, E. R.; Rizzo, T. R. *J. Am. Chem. Soc* 2005, *128*, 905.

(12) Drayss, M. K.; Blunk, D.; Oomens, J.; Schäfer, M. *J. Phys. Chem. A* 2008, *112*, 11972.

(13) Lavanant, H.; Hecquet, E.; Hoppilliard, Y. *Int. J. Mass spectrom.* 1999, *185–187*, 11.

(14) Fridgen, T. D. *Mass Spectrom. Rev.* 2009, *28*, 586.

(15) Abirami, S.; Wong, C. C. L.; Tsang, C. W.; Ma, N. L. *Chem. Eur. J.* 2005, *11*, 5289.

(16) Dunbar, R. C.; Steill, J. D.; Polfer, N. C.; Berden, G.; Oomens, J. *Angew. Chem. Int. Ed.* 2012, *51*, 4591.

(17) Dunbar, R. C.; Steill, J. D.; Polfer, N. C.; Oomens, J. *J. Phys. Chem. A* 2009, *113*, 845.

(18) Polfer , N. C.; Oomens, J.; Dunbar, R. C. *ChemPhysChem* 2008, *9*, 579.

(19) Dunbar, R. C.; Polfer, N. C.; Oomens, J. *J. Am. Chem. Soc* 2007, *129*, 14562.

(20) Dunbar, R. C.; Steill, J. D.; Polfer, N. C.; Oomens, J. *J. Phys. Chem. B* 2009, *113*, 10552.

(21) Dunbar, R. C.; Steill, J. D.; Polfer, N. C.; Oomens, J. *J. Phys. Chem. A* 2012, 1094.

(22) Burt, M. B.; Decker, S. G. A.; Atkins, C. G.; Rowsell, M.; Peremans, A.; Fridgen, T. D. *J. Phys. Chem. B* 2011, *115*, 11506.

(23) Burt, M.; Fridgen, T. *Eur. J. Mass Spectrom.* 2012, *18*, 235.

(24) Mino Jr, W. K.; Szczepanski, J.; Pearson, W. L.; Powell, D. H.; Dunbar, R. C.; Eyler, J. R.; Polfer, N. C. *Int. J. Mass spectrom.* 2010, *297*, 131.

(25) Atkins, C. G.; Banu, L.; Rowsell, M.; Blagojevic, V.; Bohme, D. K.; Fridgen, T. D. *J. Phys. Chem. B* 2009, *113*, 14457.

(26) Hofstetter, T. E.; Howder, C.; Berden, G.; Oomens, J.; Armentrout, P. B. *J. Phys. Chem. B* 2011, *115*, 12648.

(27) Rogalewicz, F.; Hoppilliard, Y.; Ohanessian, G. *Int. J. Mass spectrom.* 2000, *201*, 307.

(28) Rogalewicz, F.; Hoppilliard, Y.; Ohanessian, G. *Int. J. Mass spectrom.* 2001, *206*, 45.

(29) Rogalewicz, F.; Hoppilliard, Y.; Ohanessian, G. *Int. J. Mass spectrom.* 2003, *227*, 439.

(30) Hoppilliard, Y.; Rogalewicz, F.; Ohanessian, G. *Int. J. Mass spectrom.* 2001, *204*, 267.

(31) Rajabi, K.; Easterling, M. L.; Fridgen, T. D. *J. Am. Soc. Mass. Spectrom.* 2009, *20*, 411.

(32) Frisch et al, M. J. *Gaussian 09, Revision A.01; Gaussian, Inc.: Wallingford, CT,* 2009.

(33) Shoeib, T.; Hopkinson, A. C.; Siu, K. W. M. *J. Phys. Chem. B* 2001, *105*, 12399.

(34) Kretschmer, R.; Schlangen, M.; Kaupp, M.; Schwarz, H. *Organometallics* 2012, *31*, 3816.

(35) Hollemann, A. F.; Wiberg, E. *Lehrbuch der Anorganischen Chemie*; 101st ed.; Walter deGruyter: Berlin, New York,, 1995.

(36) Suzer, S.; Banna, M. S.; Shirley, D. A. *J. Chem. Phys.* 1975, *63*, 3473.

(37) Banu, L.; Blagojevic, V.; Bohme, D. K. *Int. J. Mass spectrom.* 2012, *330–332*, 168.

Chapter 6. Structures and Fragmentations of $[Zn(Proline-H)(Proline)]^+$ in the gas phase: H_2 Elimination of $[Zn(A-H)(A)]^+$ Complexes When A is a Secondary Amine

6.1. Introduction

Interactions between metal ions and amino acids or peptides play important roles in biological systems. Gas phase studies can provide an opportunity to understand the intrinsic binding properties and structures of metal-amino acid and peptide complexes without the added complexity of solvent as is the case for the condensed phase.[1] Knowledge about binding sites between metal ions and amino acids can be the primary step to understand the mechanism of biological processes.[2-4] Zinc can induce conformational changes in proteins, playing a role in promoting age-related diseases such as Alzheimer and Parkinson[5-12]. For example, it is possible for zinc to bind to Amyloid precursor proteins to induce conformational changes to produce Amyloid beta, which yields unfavourable aggregation of proteins in vitro which in turn causes the neurodegeneration processes in Alzheimer disease.[9,10,13] Understanding the interactions between metal cations and amino acids involved in Amyloid protein structure can be helpful for the development of new therapies for Alzheimer disease.

Even though zinc has significant biological importance, there are limited studies on zinc-bound amino acids or peptides. In the gas phase, Zn^{2+} has been shown to form deprotonated dimer complexes with histidine, phenylalanine and glycine, $[Zn(AA-H)]^+$, which is consistent with ability of zinc(II) to deprotonate a water molecule when bound to a protein.[14-17] In these experiments, $ZnCl_2$ and amino acids were electrosprayed from a methanol/water mixture to produce $[Zn(A-H)(A)]^+$ as the most abundant ion in the gas phase.[16] Ohanssien and coworkers have done a series of studies to explore the mechanism

for fragmentation of $[Zn(Gly-H)]^+$ by CID experiments.[16,18,19] The fragmentation pathways of $[Zn(Gly-H)]^+$ were loss of carbon dioxide, loss of carbon monoxide, and successive losses of water and carbon monoxide. These fragmentation results were interpreted by calculating the energy required for rearrangement of the structures leading to the observed fragments.[18,19]

IRMPD spectroscopy was also employed in conjunction with electronic structure calculations to study gas phase structure of $[Zn(Phe-H)(Phe)]^+$ (Phen = phenylalanine).[14] Two fragmentation products loss of water and loss of phenylalanine were observed upon IRMPD. The experimental IRMPD spectrum agreed well with the computed IR spectrum of the lowest energy structure predicted by calculations. In the lowest-energy structure the carboxylic acid is deprotonated, and zinc has tetrahedral coordination, bound to the amine N and a carbonyl O of both the deprotonated and the intact phenylalanine.

The focus of the present work was to study the structures and fragmentation mechanisms of $[Zn(Pro-H)(Pro)]^+$. Proline is a five membered cyclic α-amino acid with unusual protein structural conformation and properties.[20] Different from other amino acids, proline cannot be found in a regular α-helix or ß-sheet secondary structure because proline is a secondary amine, so there is no hydrogen bound to nitrogen in the amide bonds.[20-22] As a result, a helix structure is bent in the vicinity of proline and produces kinks in the protein structure due to lack of a hydrogen bond. Cyclic nature of proline also limits motion and flexibility of proline residue in protein secondary structures.

Shoeib *et al.* investigated the fragmentation reactions of Ag^+-proline complex by means of CID experiments.[23] The fragmentation products, elimination of AgH and a

neutral H_2 molecule, were observed as the most abundant products. They proposed a mechanism for these fragmentation reactions which involves the migration of a proton from α-CH_2 group toward silver.[23]

In this work, the activation/fragmentation techniques such as SORI/CID and IRMPD, have been combined with deuterium labeling experiments, and computational techniques have been employed to study the unimolecular chemistry and structures of $[Zn(Pro-H)(Pro)]^+$. Similar complexes with other amino acids such as glycine (Gly), alanine (Ala), and sarcosine (Sar), are compared with the proline results to better understand the structures and decomposition pathways of $[Zn(Pro-H)(Pro)]^+$.

6.2. Methods

6.2.1. Experimental

$[Zn(A-H)(A)]^+$ ions were electrosprayed from solution containing 0.1 mM $ZnCl_2$ and 0.1 mM amino acid in a 90/10 mixture of methanol/water using an Apollo II ion source of a Bruker Apex Qe 7 T FTICR MS. $[Zn(A-H)(A)]^+$ ions were allowed to accumulate in hexapole collision cell for almost 2s before being transferred to the ICR cell.

IRMPD activation using a continuous 25 W CO_2 laser was used as the activation/fragmentation technique to identify fragmentation pathways of the ions trapped inside the ICR cell. The ions isolated in the ICR cell were irradiated with a CO_2 laser to

induce dissociation. The CO_2 laser power and IR pulse length were between 20-50% of maximum power (25 W), and 0.1-2 sec, respectively. SORI/CID was also used to energize the complex ions. The isolated ions were fragmented by energetic collisions, 1.8-8.1 eV lab frame (E_{cm}:0.2-0.95 eV), with a pulse of argon to a pressure of 10^{-8} mbar in the ICR cell of the mass spectrometer. For IRMPD experiments, ions were isolated in the ICR cell and irradiated with a KTP OPO laser coupled to the FT-ICR for 7 sec over the range of 3200-3800 cm^{-1} at intervals of 1.5 cm^{-1}. The IRMPD spectrum was obtained by plotting the negative of the natural logarithm of normalized precursor ion intensity as a function of OPO radiation frequency.

6.2.2. Computational

Calculations were performed using the Gaussian 09 software package.[24] Many possible structures with different deprotonation sites, zinc coordination with proline, and conformers were optimized, and frequency calculations for each optimized structure were done using B3LYP density functional theory with the 6-31+G(d,p) basis function. The vibrational frequencies were scaled by factor of 0.955 to compare with the experimental IRMPD spectra. Single point energy calculations were also performed at the MP2 level of theory using the 6-311++G(2d,2p) basis set called MP2(full)/6-311++G(2d,2p)//B3LYP/6-31+G(d,p). The relative enthalpies and Gibbs energies reported are a combination of the MP2 electronic energies and the 298K thermochemistry from the B3LYP calculations.

6.3. Results and Discussion

6.3.1. CO_2 laser-IRMPD Fragmentation of $[Zn(Pro-H)(Pro)]^+$

6.3.1.1. Non-labeled $[Zn(Pro-H)(Pro)]^+$

Interestingly, all methods of excitation leading to fragmentation of $[Zn(Pro-H)(Pro)]^+$ in the ICR cell resulted in primarily loss of H_2. The IRMPD mass spectrum of $[Zn(Pro-H)(Pro)]^+$ is presented in Figure 6.1. The main fragmentation products for $[Zn(Pro-H)(Pro)]^+$ are observed at m/z 291, m/z 289, m/z 180, m/z 178, and m/z 116 corresponding to elimination of H_2, $2H_2$, Pro-H_2, Pro, and Zn+Pro-H_2, respectively. Minor fragmentation products are observed at m/z 275, m/z 273, m/z 247, m/z 245, and m/z 229 corresponding to losses equal to the mass of H_2O, H_2/H_2O, H_2/CO_2, $2H_2/CO_2$, $H_2/H_2O/CO_2$, respectively. The fragment ion at m/z 229 corresponding to the elimination of m/z 64 from m/z 293, is not the loss of neutral zinc since IRMPD of $[^{66}Zn(Pro-H)(Pro)]^+$, m/z 295, also resulted in the loss of 64 mass units to form m/z 231. The ion m/z 229 is most likely from a loss of H_2 followed by elimination of H_2O and CO_2. Isolation of m/z 291 formed by IRMPD of m/z 293 and subsequent IRMPD activation of the ion m/z 291 (see Figure 6.1b) resulted in a spectrum absent of m/z 116, m/z 180, and m/z 275, m/z 247 fragment ions corresponding to the losses of Zn+Pro-H_2, Pro-H_2, and H_2O (Figure 6.1b) indicating that these ions are born from m/z 293. The presence of m/z 229 in the IRMPD is confirmation that it is due to loss of H_2 followed by CO_2 and H_2O loss from m/z 293.

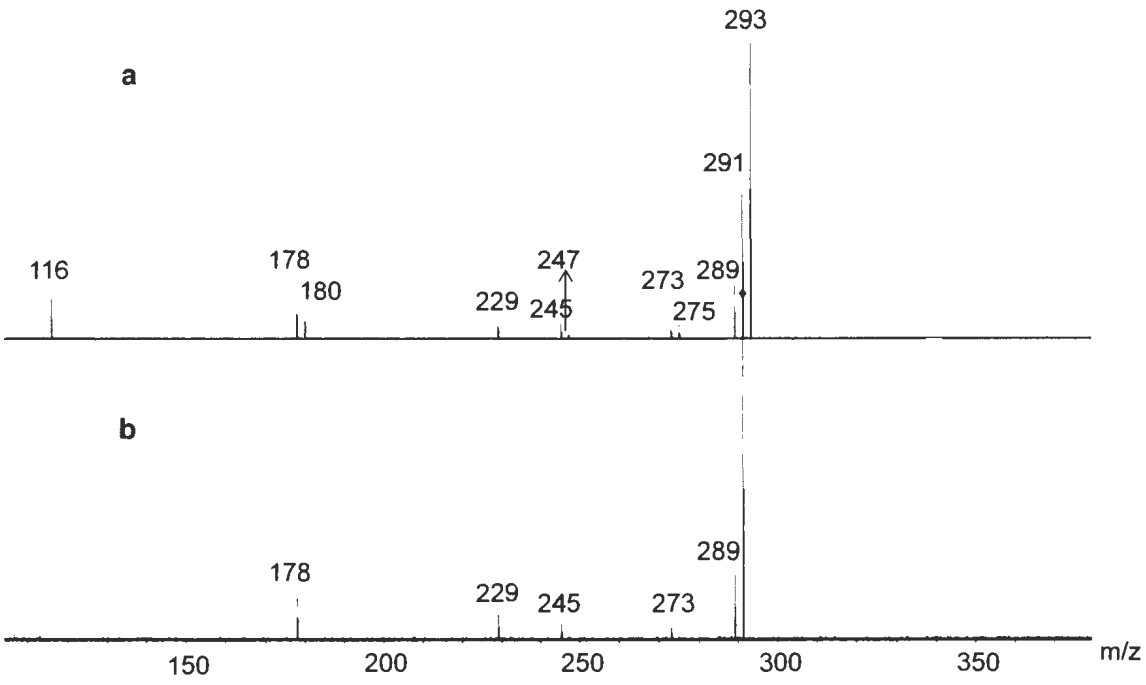

Figure 6.1. Mass spectra of CO_2 laser-IRMPD with the laser power 40 % of maximum power and 1 sec pulse length for a) $[Zn(Pro-H)(Pro)]^+$ (m/z 293) followed by isolation and b) m/z 291 formed by IRMPD of m/z 293 followed by isolation.

The mass spectra of IRMPD and SORI-CID of $[Zn(Pro-H)(Pro)]^+$ is compared in Figure 6.2. As seen in Figure 6.2b, SORI-CID of m/z 293 resulted in a spectrum absent of m/z 289, m/z 273, m/z 247, and m/z 229 corresponding to elimination of $2H_2$, H_2/H_2O, H_2/CO_2, $2H_2/CO_2$ and $H_2/H_2O/CO_2$. This can be explained by difference performance of SORI-CID and IRMPD for the excitation of ions in the ICR cell. In IRMPD, isolated ion and fragment ions born from the isolated ion all can absorb infrared photons, and consequently be excited, but in SORI-CID, the collisional energy is deposited only into the isolated ion. As a result, the secondary fragment ions born from the primary fragment ions, called grand-daughter ions (i.e. m/z 289 born from m/z 291), are absent in SORI-

CID spectrum. Appendix 2 shows that isolation of m/z 291 formed by SORI-CID of m/z 293, and subsequent SORI-CID of m/z 291 resulted in elimination of $2H_2$, H_2/H_2O, H_2/CO_2 and $H_2/H_2O/CO_2$ which is once again a confirmation that these ions are born from m/z 291.

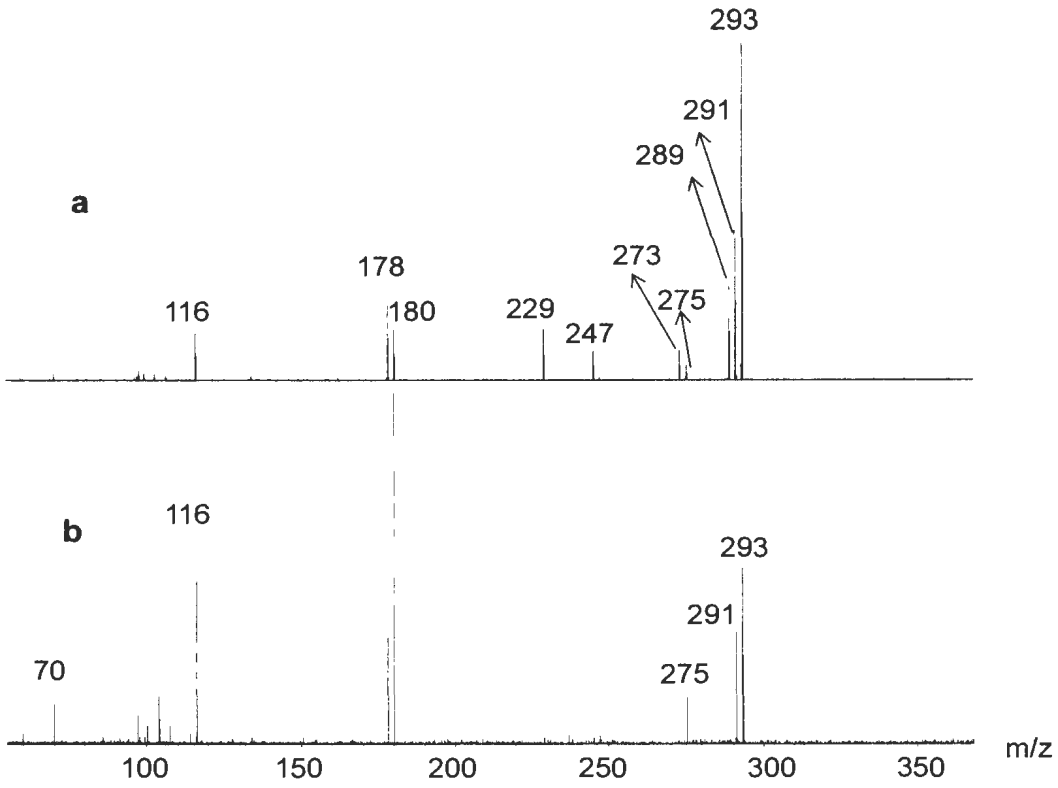

Figure 6.2. Mass spectra obtained by activation/fragmentation of $[Zn(Pro-H)(Pro)]^+$ (m/z 293) using a) IRMPD with the laser power 40 % of maximum power and 1 sec pulse length and b) SORI/CID with 0.21 ev (c.o.m).

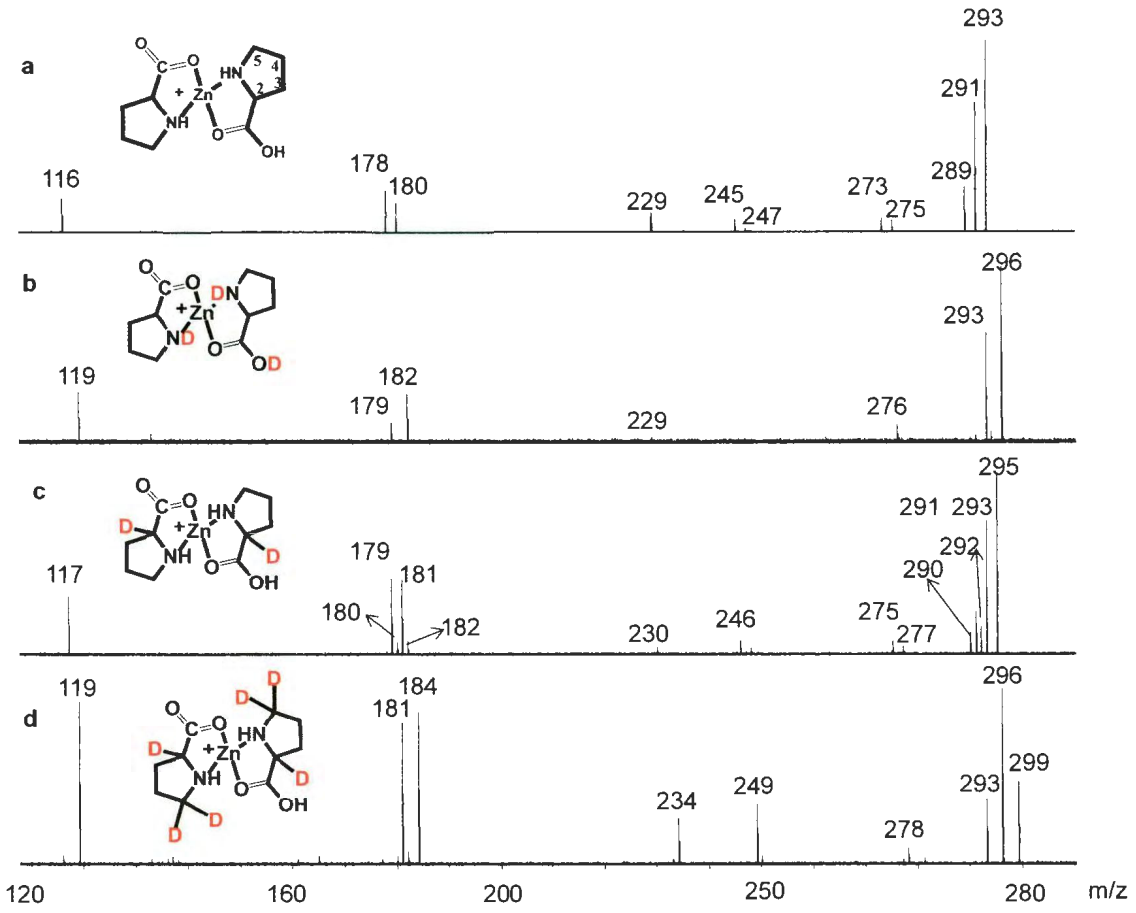

Figure 6.3. (CO_2 laser-IRMPD) activation/fragmentation of $[Zn(Pro\text{-}H)(Pro)]^+$ and its deuterated compounds using the laser power 40 % of maximum power and 1 sec pulse length for a, b. and c, and 1.5 sec pulse length for d.

6.3.1.2. $[Zn(Pro\text{-}H)(Pro)]^+$ Deuterated with D_2O in the Gas phase

Deuterium labeling experiments were performed by exchanging all the exchangeable hydrogens of proline by reacting $[Zn(Pro\text{-}H)(Pro)]^+$ with D_2O vapour in the

hexapole accumulation cell which is external to the ICR. D_2O was added to the collision cell through the vapour inlet by opening a micro-valve to exchange all labile hydrogens in $[Zn(Pro-H)(Pro)]^+$ complex.[25] A total of three hydrogens were found to exchange to produce m/z 296, leading to the conclusion that there are 3 labile hydrogens (i.e. a total of three amine or hydroxyl H's in $[Zn(Pro-H)(Pro)]^+$).

The IRMPD activation/fragmentation experiments were repeated for deuterated $[Zn(Pro-H)(Pro)]^+$ (m/z 296) as seen in Figure 6.3b. Isolation and IRMPD activation of m/z 296, resulted in loss of HD producing m/z 293. This result shows that the loss of H_2 contains one of the labile hydrogens (N-H or O-H group) since no D_2 loss was observed. The m/z 296 ion also loses 20 Da to form m/z 276 showing that the loss of H_2O contains two labile hydrogens. Furthermore m/z 296 loses 67 Da to form m/z 229 which is loss of $H_2/H_2O/CO_2$ that includes three labile hydrogens, one for loss of HD and two for loss of D_2O.

Loss of 114 Da from m/z 296 forms m/z 182, which was m/z 180 in the non-labeled proline experiments identified as loss of dehydrogenated proline and in the deuteration experiments means that the fragment ion retains two labeled hydrogens and that loss of Pro-H_2 includes only one labeled hydrogen. This suggests that the deprotonated proline moiety, which has only one labile hydrogen (either an OH or an NH group), transfers a non-labile hydrogen to the intact proline and is lost. However, a second possibility is that H_2 is formed from the intact proline but instead of leaving the ion-molecule complex, m/z 182 is produced by loss of the remaining part of the intact proline. MS/MS experiments show that m/z 293 formed by loss of HD from m/z 296 also

loses 114 Da to form m/z 179, which is consistent with loss of HD from the intact proline and successive loss of remaining part of the intact proline

The fragment ion at m/z 119 was also observed, m/z 116 in the non-deuterated experiments, which is consistent with this product ion being protonated proline formed by transfer of the labile proton from the deprotonated proline moiety to the intact proline side and loss of neutral (ZnPro-H_2).

6.3.1.3. $[Zn(Pro-H)(Pro)]^+$ with 2-d Labeled Proline

The IRMPD experiments were repeated with $[Zn(2\text{-d-Pro-H})(2\text{-d-Pro})]^+$, m/z 295, which was isotopically labeled with deuterium at C2 (see the structure in Figure 6.3c). The results of the IRMPD activation experiments are shown in Figure 6.3c. The parent ion at m/z 295 loses H_2 and $2H_2$, to form m/z 293 and 291, respectively. Fragment ions at m/z 292 and 290, corresponding to the losses of HD and HD/H_2 (or H_2/HD), were also observed, but were significantly less abundant than those formed by loss of H_2 and $2H_2$.

In this experiment the fragment ions corresponding to the loss of Pro-H_2 and the loss of H_2/Pro-H_2 are at m/z 181 and 179. That Pro-H_2 has a mass of 114 Da means that one label remains with the ion and one is lost. The ion at m/z 117 corresponds to the protonated proline with one label and is consistent with losing Zn plus Pro-H_2 after transferring the labile proton (non-labeled) from the Pro-H moiety to intact proline as discussed above. The fragment ions corresponding to the loss of H_2O and H_2/H_2O, indicating that all the hydrogens involved in these losses are non-labeled. Furthermore,

the ions at m/z 246 and m/z 230 corresponding to the loss of $2H_2/CO_2$ and $H_2/H_2O/CO_2$ are also presented that include one labeled hydrogen each for loss of HD.

6.3.1.4. $[Zn(Pro-H)(Pro)]^+$ with 2,5,5-d3 Labled Proline

The complex ion formed from 2,5,5-d3 proline, where C2 and C5 of both prolines in $[Zn(Pro-H)(Pro)]^+$ are deuterated (see Figure 6.3d) formed an ion at m/z 299 consistent with three deuterium labels for each proline. The results of IRMPD activation are shown in Figure 6.3d and clearly shows that the most abundant primary fragmentation route is loss of HD to produce m/z 296 which loses a second HD to produce m/z 293, and that the losses of HD are exclusive in that there is no loss of H_2. This result clearly shows that H_2 loss from the deprotonated Zn^{2+} bound proline dimer certainly includes one of C5 hydrogens as does the second loss of H_2. The fragment ion at m/z 184 includes four labels and is consistent with the proposal that H_2 from the intact proline is formed, one non-labeled hydrogen (either from N, O, C3, or C4) and labeled hydrogen from C5, and then the remaining part of intact proline is lost. It is also consistent with the second possibility with loss of Pro-H_2 after transfer of one labeled hydrogen from C5 of Pro-H moiety to intact side. Once again, m/z 181 comes from loss of HD from the intact proline followed by loss of the dehydrogenated proline.

The ion corresponding to protonated proline is at m/z 119 consistent with a transfer of the remaining labile H^+ from the deprotonated proline moiety to intact and triply labeled proline. The ion corresponding to the loss of H_2/H_2O is at m/z 278 which includes only one label confirming again that hydrogens involved in H_2O loss are non-

labeled since H_2 loss includes one labeled hydrogen. The fragment ions at m/z 249 and m/z 234 correspond to the losses of $H_2/H_2/CO_2$ and $H_2/H_2O/CO_2$ with two and one labeled hydrogens, respectively, that include one labeled hydrogen for each HD loss.

6.3.2. Computed Structures of $[Zn(Pro-H)(Pro)]^+$

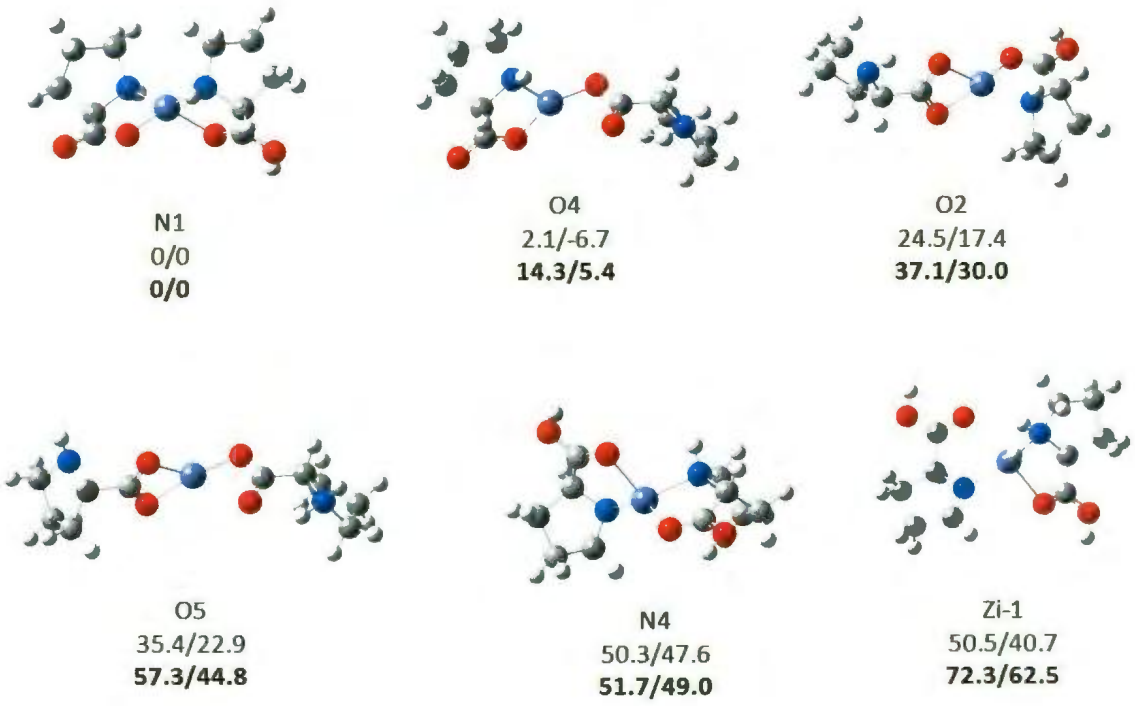

Figure 6.4. Computed structures of the $[Zn(Pro-H)(Pro)]^+$ complex. 298 K enthalpies/Gibbs energy (kJ mol^{-1}) seen are computed using B3LYP/6-31+G(d,p) and MP2(full)/6-311++G(2d,2p)//B3LYP/6-31+G(d,p) (bold).

A subset of twenty computed structures for $[Zn(Pro-H)(Pro)]^+$ as well as their relative enthalpies and 298K Gibbs energies computed using MP2 and B3LYP methods are shown in Figure 6.4. All twenty structures and their relative energies are presented in

Appendix 3. In all the structures, deprotonated proline is seen on the left side and intact proline on the right side of each structure. Many possible isomers for $[Zn(Pro-H)(Pro)]^+$ were computed. First, we tried to compute a number of structures which a proline is added upon the most stable structure computed for $[Zn(Pro-H)]^+$ (H-type structure). In our previous work, the lowest energy structure of $[Zn(Pro-H)]^+$ was determined to be the one with hydrogen transferred from α-CH_2 group to zinc, where Zn^{2+} is bound to the deprotonated amine N and the carbonyl O. Zi-1, where Zn^{2+} is bound to amine N and carbonyl O of intact side, was determined to be the most stable structure among complexes with a ZnH group, but 72.4 kJ mol^{-1} in Gibbs energy (at the MP2 level of theory) higher than the lowest energy structure found (N1). In contrast to the bare monomer complex which was found to be amine-deprotonated, the lowest energy structure of $[Zn(Pro-H)(Pro)]^+$ was determined to be carboxylic acid-deprotonated with Zn^{2+} bound to the amine N and carbonyl O in both sides. In the O4 structure, Zn^{2+} is bound to the amine N and carbonyl O of deprotonated proline and to both oxygens of intact proline, is only 5.5 kJ mol^{-1} higher in Gibbs energy than the lowest energy structure. The intact proline in this structure is zwitterionic with a strong NH—O intramolecular hydrogen bond. The O4 structure is similar to the lowest energy structure in deprotonated proline side. Comparison of these two lowest energy structures reveals that there is only a small preference, 5.4 kJ mol^{-1} in Gibbs energy, for Zn^{2+} coordinated to amine N and carbonyl O versus the carboxylate oxygens of zwitterionic proline. The other structures were computed to be at least 20 $kJmol^{-1}$ higher in energy than the lowest

energy structure (see Appendix 3). Structures including Zn^{2+} with three-coordination were computed to be considerably higher in energy.

6.3.3. Fragmentation Mechanism of $[Zn(Pro-H)(Pro)]^+$

Experiments confirmed that the main primary fragmentation pathway of $[Zn(Pro-H)(Pro)]^+$ is loss of H_2 that includes one hydrogen from the C5 carbon and one from the amine or carboxylic acid group. The potential energy surface for H_2 loss involving an H from NH and OH were calculated and compared. As seen in Figure 6.4, the fragmentation pathway for loss of H_2 involving the amine H has a significantly lower energy requirement (more than 50 kJ mol^{-1}) than the pathway involving H from the carboxylic acid group. It shows that the loss of H_2 involving an H from C5 and from the amine is the preferred fragmentation channel.

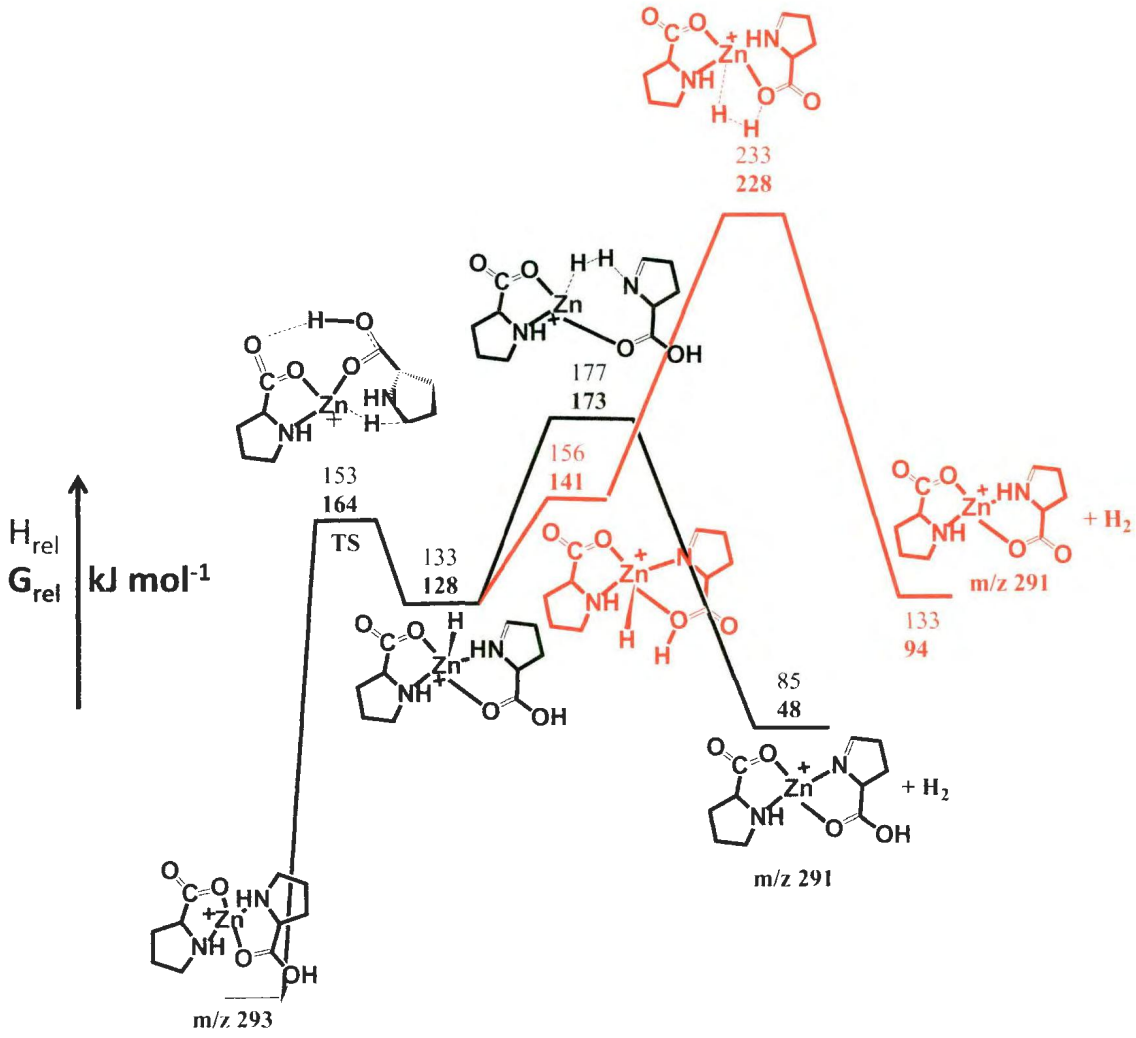

Figure 6.5. Energy diagram in kJ mol^{-1} for H_2 loss from $[Zn(Pro\text{-}H)(Pro)]^+$ complex where one H comes from either N (black) or O (red) using MP2(full)/6-311++G(2d,2p)//B3LYP/6-31+G(d,p) (unbold values are enthalpies and bold values are Gibbs energies).

IRMPD spectroscopy of $[Zn(Pro-H)(Pro)-H_2]^+$ (m/z 291) also helped to confirm the H loss from amine moiety. The IRMPD spectrum of the ion m/z 293 and m/z 291 both contain a single carboxylic acid OH stretch band. Considering the computed lowest energy structure of $[Zn(Pro-H)(Pro)]^+$ having only one carboxylic acid group in the structure, the presence of a COO-H stretch in the IRMPD spectrum for the m/z 291 confirms that carboxylic acid OH has remained intact after H_2 loss (see Figure 6.6). In addition, the carboxylic acid OH band observed in IRMPD spectrum of $[Zn(Pro-H)(Pro)-H_2]^+$ shows a significant red shift compared to the band observed in the IRMPD spectrum of $[Zn(Pro-H)(Pro)]^+$. In figure 6.6 the B3LYP/6-31+G(d,p) computed IR spectrum of the lowest energy structure of $[Zn(Pro-H)(Pro)]^+$ is compared with the computed IR spectra of $[Zn(Pro-H)(Pro)-H_2]^+$, in which H_2 is lost involving a hydrogen from the deprotonated or the intact proline. Comparing the computed IR spectra shows that the OH stretch band is predicted to red-shift to lower wavenumber position if H_2 is lost from the intact proline, but no shift would be expected for the structure where H_2 lost from the deprotonated side. All these results discussed above consistently confirm that H_2 loss observed in activation/fragmentation of $[Zn(Pro-H)(Pro)]^+$ complex comes from the intact proline where one of hydrogens is from NH and the other one is from C5.

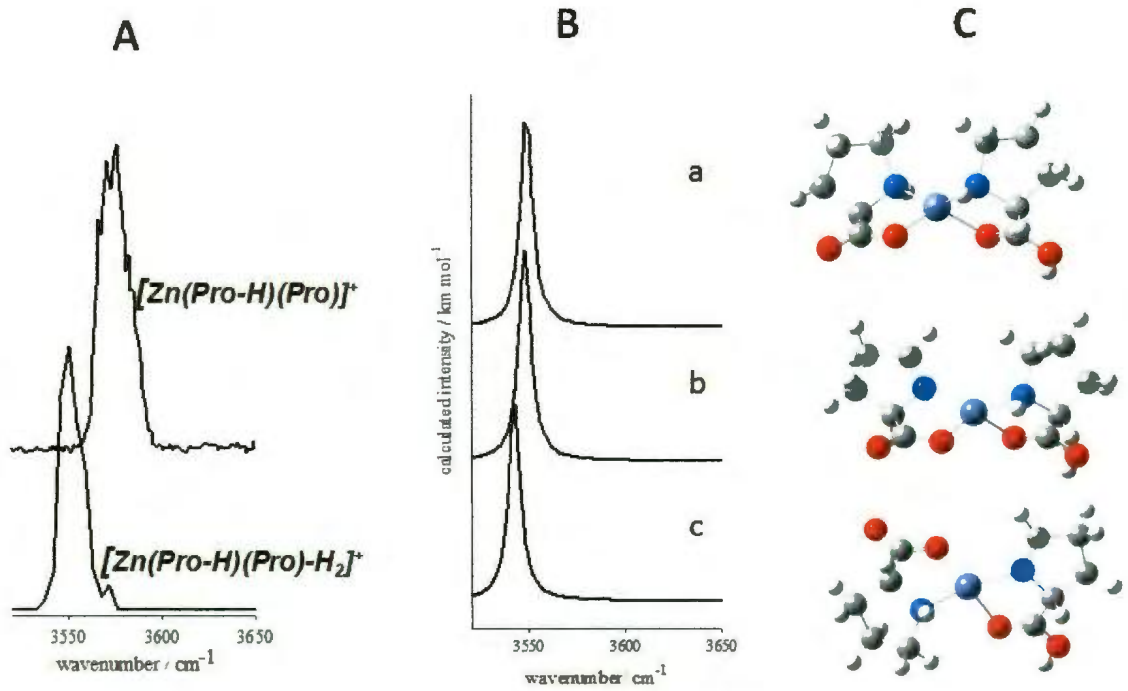

Figure 6.6. A) IRMPD spectra of $[Zn(Pro\text{-}H)(Pro)]^+$ complex and the ion produced from the loss of H_2, $[Zn(Pro\text{-}H)(Pro)\text{-}H_2]^+$ in the 3500-3600 cm^{-1} region. B) The B3LYP/6-31+G(d,p) computed IR spectrum of the lowest energy structure of a) $[Zn(Pro\text{-}H)(Pro)]^+$ and b) $[Zn(Pro\text{-}H)(Pro)\text{-}H_2]^+$ with H_2 lost in deprotonated and c) intact proline sides. C) Representation of corresponding computed structures.

The suggested mechanism involves two transition states. (Figure 6.5), The first one involves hydrogen migration from C5 of the intact proline to Zn^{2+} to produce $[Zn(Pro\text{-}H)(H)\ (Pro\text{-}H)]^+$, and the second one is a concerted reductive elimination.

Scheme 6.1 shows the pathway suggested for the fragmentation of $[Zn(Pro\text{-}H)(Pro)]^+$ to m/z 180 and m/z 178, which are the two other main fragment ions. In order for the formation of m/z 180, the deprotonated proline moiety, transfers a hydrogen from

C5 to the intact proline and then is lost. The fragment ion at m/z 178 is formed from the loss of H_2 from the intact proline followed by loss of dehydrogenated proline.

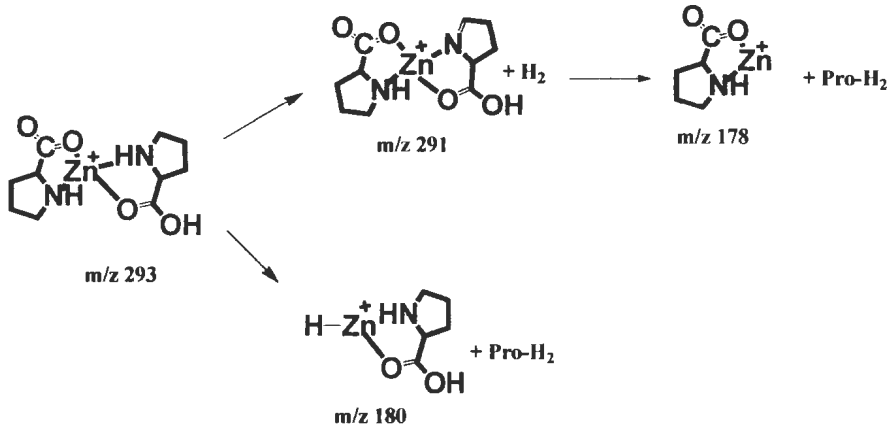

Scheme 6.1. The mechanism suggested for loss of H_2, Pro-H_2 and Pro from [Zn(Pro-H)(Pro)]$^+$.

The energy diagrams of fragmentation pathway suggested for Pro-H_2 is computed and compared with the H_2 loss pathway in Appendix 4. In the suggested mechanism for Pro-H_2 loss, hydrogen transfers from C5 of the deprotonated proline to Zn^{2+} to produce [Zn(Pro-H_2)(H)(Pro)]$^+$, and then Pro-H_2 is simply expelled from the complex. The energy required for loss of Pro-H_2 is calculated to be 179 kJ mol^{-1} in Gibbs energy and 225 kJ mol^{-1} in enthalpy which are 9 and 48 kJ mol^{-1} higher in enthalpy and Gibbs energy, respectively, than the highest barrier energy computed for H_2 loss. It can explain why H_2 loss channel is primary fragmentation in IRMPD activation (Figure 6.2). The notable difference between IRMPD and SORI-CID (Figure 6.2) spectra is the intensity of m/z 180 ion. IRMPD is a soft activation process so that the energy irradiated per photon is

approximately 10 kJ mol^{-1}, whereas 50 kJ mol^{-1} is deposited per collision in SORI-CID. Despite the higher energy requirement for the loss of Pro-H_2 compared to H_2 loss, the Pro-H_2 loss occurs with a greater rate constant due to its looser transition state.[26] In SORI-CID the sufficient energy required for both H_2 and Pro-H_2 losses is rapidly deposited into the ion, therefore, the loss of Pro-H_2 occurs more abundant than the loss of H_2 due to the greater rate constant of Pro-H_2 loss.

6.3.4. Fragmentation of $[Zn(Sar-H)(Sar)]^+$, $[Zn(Gly-H)(Gly)]^+$, and [Zn(Ala-H)(Ala)

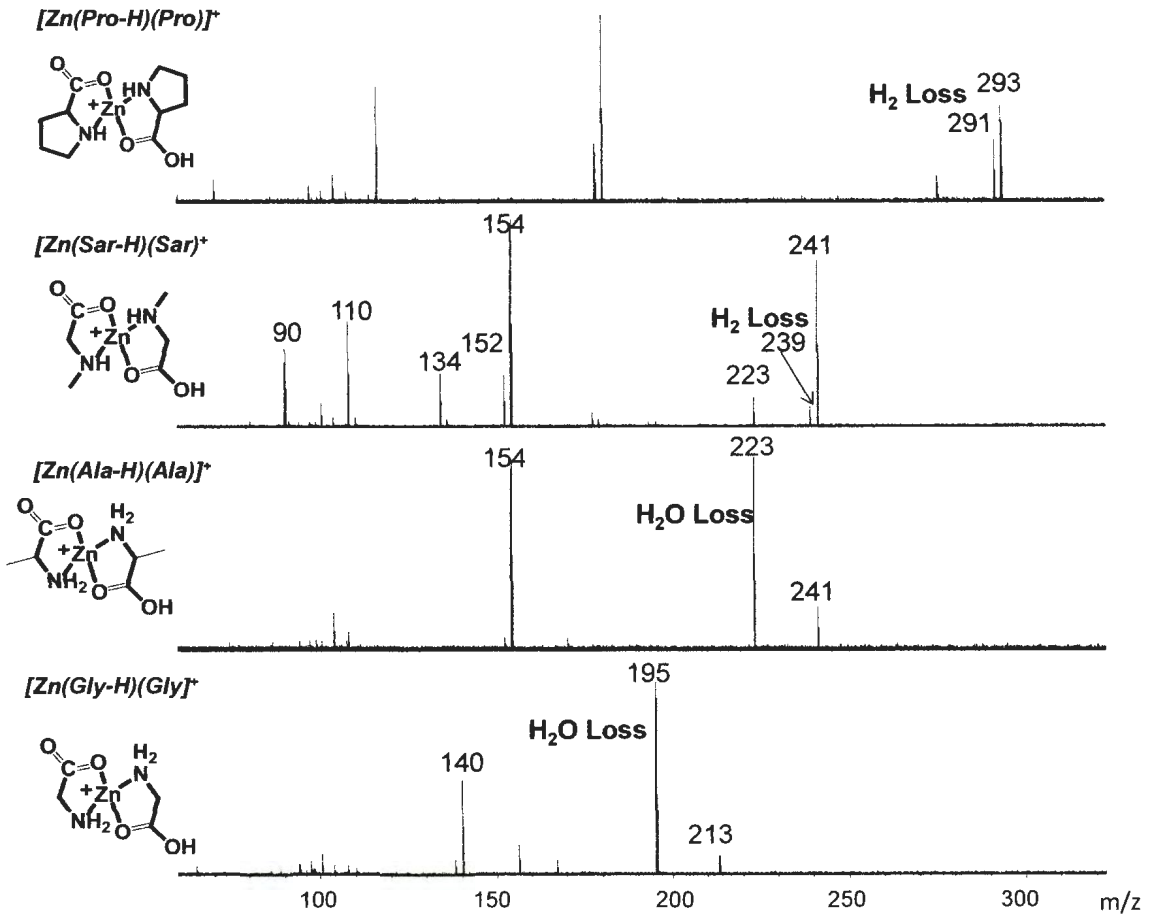

Figure 6.7. (SORI-CID) spectra of $[Zn(A-H)(A)]^+$ where A is Pro, Sar, Ala, and Gly at 0.21 eV, 0.81 eV, 0.67 eV, and 0.85 eV (c.o.m), respectively.

The SORI/CID mass spectrum of $[Zn(Sar-H)(Sar)]^+$ (m/z 241) is shown in Figure 6.7b. SORI/CID or IRMPD of m/z 241 following the isolation of m/z 241 resulted in similar fragmentation pattern to that observed for $[Zn(Pro-H)(Pro)]^+$. The main fragment ions observed were at m/z 239, 223, 154, and 152 corresponding to losses equal to the

masses of H_2, H_2O, Sar-H_2, and Sar, respectively. It should be noted that the loss of second H_2 is absent in activation/fragmentation of $[Zn(Sar-H)(Sar)]^+$,

The activation/fragmentation of $[Zn(A-H)(A)]^+$ complexes either by means of IRMPD or SORI-CID, when A is a primary amine such as glycine and alanine, resulted in losses of H_2O and A-H_2 as shown in Figure 6.7. No dehydrogenation product was observed even at higher CO_2 laser power (Appendix 5) or higher collision energies in SORI/CID experiments, in contrast to when A was a secondary amine, sarcosine or proline. The results show that the presence of a secondary amine in the complex $[Zn(A-H)(A)]^+$ is the reason for directing the reaction toward the H_2 elimination pathway.

The notable difference between IRMPD and CID spectra in both $[Zn(Gly-H)(Gly)]^+$ and $[Zn(Ala-H)(Ala)]^+$ is different intensities of fragment ions formed by losses of H_2O and A-H_2. In the IRMPD spectra m/z 154 for $[Zn(Ala-H)(Ala)]^+$ and m/z 140 for $[Zn(Gly-H)(Gly)]^+$ corresponding to the loss of Ala-H_2 and Gly-H_2, respectively, are the most abundant fragment ions (see Appendix 5), whereas m/z 223 and m/z 195 corresponding to the loss of H_2O from $[Zn(Ala-H)(Ala)]^+$ and $[Zn(Gly-H)(Gly)]^+$ are the major products by CID (see Figure 6.7) . MS/MS experiments show that isolation of m/z 195 formed by CID of m/z 213 and subsequent CID of m/z 195 resulted in elimination of 55 Da to produce m/z 140, indicating that m/z 140 can come from both m/z 213 and m/z 195. Therefore, the precursor ion at m/z 213 and the fragment ion at m/z 195 formed by loss of H_2O from m/z 213 simultaneously undergoes the fragmentation channels to form m/z 140 in IRMPD experiment, since all the ions present in the ICR cell can absorb infrared photons. In SORI-CID, the collisional energy is deposited only into the isolated

ion, m/z 213. This is why the intensity of m/z 195 is significantly lower in IRMPD spectrum than that in CID spectrum. There is also same reason for having the most abundant fragment ion at m/z 154 in the IRMPD activation of $[Zn(Ala-H)(Ala)]^+$. The fragment ion at m/z 223 is smaller than m/z 154 in IRMPD spectrum, because m/z 223 dissociates to form m/z 154, simultaneously with the dissociation of m/z 241 to m/z 223.

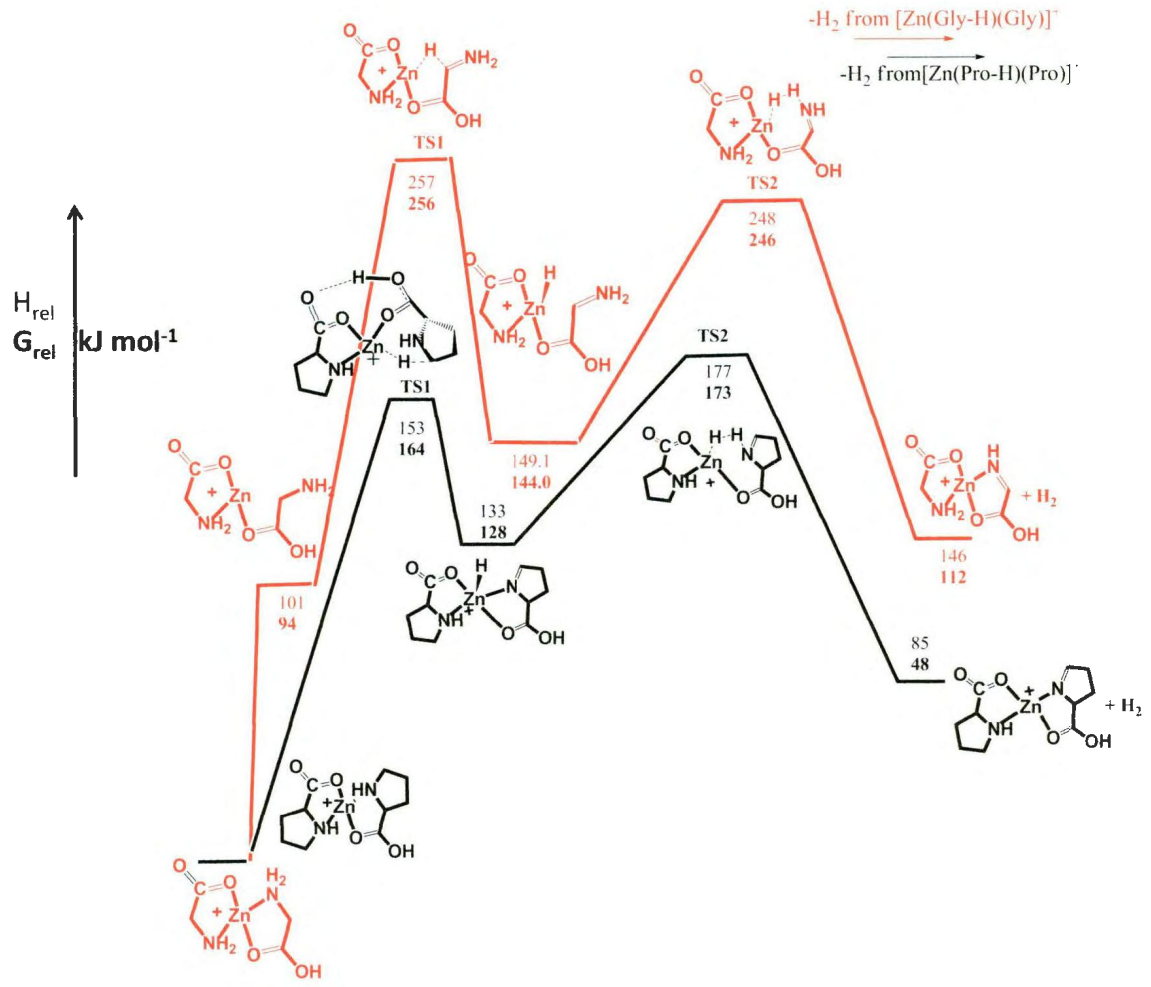

Figure 6.8. Energy diagram in kJ mol^{-1} for H_2 loss from $[Zn(Pro\text{-}H)(Pro)]^+$ complex in comparison with that from $[Zn(Gly\text{-}H)(Gly)]^+$ using MP2(full)/6-311++G(2d,2p)//B3LYP/6-31+G(d,p) (unbold values are enthalpies and bold values are Gibbs energies).

Catalytic dehydrogenation of amines to imines has been of research interest in synthetic organic chemistry.[27] For example, transition metal complexes such as iridium PCP pincer has been reported to catalyze the transformation of amines to imines.[28] This

dehydrogenation reaction is made possible by catalytic activation of a C-H bond adjacent to the N-H group followed by reductive elimination of H_2. In the present experiments, an intramolecular catalytic dehydrogenation occurs so that Zn^{2+} activates the C-H bond of the intact proline or sarcosine chelated to zinc resulting in hydrogen transfer to zinc. Hydridic hydrogen ($H^{\delta-}$) on zinc then absorbs the protic hydrogen ($H^{\delta+}$) on nitrogen to form a hydrogen molecule which would be subsequently expelled.

The energy diagram for proposed pathway for H_2 elimination from $[Zn(Pro-H)(Pro)]^+$ is shown in Figure 6.8, and is compared to the energy diagram for H_2 loss from the $[Zn(Gly-H)(Gly)]^+$ complex. The enthalpy and free energy requirements for the two transition states on route to dehydrogenation are 70-100 kJ mol^{-1} lower for the $[Zn(Pro-H)(Pro)]^+$ than for the $[Zn(Gly-H)(Gly)]^+$ complex. Furthermore, the H_2 elimination reaction for $[Zn(Pro-H)(Pro)]^+$ is 48 kJ mol^{-1} endothermic whereas the dehydrogenation of $[Zn(Gly-H)(Gly)]^+$ is 112 kJ mol^{-1} endothermic.

The energy diagram for dissociation of H_2O from $[Zn(Pro-H)(Pro)]^+$ and $[Zn(Gly-H)(Gly)]^+$ were computed and displayed in Figure 6.9 a and b in comparison with the H_2 elimination potential energy profiles. IRMPD and CID experiment for deuterated glycine and proline complexes showed that both hydrogens involved in H_2O loss are labile hydrogens. On this basis, in the proposed mechanism for H_2O loss, hydroxyl group transfers from carboxylic acid to zinc via TS1, in which OH migrating away from carboxylic acid group to attach Zn and remained carbonyl would be bound to carboxylic O of deprotonated amino acid to form a stabilized structure. In following step, NH hydrogen shifts to OH attached to zinc to form a new H-O bond via TS2. This

intermediate structure then eliminates H_2O. As seen in Figure 6.9a, in the case of glycine, elimination of H_2O is the energetically preferred fragmentation pathway. In contrast, H_2 elimination is the lower energy fragmentation pathway compared to H_2O loss for $[Zn(Pro\text{-}H)(Pro)]^+$ (Fig. 6.9b). This accounts for why H_2 elimination does not occur for $[Zn(Gly\text{-}H)(Gly)]^+$.

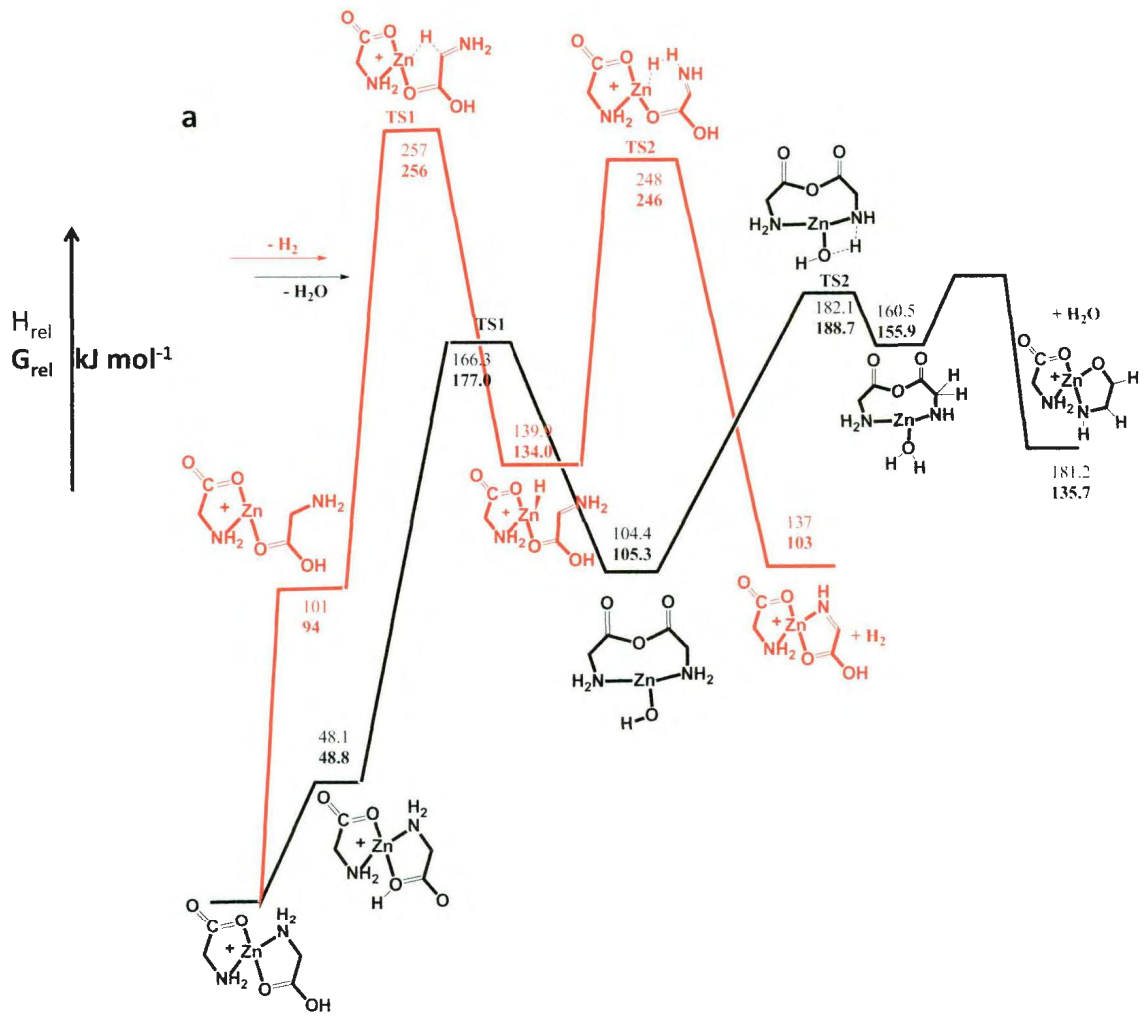
a
H_{rel}
G_{rel}
kJ mol^{-1}
- H_2
- H_2O
TS1
257
256
TS2
248
246
101
94
166.3
177.0
139.2
134.0
104.4
105.3
137
103
48.1
48.8
TS2
182.1
188.7
160.5
155.9
+ H_2O
181.2
135.7
+ H_2

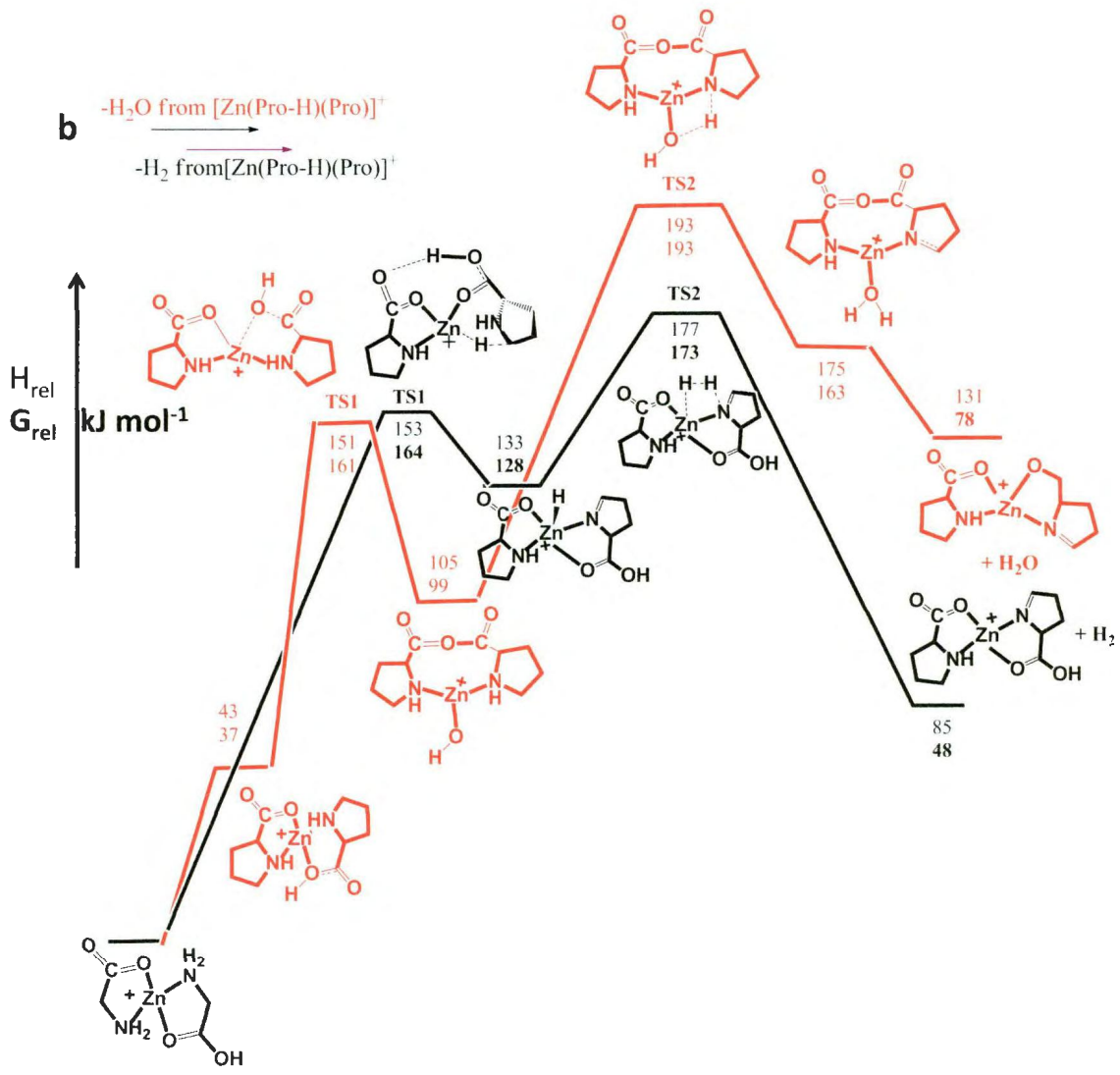

Figure 6.9. Energy diagram in kJ mol^{-1} for H_2 loss in comparison with H_2O loss from a) $[Zn(Gly\text{-}H)(Gly)]^+$ (black for H_2O loss red for H_2 loss) and b) $[Zn(Pro\text{-}H)(Pro)]^+$ (black for H_2 loss and red for H_2O loss) complex using MP2(full)/6-311++G(2d,2p)//B3LYP/6-31+G(d,p) (unbold values are enthalpies and bold values are Gibbs energies).

Different between energy barriers of glycine and proline complexes and consequently their fragmentation products can be explained by looking into the transition state structures computed for H_2 and H_2O losses. For the first transition state of H_2 loss

from $[Zn(Pro-H)(Pro)]^+$, in which hydrogen transfers from C5 to zinc, the ring of proline undergoes a rotation so that C5 places close to zinc. As a result of this rotation a hydrogen bond is formed between carboxylic acid H of intact proline and carboxylic O of deprotonated proline. This intramolecular hydrogen bond can have in stabilizing the transition state structure. This hydrogen bond is not seen in $[Zn(Gly-H)(Gly)]^+$ TS1 because the carbon that transfers its hydrogen to zinc is close enough to zinc and there is no rotation required for this process. In addition, NH_2 moiety in glycine transition state has moved away from zinc which probably destabilizes the transition state structure. This is not seen in proline because NH group is part of ring so it cannot freely move which is the case for glycine. In addition, more distance of amine moiety from zinc increases the second barrier energy of H_2 loss as well because the NH_2 hydrogen has to be aligned with the hydrogen attached to zinc for dehydrogenation process. As seen in dehydrogenation pathway for proline complex, amine H is close and aligned with ZnH in the intermediate structure before TS2. As a result, proline complex would require less rearrangement, and the barrier to the H_2 loss process would be lower in energy than H_2 elimination of glycine complex.

6.4. Conclusion

The fragmentation reactions of $[Zn(Pro-H)(Pro)]^+$ complex was probed using activation/fragmentation techniques such as IRMPD and SORI/CID. Elimination of H_2, interestingly, was the major fragmentation product of $[Zn(Pro-H)(Pro)]^+$. Using tandem

mass spectrometry of deuterium labeled complexes in conjunction with DFT calculations concluded that H_2 loss includes NH hydrogen and a hydrogen from α-CH_2 group. Furthermore, comparing fragmentation products of deprotonated proline, sarcosine, glycine, and alanine dimer complexes with Zn^{2+} showed that H_2 loss is a favourable fragmentation channel for secondary amines such as proline and sarcosine, which is not the case for primary amines such as glycine and alanine. H_2O elimination was the main fragmentation product for $[Zn(Gly-H)(Gly)]^+$ and $[Zn(Ala-H)(Ala)]^+$. The potential energy profiles for H_2 and H_2O loss revealed that in contrast to proline, H_2O loss is energetically preferred fragmentation channel for glycine.

References

(1) Kamariotis, A.; Boyarkin, O. V.; Mercier, S. R.; Beck, R. D.; Bush, M. F.; Williams, E. R.; Rizzo, T. R. *J. Am. Chem. Soc* **2005**, *128*, 905.

(2) Karlin, K. D.; Tyeklar, Z., Eds *Bioinorganic Chemistry of Copper*; Chapman and Hall, London, 1993.

(3) Lippard, S. J.; Berg, J. M. *Principles of Bioinorganic Chemistry*; University Science Books: Mill Valley, California,, 1994.

(4) Karlin, K. D.; J., Z. *Copper Coordination Chemistry*; Biological and Inorganic PerspectiVes. Adenine; Guilderland: New York,, 1983.

(5) Berg, J. M.; Shi, Y. *Sci* **1996**, *271*, 1081.

(6) Frankel, A. D.; Berg, J. M.; Pabo, C. O. *PNAS* **1987**, *84*, 4841.

(7) Cho, Y.; Gorina, S.; Jeffrey, P. D.; Pavletich, N. P. *Sci* **1994**, *265*, 346.

(8) Joerger, A. C.; Fersht, A. R. *Oncogene* **2007**, *26*, 2226.

(9) Travaglia, A.; Pietropaolo, A.; La Mendola, D.; Nicoletti, V. G.; Rizzarelli, E. *J. Inorg. Biochem.* **2012**, *111*, 130.

(10) Faller, P. *ChemBioChem* **2009**, *10*, 2837.

(11) Imanishi, M.; Matsumura, K.; Tsuji, S.; Nakaya, T.; Negi, S.; Futaki, S.; Sugiura, Y. *Biochem.* **2012**, *51*, 3342.

(12) Cuajungco, M. P.; Lees, G. J. *Brain. Res. Rev* **1997**, *23*, 219.

(13) Zhang, L.-H.; Wang, X.; Stoltenberg, M.; Danscher, G.; Huang, L.; Wang, Z.-Y. *Brain. Res. Bull* **2008**, *77*, 55.

(14) Polfer, N. C.; Oomens, J.; Moore, D. T.; von Helden, G.; Meijer, G.; Dunbar, R. C. *J. Am. Chem. Soc* **2006**, *128*, 517.

(15) Lavanant, H.; Hecquet, E.; Hoppilliard, Y. *Int. J. Mass spectrom.* **1999**, *185–187*, 11.

(16) Rogalewicz, F.; Hoppilliard, Y.; Ohanessian, G. *Int. J. Mass spectrom.* **2000**, *201*, 307.

(17) Deerfield, D. W.; Carter, C. W.; Pedersen, L. G. *Int. J. Quantum Chem* **2001**, *83*, 150.

(18) Rogalewicz, F.; Hoppilliard, Y.; Ohanessian, G. *Int. J. Mass spectrom.* **2001**, *206*, 45.

(19) Rogalewicz, F.; Hoppilliard, Y.; Ohanessian, G. *Int. J. Mass spectrom.* **2003**, *227*, 439.

(20) Woolfson, D. N.; Williams, D. H. *FEBS Lett.* **1990**, *277*, 185.

(21) Deber, C. M.; Brodsky, B.; Rath, A. In *eLS*; John Wiley & Sons, Ltd: 2001.

(22) Vitagliano, L.; Berisio, R.; Mastrangelo, A.; Mazzarella, L.; Zagari, A. *Protein Sci.* **2001**, *10*, 2627.

(23) Shoeib, T.; Hopkinson, A. C.; Siu, K. W. M. *J. Phys. Chem. B* **2001**, *105*, 12399.

(24) Frisch et al, M. J. *Gaussian 09, Revision A.01; Gaussian, Inc.: Wallingford, CT,* **2009**.

(25) Rajabi, K.; Easterling, M.; Fridgen, T. *J. Am. Soc. Mass. Spectrom.* **2009**, *20*, 411.

(26) Ali, O. Y.; Randell, N. M.; Fridgen, T. D. *ChemPhysChem* **2012**, *13*, 1507.

(27) Li, Q.; Zhou, S.; Wang, S.; Zhu, X.; Zhang, L.; Feng, Z.; Guo, L.; Wang, F.; Wei, Y. *Dalton Trans.* **2013**.

(28) Gu, X.-Q.; Chen, W.; Morales-Morales, D.; Jensen, C. M. *J. Mol. Catal. A: Chem.* **2002**, *189*, 119.

Chapter 7. Summary and Outlook

The goal of this thesis was to use mass spectrometry to obtain insight about reactions and structures of metal ion complexes in the gas phase. Ion cyclotron resonance mass spectrometry is a powerful tool to study ion-molecule reactions. It provides a low pressure environment in which elementary steps and mechanism of ion-molecule reactions can be investigated. In chapter 3 reactions between 14 electron unsaturated ruthenium complexes, $[Ru(bipy)(X)]^{2+}$, where (X = bipyridine, 2-(pyridin-4-yl)-1,3-benzothiazole, and 5-aminophenathroline), with CO and O_2 were studied at low pressures using a FTICR MS. For all three ruthenium complexes, ion-molecule association reactions were the only reaction observed in FT-ICR cell. For the mechanism of an ion-molecule association reaction, we know that the ion reacts with neutral molecule to produce a nascent adduct product, which is internally excited. This internally excited product can be stabilized either by third body collisions or by infrared radiative emission to produce a cooled adduct product. In our experiments, all observed bimolecular association rate constants were found to be independent of pressure, in a range of pressure between 10^{-8}-10^{-9} mbar, indicating that collisions within the ICR were not responsible for cooling of the initially formed excited adducts. Radiative association rate constants were also calculated to be small values, so the energy of association cannot efficiently be dissipated by radiative means. There is the other possibility for a nascent complex to be back dissociation to its reactants. However, the strong binding energies for $[Ru(bipy)(X)]^{2+}/O_2$ and $[Ru(bipy)(X)]^{2+}/CO$, which are determined by computational studies, hinders the back dissociation of nascent adduct complexes. These results reasonably explain why experimental rate constants for the association of CO and O_2 to

$[Ru(bipy)(X)]^{2+}$ complexes were determined to be very similar to the theoretical ion/molecule collision rate constants, concluding that ion-molecule reactions in the ICR cell occur at the collision rate producing a nascent ion-molecule complex which is observed in the mass spectrometer. Therefore, the observed adduct complexes were hypothesized to be internally hot or chemically activated species. In chapter 4, we employed these chemically activated ion–molecule complexes to perform dehydrogenation and demethanation reactions of hydrocarbons in the gas phase. The nascent adduct complex $[Ru(bipy)_2CO]^{2+*}$ was formed by addition of CO to $[Ru(bipy)_2]^{2+}$ in the ICR cell, and allowed to react with propane and 2-methyl-propane leading to dehydrogenation and demethanation products. On the contrary, in the reaction of $[Ru(bipy)_2]^{2+}$ with propane or 2-methyl-propane the association of the hydrocarbon was the only product observed.

In all chapters of the present thesis, computational chemistry plays a complementary role to obtain information about the structures, mechanism and energetic of reactions. The relative enthalpies and Gibbs energies of structures involved in the dehydrogenation and demethanation calculated using the MP2(full)/ 6-311+G(d,p)//B3LYP/6-311+G(d,p) level of theory for all atoms except Ru, for which LANL2DZ basis set and effective core reasonably explained the results. The significant changes in reaction pathway resulting from ligation with CO were attributed to the internal energy of the hot intermediate complex, $[Ru(bipy)_2(CO)]^{2+*}$. The dehydrogenation and demethanation can occur in the case of $[Ru(bipy)_2(CO)]^{2+*}$ since the barrier energies required can be supplied by the internal energy of the newly formed

complex. Further, it was concluded the reactions occur via a concerted mechanism rather than oxidative addition/reductive elimination. In the future it would be important to study reactions between inorganic complexes containing different metals (i.e. Pt^{2+}, Pd^{2+}) and alkanes, since it was previously reported that Pt(II) and Pd(II) complexes are active catalyst for C-H bond activation of methane in the solution phase.[1,2] Different transition metal complexes involving Ir(III), such as $Ir(H)_2(Me_2CO)(PPh_3)_2$ or $(PCP)Ir(H)_2$ [PCP= η^3-$C_6H_3(CH_2PBut'_2)_2$]$^+$ were found as active catalysts for dehydrogenation of alkanes in the solution phase.[3-5] It would be interesting to study these reactions in the gas phase.

The structures and fragmentation reactions of zinc-amino acids complexes were examined in chapters 5 and 6, using IRMPD and SORI-CID techniques. It was observed that amino acids such as glycine, alanine, sarcosine, and proline form deprotonated complexes with Zn^{2+} to produce $[Zn(A-H)]^+$ A=amino acid. Using MP2(full)/6-311++G(2d,2p)//B3LYP/6-31+G(d,p) theory, the lowest energy structure for $[Zn(Pro-H)]^+$ was computed to be one (H-type structure) in which a hydrogen is transferred from the C5 group to zinc, and Zn^{2+} is bound to the deprotonated amine nitrogen and the carbonyl oxygen of the carboxylic acid group. The B3LYP/6-31+G(d,p) infrared spectrum of H-type structure was the best match with the IRMPD spectrum confirming the structure. It was interesting that Zn^{2+} and Pb^{2+} showed different behavior in interaction with proline. The amine- and carboxlic acid-deprotonated structures for $[Pb(Pro-H)]^+$ were computed to be the lowest and responsible for the IRMPD spectrum, with Pb^{2+} coordinated between the carbonyl O and amine N. The structure $[Zn(Pro-H)]^+$ with a single water molecule added was also examined, and the analogous structure, in

which water is simply added to the H-type structures of $[Zn(Pro-H)]^+$ and intramolecularly hydrogen bonded to the amine site was found to be the best match for IRMPD spectrum. This chapter illustrated the significant influence of metal ions on the structure of small biological molecule like amino acids, which would be interesting for further studies of different transition metal that are important in biological systems, such as Cu^{2+}, Fe^{2+}, or Co^{2+}. In chapter 6, fragmentation of deprotonated Zn^{2+}/amino acid dimer complexes ($[Zn(A-H)(A)]^+$ where A=Pro, Sar, Ala, and Gly) were investigated using IRMPD and SORI-CID. Interestingly, the fragmentation reaction of $([Zn(A-H)(A)]^+$ was found to be different for when A was a secondary amine such as proline or sarcosine than when A was a primary amine such as glycine and alanine. Dehydrogenation of amines to imines was found to be primary fragmentation reaction for proline and sarcosine complexes, whereas this reaction was absent for glycine and alanine complexes and loss of water was the dominant fragmentation reaction. The dehydrogenation and dehydration pathways were compared for glycine and proline by means of computational studies, indicating that the energetically preferred fragmentation pathway is loss of H_2 for $[Zn(Pro-H)(Pro)]^+$, but is loss of H_2O for $[Zn(Gly-H)(Gly)]^+$. This study gives insight into the structures, binding sites and interactions of zinc-deprotonated di-amino acids complexes, and keeps the door open to find out more about the structures of these complexes.

For future work, it would be interesting to study interaction of Zn^{2+} with alkyl amines or alkanoamines and investigate whether dehydrogenation of amines across C-N bond can occur. Catalytic dehydrogenation of amines to imines by means of metal

complexes is of high scientific interest in synthetic organic chemistry. For example, it was previously found that the Irridium PCP princer complex can catalyze dehydrogenation of tetramethyldibutylamine to the corresponding imine.[6] Analogous to the interamolecular dehydrogenation of $Zn^{2+/}$dimeric amino acid complexes observed in our experiments, zinc would be expected to similarly catalyze dehydrogenation in a variety of organic compounds involving C-N bonds.

References

(1) Periana, R. A.; Taube, D. J.; Gamble, S.; Taube, H.; Satoh, T.; Fujii, H. *Science* **1998**, *280*, 560.

(2) Hennry, P. M. *Palladium Catalyzed Oxidation of Hydrocarbons*; Springer, 1979; Vol. 2.

(3) Renkema, K. B.; Kissin, Y. V.; Goldman, A. S. *J. Am. Chem. Soc.* **2003**, *125*, 7770.

(4) Crabtree, R. H.; Mihelcic, J. M.; Quirk, J. M. *J. Am. Chem. Soc.* **1979**, *101*, 7738.

(5) Crabtree, R. H. *J. Organomet. Chem.* **2004**, *689*, 4083.

(6) Gu, X.-Q.; Chen, W.; Morales-Morales, D.; Jensen, C. M. *J. Mol. Catal. A: Chem.* **2002**, *189*, 119.

Appendix

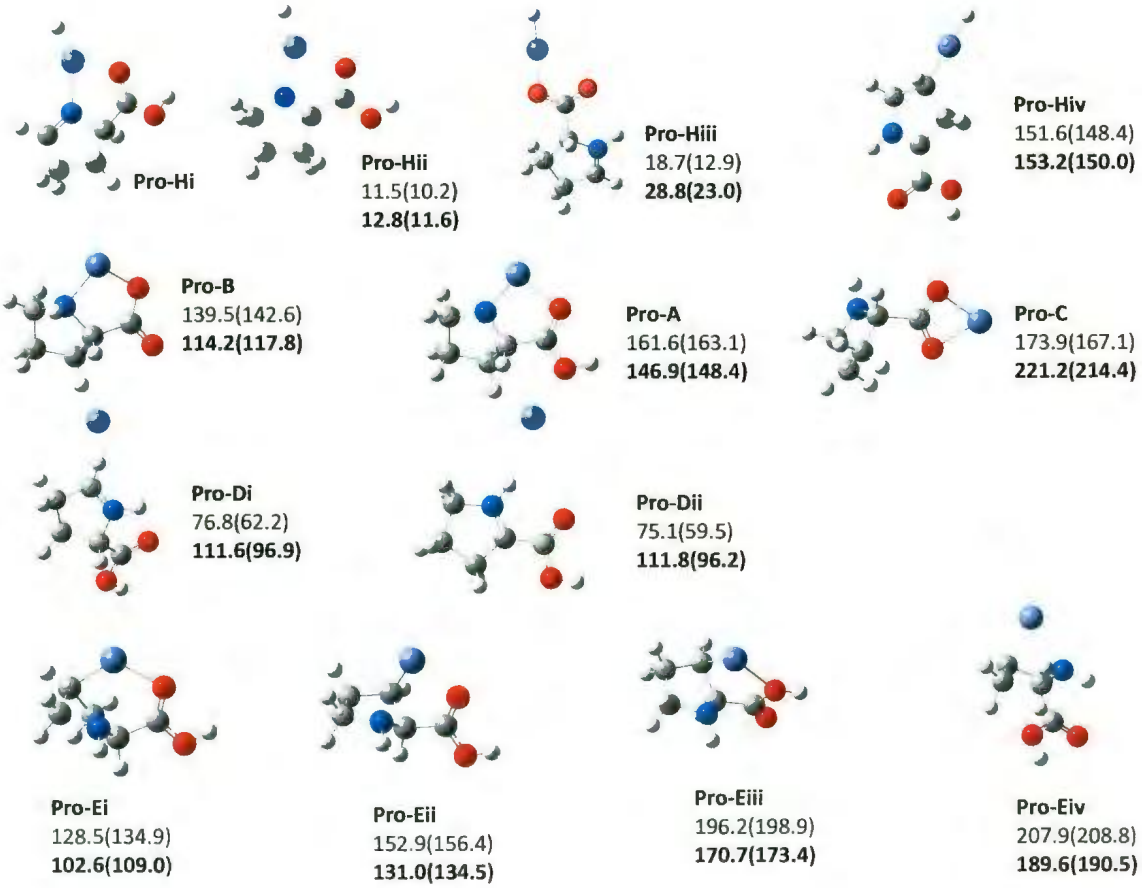
Pro-Hi
Pro-Hii
11.5(10.2)
12.8(11.6)
Pro-Hiii
18.7(12.9)
28.8(23.0)
Pro-Hiv
151.6(148.4)
153.2(150.0)
Pro-B
139.5(142.6)
114.2(117.8)
Pro-A
161.6(163.1)
146.9(148.4)
Pro-C
173.9(167.1)
221.2(214.4)
Pro-Di
76.8(62.2)
111.6(96.9)
Pro-Dii
75.1(59.5)
111.8(96.2)
Pro-Ei
128.5(134.9)
102.6(109.0)
Pro-Eii
152.9(156.4)
131.0(134.5)
Pro-Eiii
196.2(198.9)
170.7(173.4)
Pro-Eiv
207.9(208.8)
189.6(190.5)

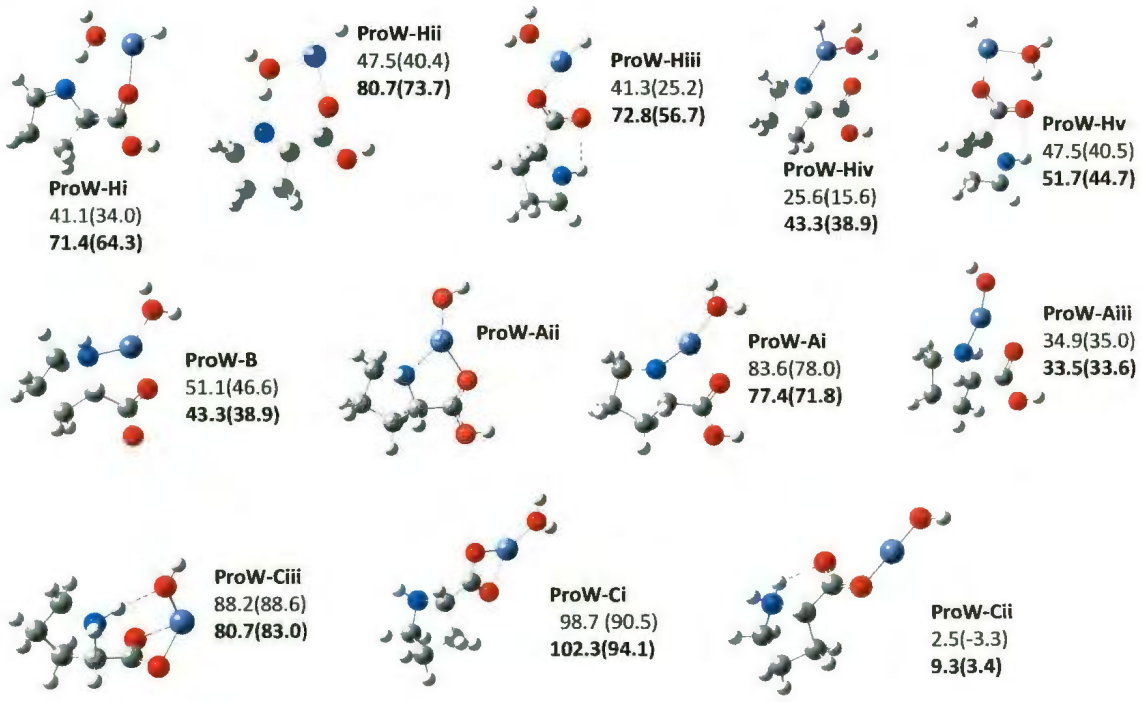

Appendix 1. Computed structures for $[Zn(Pro\text{-}H)]^+$ and $[Zn(Pro\text{-}H)(H_2O)]^+$ complexes. The 298 K enthalpies and Gibbs energies (in parentheses) are reported at the B3LYP/6-31+G(d,p) and MP2(full)/6-311++G(2d,2p)//B3LYP/6-31+G(d,p) (in bold) and are in kJ mol^{-1}.

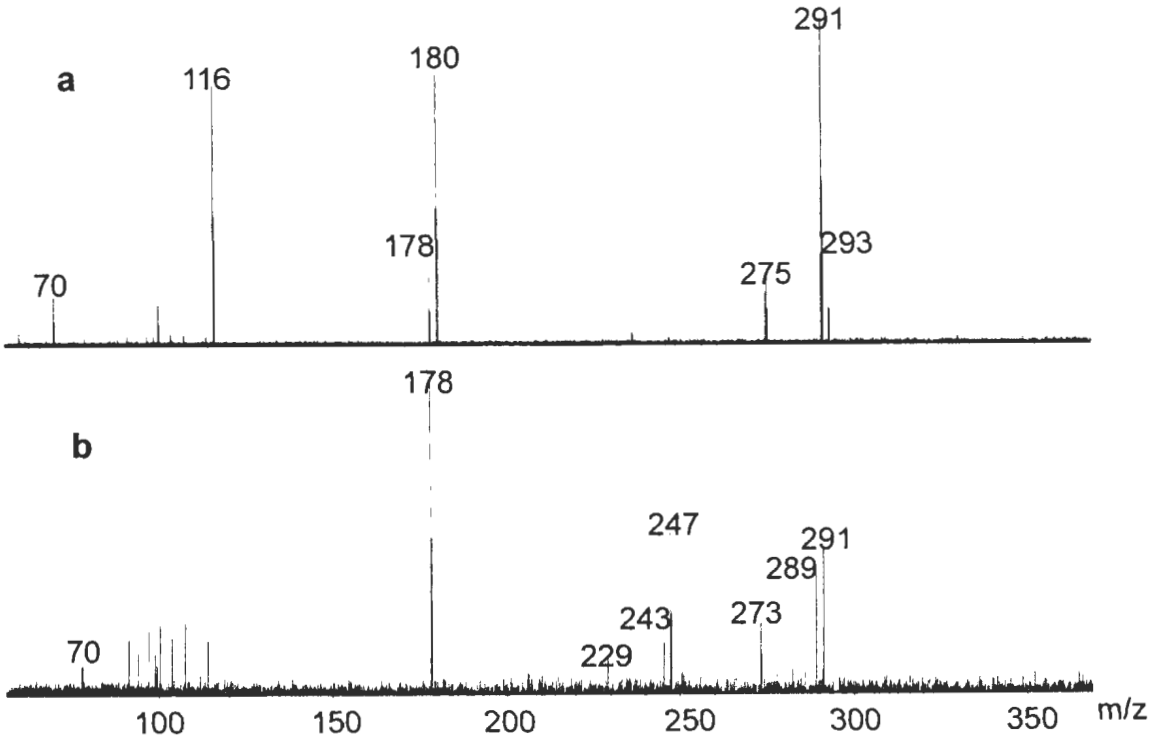

Appendix 2. SORI-CID spectra with a SORI power of 0.24 ev (c.o.m) for a) $[Zn(Pro-H)(Pro)]^+$ (m/z 293) and b) m/z 291 formed by SORI-CID of m/z 293.

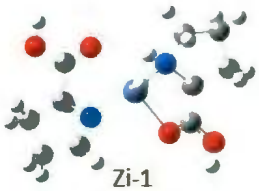

Zi-1
50.5/40.7
72.3/62.5

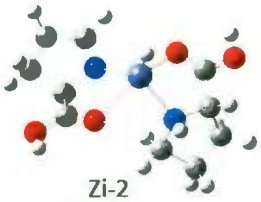

Zi-2
54.0/45.6
72.4/63.9

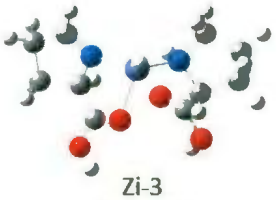

Zi-3
58.4/51.9
75.7/69.1

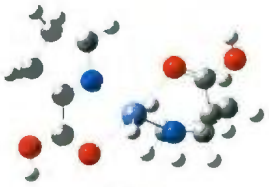

Zii-1
50.8/43.7
70.8/63.7

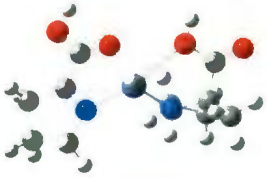

Zii-2
92.9/79.8
113.8/100.7

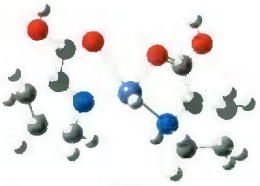

Zii-3
63.3/53.9
87.9/78.6

Ziii-1
102.9/87.2
141.1/125.3

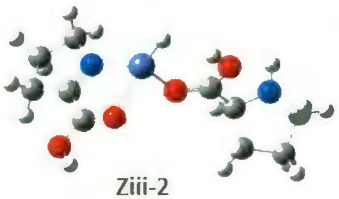

Ziii-2
102.6/89.3
141.4/128.0

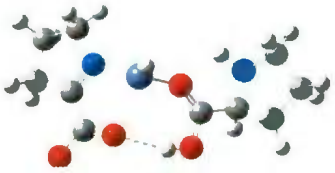

Ziii-3
109.0/96.2
150.8/138.0

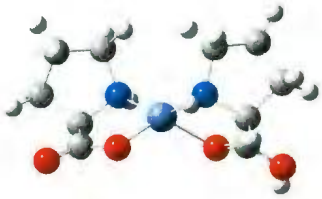

N1
0/0
0/0

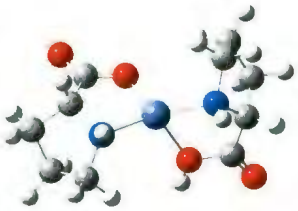

N2
43.3/41.2
36.2/34.1

N3
54.4/50.1
55.3/51.0

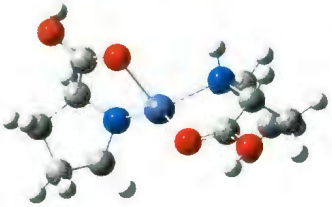

N4
50.3/47.6
51.7/49.0

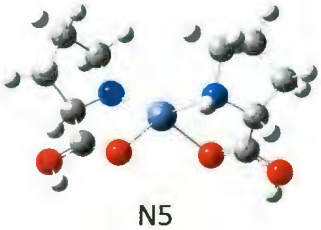

N5
58.3/57.3
65.5/64.5

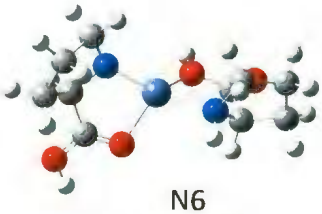

N6
90.4/81.2
89.2/80.1

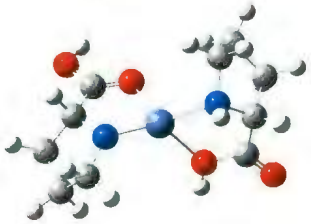

N7
95.1/87.0
33.2/25.1

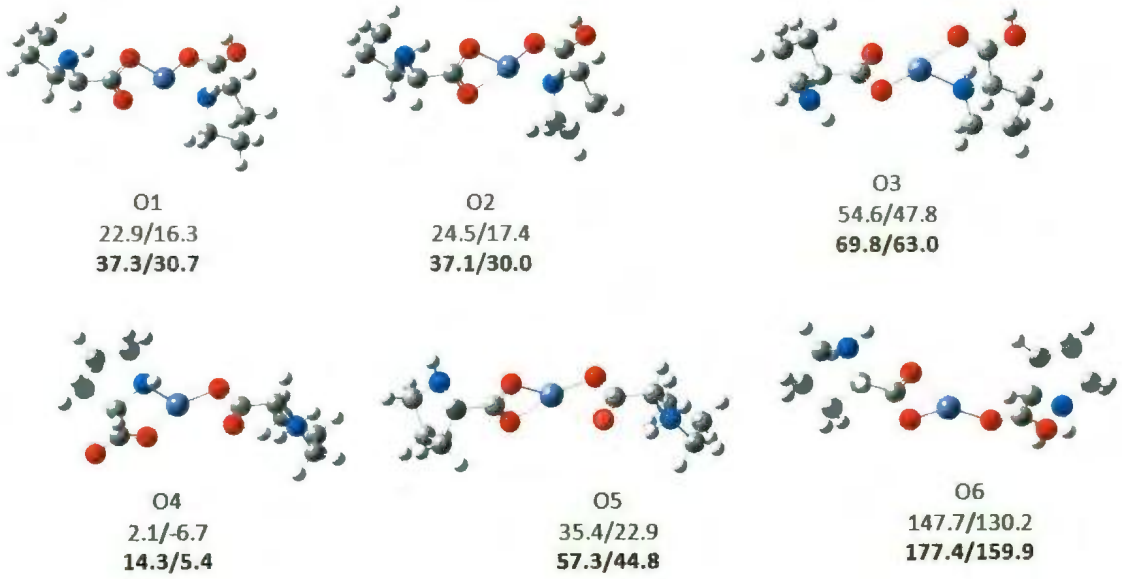

Appendix 3. Computed structures of the $[Zn(Pro\text{-}H)(Pro)]^+$ complex. 298 K enthalpies/Gibbs energy seen are computed using B3LYP/6-31+G(d,p) and MP2(full)/6-311++G(2d,2p)//B3LYP/6-31+G(d,p) (bold).

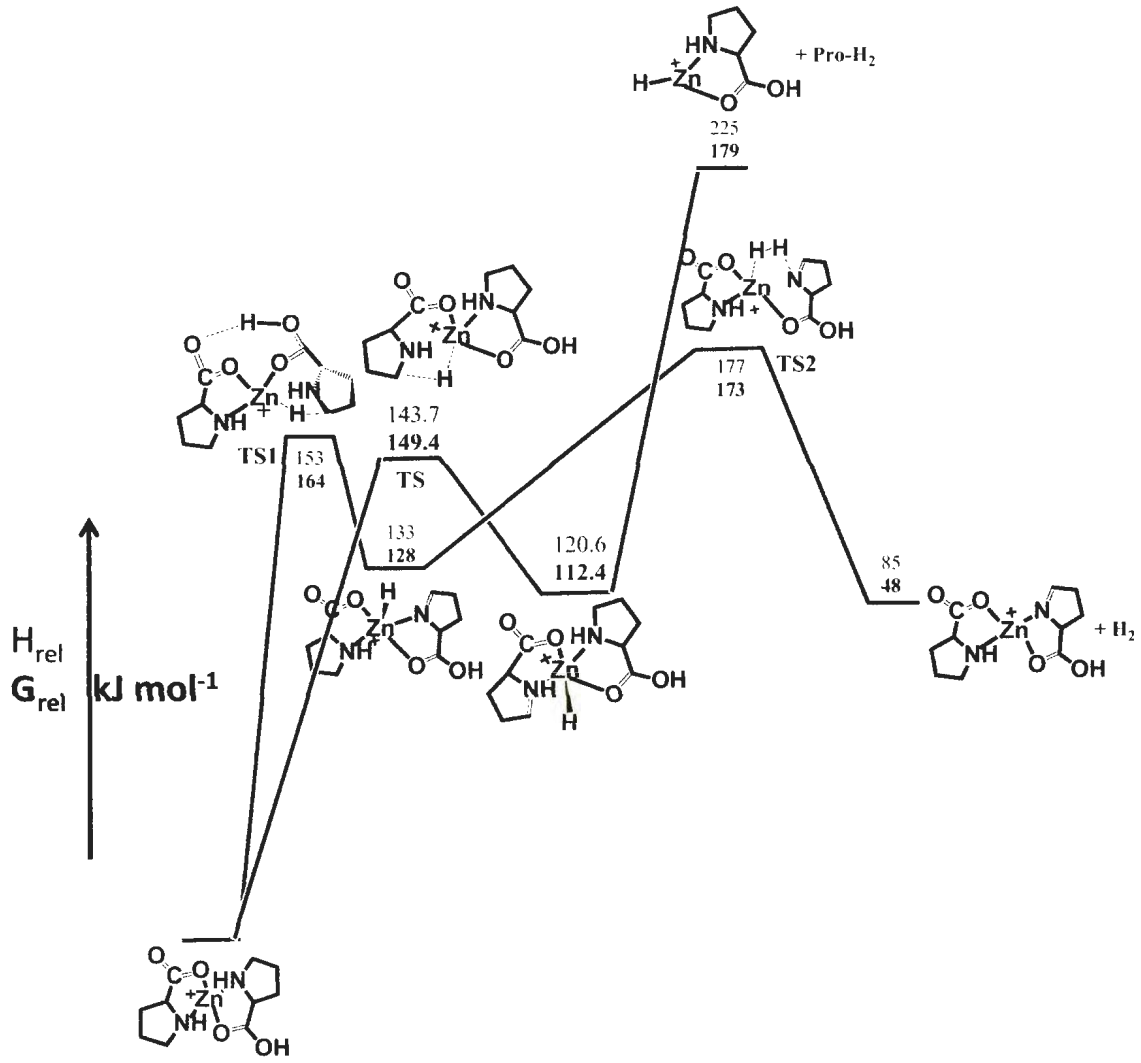

Appendix 4. Energy diagram in kJ mol^{-1} for Pro-H_2 loss in comparison with H_2 loss from $[Zn(Pro\text{-}H)(Pro)]^+$ using MP2(full)/6-311++G(2d,2p)//B3LYP/6-31+G(d,p) (unbold values are enthalpies and bold values are Gibbs energies).

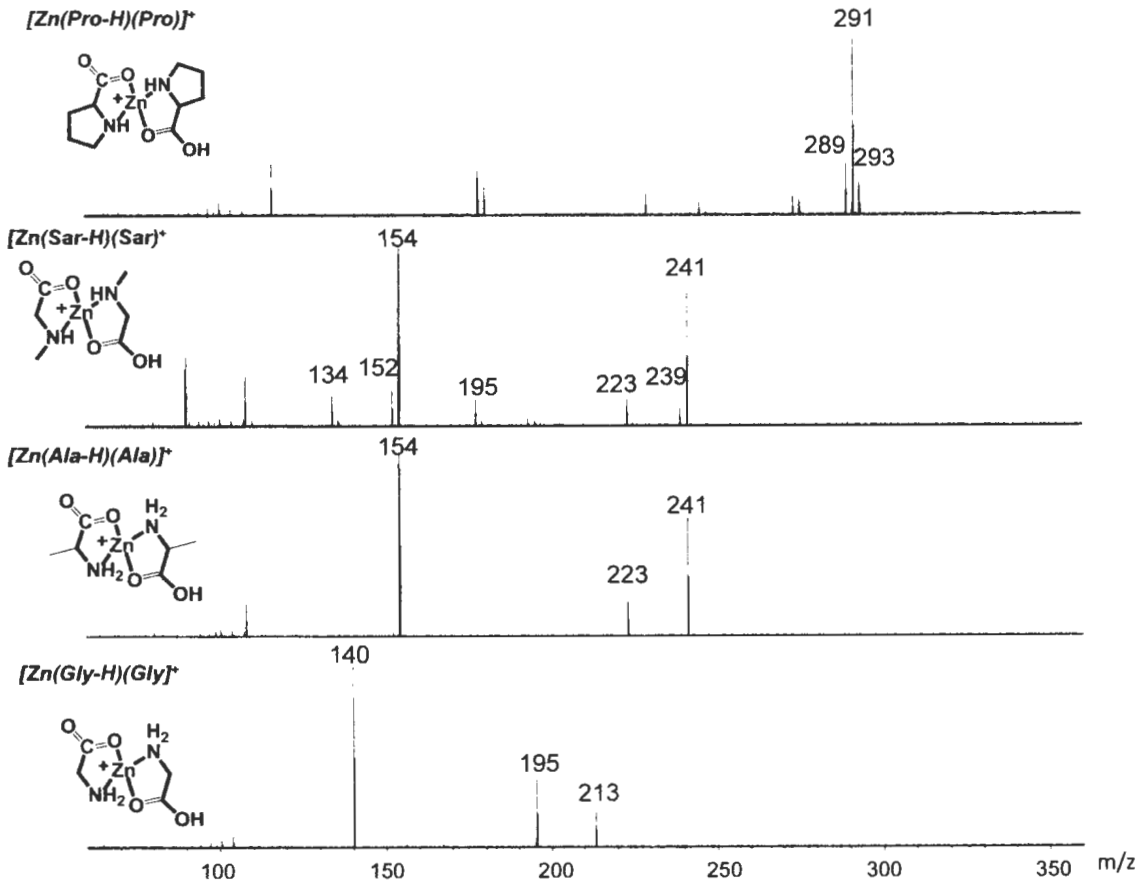

Appendix 5. (CO_2 laser-IRMPD) activation/fragmentation of $[Zn(A-H)(A)]^+$ where A is proline, sarcosine, glycine, and alanine using the laser power 40 % of maximum power and 1.5 sec pulse length.